

Durham E-Theses

Simulating salt precipitation during CO₂ injection in brine aquifers

LEWIS, HELENA,LOUISE

How to cite:

LEWIS, HELENA,LOUISE (2019) *Simulating salt precipitation during CO₂ injection in brine aquifers*, Durham theses, Durham University. Available at Durham E-Theses Online:
<http://etheses.dur.ac.uk/13040/>

Use policy

The full-text may be used and/or reproduced, and given to third parties in any format or medium, without prior permission or charge, for personal research or study, educational, or not-for-profit purposes provided that:

- a full bibliographic reference is made to the original source
- a [link](#) is made to the metadata record in Durham E-Theses
- the full-text is not changed in any way

The full-text must not be sold in any format or medium without the formal permission of the copyright holders.

Please consult the [full Durham E-Theses policy](#) for further details.

Simulating Salt Precipitation During CO₂ Injection in Brine Aquifers

Helena Louise Kelly

A thesis submitted in partial fulfilment of the requirements for the degree of
Doctor of Philosophy at Durham University

Department of Earth Sciences
Durham University

April 15, 2019

Abstract

Carbon capture and storage (CCS) is a potentially very useful way of reducing anthropogenic CO₂ emissions whilst continuing to be able to use fossil fuels. In CCS, CO₂ is prevented from entering the atmosphere by being captured from power plants and stored long-term, most commonly by being injected into rock formations deep underground. Saline aquifers have been strongly considered as target formations for CO₂ storage due to their common occurrence, large storage volumes and suitable depths. However, injecting CO₂ into a saline aquifer can remove liquid water from the site of injection, both by the water being displaced immiscibly by the advancing gas and by some water evaporating into the carbon dioxide-rich gas phase, which can cause formation dry out, leading to salt precipitating in the pores of the rock around the injection well. This salt precipitation can be enhanced by high capillary pressure gradients in the dry out zone of the formation, which provide a driving force for brine to flow back towards the site of injection in a process called counter-current imbibition, hence providing additional salt that can also precipitate. There is a concern that the loss in permeability and injectivity caused by this salt precipitation may be a limitation in the use of saline aquifers for carbon sequestration.

This work aims to simulate the build-up of salt precipitation in a saline formation when CO₂ is injected, in order to investigate the effects that various parameters have on salt precipitation and, ultimately, whether storing CO₂ in saline aquifers is a feasible method of CCS. To do this, finite difference methods and MATLAB's ordinary differential equation (ODE) solvers are used to form numerical models of both two and three phase flow within an aquifer. Pseudospectral methods are also used to find a similarity solution for three component and three phase flow. All models and solutions incorporate the effects of partial miscibility between phases and capillary pressure, both of which have been neglected in some previous studies on this subject.

It is concluded that there are several factors that affect the volume fraction of salt precipitation around the injection well of a saline formation caused by CO₂ injection, C_{30} , including the salinity of the brine, the storage depth and the relative permeabilities, but the value is largely controlled by a capillary number, Ca . This takes into account the effects of the thickness, permeability and air-entry pressure of the formation and the injection rate and dynamic viscosity of CO₂. As Ca decreases, the value of C_{30} superlinearly increases. In one scenario studied, reducing the CO₂ injection rate from 15 kg s⁻¹ to 0.9 kg s⁻¹ led to a tenfold increase in the volume fraction of precipitated salt.

Contents

Abstract	2
List of Figures	8
List of Tables	16
Nomenclature	18
Declaration	24
Acknowledgements	25
1 Introduction	26
1.1 Introduction to Carbon Capture and Storage and Saline Aquifers	26
1.2 Introduction to Numerical Modelling for Saline Aquifers	29
1.3 Salt Precipitation after CO ₂ Injection	31
1.4 Capillary Pressure and Counter-Current Imbibition	34
1.5 Project Objective	36
1.6 Thesis Overview	37

2	Governing Equations and Phase Equilibrium	38
2.1	The Multicomponent, Multiphase System	38
2.2	Governing Equations	39
2.2.1	Mass Balance Equation	39
2.2.2	Darcy's Law for Multiphase Flow	40
2.2.3	Relative Permeability	41
2.2.4	Capillary Pressure	43
2.3	Mass Fractions at Equilibrium	49
2.3.1	Chemical Potential and Gibbs Energy	49
2.3.2	Chemical Potential for Ideal Gas Mixtures	50
2.3.3	Chemical Potential for Non-Ideal Gas Mixtures	52
2.3.4	Chemical Potential of Ideal Solutions	53
2.3.5	Chemical Potential of Non-Ideal Solutions	53
2.3.6	Expressions for y_{H_2O} and x_{CO_2}	54
2.3.7	Solving for y_{H_2O} and x_{CO_2}	58
2.3.8	Solubility of Salt in the Aqueous Phase	61
2.3.9	Phase Diagrams	61
3	Solutions for Incompressible Two Component and Two Phase Flow	65
3.1	Dimensionless Transformation	66
3.2	The Two Component, Two Phase System	67

3.3	Solving PDEs using the Method of Lines	69
3.3.1	Finite Difference Approximations	69
3.3.2	Ordinary Differential Equation Solvers	73
3.3.3	Solving Equation (3.4) using the Method of Lines	75
3.3.4	Upwinding	76
3.4	Solving PDEs using the Method of Characteristics	78
3.4.1	The Method of Characteristics for an Immisible System	78
3.4.2	Discontinuities and Shocks	81
3.4.3	The Method of Characteristics for a Partially Miscible System	87
3.5	Volume Change on Mixing	91
3.6	Chapter Summary and Conclusions	96
4	Method of Lines Solution for Compressible Two Component and Two Phase Flow with Capillary Pressure	98
4.1	Conceptual Model	99
4.2	Numerical Grid	99
4.3	Primary Dependent Variables	101
4.4	Defining Regions	102
4.4.1	Finding Expressions for $\frac{\partial z_c}{\partial t}$ and $\frac{\partial P}{\partial t}$	104
4.5	Derivatives of F	105
4.5.1	Finding the Overall Derivative of F, dF	105

4.5.2	Finding an Expression for $\frac{\partial F}{\partial z_c}$	108
4.5.3	Finding an Expression for $\frac{\partial F}{\partial P}$	111
4.6	Use of Upwinding	116
4.7	Model Output	118
5	Method of Lines Solution for Compressible Three Component and Three Phase Flow with Capillary Pressure	124
5.1	The Three Component, Three Phase System	125
5.2	Primary Dependent Variables (PDVs)	125
5.3	Phases Present	126
5.3.1	No Gaseous Phase	126
5.3.2	No Aqueous Phase	128
5.3.3	Both Gaseous and Aqueous Phases Present	129
5.3.4	Presence or Absence of a Solid Phase	129
5.4	X_{ij} Values	130
5.5	Phase Saturation Values	134
5.5.1	Solid Saturation (S_s)	134
5.5.2	Aqueous Saturation (S_a)	137
5.5.3	Gaseous Saturation (S_g)	139
5.6	Finding Expressions for $\frac{\partial z_c}{\partial t}$, $\frac{\partial z_w}{\partial t}$ and $\frac{\partial P}{\partial t}$	139
5.6.1	Expressions for $\frac{\partial z_c}{\partial t}$ and $\frac{\partial z_w}{\partial t}$	139

5.6.2	An Expression for $\frac{\partial P}{\partial t}$	141
5.7	Derivatives of F	141
5.7.1	Finding the Overall Derivative of F, dF	141
5.7.2	Finding an Expression for $\frac{\partial F}{\partial z_c}$	142
5.7.3	Finding an Expression for $\frac{\partial F}{\partial z_w}$	151
5.7.4	Finding an Expression for $\frac{\partial F}{\partial P}$	156
5.8	Model Output	163
6	Self-Similar Pseudospectral Solution for Incompressible Three Component and Three Phase Flow	170
6.1	Introduction	171
6.2	The McWhorter and Sunada Solution	173
6.3	Pseudospectral Methods	176
6.4	Mathematical Model	180
6.4.1	Writing Capillary Pressure in Terms of C_1	184
6.4.2	Relative Permeability and Capillary Pressure Functions	186
6.4.3	Determination of S_{em}	187
6.4.4	Application of a Similarity Transform	188
6.4.5	Pseudospectral Solution	190
6.4.6	Dealing with Salt Precipitation in the Dry Out Zone	191
6.5	Sensitivity Analysis	193

6.5.1	Gas Displacing Oil	193
6.5.2	CO ₂ Injection in a Saline Formation	194
6.6	Discussion of Key Modelling Assumptions	203
6.6.1	Incompressible Fluids	203
6.6.2	No Volume Change on Mixing	204
6.6.3	Ignoring Gravity Effects	205
6.7	Chapter Summary and Conclusions	206
7	Summary, Conclusions and Future Work	208
7.1	Summary and Conclusions	208
7.2	Future Work	213
	Bibliography	214

List of Figures

1.1	A graph to show the variation in both global annual average temperature and CO ₂ concentration from 1880 to 2009. The grey line represents the mean global temperature from 1901 to 2000, while red bars indicate years with an average temperature above this line and blue bars indicate years with average temperatures below the line. The black line shows the change in atmospheric CO ₂ concentration in parts per million (NOAA, 2010). . . .	27
1.2	A cartoon to show how gas saturation varies from the point of injection. Adapted from Hosseini et al. (2012)	33
1.3	A graph to show how permeability reduction factor varies as the porosity reduction factor changes (Mathias et al., 2013).	34
1.4	A schematic of a two-dimensional pore body and pore throat configuration (Zhao and Wen, 2017). r_{Body} and r_{Throat} represent the radius of the pore body and pore throat respectively.	34
1.5	A figure to illustrate the ‘tubes in series’ model that is used to represent pore throat effects and the variability of the radius of the cross-section of a flow channel (Verma and Pruess, 1988).	35
1.6	A schematic of CO ₂ injection in a saline aquifer, showing the possible configuration of phases and the backflow of brine (Miri and Hellevang, 2016).	36

2.1	A diagram to illustrate the mass balance equation. Here, the cube represents the control volume V , and the diagram considers only one component i	39
2.2	Relative permeability curves for various different sandstone rocks when two phases are flowing, constructed using the power law functions in the second row of equation (2.10) (Adapted from Mathias et al. (2013)). The relative permeability of the gaseous phase is represented by a solid line and the relative permeability of the aqueous phase is shown by a dashed line. The endpoint relative permeability (k_{rg0}) and the residual aqueous saturation (S_{ar}) for Otway are shown in purple, and for Berea #1 are shown in green. The data used to construct these curves came from Perrin and Benson (2010) and Krevor et al. (2012).	43
2.3	P_c vs S_a curves for (a) the van Genuchten model and (b) the Brooks Corey model (Adapted from Li et al. (2013)). Note the S-shape of the van Genuchten model and the convex shape of the Brooks-Corey model, caused by differences in the representation of the capillary entry pressure, $P_{c,e}$. In the van Genuchten model, the region around the endpoint is termed the ‘entry slope’ region, the height of which is the pressure difference between the plateau and the endpoint of the curve at $S_a = 1$	45
2.4	A representative van Genuchten capillary pressure function including linear extension. Adapted from Webb (2000).	47
2.5	A phase diagram, plotting the mole fraction of H_2O against pressure, to illustrate the different phase combinations that occur for a two component (CO_2 and H_2O) system at a temperature of $25^\circ C$. Note that within this figure, V represents the vapor phase, L_1 is the H_2O -rich liquid phase and L_2 is the CO_2 -rich supercritical phase. The data points show CO_2 solubility in the H_2O -rich phase (open circles) and H_2O solubility in the CO_2 -rich phase (open squares), using data from Wiebe and Gaddy (1940), Wiebe and Gaddy (1941), Coan and King (1971), Gillepsie and Wilson (1982) and King et al. (1992). The inset of the figure shows the region in which all three phases can coexist in greater detail (Spycher et al., 2003).	62

2.6	A ternary phase diagram showing the structure of phases within the three component system of CO ₂ , H ₂ O and NaCl for a fixed pressure of 10 MPa and a fixed temperature of 60°C. Note that Z_i refers to the mole fraction of component i . The bubble, precipitation and dew lines have been highlighted in green, blue and red respectively in this figure. Adapted from Fuller et al. (2006).	64
2.7	Subfigures to illustrate Figure 2.6 zoomed in, in order to show the different phase combinations that are too small to be seen clearly in the original figure. Adapted from Fuller et al. (2006).	64
3.1	An illustration of how the finite difference method can be used to approximate the derivative $\frac{df}{dx}$	70
3.2	A diagram to show various finite difference approximations of $f'(\bar{x})$ interpreted as the slope of secant lines. (Adapted from LeVeque (2007, p.4)). . .	71
3.3	A diagram to show the discretisation of the ξ axis. ξ_k represents the node at the centre of a particular cell k , while ξ_{k-1} and ξ_{k+1} represent the nodes at the centres of the cells to the left and right of k , cells $k - 1$ and $k + 1$, respectively. $\xi_{k-\frac{1}{2}}$ and $\xi_{k+\frac{1}{2}}$ represent the boundaries between cells k and $k - 1$, and cells k and $k + 1$, respectively. l_k is the length of the cell k , and there are N nodes in total.	76
3.4	A diagram to show the propagation of a wave in the positive ξ direction at a given instant of time. It illustrates that choosing the value of H_{iD} at node $k + 1$ to approximate $H_{iD_{k+\frac{1}{2}}}$ would be inaccurate, because the propagating wave has not yet reached this point. v represents the velocity of the advancing wave, where v_L denotes the velocity to the left of the propagating front, and v_R denotes the velocity to the right. Adapted from Goudarzi (2017).	77
3.5	A curve $(\xi(\tau), \tau)$ in the $\xi - \tau$ plane. Adapted from (Knobel, 2000, p.128).	79
3.6	Characteristic curves for the initial composition of the fluid in the system, $S_g = 0$	80

3.7	An example of how characteristics for a particular PDE can intersect at a point (ξ, τ) . Adapted from (Knobel, 2000, p.137).	81
3.8	The gradients of the characteristic curves of equation (3.43), $\frac{df_g}{dS_g}$, for every possible value of S_g	82
3.9	Characteristic curves for a small number of compositions as they travel through the formation from the point of injection.	83
3.10	A diagram showing the motion of a shock (Adapted from Orr (2007, p.70)).	84
3.11	A tangent drawn between point a (the initial value of S_g) and point b (the value of S_g immediately upstream of the shock) as part of the construction of the shock.	86
3.12	A plot of $\frac{df_g}{dS_g}$ against S_g to illustrate the method used by Buckley and Leverett (1942) to find the location of the shock. The dotted line represents the shock while the letters A and B denote the two areas that should be equal.	87
3.13	A graph to show S_g plotted against ξ for several different values of τ , as found by both the MOC and the MOL, for the parameter values shown in Table 3.1. The MOL solution is shown by the solid lines, and the MOC solution by the dashed lines.	88
3.14	Schematic diagram illustrating the variation in gas saturation, including the discontinuities, from the point of injection for a two phase, two component system with constant fluid properties and partial miscibility.	89
3.15	A graph to show G_{cD} plotted against ξ for several different values of τ , as found by both the MOC and the MOL, for the parameter values shown in Table 3.1 as well as those given above. The MOL solution is shown by the solid lines, and the MOC solution by the dashed lines. Note that the ξ -axis is plotted on a logarithmic scale.	91

3.16	Plots showing the displacement of C_{10} by CO_2 (Adapted from Orr (2007, p.91)). Solutions found using the MOC are shown with and without volume change as components transfer between phases, and a MOL solution is plotted for values of τ ranging from 0 to 30, in which the effects of volume change on mixing are included. (a) plots ξ/τ against the non-dimensionalised mass fraction of CO_2 , z_{cD} (b) plots ξ/τ against the gas saturation, S_g (c) plots ξ/τ against the flow velocity, q_D (d) plots the values of τ against the value of q_D at the final point in space.	95
4.1	A schematic diagram showing the radial conceptual model of two component, two phase displacement. As is shown, pure CO_2 is injected into a formation initially filled with pure, aqueous H_2O at the constant rate M_0 . (Adapted from Zeidouni et al. (2009)).	100
4.2	A diagram to show the discretisation of the r axis. Note that because the nodes are logarithmically spaced, l_k will vary for each cell. It will be smaller for cells nearer the point of injection and will increase logarithmically as the radial distance from the injection well increases.	101
4.3	A diagram to illustrate how upwinding can be used to approximate the values of parameters at the cell boundaries. In this system, the wave velocity is negative at the cell boundary $k - \frac{3}{2}$, but positive elsewhere.	118
4.4	A graph to show the pressure and gas saturation output of the model for the initial parameters in Table 4.1, for the times shown in the legend. The solid lines represent the solution found by the MOL, while the dashed lines represent the analytical solution of Mathias et al. (2011b), which assumes negligible capillary pressure. The model was run for 1000 points in space.	119
4.5	A graph to show the pressure and gas saturation output of the model for the initial parameters in Table 4.1, for the times shown in the legend, with the exception that P_{cd} is now equal to 10^7 Pa. The model was again run for 1000 points in space.	120

4.6	A graph to show the pressure and gas saturation output of the model for the initial parameters in Table 4.1, for the times shown in the legend, with the exception that P_{cd} is now equal to 10^8 Pa. The model was again run for 1000 points in space.	121
4.7	A graph to show the pressure and gas saturation output of the model for the initial parameters in Table 4.1, for the times shown in the legend, with P_{cd} equal to 10^8 Pa and for 200 points in space.	122
4.8	A graph to show the pressure and gas saturation output of the model for the initial parameters in Table 4.1, for the times shown in the legend, with P_{cd} equal to 10^8 Pa and for 500 points in space.	123
4.9	A graph to show the pressure and gas saturation output of the model for the initial parameters in Table 4.1, for the times shown in the legend, with the exception that the capillary pressure is now set to zero. The model was again run for 1000 points in space.	123
5.1	A graph to show the pressure and gas saturation output of the model for the initial parameters in Table 5.1 and for the times shown in the legend. The model was run for 150 points in space.	165
5.2	A graph to show the solid saturation output of the model for the initial parameters in Table 5.1 and for the times shown in the legend. The model was run for 150 points in space.	166
5.3	A graph to show gas saturation varying with formation radius for several different values of C_a , alongside the output from the numerical reservoir simulator, TOUGH2. To create this, the model was run for 50 points in space and it was assumed that $P_{cd} = 10^7$ Pa	168
5.4	A graph to show gas saturation varying with formation radius for several different values of C_a , , alongside the output from the numerical reservoir simulator, TOUGH2. To create this, the model was run for 80 points in space and it was assumed that $P_{cd} = 10^7$ Pa	168

6.1	A figure to illustrate the spacing of the Chebyshev points. They are the projections onto the x-axis of equally spaced points on the unit circle (Adapted from Trefethen (2000, p.43)).	178
6.2	A schematic diagram illustrating the distribution of CO ₂ , water and salt around a CO ₂ injection well in a saline formation.	185
6.3	Sensitivity analysis based on gas-displacing-oil examples. The infinite Ca value curves were obtained from the method of characteristics solutions presented in Figures 4.13 and 4.15 of Orr (2007). The finite Ca value curves were obtained using the pseudospectral solution documented in this chapter.	195
6.4	Plots of CO ₂ saturation against radial distance after injecting 4.73 Mt of CO ₂ whilst assuming a range of different capillary numbers, Ca. The TOUGH2 results are from the simulations previously presented by Mathias et al. (2013). Other associated model parameters are presented in Table 6.2. The results for $Ca \rightarrow \infty$ were obtained using a method of characteristics solution, also presented by Mathias et al. (2013). The results for finite Ca values were obtained using the pseudospectral solution.	198
6.5	Plots of CO ₂ -rich phase saturation against formation radius for different values of Ca, for both the similarity solution (indicated by the dashed lines) and the three phase numerical model from Chapter 5 (indicated by the solid lines). Both solutions use the parameters in Table 5.1, with the exception that P_{cd} is set to 10^7 , and the three phase numerical model was run for 80 points in space.	199
6.6	Plots of F_1 , α_1 and β_1 against C_1 for the simulation results presented in Figure 6.4.	200

6.7	Sensitivity analysis based around the scenario presented in Figure 6.4. The different colours relate to different brine salinities, as indicated in the legend. The solid lines, dashed lines and dash-dotted lines represent results obtained using fluid properties calculated assuming the saline formation exists at a depth of 1000 m, 1500 m and 2000 m, respectively (based on hydrostatic pressure conditions and a geothermal gradient of 40°C per km as in Table 6.3). a) shows plots of the ratio of dry out zone volume (V_d) to injected CO ₂ volume (Q_0t) against capillary number (Ca). b) shows plots of the ratio of volume of evaporated water (V_e) to Q_0t against Ca. c) shows plots of the ratio of volume of dissolved CO ₂ (V_c) to Q_0t against Ca. d) shows plots of precipitated salt volume fraction in the dry out zone (C_{30}) against Ca.	201
6.8	The same as Figure 6.7d except that salt volume fraction, C_{30} , is divided by the salinity of the brine, X_{32}	203
6.9	Plot of precipitated salt volume fraction, C_{30} , against capillary number, Ca, using the 1000 m depth model scenario described in Tables 6.2 and 6.3 in conjunction with the different relative permeability parameters given in Table 6.4.	205

List of Tables

3.1	Constant parameters used to find the values of $\frac{df_g}{dS_g}$ in Figure 3.8.	82
4.1	Constant parameters inputted into the two component and two phase model, to give the output in Figure 4.4.	119
5.1	Constant parameters inputted into the three component and three phase model, to give the output in Figures 5.1 and 5.2.	164
6.1	Examples of the iterative calculation of S_{em} for different values of S_{2c} (as indicated in the top row) using equation (6.50) with $m = 0.5$, $P_{c0} = 19.6$ kPa and $P_{cd} = 10^9$ Pa. The initial guess, S_{em0} , is calculated using equation (6.56).	189
6.2	Relevant model parameters used for the CO ₂ injection in saline formation scenario, previously presented by Mathias et al. (2013).	196
6.3	Relevant model parameters used for the CO ₂ injection in a saline formation scenario with a brine salinity of 150 ppt.	197
6.4	Relative permeability parameters for six different sandstone cores (after Mathias et al., 2013). Note that for each core $k_{r20} = 1$ and $S_{1c} = 0$. Data for Cardium #1, Basal Cambrian and Viking #1 was originally obtained by Bennion and Bachu (2008). Data for Otway was originally obtained by Perrin and Benson (2010). Data for Paaratte and Tuscaloosa was originally obtained by Krevor et al. (2012).	204

Nomenclature

This is a list of the symbols used in this thesis. Some symbols have been used to represent different things in different contexts, but the intended meaning of the symbol should always be clear. The referenced page number is the page on which the symbol first appears.

Symbol	Definition	Units	Page No
a_{mi}	activity of a solvent i on the molality scale	[-]	54
a_{xi}	activity of a solvent i on the mole fraction scale	[-]	54
A	area	[L ²]	35
A_{mix}	a measure of intermolecular attraction	[ML ⁻⁵ T ⁻² N ⁻² Θ ^{0.5}]	58
B_{mix}	a measure of intermolecular repulsion	[L ³ N ⁻¹]	58
c_{ij}	the constant equilibrium volume fraction of component i in phase j	[-]	181
C	the vector containing the corresponding values of C_1 to the solution vector for F_1, \mathbf{F}	[-]	191
C_{10}	the volume fraction of CO ₂ in the dry out zone of a formation	[-]	189
C_{30}	the volume fraction of precipitated salt in the dry out zone of a formation	[-]	171
Ca	the capillary number, which is a dimensionless constant	[-]	166
C_i	the volume fraction of component i in the combined mixture	[-]	180
C_{i0}	the constant boundary value of C_i at the injection well	[-]	184
C_{iI}	the uniform initial value of C_i in the saline formation	[-]	184
D	a differentiation matrix	[-]	176
D ^(d)	the d th order Chebyshev differentiation matrix	[-]	178
E	a Chebyshev differentiation matrix that has been transformed to the required solution space	[-]	190
f_i	fugacity of component i	[ML ⁻¹ T ⁻²]	52
f_j	fractional flow of phase j	[-]	67
F	the total mass of all components within a given volume of fluid mixture	[ML ⁻³]	101

F	the solution vector for the dependent variable F_1	[-]	191
F_i	a parameter related to the volume fraction of component i present	[-]	183
g	gravity	[MT^{-2}]	41
G	Gibb's free energy	[ML^2T^{-2}]	50
G	a term used within the parameter F_i	[-]	186
G_i	mass of component i within a given volume of fluid mixture	[ML^{-3}]	40
G_{iD}	dimensionless form of G_i	[-]	66
H	enthalpy of the system	[ML^2T^{-2}]	50
H	formation thickness	[L]	99
H_i	mass flow rate per unit area of component i	[$\text{ML}^{-2}\text{T}^{-1}$]	40
H_{iD}	dimensionless form of H_i	[-]	66
H_{ij}	mass flow rate per unit area of component i in phase j	[$\text{ML}^{-2}\text{T}^{-1}$]	117
J	a term used in the partial differential equations of McWhorter and Sunada (1990) to represent the capillary-hydraulic properties of the fluid-porous medium system	[L^2T^{-1}]	175
k	permeability	[L^2]	41
K	the equilibrium constant of a chemical reaction	[-]	55
K_i	the equilibrium constant of the component i	[-]	55
k_{rj}	relative permeability of phase j	[-]	41
k_{rj0}	endpoint permeabilities for the phase j	[-]	42
l_c	the length of a cylinder	[L]	35
l_k	the length of a cell k in a discretised axis	[L]	76
L	an arbitrary length	[L]	67
m	a parameter that depends on pore geometry	[-]	45
m_i	the molality of component i	[NM^{-1}]	53
M_0	the rate of injection into a reservoir	[MT^{-1}]	99
M_{H_2O}	the molecular mass of water	[MN^{-1}]	56
n	a parameter that depends on pore geometry and is equal to $\frac{1}{1-m}$	[-]	45
n	number of moles in the system as a whole	[N]	50
n_i	number of moles of component i	[N]	50
n_j	power law exponents for the phase j	[-]	42

N	the number of nodes or interpolation points used	[-]	75
N_c	number of components	[-]	40
N_p	number of phases	[-]	40
p	a Chebyshev polynomial of the second kind	[-]	177
P	global pressure	[ML ⁻¹ T ⁻²]	44
P^0	a reference pressure	[ML ⁻¹ T ⁻²]	51
P_c	capillary pressure	[ML ⁻¹ T ⁻²]	35
P_{c0}	van Genuchten parameter that represents the air entry pressure of the porous medium. It is equal to $\frac{1}{\alpha}$	[ML ⁻¹ T ⁻²]	45
$P_{c,e}$	the capillary entry pressure in the Brooks-Corey model	[ML ⁻¹ T ⁻²]	44
P_{cd}	capillary pressure at oven dry conditions	[ML ⁻¹ T ⁻²]	46
P_{cm}	the capillary pressure at the critical effective saturation, S_{em}	[ML ⁻¹ T ⁻²]	47
P_i	the partial pressure of component i	[ML ⁻¹ T ⁻²]	51
P_i^*	the vapour pressure of the pure component i	[ML ⁻¹ T ⁻²]	53
P_j	phase pressure of phase j	[ML ⁻¹ T ⁻²]	41
q_D	a dimensionless flow velocity	[-]	67
q_{inj}	the volumetric flux of the injected fluid	[LT ⁻¹]	67
q_j	volumetric flux of phase j	[LT ⁻¹]	40
q_t	total volumetric flux	[LT ⁻¹]	67
Q_0	the rate of injection into a formation	[L ³ T ⁻¹]	68
r	radial distance	[L]	40
r_0	the radial extent of the dry out zone	[L]	192
r_c	the radius of a cylinder	[L]	35
r_e	an arbitrary reference length within a radial system	[L]	183
r_E	the radial extent of a reservoir	[L]	99
r_I	the radial extent of the injected CO ₂ plume	[L]	192
r_w	the radius of the injection well	[L]	99
R	the universal gas constant, equal to 8.31447 J·mol ⁻¹ . K ⁻¹	[ML ² T ⁻² N ⁻¹ Θ ⁻¹]	51
\mathbf{R}	the residual vector, representing the error in the matrix approximation from the exact solution	[-]	191
S	entropy of the system	[ML ² T ⁻² Θ ⁻¹]	50

S_{am}	aqueous saturation matching point, at which the capillary pressure function changes from the van Genuchten function to a linear extension on a semilog plot. Note that this is denoted as S_{2m} in Chapter 6	[-]	46
S_{ar}	residual aqueous saturation	[-]	42
S_e	effective aqueous saturation	[-]	45
S_{em}	the critical effective saturation at which the switch over between the use of the van Genuchten function and Webb's extension for capillary pressure take place	[-]	47
S_{em0}	the initial value of the critical effective saturation, S_{em}	[-]	47
S_{gc}	critical gas saturation	[-]	41
S_j	saturation of phase j	[-]	31
S_{jc}	critical or residual saturation of phase j	[-]	41
t	time	[T]	40
T	temperature	[Θ]	50
v	the stoichiometric number of ions in the dissolved salt	[-]	60
v	the wave velocity at a certain point	[LT^{-1}]	77
V	volume	[L^3]	35
V_b	the volume of brine	[L^3]	192
V_c	the volume of CO_2 dissolved in the brine	[L^3]	192
V_d	the volume of the dry out zone	[L^3]	192
V_e	the volume of H_2O evaporated by the CO_2 at any given time	[L^3]	192
V_g	the volume of the compressed gas phase	[L^3]	58
\bar{V}_i	the partial molar volume of component i	[L^3N^{-1}]	51
V_s	the volume of salt precipitated in the dry out zone	[L^3]	192
x	linear distance	[L]	40
\mathbf{x}	the collocation or interpolation points at which the d th derivative of a univariate scalar function can be calculated using the differentiation matrix \mathbf{D} in the pseudospectral method	[-]	177
x_i	the mole fraction of component i in solution	[-]	67
X_{ij}	mass fraction of component i in phase j	[-]	39
x_{ij}	mass fraction of component i in phase j at equilibrium	[-]	39
y_i	mole fraction of component i in the gaseous phase	[-]	52
z_{cD}	the dimensionless mass fraction of CO_2	[-]	95

z_i	the mass fraction of a component i	[-]	101
α	a scaling parameter related to the inverse of $P_{c,e}$	$[M^{-1}LT^2]$	45
α_{10}	the boundary value of α_1 associated with C_{10}	[-]	189
α_{1I}	the boundary value of α_1 associated with C_{1I}	[-]	189
α_i	a term used within the parameter F_i that looks at the fractional flow of component i	[-]	185
α_{ij}	the compressibility of component i in phase j	$[M^{-1}LT^2]$	112
α_j	fluid compressibility of a phase j	$[M^{-1}LT^2]$	112
α_r	the rock compressibility	$[M^{-1}LT^2]$	112
β_i	a term used within the parameter F_i that looks at the capillary-hydraulic properties of the system	[-]	186
γ_{mi}	an activity coefficient that accounts for deviation from ideality, given in terms of the molality m_i	[-]	54
γ_{xi}	an activity coefficient that accounts for deviation from ideality, given in terms of the mole fraction x_i	[-]	53
γ'_x	an activity coefficient for aqueous CO_2 that incorporates the effect of chloride salts in the aqueous phase and the departure from solubility in pure water	[-]	58
η	a dimensionless form of time, related to the radial system used in Chapter 6	[-]	183
λ	Brooks-Corey pore geometry factor	[-]	45
λ	a new variable, equal to $\frac{\omega}{\eta}$, used to reduce the PDE in equation (6.30) to an ODE by application of a similarity transform	[-]	188
Λ^{ab}	the shock wave velocity of the leading shock	[-]	93
Λ^{cd}	the shock wave velocity of the trailing shock	[-]	92
μ_i	chemical potential of the component i	$[ML^2T^{-2}N^{-1}]$	49
μ_i^0	the chemical potential of the component i at temperature T and pressure P^0	$[ML^2T^{-2}N^{-1}]$	52
μ_j	dynamic viscosity of phase j	$[ML^{-1}T^{-1}]$	41
ξ	a dimensionless form of linear space	[-]	67
ρ_{inj}	the density of the injected fluid	$[ML^{-3}]$	67
ρ_{ij}	the density of the component i in the phase j	$[ML^{-3}]$	101
ρ_j	density of the phase j	$[ML^{-3}]$	40
ρ_{jD}	dimensionless form of ρ_j	[-]	67

σ	the interfacial tension between the gaseous and aqueous phases in a porous medium	$[\text{MLT}^{-2}]$	35
σ_{ij}	the volume fraction of component i in phase j	$[-]$	181
τ	a dimensionless form of time, related to the linear system used in Chapter 3	$[-]$	67
τ_b	the earliest value of τ at which a breaking point occurs	$[-]$	82
ϕ	porosity of the medium	$[-]$	40
Φ_i	fugacity coefficient	$[-]$	52
ψ	a dimensionless form of capillary pressure	$[-]$	183
ψ_d	a dimensionless form of P_{cd}	$[-]$	186
ψ_m	a dimensionless form of P_{cm}	$[-]$	187
ω	a dimensionless form of radial space	$[-]$	183

Declaration

I declare that this thesis, presented for the degree of Doctor of Philosophy at Durham University, is the result of my own original research and has not been previously submitted to Durham University or any other institution.

The copyright of this thesis rests with the author. No quotation from it should be published without the author's prior written consent and information derived from it should be acknowledged.

Acknowledgements

I would firstly like to thank The Crown Estate for funding my PhD. This work would not have been possible without their financial support.

My huge thanks also go to my primary supervisor, Prof. Simon Mathias, for giving me the opportunity to do this project and then to extend it from an MPhil to a PhD, and for his support throughout the entirety of my studies. He has been an invaluable help from the very beginning of my PhD when I began the steep learning curve of how to write code and use MATLAB, through to writing up this thesis. As well as the PhD itself, he has been very encouraging with demonstrating, and has given me far more confidence in my ability to teach and help others.

I would also like to thank all of the postgraduates in the Department of Earth Sciences, both past and present. Lunch wouldnt be the same without being able to discuss the previous nights TV in the coffee room, and I have made some great friends. My particular thanks go to everyone who has been in the best bae eva: Jack, Salim, Cath, Fran, Charlotte, Ayo, Katharine and Eloïse. Their help with work has been invaluable and our chats (both work and non-work related) have brightened up many days. A special thanks to Jack for giving me lots of tips on LaTeX and MATLAB and for reading over some of my chapters!

My parents have been a fantastic support over these years, despite not really understanding what I'm doing! They have always been there when I've needed them and helped me to de-stress, and for that I am very grateful.

My final thanks go to my wonderful husband, James. Our wedding promises really were true in that he is the light in every darkness and every day. He has kept me going when things were tough and made me believe that I can achieve whatever I want to. I genuinely don't know if I would have been able to complete my PhD without him.

Chapter 1

Introduction

Carbon capture and storage (CCS) is a promising method of reducing anthropogenic carbon dioxide (CO₂) emissions, which scientific evidence indicates would be a major factor in slowing the warming of the planet. Deep saline aquifers are thought to have the most storage capacity for CO₂ from the possible storage options, but there is a concern that high capillary pressure values will enhance the precipitation of solid salt close to the injection zone of the aquifer. This could dramatically reduce its injectivity: the rate at which it is possible to inject CO₂ into the aquifer without the pressure becoming so high that the formation is fractured. In this thesis, various numerical models and analytical solutions have been used to simulate the salt precipitation that occurs when CO₂ is injected into a saline aquifer, taking into account the effects of both capillary pressure and the partial miscibility of the phases.

1.1 Introduction to Carbon Capture and Storage and Saline Aquifers

Scientific evidence suggests that the planet has been warming at a much higher rate in recent years than was previously observed decades ago. Figure 1.1 shows that the mean annual global temperature increased by approximately 1.4°F (or 0.8° C) from 1880 to 2009, with the majority of this increase occurring since the late 1970s. It should also be noted from the graph that the twenty warmest years have all been since 1981, and the ten warmest are all in the most recent twelve years (NOAA, 2010). This increase in

temperature could have many potential negative effects for the planet and for mankind, including changes in weather such as heat waves and more severe floods and hurricanes, sea levels rising to cause coastal flooding, and extinction of certain plant and animal species (Riebeek, 2010). Figure 1.1 also shows the change in carbon dioxide (CO₂) concentration from 1880 to 2009, which follows a similar pattern to the change in temperature; it has increased over the entire time period, but particularly rapidly from the late 1970s onwards. The evidence suggests that this correlation between CO₂ concentration and global temperature is not a coincidence. Almost all of the increase in CO₂ concentration is due to anthropogenic emissions (Celia et al., 2015), which are considered to be largely responsible for global warming due to the greenhouse effect, in which greenhouse gases such as CO₂ absorb and re-radiate the infrared radiation reflected by the surface of the Earth, and hence cause the planet to heat up (Kessel, 2000).

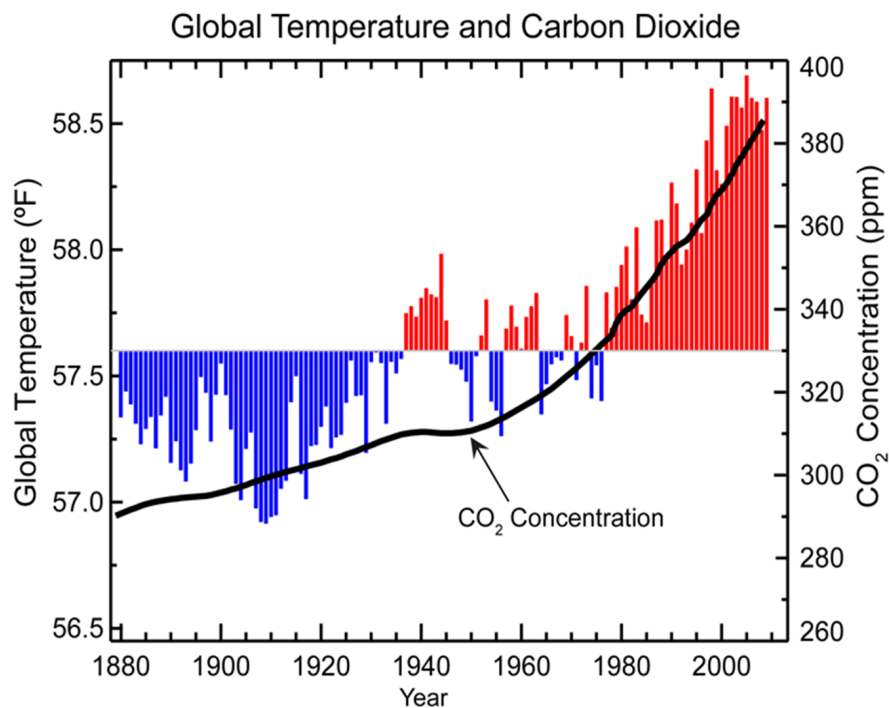


Figure 1.1: A graph to show the variation in both global annual average temperature and CO₂ concentration from 1880 to 2009. The grey line represents the mean global temperature from 1901 to 2000, while red bars indicate years with an average temperature above this line and blue bars indicate years with average temperatures below the line. The black line shows the change in atmospheric CO₂ concentration in parts per million (NOAA, 2010).

Over the decade 2005-2014, 91% of global anthropogenic CO₂ emissions were caused by fossil fuels and industry (Le Quéré et al., 2015). Therefore, a promising way to reduce these CO₂ emissions is carbon capture and storage (CCS). This is a process in which CO₂ is captured from power stations or other industrial sources, compressed, and then transported by pipeline or ship for injection into rock formations either deep underground

or beneath the sea surface (Cavanagh and Hazeldine, 2014). It also has the added benefit of being the only viable technology that reduces emissions of CO₂ released to the atmosphere while continuing to allow large scale use of fossil fuels (Celia et al., 2015). There are many potential storage options for CO₂ within CCS, using both physical and chemical trapping mechanisms for the CO₂ storage (Celia et al., 2015). One option involves injecting CO₂ into coal beds, where the CO₂ adsorbs preferentially to the coal and displaces the methane that was previously attached to the coal surface, and in another, CO₂ is injected into reactive rock formations such as periodotite, so that it will react with the silicate in the rock and form carbonate minerals for long term storage (Bickle, 2009). However, the most well understood storage options are those that simply involve storage of CO₂ underground in saline aquifers or depleted oil and gas reservoirs, with no additional chemical reactions (Bickle, 2009). Of these, storage in saline aquifers is considered to be the most feasible option for CCS on a large scale, as the cumulative global capacity estimates of saline aquifers are extremely high, vastly exceeding those of depleted oil and gas reservoirs, and comprising greater than 90% of the storage resource in most regions (Hosa et al., 2011). Globally, there is enough capacity in saline aquifers to store CO₂ emissions from large stationary sources for at least a century (Celia et al., 2015).

CCS on a large scale has not yet been implemented, but there are some industrial-scale injection operations into saline aquifers, as well as a number of demonstration or pilot-scale injections (Celia et al., 2015). The oldest of these industrial-scale operations is Sleipner, where injection of CO₂ began in 1996 and has been occurring at a rate of approximately 1 Mt per year. Other industrial-scale operations include In Salah, where injection of CO₂ occurred from 2004 until 2011 at a rate of approximately 0.5 Mt per year, and Snøhvit, where injection began in 2008 and has also been at a rate of approximately 0.5Mt per year (Celia et al., 2015). Between them, these sites have stored millions of tons of CO₂, suggesting that CCS by injection into saline aquifers may be a feasible option (Eiken et al., 2011). Pilot-scale injections generally have a short duration and inject a relatively small amount of CO₂ (0.0016Mt-1Mt) and tend to focus on specific areas and concerns about CCS (Celia et al., 2015). For example, the Frio CO₂ injection project in Texas, USA, concentrated on measuring the evolution of the CO₂ plume, and provided validation of the conceptual model of CO₂ migration over short space and time scales (Celia et al., 2015).

Generally, the saline aquifers that will make the most successful storage formations have both high porosity (a large percentage of the total rock volume available for storage)

and high permeability (a good ability to transmit fluids), as this is likely to lead to high injectivity of CO₂ (Celia et al., 2015). It must also be possible for the CO₂ to be injected into the saline aquifer at a depth at which it will be in a supercritical state (i.e. at a temperature and pressure above its critical point of 31.1° C and 7.38MPa (Celia et al., 2015), where distinct liquid and gas phases no longer exist) in order to increase the density of the CO₂ and therefore enable much more to be stored, as a high storage capacity is also a necessity for a saline aquifer to be favourable for CCS (Bickle, 2009). However, the CO₂ will still be less dense than the surrounding brine and so will rise. It is therefore necessary for it to be contained by an impermeable cap rock which will prevent it from migrating upwards any further and escaping (Bickle, 2009). For these reasons, sedimentary basins with layer-type successions of permeable rocks such as sandstones, overlain by caprocks such as shales or anhydrites, are generally the most suitable for CO₂ storage (Celia et al., 2015).

It must be considered, however, that even a saline aquifer with these features will not necessarily be successful for CCS. Leakage of CO₂ through faults and fractures of the rock is a possibility, and so the fluid pressure within the rock must be monitored to ensure that it does not increase above certain thresholds, as this could induce fracturing of the caprock and damage to wellbores in the reservoir (Chadwick et al., 2009). A geomechanically determined storage pressure, called the fracture pressure, can be established for a given aquifer (Chadwick et al., 2009), and there are often regulatory constraints on maximum allowable pressures relative to the fracture pressure. One example of this is that in Alberta, Canada, the maximum pressure that is allowable is 90% of the estimated fracture pressure (Celia et al., 2015). Another factor to consider when thinking about the feasibility of saline aquifers for CCS, and one that has not received as much focus until now, is the impact on CO₂ storage of the dissolved salt within the brine of a saline aquifer.

1.2 Introduction to Numerical Modelling for Saline Aquifers

It has been very useful to be able to monitor the behaviour of the CO₂ and saline aquifer at the injection operations that are already under way. Seismic reflection surveys at Sleipner have enabled us to track the movement of the CO₂ plume (Cavanagh and Hazeldine, 2014), and, at several of the industrial-scale injection projects, seismic reflection surveys among other geophysical monitoring methods including gravity and satellite data have been effective in showing some unpredicted geological factors as well as following changes

in fluid saturation and pressure (Eiken et al., 2011). Down-hole measurements of pressure and temperature have also been helpful in revealing changes that occur both during and after injection of CO₂ (Eiken et al., 2011). However, these observations are all specific to the conditions and geology at the site at which they were taken, and do not cover the time or length scales we would need to look at if CCS were to be implemented worldwide as a primary method of CO₂ mitigation. Therefore, to gain insight into what would occur if CCS were to be carried out over longer time periods and larger lengths, and so in order to reach a conclusive decision on whether CCS is a viable on a large scale, it is necessary to use numerical modelling.

Numerical modelling allows us to address specific problems and questions that arise in the context of CO₂ storage, over realistic time and length scales. It gives a clear idea of the movement of the CO₂ plume, the build-up of pressure in the formation, the possibility of CO₂ leakage and many other potential issues, and can therefore clarify the safety, feasibility and likely cost of CCS into saline aquifers (Class et al., 2009). Indeed, the legal framework that allows for CCS to be implemented on a large scale would be likely to require such numerical models (Class et al., 2009).

At first thought, numerical modelling of CO₂ injection into a saline aquifer may seem extremely complicated due to the number of different processes involved. The CO₂ and the water are partially miscible, which means that when they are mixed they form two phases that each contain some fraction of both CO₂ and water. A small percentage of the mass of CO₂ can dissolve into the liquid brine, while an even smaller fraction of the water from the brine can evaporate into the supercritical CO₂ (Celia et al., 2015). In addition to this, it is possible for the salt dissolved in the brine to precipitate to form a solid phase. Therefore, a multicomponent, multiphase (MCMP) system is created. Considering this in three dimensions, as well as the effects of capillary pressure (the pressure difference between the gaseous and aqueous phases, which is described in more detail in Section 1.4), the geological features of a particular aquifer, geochemical reactions, variations in temperature and energy, and many other aspects, all of which are coupled and affect and depend upon each other, makes the numerical modelling of the system seem almost impossibly complex. A model of this intricacy would involve solving a set of highly nonlinear, coupled partial differential equations and be extremely computationally demanding, as well as having practical limitations such as a lack of data to define the relevant parameters and a shortage of information on exactly how the processes and parameters relate to each other in the nonlinear feedback loops (Celia et al., 2015). Therefore, almost all simulations decouple

certain processes and disregard the effects of others, as well as simplifying the equations based on the physics of the system (Celia et al., 2015). This is often justified based on the questions being asked of a specific model (Celia et al., 2015). Examples of simplifications include the assumption of vertical equilibrium. This can be assumed when looking at a large time scale, as density differences between the gaseous and aqueous phases lead to buoyant segregation occurring rapidly, such that it occurs on a very small time scale relative to the overall time scale of the model (Celia et al., 2015). Other simplifications used in numerical models include treating the capillary pressure as negligible, and the assumption of immiscible flow (Celia et al., 2015). In some cases, the equations used to model the system can be simplified to the extent that they can be solved analytically and given an exact answer, whereas in others it is still necessary to use numerical methods to give a solution. The next chapter will go into much more detail about the governing equations of the numerical models and the assumptions and simplifications that we make, and future chapters will explain the various methods that we use to solve the equations.

It is not possible to check the reliability of any numerical models we create that cover very large time or length scales using real-life injection, as even the industrial-scale projects currently running do not inject on a scale that would be necessary to significantly reduce CO₂ emissions, and so Class et al. (2009) have looked into the accuracy of current models by formulating benchmark problems for model intercomparisons. The results show that the models are capable of accounting for the processes, parameters and properties involved in CCS reasonably, only varying with minor quantitative deviations.

1.3 Salt Precipitation after CO₂ Injection

If we consider one-dimensional injection of CO₂ into a radially symmetric, infinitely large saline aquifer, Figure 1.2 shows a simplified version of how gas saturation, S_g [-], will vary with distance from the point of injection within the aquifer, which is considered to be the left hand axis of the graph. The saturation of a phase j is defined as (Marle, 1981, p.16):

$$S_j = \frac{\text{Volume of pore space occupied by phase } j}{\text{Total volume of pore space in the rock}}. \quad (1.1)$$

Although these conditions are a drastic simplification of injection into a saline aquifer in field-scale, they are adequate to illustrate the pattern of gas saturation over the length of an aquifer. Near the wellbore in particular, viscous forces dominate gravitational forces, and so flow can be reasonably approximated as one-dimensional (Zeidouni et al., 2009).

As was mentioned in Section 1.2, CO₂ and water are partially miscible. This means that the supercritical phase (referred to as the gaseous phase for the rest of the thesis) is able to contain a small amount of evaporated water, and the aqueous phase is soluble to a small amount of dissolved CO₂. CO₂ dissolving in the formation water is one of the primary mechanisms for the trapping of CO₂ in saline aquifers (Zeidouni et al., 2009). This miscibility means that as well as CO₂ displacing the brine that was previously resident in the pores of the aquifer upon injection, the water in the brine can also be evaporated into the gaseous phase.

The effects of these physical mechanisms can be seen from Figure 1.2. Discontinuities or ‘shocks’ in the gas saturation develop that effectively separate the aquifer into three different regions (Zeidouni et al., 2009). The region furthest from the point of injection is just fresh brine that has not yet been in contact with the advancing CO₂ plume, and this brine is still in the aqueous state it was in before the injection of CO₂. Upstream of this is a region in which there is both an aqueous and gaseous phase, and both phases are made up of CO₂ and water, as well as dissolved salt being present in the aqueous phase. The assumption of equilibrium is made in this region: the composition of the phases is set to what it would be at equilibrium for the specified temperature and phase pressure at all times. This is because the compositions reach equilibrium very quickly relative to the time scale we are looking at, and would then not change with time, so this is a helpful simplifying assumption to make. Finally, the region nearest to the point of injection is referred to as the dry out zone, and it contains the gaseous and solid phases, with no aqueous phase. This is due to a combination of the mechanisms CO₂ has for removing liquid water from the site of injection. Firstly, brine is displaced by the advancing gas. Any residual brine that is left behind in the vicinity of the injection site will then be flowing so slowly that the water can be fully vaporised by the CO₂-rich gaseous phase (Zeidouni et al., 2009). This vaporisation of water can cause formation dry out, and due to the fact that salt is considered to flow with the aqueous phase as a part of liquid brine, can leave behind immobile solid salt to precipitate in the pores of the rock in the region of the injection well (Pruess and Müller, 2009). There is a concern that the loss in injectivity that could be caused by this salt precipitation may be a limitation in the use of saline aquifers for carbon sequestration.

As mentioned earlier, a saline aquifer that is effective for CCS will generally have both high porosity and high permeability. Figure 1.3 shows how the permeability of a rock is affected by changes in the porosity. It indicates that a relatively small reduction in porosity

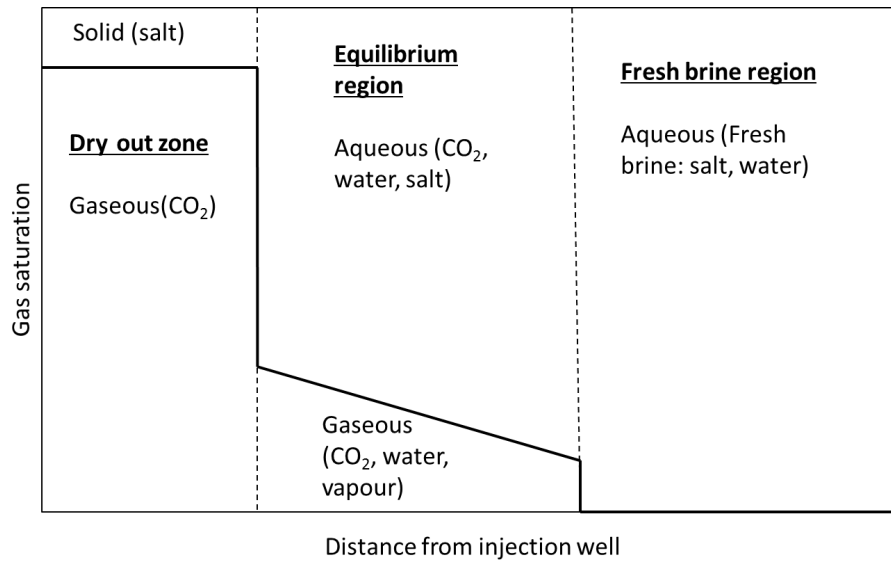


Figure 1.2: A cartoon to show how gas saturation varies from the point of injection. Adapted from [Hosseini et al. \(2012\)](#)

can lead to a dramatic reduction in permeability: if the porosity is reduced by only 30%, the permeability can reduce by approximately 80%, and the porosity being reduced by as little as 60% can result in a permeability of zero. Figure 1.3 therefore illustrates that even a very small amount of salt precipitation that may not have much of an effect on porosity can have a huge effect on the permeability of an aquifer. This is likely to be due to the way that pore channels can converge and diverge ([Pruess and Müller, 2009](#)); salt precipitation can reduce rock permeability by clogging pores or by pore throat restriction ([Peysson et al., 2014](#)). Figure 1.4 is a schematic of a pore configuration in two dimensions, and shows how pore bodies are connected by pore throats with a much smaller radius. It is clear that salt precipitating in the throat of a pore would restrict the potential fluid flow, and therefore reduce the permeability of the aquifer, much more than if the same amount of salt had precipitated in the body of the pore, and that it would only take a small volume of salt to precipitate in the pore throat to restrict fluid flow entirely due to its narrow radius. The variability in pore radius and the impact of pore throat effects are often included in models through the use of the ‘tubes in series’ model ([Verma and Pruess, 1988](#)), which is illustrated in Figure 1.5. Reduced permeability leads to increased pressure build-up when injecting CO₂ ([Pruess and Müller, 2009](#)), and CO₂ injection needs to be terminated as pressures reach the fracture pressure. Therefore, salt precipitation can have a significant effect on the amount of CO₂ that can be stored in a given aquifer.

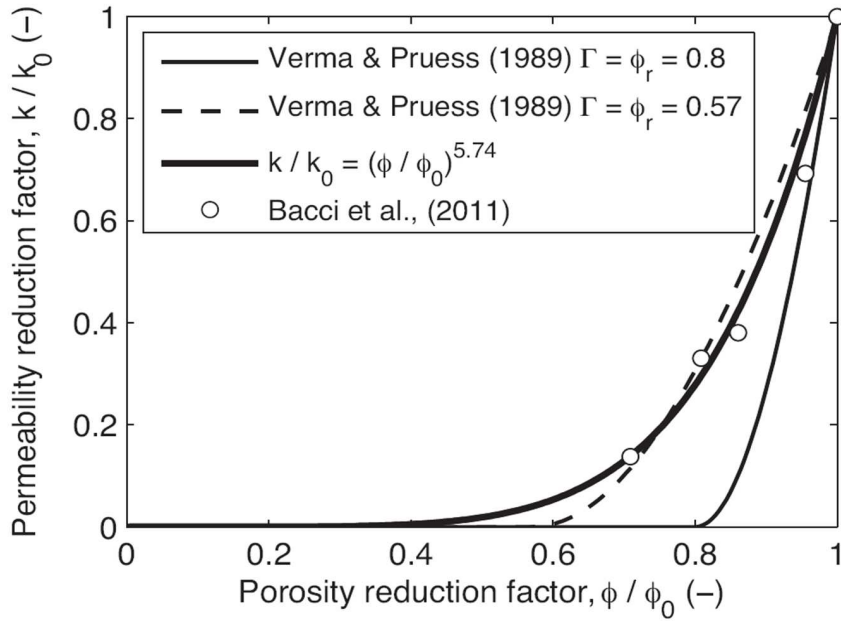


Figure 1.3: A graph to show how permeability reduction factor varies as the porosity reduction factor changes (Mathias et al., 2013).

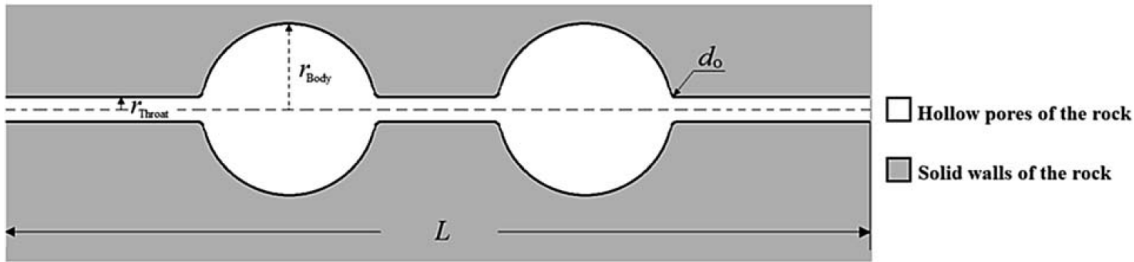


Figure 1.4: A schematic of a two-dimensional pore body and pore throat configuration (Zhao and Wen, 2017). r_{Body} and r_{Throat} represent the radius of the pore body and pore throat respectively.

Many earlier studies, including Zeidouni et al. (2009), concluded that the amount of salt precipitation formed in a saline aquifer upon injection of carbon dioxide should be sufficiently small not to significantly affect porosity, permeability or injectivity. However, these studies make the simplifying assumption of neglecting the capillary pressure, and the inclusion of this could potentially have a considerable effect on the amount of salt precipitation formed.

1.4 Capillary Pressure and Counter-Current Imbibition

When two fluid phases are present in a porous medium, their arrangement in contact with each other and the solid walls of the medium is controlled locally by an energy balance

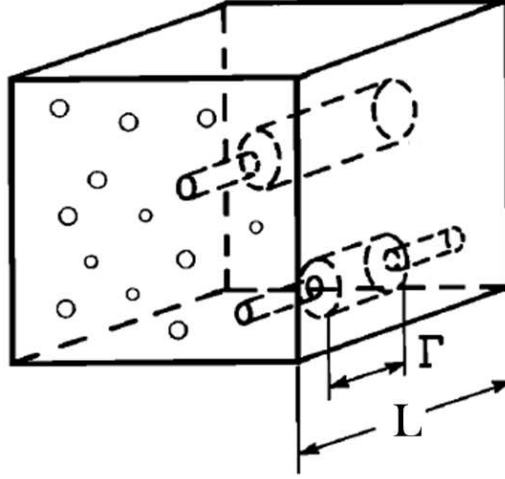


Figure 1.5: A figure to illustrate the ‘tubes in series’ model that is used to represent pore throat effects and the variability of the radius of the cross-section of a flow channel (Verma and Pruess, 1988).

(Blunt, 2017, p.4). The non-wetting phase (in this case, the gaseous phase primarily made up of CO₂) has less of a preference to reside next to the solid phase than the wetting phase (here, the aqueous phase primarily composed of brine), hence leading to a curved interface between the two phases and a difference in pressure between them (Blunt, 2017, p.4). This pressure difference is called the capillary pressure. The Young-Laplace equation relates the capillary pressure to the curvature of the interface between the two phases, and helps to determine how fluids are configured in the pore space and how they move (Blunt, 2017, p.4). It is found by considering that the work done against the pressure difference will be equal to the change in interfacial energy, and hence:

$$P_c dV = \sigma dA \quad (1.2)$$

where P_c [ML⁻¹T⁻²] is the capillary pressure, σ [MLT⁻²] represents the interfacial tension between the phases, dV [L³] is an infinitesimal change in volume and dA [L²] is the corresponding change in surface area (Blunt, 2017, p.5). This means that, using the ‘tubes in series’ model illustrated in Figure 1.5 and hence considering the porous medium to be made up of cylinders of a fixed length, the capillary pressure can be found by taking the derivatives of the volume and area of a cylinder, i.e. the derivatives of $\pi r_c^2 l_c$ and $2\pi r_c l_c$ respectively, where r_c is the radius and l_c is the length of the cylinder being considered, and substituting the results into equation (1.2) to give:

$$P_c = \frac{\sigma}{r} \quad (1.3)$$

This shows that the capillary pressure is inversely proportional to the radius of the cylinder.

One significant consequence of capillary pressure is that high capillary pressure gradients will occur particularly in the dry out zone of a saline aquifer, as the evaporation of water will lead to low wetting saturations (Carpita et al., 2006). This causes a reversal of the direction of the wetting pressure gradient, and therefore will provide a driving force for drawing water towards regions that have higher gas saturations. Consequently, an additional flow component of brine back towards the point of injection that opposes the generally outward flow caused by the injection of CO₂ is added (Pruess and Müller, 2009), in a process called counter-current imbibition. Without it, only the salt that is initially in the dry out zone can precipitate, but when counter-current imbibition occurs, additional brine is fed back into the dry out zone, carrying with it additional salt (Zeidouni et al., 2009), potentially leading to much higher volumes of precipitated salt and associated losses in permeability. Figure 1.6 illustrates the process of counter-current imbibition in a saline aquifer, showing the backflow of brine and the increased precipitation of salt in the dry out zone.

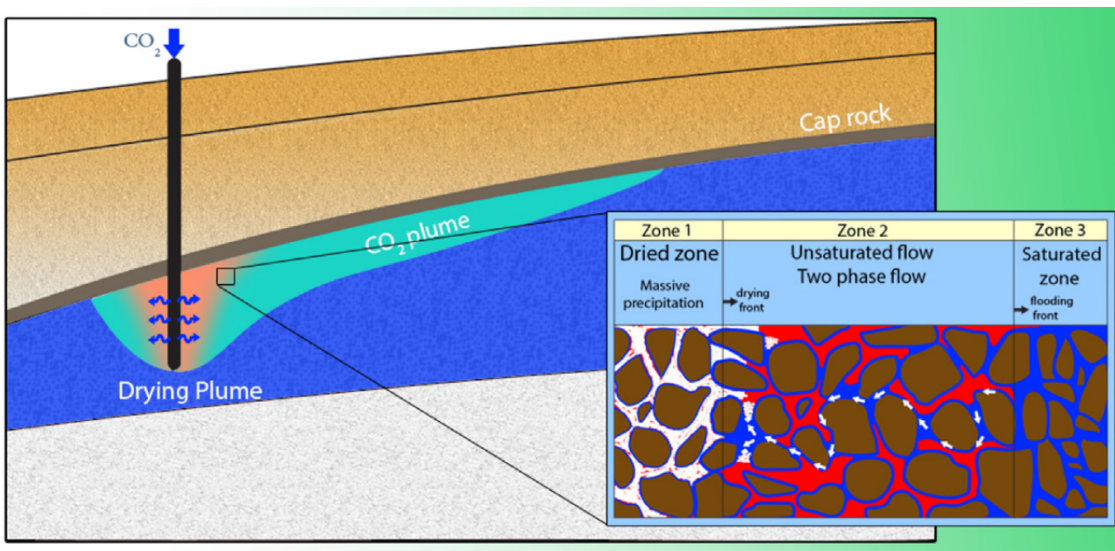


Figure 1.6: A schematic of CO₂ injection in a saline aquifer, showing the possible configuration of phases and the backflow of brine (Miri and Hellevang, 2016).

1.5 Project Objective

The main objective of this project is to investigate the amount of salt precipitation that is likely to occur within a saline aquifer upon injection of CO₂, and in particular the effect of the inclusion of capillary pressure and therefore counter-current imbibition on salt precipitation, in order to provide further insight into whether CCS by injection into saline aquifers is a feasible method of greenhouse gas mitigation on a large scale. In order

to do this, both numerical and analytical solutions of mathematical models will be used to look into the effects that changing various different parameters has on the rate of counter-current imbibition and the amount of salt precipitate formed, including the injection rate of CO_2 , the porosity and permeability of the aquifer, and the relative permeabilities of the fluids concerned.

1.6 Thesis Overview

Chapter 2 introduces the fluid properties to be calculated, and shows how they link together in the governing equations that are key to forming the models. It will also go further into the concept of partial miscibility, which has been briefly mentioned earlier in this chapter, and describe the composition of the different phases within the fluid mixture.

Chapter 3 introduces two established techniques for solving the problem of two component, two phase incompressible flow in porous media in the absence of capillary pressure. The two techniques studied are the method of characteristics (MOC) and the method of lines (MOL). The developed solutions are compared to each other and are subsequently used as a benchmark for results from the more sophisticated models developed later on in the thesis.

Chapter 4 extends the method of lines solution developed in the previous chapter by incorporating compressible fluids and by allowing for capillary pressure.

Chapter 5 develops the work in Chapter 4 further by accounting for salt, and therefore forming a numerical model that can simulate the conditions in a saline aquifer: three components (CO_2 , water and salt) and three phases (gaseous, aqueous and solid).

Chapter 6 introduces pseudospectral methods, and explores the McWhorter and Sunada equation, which accounts for two phase immiscible flow with capillary pressure effects included. The similarity solution of McWhorter and Sunada is then extended to account for partial miscibility and for three components and three phases, therefore enabling us to study the effect that capillary pressure has on counter-current imbibition and the build-up of salt precipitation in a saline aquifer.

Chapter 7 brings the previous chapters together to provide a summary and a set of conclusions.

Chapter 2

Governing Equations and Phase Equilibrium

This chapter presents the governing equations that are necessary in order to form a mathematical model to illustrate the dynamic processes involved when CO₂ is injected into a saline formation. The different components and phases to be considered, how components can move between certain phases due to the effects of partial miscibility and the concept of phase equilibrium are also explained.

2.1 The Multicomponent, Multiphase System

In Chapter 1, the concept of partial miscibility and how it leads to a multicomponent and multiphase (MCMP) system upon the injection of CO₂ into a saline aquifer was explained. The dissolution, evaporation and precipitation of components into other phases will result in a three component, three phase system. In order to form governing equations and mathematical models that accurately represent the conditions within the aquifer, it is necessary to clearly define what the three phases and three components are, and which components can exist in which phases.

The three possible phases within the system are gaseous (recall from Chapter 1 that what we refer to as the gaseous phase is actually in a supercritical state), aqueous and solid, denoted by g , a and s , respectively, in the equations that follow. The three components are CO₂ (denoted by c) which can exist in the gaseous phase or dissolve into the aqueous

phase, water (denoted by w) which can also exist in the aqueous phase or evaporate into the gaseous phase, and salt (denoted by n) which can either be dissolved in the aqueous phase or can precipitate to form a solid phase.

In the following equations, i is used to represent a component and j to represent a phase. Due to the transfer of components between phases, the amount of each component in each phase can vary with space and time. Let X_{ij} [-] denote the mass fraction of component i in phase j , and x_{ij} [-] denote the mass fraction of component i in phase j at equilibrium. Further details about the concept of equilibrium and methods for determining x_{ij} are provided in Section 2.3.

2.2 Governing Equations

The following equations are used throughout the thesis to model multiphase, multicomponent flow. It should be noted, however, that the system is assumed to be isothermal such that the equations do not take into account the effects of variation in temperature.

2.2.1 Mass Balance Equation

The starting point of forming a mathematical model to describe MCMP flow and transport in porous media is to formulate a mass conservation statement. The basis of this is that, considering a control volume, V , the rate of change of mass of a component i within V must be equal to the net rate of flow of component i into V minus the net rate of flow of component i out of V . Figure 2.1 shows this concept in diagrammatic form.

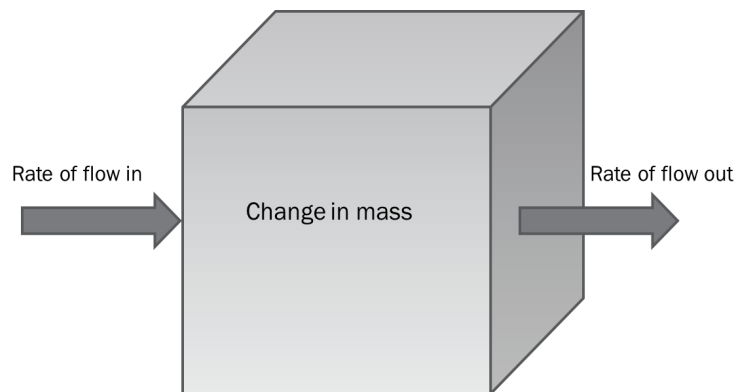


Figure 2.1: A diagram to illustrate the mass balance equation. Here, the cube represents the control volume V , and the diagram considers only one component i .

Let G_i [ML^{-3}] represent the mass of the component i within a given volume of fluid mixture, such that:

$$G_i = \phi \sum_{j=1}^{N_p} \rho_j X_{ij} S_j \quad (2.1)$$

where ϕ [-] is the porosity of the medium, ρ_j [ML^{-3}] is the density of the phase j , X_{ij} [-] is the mass fraction of component i in phase j , S_j [-] is the saturation of phase j , and N_p [-] is the number of phases that component i can appear in.

Now let H_i [$\text{ML}^{-2}\text{T}^{-1}$] be the mass flow rate per unit area of component i , hereafter referred to as the mass flux, given by:

$$H_i = \sum_{j=1}^{N_p} \rho_j X_{ij} q_j \quad (2.2)$$

where q_j [LT^{-1}] is the volumetric flux of phase j .

It is assumed that flow is convection-dominated, and hence molecular diffusion and hydrodynamic dispersion can be considered to be negligible. Under these conditions, mass conservation requires that:

$$\frac{\partial G_i}{\partial t} = -\nabla \cdot H_i \quad i = 1, \dots, N_c \quad (2.3)$$

where N_c [-] denotes the number of components within the system .

In equation (2.3), $\nabla \cdot (\cdot)$ is the divergence operator. Within this thesis, the main systems considered are one-dimensional linear and one-dimensional radial systems. In a one-dimensional linear system using Cartesian coordinates, where x [L] is the linear distance from the point of injection, equation (2.3) reduces to:

$$\frac{\partial G_i}{\partial t} = -\frac{\partial H_i}{\partial x} \quad i = 1, \dots, N_c \quad (2.4)$$

whereas for a one-dimensional radial system using cylindrical coordinates, where r [L] is the radial distance from the point of injection, it will be:

$$\frac{\partial G_i}{\partial t} = -\frac{1}{r} \frac{\partial (r H_i)}{\partial r} \quad i = 1, \dots, N_c \quad (2.5)$$

2.2.2 Darcy's Law for Multiphase Flow

The volumetric flux of a phase j , \mathbf{q}_j , is defined by Darcy's Law:

$$\mathbf{q}_j = -\frac{k k_{rj}}{\mu_j} (\nabla P_j + \rho_j \mathbf{g}) \quad (2.6)$$

where k [L^2] is the permeability of the system, assumed here to be an isotropic scalar quantity, k_{rj} [-] is the relative permeability of phase j (this will be explained fully in Section 2.2.3), μ_j [$ML^{-1}T^{-1}$] is the dynamic viscosity of phase j , P_j [$ML^{-1}T^{-2}$] is the phase pressure for phase j , and \mathbf{g} [MT^{-2}] represents gravity.

In equation (2.6), $\nabla()$ is the gradient operator. For a one-dimensional linear system, the volumetric flux will be given by:

$$q_j = -\frac{kk_{rj}}{\mu_j} \frac{\partial P_j}{\partial x} \quad (2.7)$$

and for a one-dimensional radial system it will be:

$$q_j = -\frac{kk_{rj}}{\mu_j} \frac{\partial P_j}{\partial r} \quad (2.8)$$

2.2.3 Relative Permeability

As well as the absolute permeability of the system, the relative permeability of different phases in a multiphase system must also be considered. If more than one phase is present, the permeability of a given fluid phase will be less than the absolute permeability of the system due to the pore space being occupied by other phases. Relative permeability therefore depends on saturation, and is formally defined as the ratio of the permeability of one phase in a multiphase system to the overall permeability of the system. It allows us to examine how easily certain fluid phases flow in the presence of others.

An effective way to think of relative permeability is to imagine that each fluid establishes its own path through the porous medium, and a unique set of channels corresponds to every degree of saturation. As the saturation of a phase decreases, the channels begin to break down and eventually become discontinuous. When this happens throughout the whole domain, the fluid can no longer flow, despite the fact that some may still be present (Bear, 1988, p.458). The saturation at which a phase becomes discontinuous is generally referred to as the critical, or residual, saturation, S_{jc} [-].

For immiscible systems, the relative permeability of a phase j , k_{rj} , can be defined using power laws, such that (Corey, 1954):

$$k_{rj} = k_{rj0} \left(\frac{S_j - S_{jc}}{1 - S_{gc} - S_{ar}} \right)^{n_j} \quad (2.9)$$

Here, S_{gc} [-] is the critical gas saturation, which is the gas saturation below which the gaseous phase can no longer flow, and S_{ar} [-] is the residual aqueous saturation, which

represents the aqueous saturation below which the aqueous phase cannot flow. n_j [-] are power law exponents for the phase j . k_{rj0} [-] represent endpoint permeabilities, which are the largest experimentally obtained value of k_{rj} for each phase j . These will be the value of k_{rj} at the saturation S_j when $S_j = 1 - S_{hc}$, i.e. at the point where the saturation of the phase j is equal to one minus the critical saturation of the phase h , where $h \neq j$.

Figure 2.2 shows how the relative permeabilities of CO₂ and brine in several different sandstone cores vary as the gas saturation increases. It can be seen that the nonlinearity of the curves (controlled by the power law exponent, n_j) have wide variations, and there are also differences in the values of the endpoint permeabilities and critical saturations for the different formations. The endpoint gas phase permeability, k_{rg0} , and the residual aqueous saturation, S_{ar} , are highlighted on the figure for Otway and Berea #1, and it can be seen that k_{rg0} reduces hugely from 0.6594 in Otway to 0.007 in Berea #1, while S_{ar} increases from 0.4370 in Otway to 0.5890 in Berea #1. It should also be noted that only the gas and aqueous phases are present here, so the aqueous saturation (S_a) is equal to $1 - S_g$.

However, equation (2.9) assumes that the residual water is immobile and has to remain in the aqueous phase, which is not the case in a partially miscible system such as for CO₂ injection into a saline formation (Zhang et al., 2016). When partial miscibility can occur, the saturation of the aqueous phase can reduce all the way to zero due to residual water evaporating into the gaseous phase, in contrast to the immiscible system in which the minimum saturation of the aqueous phase is the residual aqueous saturation. It would also be inaccurate to describe the residual water as immobile in the situation of the saline formation, due to the process of counter-current imbibition. This is when brine flows back to the injection point of the formation, against the general direction of flow of the CO₂. It is caused by the evaporation of residual water leading to very low aqueous saturations in the dry out zone of the aquifer, which therefore causes high capillary pressure gradients and a driving force for brine to flow towards regions with higher gaseous and lower aqueous saturations, i.e. those near the injection point of the aquifer. This means that, in order to define relative permeability across the full range of saturations possible in a partially miscible system, it is necessary to add an extension to equation (2.9). As the simplest alternative to reality, it is assumed that the relative permeability of a phase j , k_{rj} , linearly increases with saturation to one beyond residual saturations (Oostrom et al., 2016), such that:

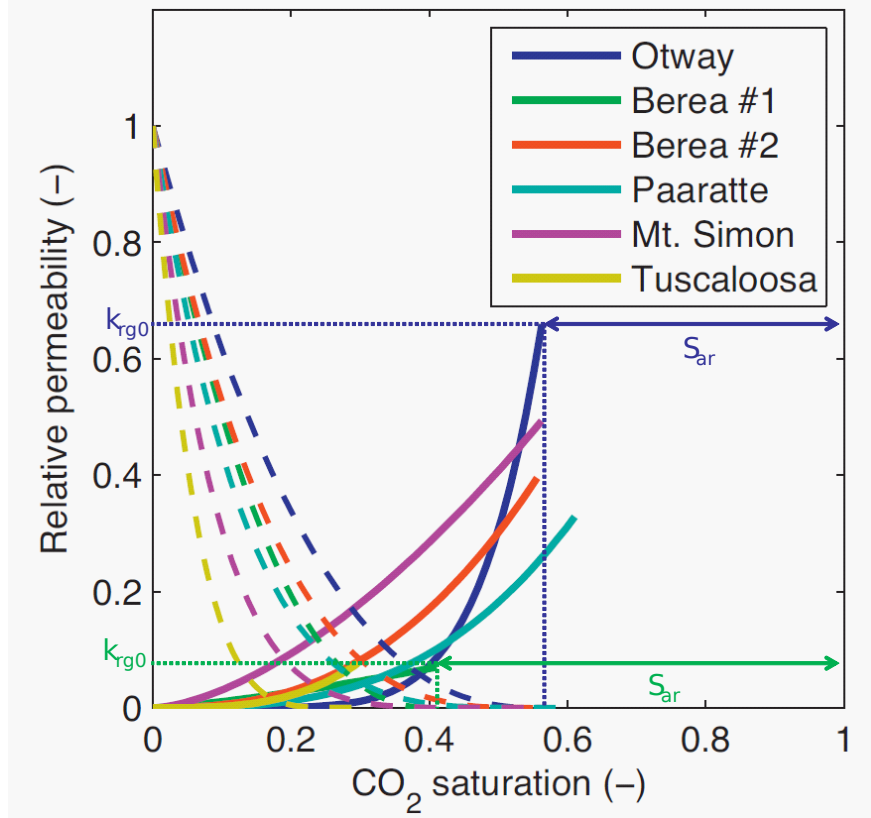


Figure 2.2: Relative permeability curves for various different sandstone rocks when two phases are flowing, constructed using the power law functions in the second row of equation (2.10) (Adapted from Mathias et al. (2013)). The relative permeability of the gaseous phase is represented by a solid line and the relative permeability of the aqueous phase is shown by a dashed line. The endpoint relative permeability (k_{rg0}) and the residual aqueous saturation (S_{ar}) for Otway are shown in purple, and for Berea #1 are shown in green. The data used to construct these curves came from Perrin and Benson (2010) and Krevor et al. (2012).

$$k_{rj} = \begin{cases} 0, & S_j \leq S_{jc} \\ k_{rj0} \left(\frac{S_j - S_{jc}}{1 - S_{gc} - S_{ar}} \right)^{n_j}, & S_{jc} < S_j < 1 - S_{hc} \text{ , } h \neq j \\ k_{rj0} + (1 - k_{rj0}) \left(\frac{S_j - 1 + S_{hc}}{S_{hc}} \right), & S_j \geq 1 - S_{hc} \end{cases} \quad (2.10)$$

2.2.4 Capillary Pressure

In order to form a numerical model, the partial differential equations (PDEs) are solved for certain dependent variables, referred to as primary dependent variables (PDVs). The variables chosen as PDVs will vary for different models described within this thesis, but one PDV which is consistent across all of the models in the thesis is global pressure, P

[ML⁻¹T⁻²]. This is defined as:

$$P = \sum_{j=1}^{N_p} S_j P_j \quad (2.11)$$

P is convenient as a PDV compared to phase pressures as it is persistent for all time and space, unlike the phase pressures which are only defined at points at which the respective phases are present.

It can be seen from Section 2.2.2 that it is necessary to define the phase pressure P_j within a model in order to find the associated volumetric flux, q_j . Phase pressures are found from the global pressure, P , the capillary pressure, P_c [ML⁻¹T⁻²], which is defined as the difference between the gaseous and aqueous pressure:

$$P_c = P_g - P_a \quad (2.12)$$

and the phase saturations, S_j , such that:

$$P_g = \frac{P(S_g + S_a) + P_c S_a}{S_g + S_a} \quad (2.13)$$

and

$$P_a = \frac{P(S_g + S_a) - P_c S_g}{S_g + S_a} \quad (2.14)$$

As was mentioned in Chapter 1, a pressure difference between the gaseous and aqueous phases is caused by interfacial tension between the two phases. This interfacial tension is caused by differences in the relative strength of inter-molecular forces between the phases, which are in turn directly affected by the relative amount of each of the phases present, i.e., the phase saturation S_j . It can therefore be seen that capillary pressure is solely a function of S_j .

The Brooks-Corey and van Genuchten curves are the two main functions used to represent capillary pressure within the literature. The difference between these models is that the Brooks-Corey model represents a capillary entry pressure, $P_{c,e}$ [ML⁻¹T⁻²], meaning that the capillary pressure is not equal to zero when the aqueous saturation is at zero, while the van Genuchten function does not (Gershenson et al., 2016). Instead, the van Genuchten function assumes the existence of at least one pore connected pathway in the formation that has pores large enough that the capillary pressure can be considered negligible (Gershenson et al., 2016). This leads to the Brooks-Corey curve being convex, and the van Genuchten curve being S-shaped (Li et al., 2013), as can be seen in Figure 2.3.

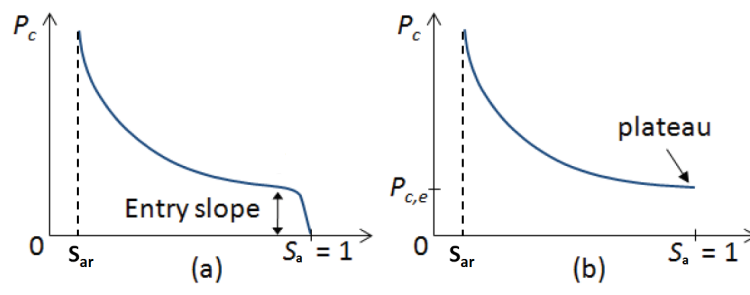


Figure 2.3: P_c vs S_a curves for (a) the van Genuchten model and (b) the Brooks Corey model (Adapted from Li et al. (2013)). Note the S-shape of the van Genuchten model and the convex shape of the Brooks-Corey model, caused by differences in the representation of the capillary entry pressure, $P_{c,e}$. In the van Genuchten model, the region around the endpoint is termed the ‘entry slope’ region, the height of which is the pressure difference between the plateau and the endpoint of the curve at $S_a = 1$.

In the Brooks-Corey model (Brooks and Corey, 1964),

$$P_c = P_{c,e} S_e^{-\frac{1}{\lambda}} \quad \text{for } P_c > P_{c,e} \quad (2.15)$$

where S_e [-] is an effective aqueous saturation, found from:

$$S_e = \frac{S_a - S_{ar}}{1 - S_{ar}} \quad (2.16)$$

and λ [-] is a Brooks-Corey pore geometry factor.

For the van Genuchten function (van Genuchten, 1980),

$$P_c = P_{c0} \left(S_e^{-\frac{1}{m}} - 1 \right)^{-\frac{1}{n}} \quad (2.17)$$

where P_{c0} [$\text{ML}^{-1}\text{T}^{-2}$] is a van Genuchten parameter, equal to $\frac{1}{\alpha}$, in which α [M^{-1}LT^2] is a scaling parameter related to the inverse of $P_{c,e}$, m is a parameter that depends on pore geometry (Pruess and Müller, 2009), and:

$$n = \frac{1}{1 - m} \quad (2.18)$$

Both the van Genuchten and Brooks-Corey models can be easily fitted to experimental data (Ostrom et al., 2016), and which is more realistic will vary depending on numerous factors including the relative permeability relations used and the permeability of the individual rock. However, the van Genuchten function is more widely used in reservoir simulation packages such as TOUGH2, and generally has a faster calculation time and fewer convergence problems (Gershenzon et al., 2016), and so for all work done in this thesis, the van Genuchten model will be used.

One drawback of existing capillary pressure functions, including both the van Genuchten and Brooks-Corey functions, is that they do not describe the changes in capillary pressure that occur as the residual aqueous phase is evaporated. In the current functions, as the aqueous saturation approaches its residual value, the capillary pressure approaches infinity, as can be seen in Figure 2.3. This can cause serious issues in numerical simulators (Webb, 2000). A considerable proportion of the work in this thesis focuses on the dry out zone, in which the aqueous saturation has gone all the way down to zero, so this could have had a significant effect on the numerical models produced.

However, several methods have been derived to avoid this problem, the most commonly used (and one of the easiest to implement) of which was formed by Webb (2000). Campbell and Shiozawa (1992) observed from dry region capillary pressure data that in the dry out zone, capillary pressure plots as a linear function of aqueous saturation on a semilog plot, on which aqueous saturation is plotted against $\log_{10} P_c$. Webb (2000) used this idea to conclude that a capillary pressure function for all aqueous saturations can be found by using the van Genuchten function above a certain aqueous saturation matching point, $S_{am}[-]$ (in what is termed the capillary flow region), and a linear extension of the van Genuchten curve on a semilog plot to zero aqueous saturation for aqueous saturations below this matching point (in the dry region). Figure 2.4 shows these extensions for several different values of S_{am} . It can be seen that the capillary pressure at zero aqueous saturation increases superlinearly as the value of S_{am} decreases.

The appropriate value of S_{am} is the one at which the extension of the van Genuchten capillary pressure curve results in the desired capillary pressure at zero aqueous saturation, taken by Webb (2000) to be 10^9 Pa, and referred to as the capillary pressure at oven dry conditions, P_{cd} [$\text{ML}^{-1}\text{T}^{-2}$]. Webb (2000) defined S_{am} as the value of S_a where the derivatives of the van Genuchten function and the linear-log relationship are equal. Such a value must be found by iteration.

Mathematically this leads to the following extension of equation (2.17):

$$P_c = \begin{cases} P_{c0} \left(S_e^{-\frac{1}{m}} - 1 \right)^{\frac{1}{n}}, & S_a > S_{am} \\ P_{cd} \exp \left[\ln \left(\frac{P_{cm}}{P_{cd}} \right) \frac{S_a}{S_{am}} \right], & S_a \leq S_{am} \end{cases} \quad (2.19)$$

The matching point S_{am} can be given as:

$$S_{am} = (1 - S_{ar})S_{em} + S_{ar} \quad (2.20)$$

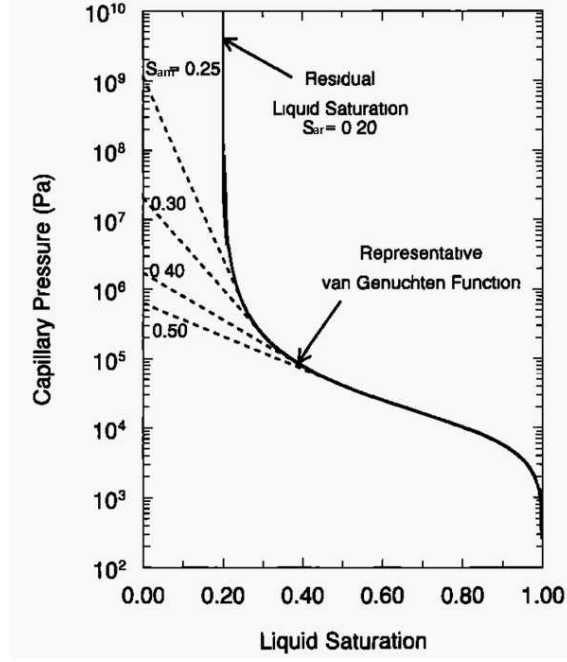


Figure 2.4: A representative van Genuchten capillary pressure function including linear extension. Adapted from Webb (2000).

and P_{cm} [$\text{ML}^{-1}\text{T}^{-2}$] as

$$P_{cm} = P_{c0} \left(S_{em}^{-\frac{1}{m}} - 1 \right)^{\frac{1}{n}} \quad (2.21)$$

where S_{em} [-] is the critical effective saturation at which the switch over between the van Genuchten function and Webb's extension takes place.

Differentiation of equation (2.19) with respect to S_a leads to

$$\frac{\partial P_c}{\partial S_a} = \begin{cases} \frac{P_c}{(1 - S_{ar})mnS_e(S_e^{\frac{1}{m}} - 1)}, & S_a > S_{am} \\ \frac{P_c}{S_{am}} \ln \left(\frac{P_{cm}}{P_{cd}} \right), & S_a \leq S_{am} \end{cases} \quad (2.22)$$

Considering equation (2.22), Webb (2000) defines S_{em} as the effective saturation at which

$$\frac{P_{cm}}{(1 - S_{ar})mnS_{em}(S_{em}^{\frac{1}{m}} - 1)} = \frac{P_{cm}}{S_{am}} \ln \left(\frac{P_{cm}}{P_{cd}} \right) \quad (2.23)$$

Substituting equation (2.21) and equation (2.20) into equation (2.23) and rearranging leads to

$$S_{em} = \frac{S_{em} + S_{ar}(1 - S_{ar})^{-1}}{mn(S_{em}^{\frac{1}{m}} - 1) \ln \left[(S_{em}^{\frac{1}{m}} - 1)^{\frac{1}{n}} \left(\frac{P_{cd}}{P_{c0}} \right)^{-1} \right]} \quad (2.24)$$

which must be solved iteratively. Webb (2000) suggests that four to five iterations are sufficient. However, this will be strongly dependent on the value used for the initial estimate of S_{em} , S_{em0} .

In order to find an accurate value for S_{em0} , [Kelly and Mathias \(2018\)](#) showed that it is possible to use the Lambert W function, which is defined as the inverse of the function $w \mapsto we^w$. $W(z)$ is therefore the function that satisfies ([Corless et al., 1996](#)):

$$W(z)e^{W(z)} = z \quad (2.25)$$

This can be shown as follows. For cases in which $S_{ar} > 0$, firstly assume that $S_{em0} \ll 1$ such that equation (2.24) reduces to

$$S_{em0} = \frac{S_{ar}(1 - S_{ar})^{-1}}{\ln \left[S_{em0} \left(\frac{P_{cd}}{P_{c0}} \right)^{nm} \right]} \quad (2.26)$$

This can be rearranged to give:

$$z = W \exp(W) \quad (2.27)$$

where

$$z = \frac{S_{ar} \left(\frac{P_{cd}}{P_{c0}} \right)^{nm}}{(1 - S_{ar})} \quad (2.28)$$

and

$$W = \frac{S_{ar}}{(1 - S_{ar})S_{em0}} \quad (2.29)$$

By comparing equation (2.27) to equation (2.25), it can be seen that the functional inverse of $z(W)$ in equation (2.27), $W(z)$, is given by the Lambert W function. Furthermore, because z is always positive and real, $W(z) = W_0(z)$, otherwise referred to as the zero branch. This has the following asymptotic expansion ([Corless et al., 1996](#)):

$$W_0(z) = L_1 - L_2 + \frac{L_2}{L_1} + O\left(\left[\frac{L_2}{L_1}\right]^2\right) \quad (2.30)$$

where $L_2 = \ln L_1$ and $L_1 = \ln z$.

Once a value for W has been found using equation (2.30), a good initial estimate for S_{em} , S_{em0} can be found by rearranging equation (2.29) to give:

$$S_{em0} = \frac{S_{ar}}{W(1 - S_{ar})} \quad (2.31)$$

S_{em} , P_{cm} and S_{am} can then be found iteratively using equations (2.20), (2.21) and (2.24), providing all necessary terms to find the capillary pressure, P_c , for all values of aqueous saturation from equation (2.19).

2.3 Mass Fractions at Equilibrium

As was explained in Section 2.1, the injection of CO₂ into a saline formation leads to a three phase, three component system, in which each of the components can exist in two different phases. It is assumed that if more than one phase is present, the phases are in equilibrium, which means that the maximum solubility of each component in each phase has been reached. This assumption can be made because the diffusion timescale is very short relative to the convection timescale, and hence the solubility limits, or equilibrium concentrations, are reached very quickly. The equilibrium concentrations will vary with pressure, temperature and brine salinity. It is important to know these equilibrium concentrations to enable us to track the phases present in the system and their composition. For example, if CO₂ is injected into an aqueous phase, it can only dissolve in the aqueous phase up to its equilibrium concentration. Beyond this, the aqueous phase has reached its maximum solubility for CO₂, so a higher concentration of CO₂ will result in the formation of a separate gaseous phase.

[Spycher et al. \(2003\)](#) and [Spycher and Pruess \(2005\)](#) present a methodology to estimate the mutual solubilities of CO₂ and H₂O in coexisting phases. [Spycher et al. \(2003\)](#) looked at these solubilities for a two component, two phase system of water and CO₂, both able to exist in gaseous and aqueous phases, while [Spycher and Pruess \(2005\)](#) extended this work to account for the effects of chloride salts in the aqueous phase. Within the models used in this thesis, the work of [Spycher et al. \(2003\)](#) and [Spycher and Pruess \(2005\)](#) is used to find the solubility of CO₂ in the aqueous phase and H₂O in the gaseous phase, while the solubility of NaCl in the aqueous phase is found using an equation by [Potter et al. \(1977\)](#). The following subsections will explain the thermodynamics of systems at equilibrium, before using this to explain further the work of [Spycher et al. \(2003\)](#), [Spycher and Pruess \(2005\)](#) and [Potter et al. \(1977\)](#).

2.3.1 Chemical Potential and Gibbs Energy

When a system is in chemical equilibrium, the chemical potential of each component, μ_i [ML²T⁻²N⁻¹], must be equal in all parts of the system ([Smith, 2004](#), p.49). Therefore, for a component i distributed between two phases g and a , it must be that $\mu_i(g) = \mu_i(a)$ at equilibrium. The chemical potential of a component i , μ_i , represents the force that drives chemical systems to equilibrium, and is formally defined as the increase in the free energy

of a system when one mole of component i is added to an infinitely large quantity of the mixture, so that it does not significantly alter the overall composition of the system, and the temperature, pressure and amounts of all other components are held constant (Smith, 2004, p.49). Writing this mathematically:

$$\mu_i = \left(\frac{\partial G}{\partial n_i} \right)_{T,P,n_k} \quad (2.32)$$

Here, n_i [N] is the number of moles of component i , T [Θ] is temperature and G [ML²T⁻²] represents the Gibbs free energy, which is the maximum amount of non-expansion work that can be done by a closed system. Mathematically, this is defined as (Smith, 2004, p.38):

$$G = H - TS \quad (2.33)$$

where H [ML²T⁻²] is the enthalpy and S [ML²T⁻²Θ⁻¹] is the entropy of the system.

When the system is capable of doing no work and is at equilibrium, G is at a minimum and $dG = 0$ (Smith, 2004, p.38).

2.3.2 Chemical Potential for Ideal Gas Mixtures

Using equation (2.33) and the relation $dH = TdS + VdP$, where V [L³] is the volume of the system, the total derivative of G for a pure substance is found to be (Cengel and Boles, 2002, p.697):

$$dG = VdP - SdT \quad (2.34)$$

In a mixture, the Gibbs free energy is a function of two independent properties (pressure and temperature) as well as the composition of the mixture. Therefore (Cengel and Boles, 2002, p.697):

$$G = G(T, P, n_i, n_k, \dots) \quad (2.35)$$

where n_k [N] is the number of moles of component k . The total derivative of G for a mixture is therefore found from:

$$dG = \left(\frac{\partial G}{\partial P} \right)_{T,n} dP + \left(\frac{\partial G}{\partial T} \right)_{P,n} dT + \sum_i \left(\frac{\partial G}{\partial n_i} \right)_{P,T,n_k} dn_i \quad (2.36)$$

where n [N] is the number of moles in the system as a whole. Equation (2.36) is also valid for pure substances, except that the final term would be equal to zero because the composition of a pure substance is constant.

Comparing equation (2.34) and equation (2.36), it can be seen that for a mixture (Cengel and Boles, 2002, p.697):

$$dG = VdP - SdT + \sum_i \mu_i dn_i \quad (2.37)$$

where

$$\left(\frac{\partial G}{\partial P}\right)_{T,n} = V \quad (2.38)$$

and

$$\left(\frac{\partial G}{\partial T}\right)_{P,n} = -S \quad (2.39)$$

Differentiating both sides of equation (2.38) with respect to n_i gives:

$$\frac{\partial}{\partial n_i} \left(\frac{\partial G}{\partial P}\right)_{T,n_k} = \left(\frac{\partial V}{\partial n_i}\right)_{T,P,n_k} \quad (2.40)$$

which is equivalent to:

$$\left(\frac{\partial \mu_i}{\partial P}\right)_{T,n} = \bar{V}_i \quad (2.41)$$

where \bar{V}_i [L^3N^{-1}] is the partial molar volume of component i .

An ideal gas is an imaginary substance that does not take into account the effect of any intermolecular forces or the sizes of molecules. A real gas behaves similar to an ideal gas at relatively low pressures and high temperatures (Cengel and Boles, 2002, p.153). The ideal gas equation of state is (Cengel and Boles, 2002, p.137):

$$PV = nRT \quad (2.42)$$

and so

$$\frac{V}{n} = \frac{\sum_{i=1}^{N_c} n_i \bar{V}_i}{\sum_{i=1}^{N_c} n_i} = \bar{V}_i = \frac{RT}{P} \quad (2.43)$$

Here, R [$ML^2T^{-2}N^{-1}\Theta^{-1}$] is the universal gas constant, equal to $8.31447 \text{ J} \cdot \text{mol}^{-1} \cdot \text{K}^{-1}$. It should be noted from this equation that \bar{V}_i is the same for all components i , as \bar{V}_i can be written solely as a function of the terms V and n , both of which depend on the system as a whole rather than an individual component (Denbigh, 1966, p.116). Substituting equation (2.43) into equation (2.41) gives that, for an ideal gas mixture at temperature T and pressure P :

$$d\mu_i = \frac{RT}{P} dP \quad (2.44)$$

Integrating both sides of equation (2.44) with respect to P between a reference pressure, P^0 [$ML^{-1}T^{-2}$], and the partial pressure of component i , P_i [$ML^{-1}T^{-2}$], gives (Denbigh, 1966, p.115):

$$\mu_i = \mu_i^0 + RT \ln \left(\frac{P_i}{P^0}\right) \quad (2.45)$$

where the partial pressure, P_i , is defined as:

$$P_i = y_i P \quad (2.46)$$

and y_i [-] is the mole fraction of component i in the gas and μ_i^0 [ML²T⁻²N⁻¹] represents the chemical potential of the component i at temperature T and pressure P^0 . It is often assumed that the reference pressure, P^0 , is equal to 1 bar, and so equations are sometimes written as though this is the case.

Equation (2.45) gives an expression for chemical potential in terms of measurable quantities.

2.3.3 Chemical Potential for Non-Ideal Gas Mixtures

Equation (2.45) only holds for ideal gas mixtures. For non-ideal gas mixtures, the partial pressure of a component i , P_i , should be replaced with the fugacity of that component, f_i [ML⁻¹T⁻²], which is an effective partial pressure for a non-ideal gas, such that (Denbigh, 1966, p.125):

$$\mu_i = \mu_i^0 + RT \ln \left(\frac{f_i}{P^0} \right) \quad (2.47)$$

Fugacity and partial pressure of a component i are linked by the fugacity coefficient Φ_i [-] of the component i such that:

$$\Phi_i = \frac{f_i}{P_i} \quad (2.48)$$

and it is the case that (Denbigh, 1966, p.125) :

$$\Phi_i = \frac{f_i}{P_i} \rightarrow 1 \quad \text{as} \quad P \rightarrow 0 \quad (2.49)$$

so that the fugacity is equal to the partial pressure under conditions where the gas obeys the ideal gas equation of state.

Fugacity can therefore be defined in terms of pressure by rearranging equation (2.48) and substituting in equation (2.46) to give:

$$f_i = \Phi_i P_i = \Phi_i y_i P \quad (2.50)$$

2.3.4 Chemical Potential of Ideal Solutions

Ideal solutions are analogous to ideal gas mixtures, with the difference being that the intermolecular interactions in ideal solutions are assumed to be equal between all molecules of the solution rather than neglected entirely as in ideal gases.

A solution is ideal if it obeys Raoult's Law, which is that the partial pressure of a component i is equal to P_i^* [ML⁻¹T⁻²], the vapour pressure of the pure component i , multiplied by x_i [-], the mole fraction of component i in the solution. Mathematically, this is written as (Denbigh, 1966, p.223):

$$P_i = P_i^* x_i \quad (2.51)$$

As was explained in Section 2.3.1, at equilibrium the chemical potential of component i in the gaseous and aqueous phases will be equal. Therefore, the chemical potential of a component i in an ideal solution can be found by substituting equation (2.51) into the equation for chemical potential of component i in an ideal gas mixture, equation (2.45), to give:

$$\mu_i = \mu_i^0 + RT \ln \left(\frac{P_i^*}{P^0} \right) + RT \ln x_i \quad (2.52)$$

which can also be written as (Denbigh, 1966, p.249):

$$\mu_i = \mu_i^* + RT \ln x_i \quad (2.53)$$

2.3.5 Chemical Potential of Non-Ideal Solutions

Again, equation (2.53) is only valid for ideal solutions. However, as for gas mixtures, a similar equation can be used to give the chemical potential for component i for non-ideal solutions (Denbigh, 1966, p.270):

$$\mu_i = \mu_i^* + RT \ln \gamma_{xi} x_i \quad (2.54)$$

It can be seen that equation (2.54) is identical to equation (2.53) except that an activity coefficient, γ_{xi} [-], has been introduced to account for the deviation from ideality.

It should also be noted that the activity coefficient can be expressed in terms of the molality of component i , m_i [NM⁻¹], rather than in terms of its mole fraction. This convention is

often used when the component i is a solute in the solution. The molality of a solute i is a measure of concentration and is defined as the number of moles of component i in the solution per kilogram of solvent.

In the case of the solvent in a solution (Denbigh, 1966, p.276):

$$\gamma_{xi} \rightarrow 1 \quad \text{as} \quad x_i \rightarrow 1 \quad (2.55)$$

whereas for the solute:

$$\gamma_{mi} \rightarrow 1 \quad \text{as} \quad m_i \rightarrow 0 \quad (2.56)$$

Note that γ_{xi} indicates an activity coefficient given in terms of the mole fraction x_i , whereas γ_{mi} [-] indicates an activity coefficient in terms of the molality m_i . These expressions indicate that the activity coefficient approaches unity, and so the deviation from ideality reduces and the behaviour of component i within the solution becomes similar to within the ideal solution, as either the mole fraction of component i tends towards unity if i is a solvent, or as the molality of component i tends towards infinite dilution if i is a solute.

The activity of component i is a measure of the ‘effective concentration’ of a component in a mixture. The activity of a solvent i on the mole fraction scale, a_{xi} [-], is defined as (Denbigh, 1966, p.287):

$$a_{xi} = \gamma_{xi}x_i \quad (2.57)$$

while the activity of a solute i on the molality scale, a_{mi} [-] is:

$$a_{mi} = \gamma_{mi}m_i \quad (2.58)$$

Equation (2.54) can be equivalently written on the mole fraction scale as:

$$\mu_i = \mu_i^* + RT \ln a_{xi} \quad (2.59)$$

or on the molality scale as:

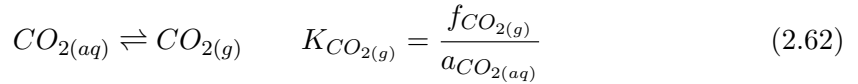
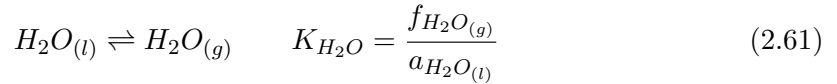
$$\mu_i = \mu_i^\square + RT \ln a_{mi} \quad (2.60)$$

2.3.6 Expressions for y_{H_2O} and x_{CO_2}

This subsection explains how Spycher et al. (2003) and Spycher and Pruess (2005) estimate the mutual solubilities of H₂O and CO₂, including the effect of chloride salts in the aqueous phase.

The equilibrium constant of a chemical reaction, K [-], gives the relationship between the amounts of reactants and products that are present at equilibrium. In general, a large value of K tells us that mostly products are present at equilibrium and so the reaction is at a position close to completion, whereas a small K value means that mainly reactants are still present, so the reaction has not gone far before enough products have been formed to stop it (Anderson, 2005, p.240).

In a two phase region in which CO_2 and H_2O exist, the following reactions can be written at equilibrium, with their corresponding equilibrium constants:



If a component i is in phase equilibrium, the chemical potentials of i in the gaseous and aqueous phases should be equal. This means that, using equations (2.47) and (2.59)

$$\mu_i^0 + RT \ln \left(\frac{f_i}{P^0} \right) = \mu_i^* + RT \ln a_{xi} \quad (2.63)$$

Assuming that P^0 is equal to 1 bar, this simplifies to:

$$\mu_i^0 + RT \ln f_i = \mu_i^* + RT \ln a_{xi} \quad (2.64)$$

which can be rearranged to give:

$$\ln \left(\frac{f_i}{a_{xi}} \right) = \ln K_i = \frac{(\mu_i^* - \mu_i^0)}{RT} \quad (2.65)$$

where K_i [-] is the equilibrium constant of the component i .

Differentiating both sides of this equation with respect to pressure P , and recalling equation (2.41) gives:

$$\frac{\partial \ln K_i}{\partial P} = \frac{\bar{V}_i}{RT} \quad (2.66)$$

which can be integrated with respect to P between the values of P^0 and P to give the pressure correction for K_i :

$$K_{i(T,P)} = K_{i(T,P^0)} \exp \left(\frac{(P - P^0)\bar{V}_i}{RT} \right) \quad (2.67)$$

Recall from equation (2.50) that:

$$f_i = \Phi_i y_i P \quad (2.68)$$

Combining equation (2.68) with equations (2.61) and (2.62) gives:

$$f_{H_2O} = \Phi_{H_2O} y_{H_2O} P = K_{H_2O} a_{H_2O(l)} \quad (2.69)$$

and

$$f_{CO_2} = \Phi_{CO_2} y_{CO_2} P = K_{CO_2} a_{CO_2(aq)} \quad (2.70)$$

Rearranging equation (2.69) to give the mole fraction of H₂O in the gaseous phase, y_{H_2O} :

$$y_{H_2O} = \frac{K_{H_2O} a_{H_2O}}{\Phi_{H_2O} P} \quad (2.71)$$

Equation (2.67) can now be substituted in to this to obtain:

$$y_{H_2O} = \frac{K_{H_2O}^0 a_{H_2O}}{\Phi_{H_2O} P} \exp\left(\frac{(P - P^0) \bar{V}_{H_2O}}{RT}\right) \quad (2.72)$$

where $K_{H_2O}^0$ is shorthand for $K_{(T,P^0)}$ for the component H₂O.

It is also necessary to find an expression for the mole fraction of CO₂ in the aqueous phase, x_{CO_2} . Recalling the definition of molality given in Section 2.3.5, and assuming for now that only CO₂ and H₂O are present, the molality of CO₂ in solution, m_{CO_2} , can be given by (Denbigh, 1966, p.274):

$$m_{CO_2} = \frac{1000 n_{CO_2}}{M_{H_2O} n_{H_2O}} \quad (2.73)$$

where M_{H_2O} [MN⁻¹] is the molecular mass of water.

The mole fraction of CO₂ in the aqueous phase, x_{CO_2} , is found by (Denbigh, 1966, p.275):

$$x_{CO_2} = \frac{n_{CO_2}}{n_{H_2O} + n_{CO_2}} \quad (2.74)$$

Therefore, using equations (2.73) and (2.74), the ratio of molality to mole fraction of CO₂ is found to be (Denbigh, 1966, p.275):

$$\frac{m_{CO_2}}{x_{CO_2}} = \frac{1000(n_{H_2O} + n_{CO_2})}{M_{H_2O} n_{H_2O}} = \frac{1000}{M_{H_2O} x_{H_2O}} \quad (2.75)$$

In a very dilute solution, $x_{H_2O} \rightarrow 1$. Therefore, in this case, it can be taken that:

$$\frac{m_{CO_2}}{x_{CO_2}} \approx \frac{1000}{M_{H_2O}} \quad (2.76)$$

Recall from Section 2.3.5 that chemical potential can be given on either the mole fraction or molality scales. Regardless of the scale that is used, the chemical potential of a component

i will be the same, and so equating equations (2.59) and (2.60) for the component CO_2 leads to (Denbigh, 1966, p.277):

$$\mu_{\text{CO}_2} = \mu_{\text{CO}_2}^* + RT \ln a_{x_{\text{CO}_2}} = \mu_{\text{CO}_2}^\square + RT \ln a_{m_{\text{CO}_2}} \quad (2.77)$$

or equivalently:

$$\mu_{\text{CO}_2}^* + RT \ln(\gamma_{x_{\text{CO}_2}} x_{\text{CO}_2}) = \mu_{\text{CO}_2}^\square + RT \ln(\gamma_{m_{\text{CO}_2}} m_{\text{CO}_2}) \quad (2.78)$$

which can be rearranged to get:

$$RT \ln \left(\frac{\gamma_{m_{\text{CO}_2}} m_{\text{CO}_2}}{\gamma_{x_{\text{CO}_2}} x_{\text{CO}_2}} \right) = \mu_{\text{CO}_2}^* - \mu_{\text{CO}_2}^\square \quad (2.79)$$

In a very dilute solution, $\gamma_{m_{\text{CO}_2}} \rightarrow 1$ as $m_{\text{CO}_2} \rightarrow 0$ and $\gamma_{x_{\text{CO}_2}} \rightarrow 1$ as $x_{\text{CO}_2} \rightarrow 0$, which means that equation (2.79) reduces to:

$$RT \ln \left(\frac{m_{\text{CO}_2}}{x_{\text{CO}_2}} \right) = \mu_{\text{CO}_2}^* - \mu_{\text{CO}_2}^\square \quad (2.80)$$

which, using equation (2.76), becomes:

$$RT \ln \left(\frac{1000}{M_{\text{H}_2\text{O}}} \right) = \mu_{\text{CO}_2}^* - \mu_{\text{CO}_2}^\square \quad (2.81)$$

The quantities μ^* and μ^\square are independent of composition, so the difference between them in equation (2.79) is the same as the difference between them in equation (2.81), despite the fact that equation (2.81) only applies in limiting conditions of high dilution (Denbigh, 1966, p.277). This means that:

$$RT \ln \left(\frac{\gamma_{m_{\text{CO}_2}} m_{\text{CO}_2}}{\gamma_{x_{\text{CO}_2}} x_{\text{CO}_2}} \right) = RT \ln \left(\frac{1000}{M_{\text{H}_2\text{O}}} \right) \quad (2.82)$$

and so:

$$\frac{\gamma_{m_{\text{CO}_2}}}{\gamma_{x_{\text{CO}_2}}} = \frac{1000 x_{\text{CO}_2}}{M_{\text{H}_2\text{O}} m_{\text{CO}_2}} \quad (2.83)$$

Spycher et al. (2003) find the activity of CO_2 using a molality to mole fraction correction, which gives a unit activity coefficient on the mole fraction scale. Therefore, using equations (2.58) and (2.83):

$$a_{m_{\text{CO}_2}} = \gamma_{m_{\text{CO}_2}} m_{\text{CO}_2} = \frac{1000 x_{\text{CO}_2} \gamma_{x_{\text{CO}_2}}}{M_{\text{H}_2\text{O}}} = 55.508 x_{\text{CO}_2} \quad (2.84)$$

as $M_{\text{H}_2\text{O}}$ is equal to 18.015g/mol.

This can be substituted into equation (2.70) to give:

$$\Phi_{\text{CO}_2} y_{\text{CO}_2} P = K_{\text{CO}_2} 55.508 x_{\text{CO}_2} \quad (2.85)$$

which can be rearranged to make x_{CO_2} the subject:

$$x_{CO_2} = \frac{\Phi_{CO_2} y_{CO_2} P}{55.508 K_{CO_2}} \quad (2.86)$$

Only CO_2 and H_2O can be present in the gaseous phase, regardless of whether or not salts are in the system, meaning that $y_{CO_2} = 1 - y_{H_2O}$. Substituting in both this and the equation for K_{CO_2} from equation (2.67) gives the expression that [Spycher et al. \(2003\)](#) found for x_{CO_2} when only CO_2 and H_2O were present in the system:

$$x_{CO_2} = \frac{\Phi_{CO_2}(1 - y_{H_2O})P}{55.508 K_{CO_2}^0} \exp\left(-\frac{(P - P^0)\overline{V}_{CO_2}}{RT}\right) \quad (2.87)$$

[Spycher and Pruess \(2005\)](#) took this further and introduced an activity coefficient for aqueous CO_2 , γ'_x , which incorporates the effect of chloride salts in the aqueous phase and the departure from solubility in pure water. Several different literature sources have different techniques for calculating γ'_x , but the best results are obtained when using the formulation of [Rumpf et al. \(1994\)](#) and [Duan and Sun \(2003\)](#).

Incorporating γ'_x into equation (2.87) gives the overall expression for x_{CO_2} in a three component system:

$$x_{CO_2} = \frac{\Phi_{CO_2}(1 - y_{H_2O})P}{55.508 \gamma'_x K_{CO_2}^0} \exp\left(-\frac{(P - P^0)\overline{V}_{CO_2}}{RT}\right) \quad (2.88)$$

Note that γ'_x is on a mole fraction scale and $\gamma'_x \rightarrow 1$ as $x_{salt} \rightarrow 0$, where x_{salt} is the mole fraction of fully ionized salt dissolved in the aqueous phase. This means that equation (2.88) reduces to equation (2.87) when no salt is present in the system.

2.3.7 Solving for y_{H_2O} and x_{CO_2}

It should be noted that equations (2.72) and (2.88) depend on each other. In order to solve these equations and find the mutual solubilities of CO_2 and H_2O in a saline formation, it is necessary to be able to define all other terms in the equations.

The Redlich-Kwong equation of state is of the form ([Redlich and Kwong, 1949](#)):

$$P = \left(\frac{RT}{V_g - B_{mix}}\right) - \left(\frac{A_{mix}}{T^{0.5} V_g (V_g + B_{mix})}\right) \quad (2.89)$$

where the parameters A_{mix} [$ML^{-5}T^{-2}N^{-2}\Theta^{0.5}$] and B_{mix} [L^3N^{-1}] represent measures of intermolecular attraction and repulsion, respectively, and V_g [L^3] is the volume of the compressed gas phase at pressure P and temperature T .

Within the Redlich-Kwong equation, A_{mix} and B_{mix} are calculated using the following mixing rules (e.g. Prausnitz et al., 1999):

$$A_{mix} = \sum_{i=1}^{N_i} \sum_{k=1}^{N_k} y_i y_k A_{ik} \quad (2.90)$$

and

$$B_{mix} = \sum_{i=1}^{N_k} y_i B_i \quad (2.91)$$

which, for the mixture of CO₂ and H₂O in the gaseous phase, become:

$$A_{mix} = y_{H_2O}^2 A_{H_2O} + 2y_{H_2O} y_{CO_2} A_{H_2O-CO_2} + y_{CO_2}^2 A_{CO_2} \quad (2.92)$$

and

$$B_{mix} = y_{H_2O} B_{H_2O} + y_{CO_2} B_{CO_2} \quad (2.93)$$

Once A_{mix} and B_{mix} have been found, V_g can be calculated from these values and the inputted values of P and T into the Redlich-Kwong equation. The fugacity coefficient Φ_k of a component k in a mixture with other components i can then be found from the equation (e.g. Prausnitz et al., 1999):

$$\begin{aligned} \ln(\Phi_k) = & \ln\left(\frac{V_g}{V_g - B_{mix}}\right) + \left(\frac{B_k}{V_g - B_{mix}}\right) - \left(\frac{2 \sum_{i=1}^{N_i} y_i A_{ik}}{RT^{1.5} b_{mix}}\right) \ln\left(\frac{V_g + B_{mix}}{V_g}\right) \\ & + \left(\frac{A_{mix} B_k}{RT^{1.5} B_{mix}^2}\right) \left[\ln\left(\frac{V_g + B_k}{V_g}\right) - \left(\frac{B_{mix}}{V_g + B_{mix}}\right) \right] - \ln\left(\frac{PV_g}{RT}\right) \end{aligned} \quad (2.94)$$

However, it can be seen from this equation that the fugacity coefficients Φ_k depend on the composition of the mixture, which means that both the rearranged version of the Redlich-Kwong equation to find V_g and equation (2.94) need to be solved simultaneously with equations (2.72) and (2.88), therefore requiring an iterative solution scheme. However, if an assumption of infinite H₂O dilution is made in the gaseous phase in equations (2.92) to (2.94), such that $y_{H_2O} = 0$ and $y_{CO_2} = 1$, it can be seen that A_{mix} and B_{mix} reduce to:

$$A_{mix} = A_{CO_2} \quad (2.95)$$

and

$$B_{mix} = B_{CO_2} \quad (2.96)$$

This means that the fugacity coefficients for both components, Φ_{CO_2} and Φ_{H_2O} can be found in a direct way, and an iterative solution scheme is not required. The non-ideal mixing behavior is still captured, despite the simplification of A_{mix} and B_{mix} , by the molecule interaction parameters $A_{H_2O-CO_2}$ and B_{H_2O} . These molecule interaction

parameters, as well as the equilibrium constants K_i^0 and the partial molar volumes \bar{V}_i , were found from the literature, where available, and by being fitted to P - V - T and P - T - X data.

All terms in equations (2.72) and (2.88) have now been defined, so they can be solved to find the mutual solubilities x_{CO_2} and y_{H_2O} . This is done in [Spycher and Pruess \(2005\)](#) by setting:

$$C = \frac{K_{H_2O}^0}{\Phi_{H_2O} P} \exp\left(\frac{(P - P^0)\bar{V}_{H_2O}}{RT}\right) \quad (2.97)$$

and

$$D = \frac{\Phi_{CO_2} P}{55.508 \gamma'_x K_{CO_2}^0} \exp\left(-\frac{(P - P^0)\bar{V}_{CO_2}}{RT}\right) \quad (2.98)$$

and approximating the activity of H_2O as the mole fraction of H_2O , such that equations (2.72) and (2.88) are written as:

$$y_{H_2O} = C(1 - x_{CO_2} - x_{salt}) \quad (2.99)$$

and

$$x_{CO_2} = D(1 - y_{H_2O}) \quad (2.100)$$

Equation (2.100) can now be substituted into equation (2.99) and rearranged to give:

$$y_{H_2O} = \frac{(1 - D - x_{salt})}{\left(\frac{1}{C} - D\right)} \quad (2.101)$$

x_{salt} is defined in terms of molalities as:

$$x_{salt} = \frac{vm_{salt}}{55.508 + vm_{salt} + m_{CO_2}} \quad (2.102)$$

where v [-] is the stoichiometric number of ions in the dissolved salt. In the case of a saline formation in which the salt present is assumed to be NaCl, the stoichiometric number will be 2.

x_{CO_2} can also be expressed in terms of molalities as:

$$x_{CO_2} = \frac{m_{CO_2}}{m_{CO_2} + 55.508 + vm_{salt}} \quad (2.103)$$

which can be rearranged to define m_{CO_2} as:

$$m_{CO_2} = \frac{x_{CO_2}(vm_{salt} + 55.508)}{1 - x_{CO_2}} \quad (2.104)$$

As m_{salt} is independent of CO_2 solubility, it is more practical to use as an input parameter than x_{salt} . Therefore, equation (2.100) can be substituted into equation (2.104), and the

resulting expression for m_{CO_2} can then be put into equation (2.102) to give:

$$x_{salt} = \frac{vm_{salt} - vm_{salt}D + vm_{salt}Dy_{H_2O}}{vm_{salt} + 55.508} \quad (2.105)$$

Finally, this equation for x_{salt} in terms of salt molality is substituted into equation (2.99), which after rearrangement gives:

$$y_{H_2O} = \frac{(1 - D)55.508}{\left(\frac{1}{C} - D\right)(vm_{salt} + 55.508) + vm_{salt}D} \quad (2.106)$$

Equation (2.106) no longer depends on x_{CO_2} , so can be solved independently. Its result can then be substituted into equation (2.100) to give the corresponding value of x_{CO_2} .

This method gives the values for the mutual solubilities of CO₂ and H₂O, x_{CO_2} and y_{H_2O} , in a saline formation for inputted temperature, pressure and molal conditions of between 12-100°C, up to 600 bar and up to 6 molal NaCl, without the need for an iterative solution scheme.

2.3.8 Solubility of Salt in the Aqueous Phase

As well as the mutual solubilities of CO₂ and H₂O, it is also necessary to define the solubility of salt, assumed to be NaCl in saline formations, in the aqueous phase, x_{NaCl} . Beyond this solubility, a separate solid phase consisting of only salt will form. In the models used in this thesis, x_{NaCl} is found using the following equation (Potter et al., 1977):

$$x_{NaCl} = 26.218 + 0.0072T + 0.000106T^2 \quad (2.107)$$

This equation is thought to be valid over the temperature range 0-800°C, and it should be noted that it only considers the effect of temperature on NaCl solubility, and does not take into account the effect of changes in pressure.

2.3.9 Phase Diagrams

A phase diagram is a chart to show the different conditions at which different phases exist at equilibrium. Figure 2.5 shows a phase diagram for the two component system of CO₂ and H₂O by Spycher et al. (2003), using data from several different sources. It illustrates the different phase combinations that can exist for varying compositions, shown on the

x-axis by the mole fraction of H_2O , plotted against a full range of pressures, at a fixed temperature of 25°C . Within this figure, V represents a vapour phase, L_1 is the H_2O -rich liquid phase (referred to as the aqueous phase elsewhere in this thesis), and L_2 is the CO_2 -rich supercritical phase (referred to as the gaseous phase in this thesis). It should be noted that for the pressures and temperatures associated with geological sequestration, CO_2 will always be above the critical pressure and temperature at which distinct gaseous and liquid phases become indistinguishable, meaning that it will be in a supercritical state, and hence the vapour phase shown in Figure 2.5 will not be present in any of the models produced in this thesis.

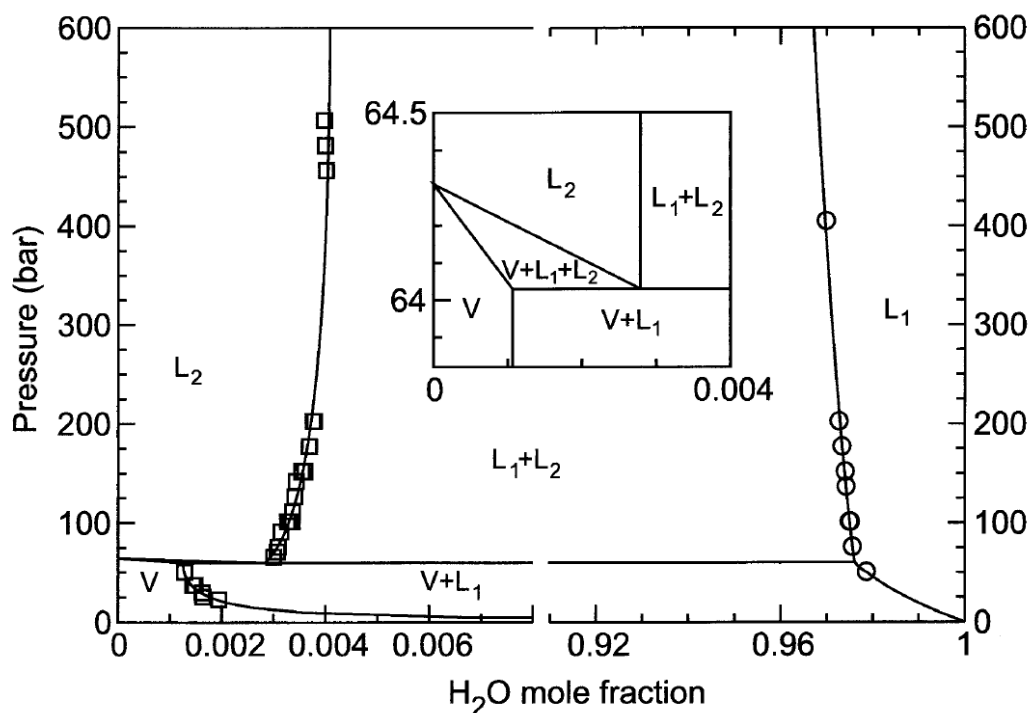


Figure 2.5: A phase diagram, plotting the mole fraction of H_2O against pressure, to illustrate the different phase combinations that occur for a two component (CO_2 and H_2O) system at a temperature of 25°C . Note that within this figure, V represents the vapor phase, L_1 is the H_2O -rich liquid phase and L_2 is the CO_2 -rich supercritical phase. The data points show CO_2 solubility in the H_2O -rich phase (open circles) and H_2O solubility in the CO_2 -rich phase (open squares), using data from [Wiebe and Gaddy \(1940\)](#), [Wiebe and Gaddy \(1941\)](#), [Coan and King \(1971\)](#), [Gillepsie and Wilson \(1982\)](#) and [King et al. \(1992\)](#). The inset of the figure shows the region in which all three phases can coexist in greater detail ([Spycher et al., 2003](#)).

The open circles and squares represent data points from the literature, with the circles showing CO_2 solubility in the H_2O -rich phase and the squares representing H_2O solubility in the CO_2 -rich phase. These data points are used to create lines that show the solubility of the components for the full range of required compositions and pressures, and therefore

separate the diagram into different phase combinations. This can be illustrated by an example. If we are at a point for which the H₂O mole fraction is 0.002 and the pressure is 100 bar, we are below the solubility limit of H₂O in the CO₂-rich phase, and to the left of the line that represents this solubility limit. Therefore, all H₂O present can be in the CO₂-rich phase, meaning that only a CO₂-rich phase is present and we are in the L₂ region as shown by the diagram. However, if more H₂O is added to the system, the mole fraction of H₂O increases, and so the point we are at in the diagram will move to the right. If it reaches a point where it has crossed the line that represents the solubility of H₂O in the CO₂-rich phase, there will be more H₂O than can be accommodated in the CO₂-rich phase at the given pressure and temperature, and hence a separate H₂O-rich phase must also form. Crossing this line therefore means moving into the region of L₁+L₂, where both phases are present. Figure 2.5 hence illustrates that, at 25°C and above approximately 64.5 bar, there will solely be a CO₂-rich supercritical phase (L₂) present for mole fractions of H₂O below the solubility limit of H₂O in the CO₂-rich phase, and solely a H₂O-rich liquid phase (L₁) present for H₂O mole fractions above the solubility limit of CO₂ in the H₂O-rich phase. For mole fractions of H₂O between these solubility limits, both the L₁ and L₂ phases will be present.

When a system is comprised of three components, it is clearer to use a ternary phase diagram, which shows phase behaviour information for varying compositions at a fixed pressure and temperature. As the fractions of composition at any point in the diagram will always sum to one, the equilibrium phase compositions can be plotted on an equilateral triangle (Orr, 2007, p.52). Each corner of the triangle represents 100% of the component with which it is labelled, and the opposite side represents 0% of that component. The fraction of each component at any given point within the triangle can therefore be read from the perpendicular distances from the point to the three sides (Orr, 2007, p.52).

Figure 2.6 shows a ternary phase diagram for the three component CO₂-H₂O-NaCl system at a pressure of 10 MPa and 60°C, which are realistic pressure and temperature figures for geological sequestration, and Figure 2.7 illustrates the zoomed in corners of Figure 2.6 to show the different phase combinations on a scale for which they can be more easily seen. Note that in these figures, V represents the supercritical CO₂-rich phase (referred to as the gaseous phase elsewhere in this thesis), L is the H₂O-rich liquid phase (referred to as the aqueous phase elsewhere), and S is the solid phase. *Z-i* refers to the mole fraction of component *i*. The bubble, precipitation and dew lines represent the lines for which the gaseous, solid and liquid phases, respectively, emerge.

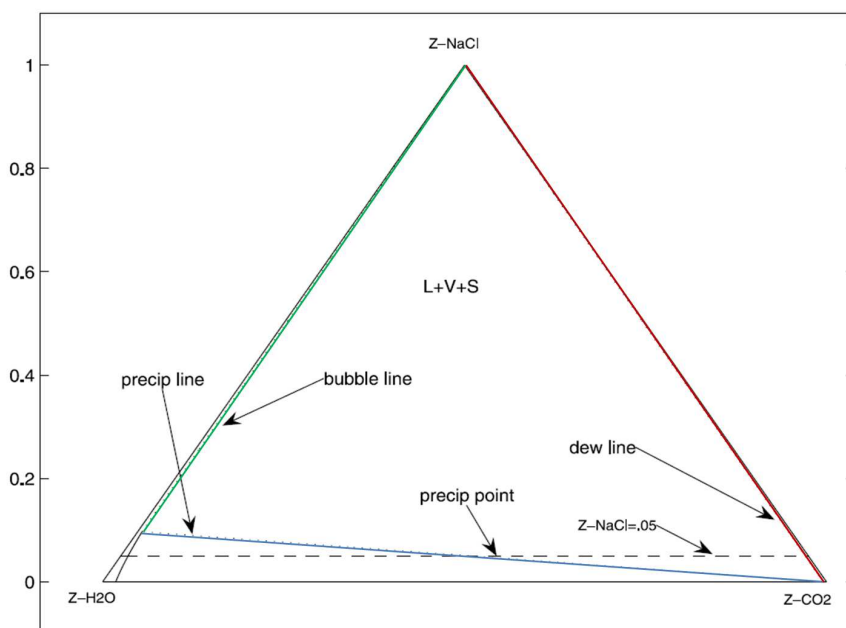


Figure 2.6: A ternary phase diagram showing the structure of phases within the three component system of CO₂, H₂O and NaCl for a fixed pressure of 10 MPa and a fixed temperature of 60°C. Note that $Z-i$ refers to the mole fraction of component i . The bubble, precipitation and dew lines have been highlighted in green, blue and red respectively in this figure. Adapted from Fuller et al. (2006).

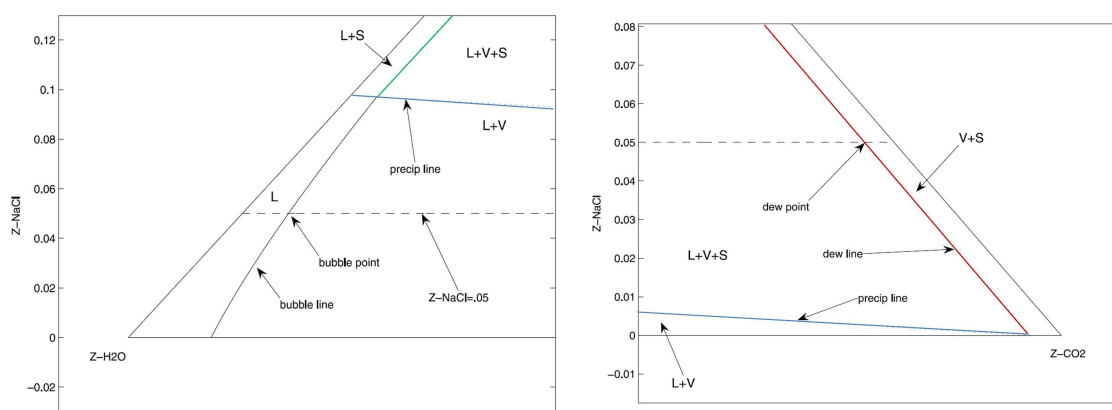


Figure 2.7: Subfigures to illustrate Figure 2.6 zoomed in, in order to show the different phase combinations that are too small to be seen clearly in the original figure. Adapted from Fuller et al. (2006).

Chapter 3

Solutions for Incompressible Two Component and Two Phase Flow

In order to form simulations of salt precipitation in saline aquifers, various methods can be used to solve the governing equations in Chapter 2. One useful method, in particular for forming analytical solutions, is the method of characteristics (MOC). This method is used for solving hyperbolic partial differential equations (PDEs), and can hence be used to solve the mass conservation equation given in equation (2.3) if it can be assumed that the fluid properties are constant with pressure and temperature, no diffusion or dispersion takes place and the capillary pressure is negligible. One of the main implications of these assumptions is that all flow will be considered to be in an outward direction, as without high capillary pressure gradients there will be no counter-current imbibition, in which the aqueous phase flows back to the injection point of the formation, against the general flow of CO₂.

Another method for solving partial differential equations is the method of lines (MOL). This method is not limited to hyperbolic PDEs, and so can be used to solve equations representing more complex systems in which the fluid properties vary with pressure and temperature and capillary pressure effects are included, but it is a numerical method that uses approximations, and so can be generally considered to be less accurate than the MOC. It should be noted that both the MOC and the MOL are mass conservative.

This chapter will introduce both the MOC and the MOL, and will look at the outputs of both methods for a two phase and two component system with constant fluid properties

and negligible capillary pressure in order to investigate how effective they are at solving the relevant PDEs and how well they compare.

3.1 Dimensionless Transformation

For a one-dimensional, linear system, the mass conservation equation in equation (2.3) reduces to:

$$\frac{\partial G_i}{\partial t} + \frac{\partial H_i}{\partial x} = 0 \quad (3.1)$$

where it should be recalled from equations (2.1) and (2.2) that G_i [ML^{-3}] and H_i [$\text{ML}^{-2}\text{T}^{-1}$] represent the mass of component i within a given volume of fluid mixture and the mass flux of component i , respectively, such that:

$$G_i = \phi \sum_{j=1}^{N_p} \rho_j X_{ij} S_j \quad (3.2)$$

and

$$H_i = \sum_{j=1}^{N_p} \rho_j X_{ij} q_j \quad (3.3)$$

and x [L] and t [T] refer to space and time, respectively.

However, equation (3.1) can also be written in a dimensionless form, in which the units are removed from each of the terms in the equation by substitution of other variables. The advantages of converting the equation to this form are that it enables us to look at the trends and patterns of the output of a system without the issue of units, and helps us to identify the strength of various parameters in governing the behaviour of the system by comparing the variables against each other (Younis, 2011, p.157). In this chapter, we are considering a one-dimensional, linear system with constant fluid properties and negligible capillary pressure, for which the dimensionless version of the mass conservation equation is: (Orr, 2007, p.84):

$$\frac{\partial G_{iD}}{\partial \tau} + \frac{\partial H_{iD}}{\partial \xi} = 0 \quad (3.4)$$

where G_{iD} [-] and H_{iD} [-] denote the dimensionless forms of G_i and H_i , respectively, such that:

$$G_{iD} = \sum_{j=1}^{N_p} \rho_{jD} X_{ij} S_j \quad (3.5)$$

and

$$H_{iD} = q_D \left(\sum_{j=1}^{N_p} \rho_{jD} X_{ij} f_j \right) \quad (3.6)$$

where:

$$f_j = \frac{q_j}{q_t} \quad (3.7)$$

$$\rho_{jD} = \frac{\rho_j}{\rho_{inj}} \quad (3.8)$$

$$q_D = \frac{q_t}{q_{inj}} \quad (3.9)$$

$$\tau = \frac{q_{inj}t}{\phi L} \quad (3.10)$$

and

$$\xi = \frac{x}{L} \quad (3.11)$$

Within these equations, f_j [-] represents the fractional flow of phase j , q_t [LT⁻¹] is the total volumetric flux, ρ_{inj} [ML⁻³] is the density of the injected fluid, q_{inj} [LT⁻¹] is the volumetric flux of the injected fluid and L [L] is an arbitrary length.

It can be immediately seen by comparing equation (3.2) and equation (3.5) that G_i and G_{iD} are related by a constant ratio, such that $G_{iD} = \frac{G_i}{\phi \rho_{inj}}$, but at first glance it may appear that the relationship between H_i and H_{iD} is not straightforward. However, equation (3.7) can be rearranged to show that:

$$q_j = f_j q_t \quad (3.12)$$

and this can be substituted into equation (3.3) to show that an alternative representation of H_i is:

$$H_i = q_t \left(\sum_{j=1}^{N_p} \rho_j X_{ij} f_j \right) \quad (3.13)$$

It can then be understood that $H_{iD} = \frac{H_i}{q_{inj} \rho_{inj}}$.

3.2 The Two Component, Two Phase System

Firstly, assume that only two components (CO₂ and H₂O) and two phases (gaseous and aqueous) are present in a one-dimensional, linear system, with constant fluid properties and negligible capillary pressure. This means that, in the two phase region, the non-dimensionalised mass of component i , G_{iD} , can be written as (Orr, 2007, p.84):

$$G_{iD} = \rho_{gD} x_{ig} S_g + \rho_{aD} x_{ia} (1 - S_g) \quad (3.14)$$

and the non-dimensionalised mass flux of component i , H_{iD} , can be written as (Orr, 2007, p.84):

$$H_{iD} = q_D[\rho_{gD}x_{ig}f_g + \rho_{aD}x_{ia}(1 - f_g)] \quad (3.15)$$

Note that the mass fractions of component i in phase j , X_{ij} , are assumed to be at constant equilibrium values, x_{ij} , due to the presence of both phases and the assumption of constant fluid properties.

Equation (3.14) can be rearranged to give:

$$S_g = \frac{G_{iD} - \rho_{aD}x_{ia}}{\rho_{gD}x_{ig} - \rho_{aD}x_{ia}} \quad (3.16)$$

which shows that the saturation of the gaseous phase, S_g , is a function of only G_{iD} , as all other variables in the equation are constant.

Because of the assumption of negligible capillary pressure, $P_g = P_a = P$. This means that:

$$q_t = q_g + q_a = -k \left(\frac{k_{rg}}{\mu_g} + \frac{k_{ra}}{\mu_a} \right) \frac{\partial P}{\partial x} \quad (3.17)$$

and so the fractional flow of phase j , f_j [-], can be found to be:

$$f_j = \frac{q_j}{q_t} = \frac{-\frac{k k_{rj}}{\mu_j} \frac{\partial P}{\partial x}}{-k \left(\frac{k_{rg}}{\mu_g} + \frac{k_{ra}}{\mu_a} \right) \frac{\partial P}{\partial x}} = \frac{\frac{k_{rj}}{\mu_j}}{\frac{k_{rg}}{\mu_g} + \frac{k_{ra}}{\mu_a}} \quad (3.18)$$

It should be noted that, in this case with constant fluid properties, q_t is a constant term, equal to $\frac{Q_0}{A}$, where Q_0 [L^3T^{-1}] is the constant rate of injection of CO_2 into the formation and A [L^2] is the cross-sectional area of the formation. This means that $q_t = q_{inj}$ and so $q_D = 1$.

Equation (3.15) illustrates that H_{iD} is solely a function of f_g . In turn, because of the fixed viscosities, equation (3.18) shows that f_g depend only on the relative permeabilities, which themselves depend only on the fluid saturations. It is also the case that $S_a = 1 - S_g$, and S_g is a function of only G_{iD} , as was shown in equation (3.16). Therefore, it can be seen that, under these conditions, H_{iD} is solely a function of G_{iD} .

This is also true if only one phase, j , is present. If this were the case:

$$G_{iD} = \rho_{jD}X_{ij} \quad (3.19)$$

and

$$H_{iD} = q_D \rho_{jD} X_{ij} f_j \quad (3.20)$$

In this single phase system, $f_j = 1$, and, as explained above, it is always the case in this system that $q_D = 1$. Therefore, equation (3.20) can also be written as:

$$H_{iD} = \rho_{jD} X_{ij} \quad (3.21)$$

and so:

$$H_{iD} = G_{iD} \quad (3.22)$$

showing again that H_{iD} is a function of only G_{iD} .

As it is always the case that H_{iD} is solely a function of G_{iD} , regardless of the phases present, it must be that equation (3.4):

$$\frac{\partial G_{iD}}{\partial \tau} + \frac{\partial H_{iD}}{\partial \xi} = 0 \quad (3.23)$$

can be alternatively written as a partial differential equation (PDE) which is solely a function of G_{iD} (Orr, 2007, p.85):

$$\frac{\partial G_{iD}}{\partial \tau} + \frac{dH_{iD}}{dG_{iD}} \frac{\partial G_{iD}}{\partial \xi} = 0 \quad (3.24)$$

3.3 Solving PDEs using the Method of Lines

The method of lines (MOL) is a numerical method in which PDEs are discretised in space, in this case using finite differences. This reduces them to a coupled set of ordinary differential equations (ODEs), which can then be solved simultaneously using one of the ODE solvers in MATLAB (Goudarzi et al., 2016).

3.3.1 Finite Difference Approximations

One numerical method that can help to approximate solutions to differential equations by discretisation is the finite difference method. The idea behind this is that derivatives of a general function f within differential equations are replaced by approximations based on the differences between f at known discrete values of space and time as required, i.e. replaced by appropriate finite difference approximations (LeVeque, 1992, p.98). There are several different forms of finite difference approximation, but Figure 3.1 illustrates the general idea of the method to approximate the derivative $\frac{df}{dx}$. Because we know the value of the function f at two discrete points in x , x_{left} and x_{right} , $\frac{df}{dx}$ can be approximated by

using the differences between these values of f and x , such that:

$$\frac{df}{dx} = \frac{\Delta f}{\Delta x} = \frac{f_{\text{right}} - f_{\text{left}}}{x_{\text{right}} - x_{\text{left}}} \quad (3.25)$$

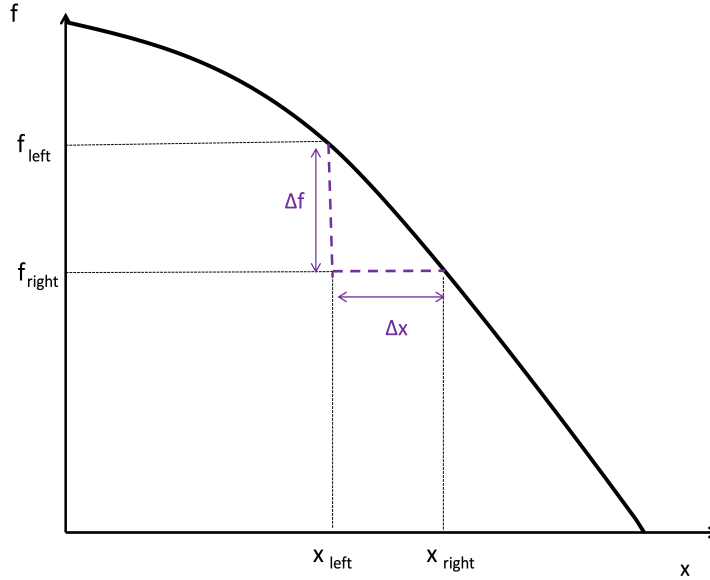


Figure 3.1: An illustration of how the finite difference method can be used to approximate the derivative $\frac{df}{dx}$.

If the point \bar{x} is the point at which we wish to approximate the derivative of the function f , there are several different choices of finite difference approximation to make, depending on the points available near \bar{x} . One option would be to use \bar{x} and the point $\bar{x} + h$, for some small value of h . This is called the forward difference method, and the approximation for these points, $D_+ f(\bar{x})$, is written as (LeVeque, 2007, p.3):

$$D_+ f(\bar{x}) = \frac{f(\bar{x} + h) - f(\bar{x})}{h} \quad (3.26)$$

Alternatively, it is possible to use the points \bar{x} and $\bar{x} - h$, which is known as the backward difference method. This approximation, $D_- f(\bar{x})$, is (LeVeque, 2007, p.3):

$$D_- f(\bar{x}) = \frac{f(\bar{x}) - f(\bar{x} - h)}{h} \quad (3.27)$$

These approximations are both known as one-sided, because f is evaluated at points only for which $x \geq \bar{x}$ for the forward difference method, or for which $x \leq \bar{x}$ for the backward difference method. Another common finite difference approximation, which this time uses points either side of \bar{x} , is the central difference approximation, denoted as $D_0 f(\bar{x})$. This

is written as (LeVeque, 2007, p.4):

$$D_0 f(\bar{x}) = \frac{f(\bar{x} + h) - f(\bar{x} - h)}{2h} \quad (3.28)$$

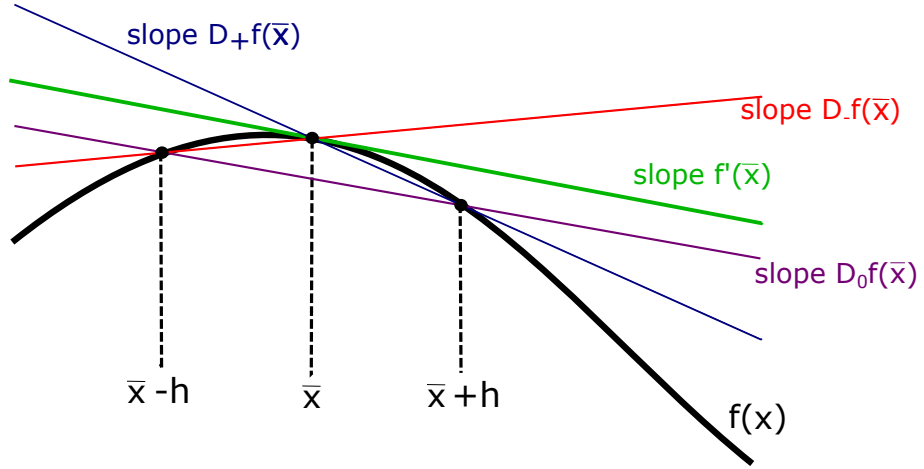


Figure 3.2: A diagram to show various finite difference approximations of $f'(\bar{x})$ interpreted as the slope of secant lines. (Adapted from LeVeque (2007, p.4)).

The points used in all of these approximations and the resultant slopes are shown in Figure 3.2, as well as the actual slope that the approximations are trying to find, $f'(\bar{x})$. It can be seen from the figure that the slope found from the central difference approximation is significantly more accurate than those found by the forward and backward difference approximations. The accuracies of different finite difference approximations vary hugely, and the error of a particular approximation can be analysed by looking at the appropriate Taylor series expansion. For example, Taylor expansion shows that (LeVeque, 2007, p.5):

$$f(\bar{x} + h) = f(\bar{x}) + hf'(\bar{x}) + \frac{h^2}{2!}f''(\bar{x}) + \frac{h^3}{3!}f'''(\bar{x}) + O(h^4) \quad (3.29)$$

and

$$f(\bar{x} - h) = f(\bar{x}) - hf'(\bar{x}) + \frac{h^2}{2!}f''(\bar{x}) - \frac{h^3}{3!}f'''(\bar{x}) + O(h^4) \quad (3.30)$$

Substituting equation (3.29) into equation (3.26) shows that:

$$D_+ f(\bar{x}) = \frac{f(\bar{x} + h) - f(\bar{x})}{h} = f'(\bar{x}) + \frac{h}{2!}f''(\bar{x}) + \frac{h^2}{3!}f'''(\bar{x}) + O(h^3) \quad (3.31)$$

meaning that the error associated with the forward difference method is:

$$E_+ f(\bar{x}) = D_+ f(\bar{x}) - f'(\bar{x}) = \frac{h}{2!}f''(\bar{x}) + \frac{h^2}{3!}f'''(\bar{x}) + O(h^3) \quad (3.32)$$

It should be noted that \bar{x} is a fixed point, meaning that the derivatives of f at point \bar{x} are fixed constants that are independent of the value of h (LeVeque, 2007, p.6). When h is set to a sufficiently small value, the value of $E_+ f(\bar{x})$ is dominated by the first term,

$\frac{h}{2!}f''(\bar{x})$, which is equivalent to a constant value multiplied by h , and all other terms are so small that they can be considered negligible (LeVeque, 2007, p.6). Therefore, the forward difference method can be considered to be first order accurate, as its error is proportional to h .

Similarly, equation (3.30) can be substituted into equation (3.27) to give the error for the backward difference method, $E_-f(\bar{x})$, as:

$$E_-f(\bar{x}) = D_-f(\bar{x}) - f'(\bar{x}) = -\frac{h}{2!}f''(\bar{x}) + \frac{h^2}{3!}f'''(\bar{x}) + O(h^3) \quad (3.33)$$

which shows that the backward difference method is also first order accurate, with a dominant error term proportional to h .

Using both equations (3.29) and (3.30), the central difference approximation can be expressed as:

$$D_0f(\bar{x}) = \frac{f(\bar{x} + h) - f(\bar{x} - h)}{2h} = f'(\bar{x}) + \frac{h^2}{3}f''(\bar{x}) + O(h^4) \quad (3.34)$$

meaning that its error is (LeVeque, 2007, p.6):

$$E_0f(\bar{x}) = D_0f(\bar{x}) - f'(\bar{x}) = \frac{h^2}{3}f''(\bar{x}) + O(h^4) \quad (3.35)$$

As the error $E_0f(\bar{x})$ has a dominant term that is proportional to h^2 , the central difference approximation can be considered to be second order accurate. This explains its higher accuracy at estimating the slope of $f'(\bar{x})$ than the forward and backward difference schemes, as illustrated in Figure 3.2.

It should be noted that the possible finite difference approximations are in no means limited to the ones mentioned here. Many more approximations using varying numbers of points and with differing degrees of accuracy can be found; the ones included here are those thought to be among the simplest and most commonly used.

Although only finite difference approximations to first order derivatives have been outlined here, it is also possible to use finite difference methods to find approximations of higher order derivatives. Among the most straightforward ways to do this is to repeatedly difference approximations to lower order derivatives (LeVeque, 2007, p.9).

Once a PDE has been discretised in space using the finite difference method, and therefore reduced to an ODE with derivatives depending only on time, it can then be solved using one of the ODE solvers in MATLAB as part of the MOL.

3.3.2 Ordinary Differential Equation Solvers

The ODE solvers in MATLAB are a set of finite difference codes that solve first order systems of N ODEs that are of the form (Ashino et al., 2000):

$$\frac{\partial \mathbf{y}}{\partial t} = g(\mathbf{y}, t) \quad \mathbf{y}(t_0) = \mathbf{y}_0 \quad (3.36)$$

where $\mathbf{y} = [y_1, y_2, \dots, y_N]^T$ and represents the set of primary dependent variables (PDVs) that the ODEs are being solved for, and $g(\mathbf{y}, t)$ is a function that depends on \mathbf{y} and time. The ODE solvers are able to vary the time step size, Δt , used in their calculations, such that the maximum possible value is used to compromise the speed, accuracy and stability of the solver (Goudarzi et al., 2016).

In order to reduce the initial PDEs to the format shown in equation (3.36), it is necessary to use a scheme such as the finite difference method to discretise them with respect to space and hence find an expression for the derivative of each PDV with respect to time that depends solely on the PDVs and time. It is also necessary to define the initial value of the PDVs, \mathbf{y}_0 , and provide the ODE solver with both of these expressions.

There are several different ODE solvers within MATLAB that are designed for different types of problem and have different levels of accuracy. The most commonly used of these, and the most useful for modelling the problem of injecting CO₂ into an aqueous formation, are ode45 and ode15s.

ode45 uses an explicit method to solve equation (3.36), which means that the terms within $g(\mathbf{y}, t)$ are defined at the current point in time, t^n . This means that in an explicit scheme, the value of \mathbf{y} at the later time, t^{n+1} , depends explicitly on the value of \mathbf{y} at time t^n . Explicit schemes are therefore relatively simple and generally computationally fast. However, they do have the disadvantage of having limited stability due to the Courant-Lewy-Friedrichs (CFL) condition (Goudarzi et al., 2016), which relates the length of the time step (Δt) to the interval length (Δx) and the speed with which it is physically possible for a wave to travel. Use of a time step that is too large to meet this condition will result in incorrect and unstable solutions, meaning that ODE solvers such as ode45 that use explicit schemes can be limited to very small time steps for certain problems. This can lead to the ODE solver taking an extremely long time or being forced to use a time step so small that machine precision causes it to fail, and therefore be unable to produce a solution. This is most likely to happen for problems that are stiff, which means that some terms in the equation change very rapidly as the independent variable (in this case, time)

changes, and others vary slowly with the independent variable (Goudarzi et al., 2016).

However, some ODE solvers are specifically designed to deal with stiff problems, such as ode15s (Ashino et al., 2000). This solver uses an implicit method, meaning that at least some of the terms in $g(\mathbf{y}, t)$ are defined as being at a later time than the current time, t^n . Due to this, the implementation of the scheme requires the solution of a linear system of equations, involving terms that are defined at both the current time and a later time, which makes it more challenging to find a solution than if an explicit method is used. It does, however, have the advantage of being unconditionally stable, regardless of the size of the time step used (Goudarzi et al., 2016).

The simplest explicit finite difference method is the one-step forward Euler method. The forward Euler expression needed to solve equation (3.36) would be:

$$\mathbf{y}^{n+1} = \mathbf{y}^n + \Delta t g(\mathbf{y}^n, t^n) \quad (3.37)$$

Note that this is an explicit solution due to the terms in $g(\mathbf{y}, t)$ being defined at the current point in time, t^n .

The simplest implicit finite difference method is the one-step backward Euler method. In the form to solve equation (3.36), this would be:

$$\mathbf{y}^{n+1} = \mathbf{y}^n + \Delta t g(\mathbf{y}^{n+1}, t^{n+1}) \quad (3.38)$$

Here, the terms within $g(\mathbf{y}, t)$ are defined at the later time point, t^{n+1} , due to the solution scheme being implicit.

The ODE solvers do not use the forward or backward Euler methods; they are simply shown here to illustrate the difference between explicit and implicit solution schemes. More accurate finite difference methods have been developed from Euler's method, which combines values of \mathbf{y}^{n-1} , \mathbf{y}^n , \mathbf{y}^{n+1}, \dots and $g(\mathbf{y}^{n-1}, t^{n-1})$, $g(\mathbf{y}^n, t^n)$ and $g(\mathbf{y}^{n+1}, t^{n+1}), \dots$ in either linear or nonlinear ways to achieve a higher level of accuracy (Ashino et al., 2000). A linear combination (the use of which is referred to as a linear multistep method) makes it easier to estimate the local error of the approximation used, but sacrifices the one-step format. This will make it more difficult to change the time step as appropriate to the problem during the simulation. The reverse is true of the nonlinear combinations, which are called Runge-Kutta methods: the one-step format is maintained, but it is more challenging to estimate the local error (Ashino et al., 2000).

The method of lines, using finite differences to discretise in space followed by one of MAT-

LAB's ODE solvers, was chosen as a method to solve this multicomponent, multiphase system for reasons of stability, accuracy and ease of use. Other methods are sometimes used for spatial discretisation, including finite volume, which makes use of the fact that the flux entering a small volume surrounding a node point has to be equal to the flux leaving the volume around the previous node, and the finite element method, in which the system is divided into smaller subdomains and the simpler equations that represent each of these parts are put together into a larger equation system for the whole domain. However, these can lead to either stability issues or numerical diffusion due to truncation terms linked to Taylor's expansion (Goudarzi et al., 2016), as can many methods of higher order. The temporal term can be treated with alternative fully implicit or semi-implicit methods, but these can be significantly more complicated to implement, and can again lead to additional numerical diffusion (Goudarzi et al., 2016). It is also necessary to choose time steps with care in a semi-implicit method as the system is not unconditionally stable (Doster et al., 2014). The ODE solvers are easily available, extremely useful algorithms that maintain a specific time integration error while maximising the time step size (Goudarzi et al., 2016), and are hence the method of choice here. For the particular problem being investigated within this thesis, the most appropriate ODE solver to use is ode15s, despite only being first order accurate. This is because, upon injection of CO₂ into a saline aquifer, the pressure waves move through the system at a much faster rate than the compositions (Goudarzi et al., 2016), meaning that the problem is stiff and hence the higher order solver, ode45, would be extremely slow. This illustrates that efficiency must be considered when choosing the best methods to solve problems, and that it is not always the case that the most accurate method is the most appropriate.

3.3.3 Solving Equation (3.4) using the Method of Lines

In order to use the MOL to solve equation (3.4), it is necessary to firstly discretise the ξ axis into a block centered grid with N nodes, as shown in Figure 3.3. The ODE solver then needs to be provided with a vector giving the initial value of G_{iD} at all nodes, which will be zero for all points for G_{cD} and one for all points for G_{wD} because there is initially only water present in the system, and an expression for $\frac{\partial G_{iD}}{\partial \tau}$ at each node k along the discretised ξ axis. Using equation (3.4), this will be:

$$\left. \frac{\partial G_{iD}}{\partial \tau} \right|_k = - \left. \frac{\partial H_{iD}}{\partial \xi} \right|_k \quad (3.39)$$

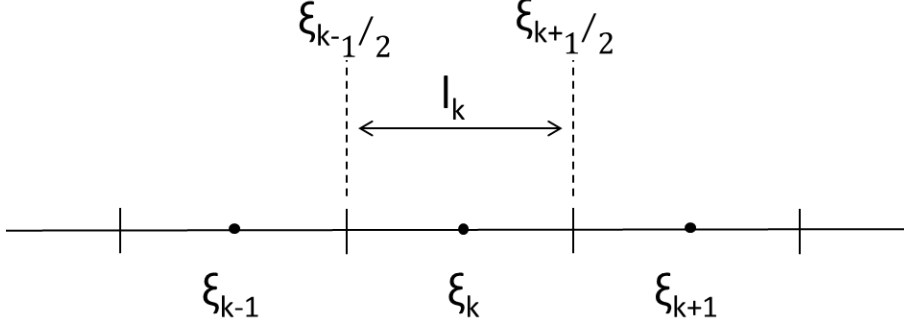


Figure 3.3: A diagram to show the discretisation of the ξ axis. ξ_k represents the node at the centre of a particular cell k , while ξ_{k-1} and ξ_{k+1} represent the nodes at the centres of the cells to the left and right of k , cells $k-1$ and $k+1$, respectively. $\xi_{k-\frac{1}{2}}$ and $\xi_{k+\frac{1}{2}}$ represent the boundaries between cells k and $k-1$, and cells k and $k+1$, respectively. l_k is the length of the cell k , and there are N nodes in total.

$\left. \frac{\partial H_{iD}}{\partial \xi} \right|_k$ can be found by defining H_{iD} in the code using equation (3.15), and then using finite difference to give:

$$\left. \frac{\partial H_{iD}}{\partial \xi} \right|_k = \frac{H_{iD_{k+\frac{1}{2}}} - H_{iD_{k-\frac{1}{2}}}}{\xi_{k+\frac{1}{2}} - \xi_{k-\frac{1}{2}}} \quad (3.40)$$

An issue with this equation, however, is that H_{iD} is required to be defined at the cell boundaries, $k+\frac{1}{2}$ and $k-\frac{1}{2}$, when, without any intervention, it will actually be calculated by the numerical code to be at the nodes k , as this is where the terms that it is made up from are defined. Upwinding is considered to be an accurate method of approximating the value of H_{iD} at the cell boundaries in order to use equation (3.40). This is because it interpolates using values at the two nearest grid points, as well as avoiding adding additional dissipation to the system (LeVeque, 1992, p.136).

3.3.4 Upwinding

The principle behind upwinding is that there are two values that could possibly be chosen to represent $H_{iD_{k+\frac{1}{2}}}$. These are the values of H_{iD} at the nodes on either side of the boundary: H_{iD_k} and $H_{iD_{k+1}}$. In the system being considered, capillary pressure is assumed to be negligible. This means that no counter-current imbibition will occur, and so the direction of the propagating front can be considered to be outwards from the point of injection at all points. H_{iD_k} must therefore be chosen to represent $H_{iD_{k+\frac{1}{2}}}$ because $H_{iD_{k+1}}$ is further from the injection point than $H_{iD_{k+\frac{1}{2}}}$, and so has not yet felt the effects of the advancing front. This means that choosing it to represent $H_{iD_{k+\frac{1}{2}}}$ would ignore the effects

of the injection of CO₂, which are essential to the model. This is illustrated in Figure 3.4.

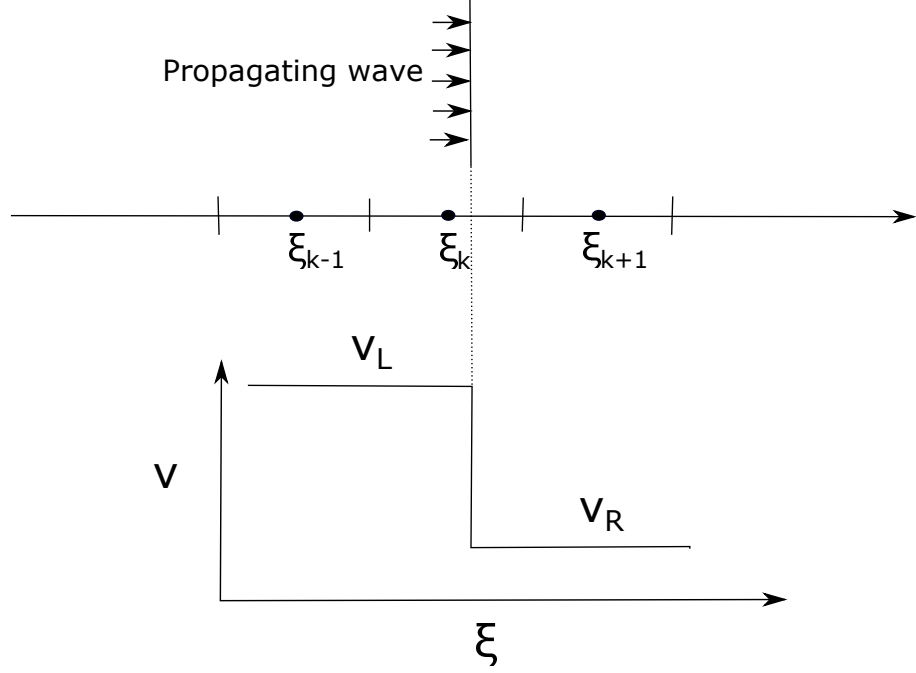


Figure 3.4: A diagram to show the propagation of a wave in the positive ξ direction at a given instant of time. It illustrates that choosing the value of H_{iD} at node $k+1$ to approximate $H_{iD_{k+\frac{1}{2}}}$ would be inaccurate, because the propagating wave has not yet reached this point. v represents the velocity of the advancing wave, where v_L denotes the velocity to the left of the propagating front, and v_R denotes the velocity to the right. Adapted from Goudarzi (2017).

However, in other, more complex systems in which capillary pressure effects are taken into account, not all flow will be in an outwards direction. High capillary pressure gradients near the injection point of a formation can cause a reversal in the wetting pressure gradient, leading to counter-current imbibition, in which some of the aqueous phase flows back towards the point of injection, opposing the outward flow of the injected CO₂. Therefore, if capillary pressure effects were included in this system, the issue of whether it is more appropriate to use H_{iD_k} or $H_{iD_{k+1}}$ to represent $H_{iD_{k+\frac{1}{2}}}$ within upwinding becomes far more complicated, and the wave velocity at each individual point must be considered. The appropriate value of $H_{iD_{k+\frac{1}{2}}}$ at each point can therefore be found by:

$$H_{iD_{k+\frac{1}{2}}} = \begin{cases} H_{iD_k}, & v > 0 \\ H_{iD_{k+1}}, & v \leq 0 \end{cases} \quad (3.41)$$

where v represents the wave velocity at each point.

Within this chapter, equation (3.4) will be solved by the MOL and the MOC, and the solutions found by the two methods compared. This will highlight the effectiveness of both methods and illustrate the need to have analytical solutions to compare to those solutions

found from numerical methods.

3.4 Solving PDEs using the Method of Characteristics

The idea of using the MOC to find a solution to a PDE is to find curves, called characteristic curves or characteristics, along which the PDE reduces to an ODE (Knobel, 2000, p.128). Once these have been found, the ODE can be solved along the characteristic curves, and this solution can be transformed into a solution for the original PDE.

3.4.1 The Method of Characteristics for an Immisible System

The MOC will first be illustrated to solve equation (3.4) for very simple conditions, in which two phases and two components with constant fluid properties and negligible capillary pressure flow horizontally, as described previously, but the miscibility of the fluids is not taken into account. This means that they are considered to be immiscible and so all of the gas phase is made up of CO₂, while all of the aqueous phase is made up of water. This problem was originally solved by Buckley and Leverett (1942), and hence the resulting analytical solution is sometimes referred to as the Buckley-Leverett solution. The solution was originally intended to model the displacement of oil by either gas or water, but can be easily applied to the problem concerned in this thesis of the displacement of water by CO₂. The elimination of phase miscibility simplifies the problem considerably, as the component mass fractions, X_{ij} , no longer need to be considered, because they will be equal to either zero or one depending on the component and phase in question. Under the conditions relevant to gaseous CO₂ displacing aqueous water, $X_{cg} = 1$ and $X_{ca} = 0$, meaning that equations (3.23) and (3.24) can be reduced to be given purely in terms of phase saturation, S_j , and fractional flow, f_j , such that:

$$\frac{\partial S_g}{\partial \tau} = -\frac{\partial f_g}{\partial \xi} \quad (3.42)$$

or equivalently:

$$\frac{\partial S_g}{\partial \tau} + \frac{df_g}{dS_g} \frac{\partial S_g}{\partial \xi} = 0 \quad (3.43)$$

Equation (3.43) can be solved by the MOC by firstly considering that S_g is a function of both ξ and τ , and thinking about the curve $(\xi(\tau), \tau)$ as a curve in the $\xi - \tau$ plane that begins from the point $(\xi_0, 0)$, as shown in Figure 3.5 (Knobel, 2000, p.128).

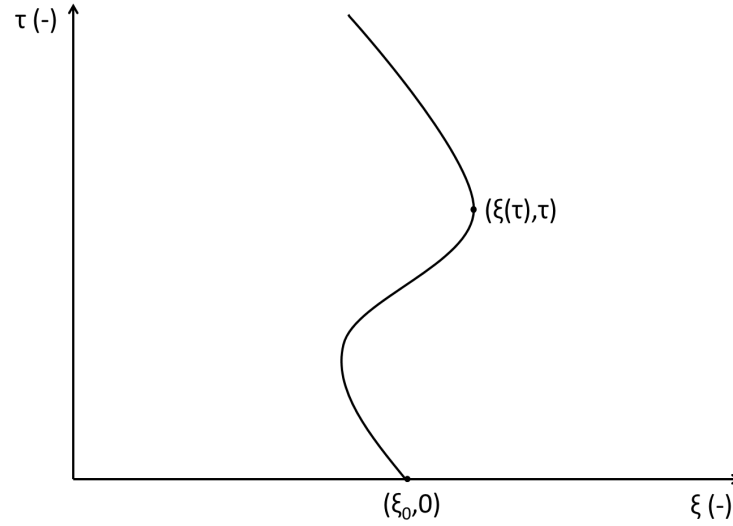


Figure 3.5: A curve $(\xi(\tau), \tau)$ in the $\xi - \tau$ plane. Adapted from (Knobel, 2000, p.128).

As $(\xi(\tau), \tau)$ moves along this curve, the value of $S_g(\xi(\tau), \tau)$ changes at a rate of $\frac{d}{d\tau}S_g(\xi(\tau), \tau)$.

Using the chain rule, this derivative can be expressed as:

$$\frac{d}{d\tau}S_g(\xi(\tau), \tau) = \frac{\partial S_g(\xi(\tau), \tau)}{\partial \xi} \frac{d\xi}{d\tau} + \frac{\partial S_g(\xi(\tau), \tau)}{\partial \tau} \frac{d\tau}{d\tau} \quad (3.44)$$

or, alternatively:

$$\frac{dS_g}{d\tau} = \frac{\partial S_g}{\partial \xi} \frac{d\xi}{d\tau} + \frac{\partial S_g}{\partial \tau} \quad (3.45)$$

The right-hand side of equation (3.45) closely resembles the left-hand side of equation (3.43)-the equation that we are attempting to solve. By comparing the two equations, it can be seen that if we choose the curve $(\xi(\tau), \tau)$ so that:

$$\frac{d\xi}{d\tau} = \frac{df_g}{dS_g} \quad (3.46)$$

then equations (3.43) and (3.45) can be combined to show that:

$$\frac{dS_g}{d\tau} = \frac{df_g}{dS_g} \frac{\partial S_g}{\partial \xi} + \frac{\partial S_g}{\partial \tau} = 0 \quad (3.47)$$

therefore indicating that the value of S_g is constant along this particular curve (Knobel, 2000, p.128). This means that at every point along the curve, S_g must have the the value that it has at its initial point of $(\xi_0, 0)$, denoted by $S_{g_0}(\xi_0)$. It follows that $\frac{df_g}{dS_g}$ is also constant along this curve.

An expression for $\xi(\tau)$ to represent the special curve $(\xi(\tau), \tau)$ beginning at the point $(\xi_0, 0)$ can be found by integrating equation (3.46) with respect to τ , to find that:

$$\xi = \frac{df_g}{dS_g} \tau + \xi_0 \quad (3.48)$$

Equation (3.48) gives the equation of the characteristic curves (or characteristics) of equation (3.43). As $\frac{df_g}{dS_g}$ is constant along the curves, the characteristic curves are therefore represented by parallel, straight lines in the $\xi - \tau$ plane, all of which with the slope $\frac{1}{\frac{df_g}{dS_g}}$, but with different initial points $(\xi_0, 0)$ on the ξ axis (Knobel, 2000, p.129). The characteristic curves for the initial composition in the formation, at which $S_g = 0$ and so $\frac{df_g}{dS_g} = 1$, are shown in Figure 3.6.

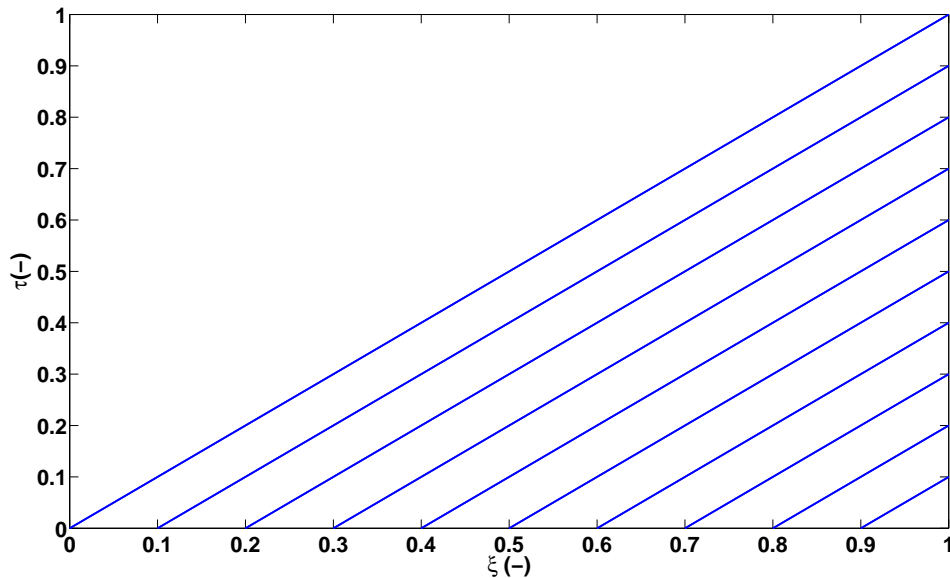


Figure 3.6: Characteristic curves for the initial composition of the fluid in the system, $S_g = 0$.

As we know that S_g is constant along the characteristic curves, the lines $\xi = \frac{df_g}{dS_g}\tau + \xi_0$, it is possible to find the value of S_g at any point (ξ, τ) (Knobel, 2000, p.129). For a given point (ξ, τ) , a characteristic curve goes from the point to the point $(\xi_0, 0)$ on the ξ axis, where ξ_0 can be found by rearranging equation (3.48) to give:

$$\xi_0 = \xi - \frac{df_g}{dS_g}\tau \quad (3.49)$$

The fact that S_g is known to be constant along characteristic curves can then be used to conclude that the value of S_g at (ξ, τ) is the same as the value of S_g at $(\xi_0, 0)$ (Knobel, 2000, p.129). Therefore:

$$S_g(\xi, \tau) = S_g(\xi_0, 0) = S_{g_0}(\xi_0) = S_{g_0} \left(\xi - \frac{df_g}{dS_g}\tau \right) \quad (3.50)$$

The solution $S_g(\xi, \tau) = S_{g_0} \left(\xi - \frac{df_g}{dS_g}\tau \right)$ of equation (3.43) is a travelling wave with initial profile $S_g = S_{g_0}$, which moves through the formation with velocity $\frac{df_g}{dS_g}$ (Knobel, 2000, p.129).

3.4.2 Discontinuities and Shocks

Solving a PDE in the way described above assumes that, for any point (ξ, τ) , there is only one characteristic curve extending from the ξ -axis to (ξ, τ) . In fact, this is not necessarily the case for nonlinear PDEs such as equation (3.43), and it is possible for two or more characteristic curves to intersect at a point (ξ, τ) (Knobel, 2000, p.137). An example of characteristic curves intersecting is shown in Figure 3.7.

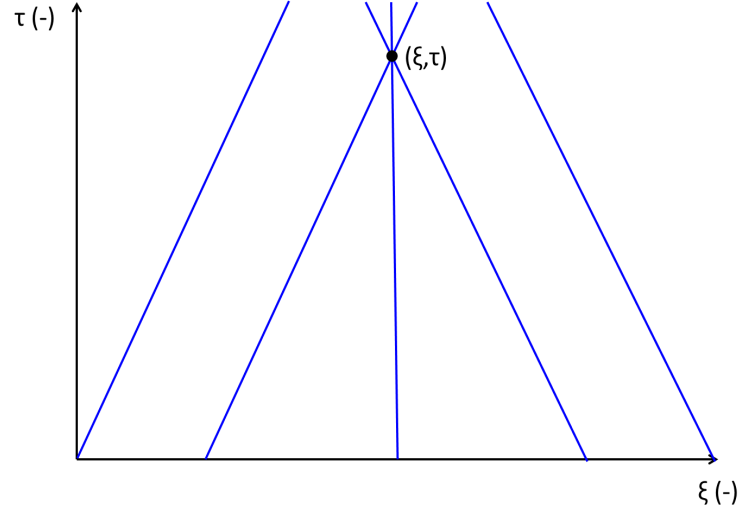


Figure 3.7: An example of how characteristics for a particular PDE can intersect at a point (ξ, τ) . Adapted from (Knobel, 2000, p.137).

The reason that the characteristic curves will intersect for equation (3.43) is that their slope in the $\xi - \tau$ plane is equal to $\frac{df_g}{dS_g}$, which, although constant along a characteristic curve, will vary as S_g changes, meaning that characteristics corresponding to different values of S_g will have different slopes. The relative permeabilities, k_{rj} , in this system are assumed to be the power law expressions used in equation (2.9). $\frac{df_g}{dS_g}$ can be found by substituting these expressions for relative permeability into the equation for f_g , equation (3.18), and then differentiating with respect to S_g to give (Mathias et al., 2011b):

$$\frac{df_g}{dS_g} = f_g(1 - f_g) \left[\frac{n_g(1 - S_g - S_{ar}) + n_a(S_g - S_{gc})}{(S_g - S_{gc})(1 - S_g - S_{ar})} \right] \quad (3.51)$$

The differing values of $\frac{df_g}{dS_g}$ found from using this equation for the constant fluid properties in Table 3.1 are shown in Figure 3.8, and the characteristic curves for a selection of compositions as they form at the origin are shown in Figure 3.9. It can be clearly seen that all of these characteristic curves have different gradients, $\frac{df_g}{dS_g}$, and also have different gradients from the gradient of one that the characteristic curves for $S_g = 0$ have in Figure 3.6. This therefore indicates that the characteristics are not parallel and there will be some points of intersection between them (Knobel, 2000, p.138).

Parameter	Value	Parameter	Value
μ_g (Pa s ⁻¹)	8.47×10^{-5}	n_g (-)	2
μ_a (Pa s ⁻¹)	9.63×10^{-4}	n_a (-)	2
k_{rg0} (-)	0.3	S_{ar} (-)	0.5
k_{ra0} (-)	1	S_{gc} (-)	0

Table 3.1: Constant parameters used to find the values of $\frac{df_g}{dS_g}$ in Figure 3.8.

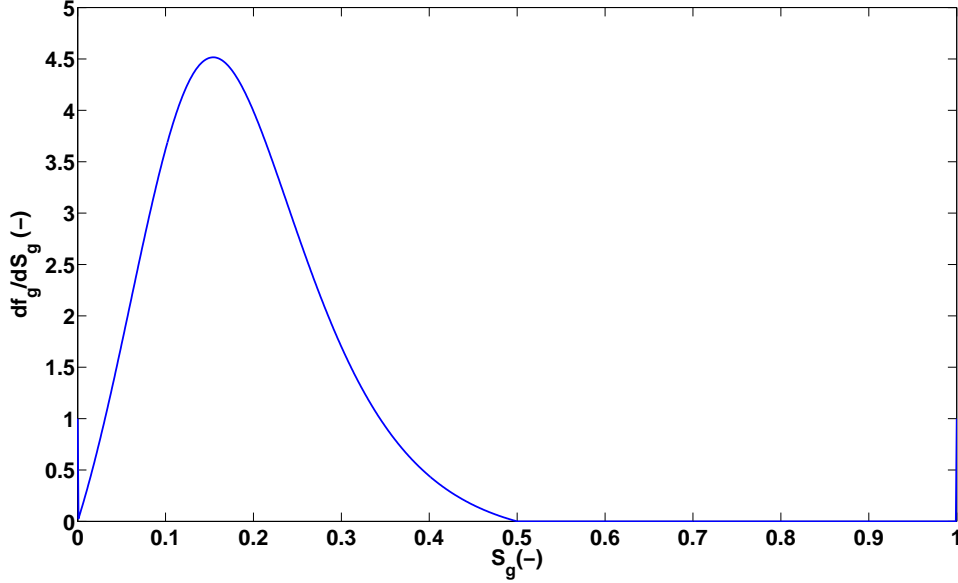


Figure 3.8: The gradients of the characteristic curves of equation (3.43), $\frac{df_g}{dS_g}$, for every possible value of S_g .

Two or more characteristic curves intersecting at a point (ξ, τ) is incompatible with the MOC, as, due to the value of S_g being constant along a particular characteristic curve, it indicates that two or more values of S_g are present at a particular point within the formation, which is physically impossible. The intersection of characteristic curves along which the value of S_g is different will also lead to the slope $\frac{\partial S_g}{\partial \xi}$ becoming infinite as τ approaches the value at which the characteristic curves cross. This is called a gradient catastrophe (Knobel, 2000, p.138), and the earliest value of τ at which it occurs is referred to as the breaking time, τ_b (Knobel, 2000, p.141).

The MOC as previously described can only construct the solution to a PDE until the breaking time, τ_b . However, it is possible to extend the solution beyond τ_b by allowing the solution S_g to be a piecewise smooth function, rather than being a continuous function at all points (Knobel, 2000, p.145). A function S_g can be described as a piecewise smooth function if it can be broken into distinct regions, and within each region the function itself

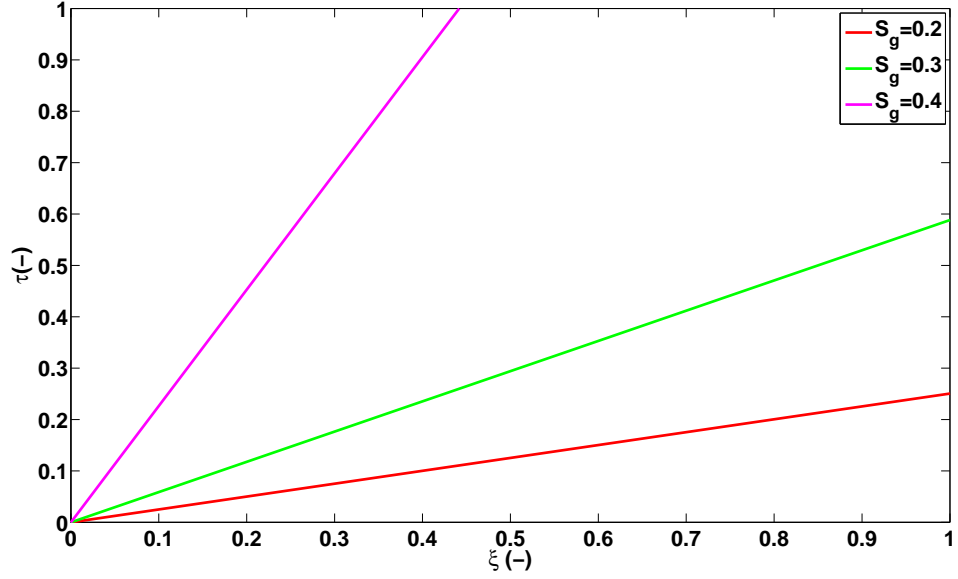


Figure 3.9: Characteristic curves for a small number of compositions as they travel through the formation from the point of injection.

is continuous, as well as having continuous first derivatives. The only discontinuities that may be present are a finite number of jump discontinuities, or shocks: a dramatic change in the nature of S_g at which the limits of the function to the left and right both exist but are not necessarily equal to each other (Knobel, 2000, p.146). Shocks must form due to the gradient catastrophes present in the solution, and are formed by a curve, $(\xi_s(\tau), \tau)$, being drawn through the region of crossing characteristic curves on the $\xi - \tau$ axes to separate the characteristic curves approaching from the left and right (Knobel, 2000, p.148).

When gaseous CO_2 is injected into aqueous water, a shock will form at any point at which the number of phases present changes (Orr, 2007, p.75). In order to solve a problem using the MOC, it is necessary to have prior knowledge of the structure of the solution, i.e. the number of shocks that will be present in the solution. For the problem we are currently solving, in which the phases are considered to be immiscible, just one shock will develop, separating the aqueous only region which has not yet been in contact with the approaching CO_2 , and the two phase region closer to the point of injection. Therefore, to solve this problem using the MOC, we need to know that one shock will be present, and then, as is done later in this subsection, look at how the discontinuity will propagate through the system to find the location of this shock. In contrast, solving the problem using the MOL does not require knowledge of the solution structure.

As explained above, to find the curve $\xi_s(\tau)$ that separates the characteristics while con-

tinuing the satisfy the conservation laws, and therefore find the location of a shock, it is necessary to find the compositions that form on either side of the shock and determine how the shock propagates. Consider the situation shown in Figure 3.10. The shock is

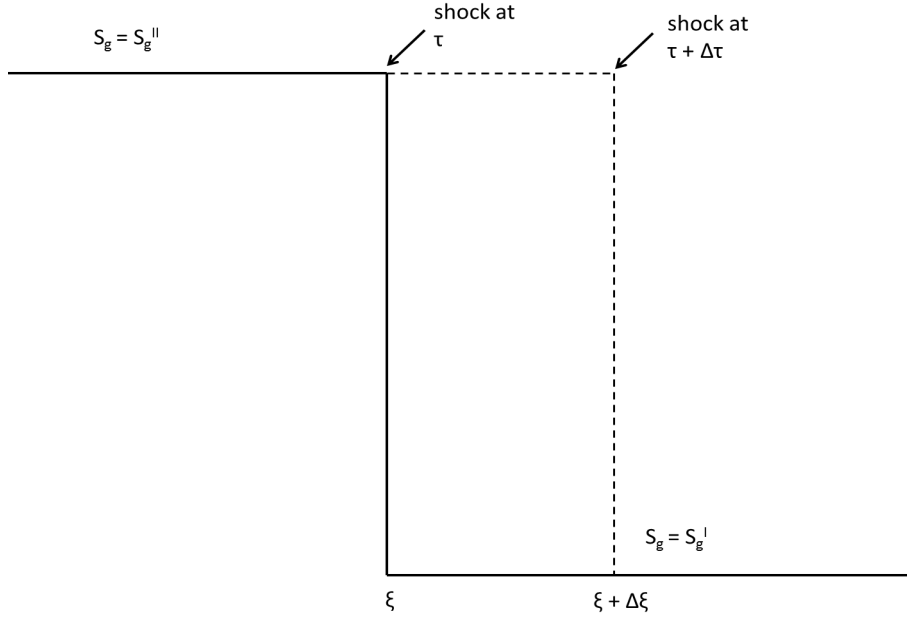


Figure 3.10: A diagram showing the motion of a shock (Adapted from Orr (2007, p.70)).

located at distance ξ at time τ , and moves to its new position, $\xi + \Delta\xi$, over a period of time, $\Delta\tau$. It can be seen from the diagram that S_g has a value of S_g^{II} on the upstream side of the shock and a value of S_g^I on the downstream side. As there is no accumulation of material at the shock, the change in the fractional volume of CO_2 present in a control volume that includes the porous medium between the positions ξ and $\xi + \Delta\xi$ is balanced by the fractional inflow of CO_2 (Orr, 2007, p.70). Therefore:

$$\Delta\xi(S_g^{II} - S_g^I) = \Delta\tau(f_g^{II} - f_g^I) \quad (3.52)$$

and so, as ξ and τ tend towards zero:

$$\frac{d\xi}{d\tau} = \frac{f_g^{II} - f_g^I}{S_g^{II} - S_g^I} \quad (3.53)$$

Equation (3.53) is called a jump condition or Rankine-Hugoniot relation, and is an integral version of the original conservation equation (Orr, 2007, p.71). It illustrates that volume is conserved across the shock, and also that the velocity at which a shock propagates is set by the gradient of the line connecting the two states on either side of the shock on a plot of f_g against S_g (Orr, 2007, p.71).

There will be several different shock constructions that can satisfy the Rankine-Hugoniot condition. Therefore, in order to find the shock that is part of the unique solution to

the flow problem, it is necessary to use two additional constraints that are based on physical ideas (Orr, 2007, p.71). Firstly, it must be that slower compositions within a system have travelled a shorter distance than faster compositions, and will therefore be upstream of these faster compositions and hence closer to the point of injection (Helfferich, 1981). If this were not the case, then the downstream compositions would have been overtaken by the faster-moving compositions further upstream. This idea gives us the so-called velocity constraint, which states that wave velocities in the two phase region must decrease monotonically for zones in which compositions continuously vary as the solution composition path moves from downstream compositions to upstream compositions (Orr, 2007, p.71). The second constraint is called the entropy condition. It focuses on the fact that, in order for the shock to be stable to perturbations and be able to form again if it was smeared from a sharp jump, which could be caused by a small amount of dispersion, it is necessary that the characteristics are going into the shock as time advances, rather than coming out of it. For this to be the case, the speed of the shock must be greater than or equal to the characteristic speed upstream of it, and smaller than or equal to the characteristic speed downstream of it (LeVeque, 2004, p.218). Shocks that satisfy this condition, and are therefore stable, are referred to as self-sharpening.

In order to satisfy the Rankine-Hugoniot condition, the velocity constraint and the entropy condition, it must be that the line drawn between the initial composition and the composition immediately upstream of the shock on the plot of f_g against S_g is a tangent to the curve, as shown in Figure 3.11, where the initial composition and the composition immediately upstream of the shock are labelled as points a and b respectively (Orr, 2007, p.74).

This line on the plot of f_g against S_g is equivalent to $\xi_s(\tau)$ on a $\xi - \tau$ plot. As explained above, the velocity of the shock is given by the gradient of the line between points a and b, but, as this is a tangent to the curve at point b, this is the same as $\frac{df_g}{dS_g}$ at point b. This means that the wave velocity at point b is the same as the shock velocity, and so the entropy condition must be satisfied in a special way- by the shock velocity being equal to the wave velocity immediately upstream of the shock. A shock such as this, for which the wave velocity on one side of the shock is the same as the velocity of the shock, is often called a semishock. The composition of the fluid upstream of the shock, S_g^{II} can therefore be found by solving (Orr, 2007, p.74):

$$\left. \frac{df_g}{dS_g} \right|^{II} = \frac{f_g^{II} - f_g^I}{S_g^{II} - S_g^I} \quad (3.54)$$

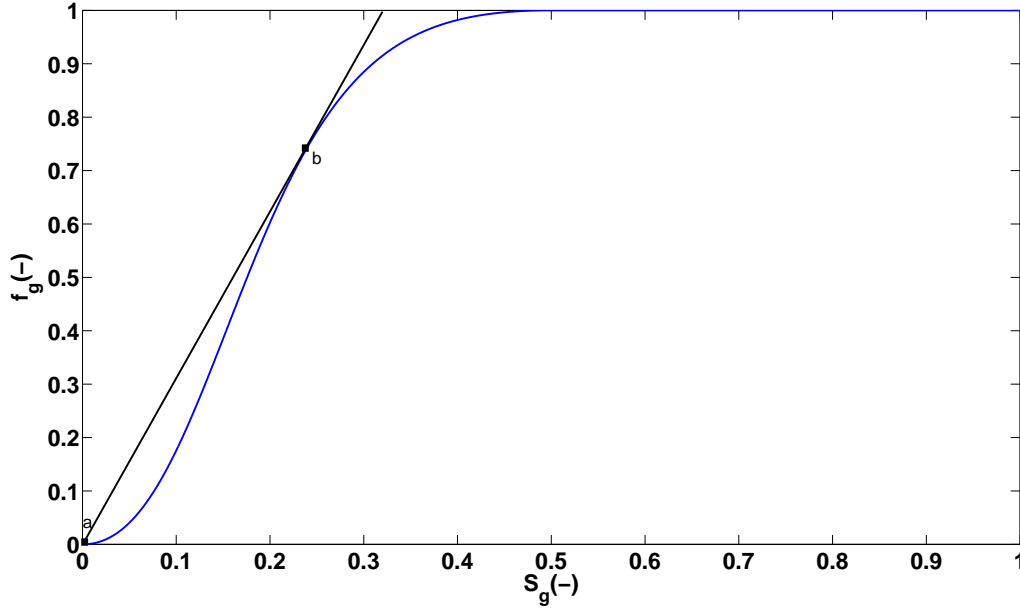


Figure 3.11: A tangent drawn between point a (the initial value of S_g) and point b (the value of S_g immediately upstream of the shock) as part of the construction of the shock.

When this problem was originally solved by [Buckley and Leverett \(1942\)](#), the location of the shock in their system was found graphically, in a method equivalent to choosing a shock such that the two areas enclosed by the curve and the shock, denoted by A and B in [Figure 3.12](#), have an equal area. [Welge \(1952\)](#) improved on this by finding the shock location using a method equivalent to that described above and shown in [Figure 3.11](#).

[Figure 3.13](#) shows both the MOC and MOL solutions for S_g , plotted against ξ for several values of τ . Both methods give very similar solutions, and the shock separating the two phase region from the aqueous only region, at which S_g drops to zero, is clear in both solutions. The only noticeable difference between the solutions is that the start of the shock is less pronounced in the MOL solution, and this is due to the numerical approximations necessary within this method. It should be noted that S_g only goes up to a maximum value of $1 - S_{ar}$ in the solutions to this problem. This is due to the assumption of the phases being immiscible, meaning that the lowest possible aqueous phase saturation will be the residual saturation. In later problems, when partial miscibility between the phases is assumed, the aqueous saturation will be able to drop all the way to zero as it will be possible for the water in the aqueous phase to evaporate into the gaseous phase, in addition to being forced out of the pores by the advancing CO_2 .

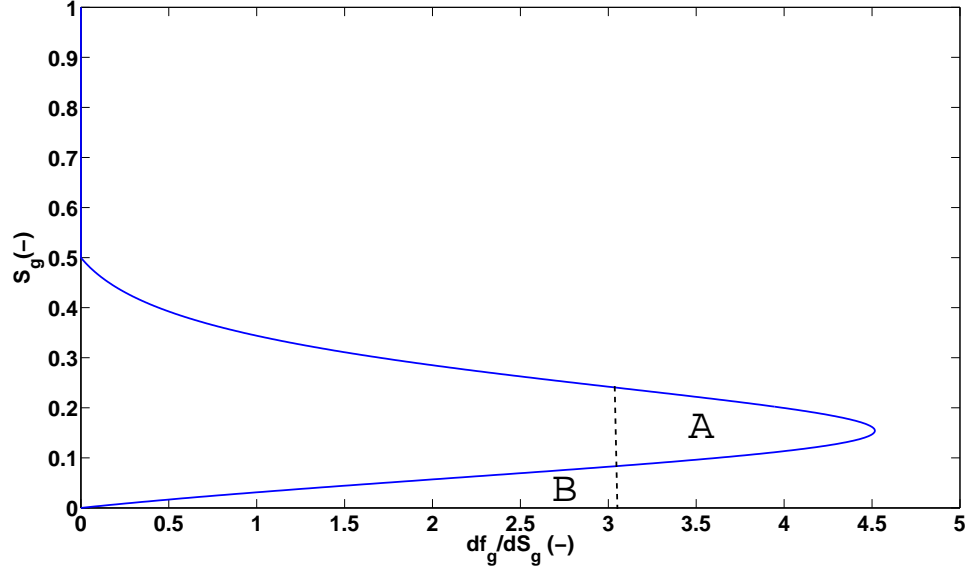


Figure 3.12: A plot of $\frac{df_g}{dS_g}$ against S_g to illustrate the method used by Buckley and Leverett (1942) to find the location of the shock. The dotted line represents the shock while the letters A and B denote the two areas that should be equal.

3.4.3 The Method of Characteristics for a Partially Miscible System

The MOC can also be used to solve equation (3.24) for the CO₂ component:

$$\frac{\partial G_{cD}}{\partial \tau} + \frac{dH_{cD}}{dG_{cD}} \frac{\partial G_{cD}}{\partial \xi} = 0 \quad (3.55)$$

to find how G_{cD} varies with time and space for a two phase, two component, partially miscible system with constant fluid properties and negligible capillary pressure. This can be done in a way very similar to that described in Section 3.4.1.

Considering again the curve $(\xi(\tau), \tau)$ in the $\xi - \tau$ plane shown in Figure 3.5, it can be seen that the value of G_{cD} will vary at a rate of $\frac{d}{d\tau} G_{cD}(\xi(\tau), \tau)$ as $(\xi(\tau), \tau)$ moves along the curve. Using the chain rule:

$$\frac{d}{d\tau} G_{cD}(\xi(\tau), \tau) = \frac{\partial G_{cD}(\xi(\tau), \tau)}{\partial \xi} \frac{d\xi}{d\tau} + \frac{\partial G_{cD}(\xi(\tau), \tau)}{\partial \tau} \frac{d\tau}{d\tau} \quad (3.56)$$

or, equivalently:

$$\frac{dG_{cD}}{d\tau} = \frac{\partial G_{cD}}{\partial \xi} \frac{d\xi}{d\tau} + \frac{\partial G_{cD}}{\partial \tau} \quad (3.57)$$

Comparing equations (3.55) and (3.57) illustrates that choosing:

$$\frac{d\xi}{d\tau} = \frac{dH_{cD}}{dG_{cD}} \quad (3.58)$$

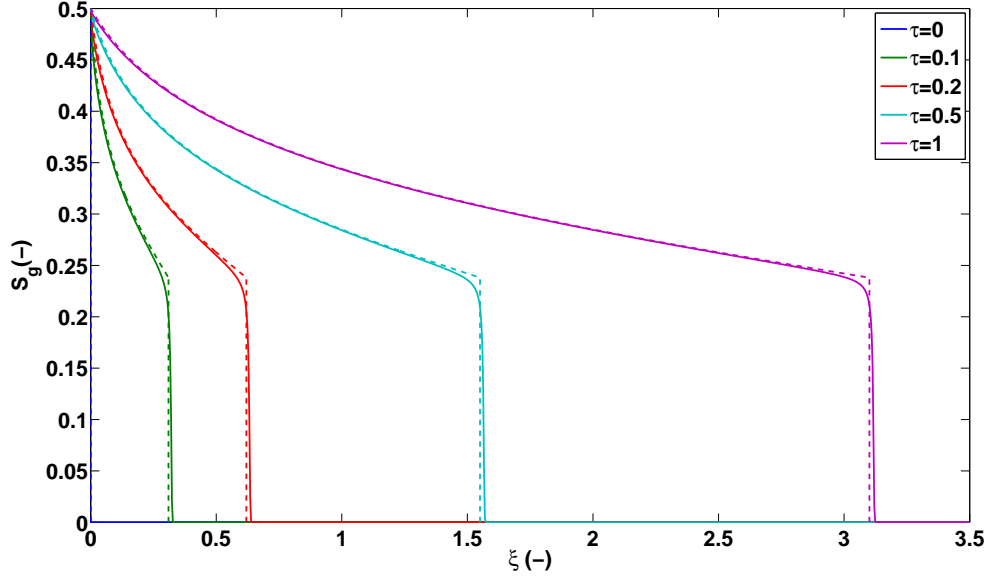


Figure 3.13: A graph to show S_g plotted against ξ for several different values of τ , as found by both the MOC and the MOL, for the parameter values shown in Table 3.1. The MOL solution is shown by the solid lines, and the MOC solution by the dashed lines.

means that:

$$\frac{dG_{cD}}{d\tau} = \frac{\partial G_{cD}}{\partial \tau} + \frac{dH_{cD}}{dG_{cD}} \frac{\partial G_{cD}}{\partial \xi} = 0 \quad (3.59)$$

showing that G_{cD} is constant along this curve (Knobel, 2000, p.128), and therefore must have the same value that it has on its initial point on the curve, $G_{cD_0}(\xi_0)$. $\frac{dH_{cD}}{dG_{cD}}$ is also constant along this curve.

Therefore, equation (3.58) can be integrated with respect to τ to give the equation of the characteristic curves of equation (3.55):

$$\xi = \frac{dH_{cD}}{dG_{cD}} \tau + \xi_0 \quad (3.60)$$

As G_{cD} has to be constant along these curves, equation (3.60) can be used to find the solution:

$$G_{cD}(\xi, \tau) = G_{cD}(\xi_0, 0) = G_{cD_0}(\xi_0) = G_{cD_0} \left(\xi - \frac{dH_{cD}}{dG_{cD}} \tau \right) \quad (3.61)$$

which again gives a travelling wave, which this time moves through the formation with velocity $\frac{dH_{cD}}{dG_{cD}}$.

In the single phase regions, equation (3.22) can be used to show that the wave velocity of a particular composition, $\frac{dH_{cD}}{dG_{cD}}$, is equal to one. It is possible to find $\frac{dH_{cD}}{dG_{cD}}$ for the compositions in the two phase region by considering that f_g depends only on S_g , which depends only on G_{cD} , as was proved in Section 3.2. By also recalling that $q_D = 1$ due to

the total flow rate being equal to the injection flow rate in this case, it can be seen that in the two phase region:

$$H_{cD} = f_g(\rho_{gD}x_{cg} - \rho_{aD}x_{ca}) + \rho_{aD}x_{ca} \quad (3.62)$$

from which it follows that:

$$\frac{dH_{cD}}{dG_{cD}} = (\rho_{gD}x_{cg} - \rho_{aD}x_{ca})\frac{df_g}{dG_{cD}} = (\rho_{gD}x_{cg} - \rho_{aD}x_{ca})\frac{df_g}{dS_g}\frac{dS_g}{dG_{cD}} \quad (3.63)$$

which, evaluating $\frac{dS_g}{dG_{cD}}$ from the expression for S_g in terms of G_{cD} given in equation (3.16), gives:

$$\frac{dH_{cD}}{dG_{cD}} = \frac{df_g}{dS_g} \quad (3.64)$$

$\frac{df_g}{dS_g}$ can be found from equation (3.51). By again considering the differing values of $\frac{df_g}{dS_g}$ shown in Figure 3.8, it can again be seen that many different compositions will have different wave velocities, resulting in the intersection of characteristic curves for the partially miscible system. This will lead to gradient catastrophes which must be solved by making the solution for G_{cD} a smooth piecewise function, with the regions separated by discontinuities. In this case, as partial miscibility can occur between the phases, there will be two points within the formation at which the number of phases present changes, meaning that two discontinuities will be necessary, rather than just one as in the immiscible system. These two discontinuities will separate the formation into three separate regions, as shown in Figure 3.14.

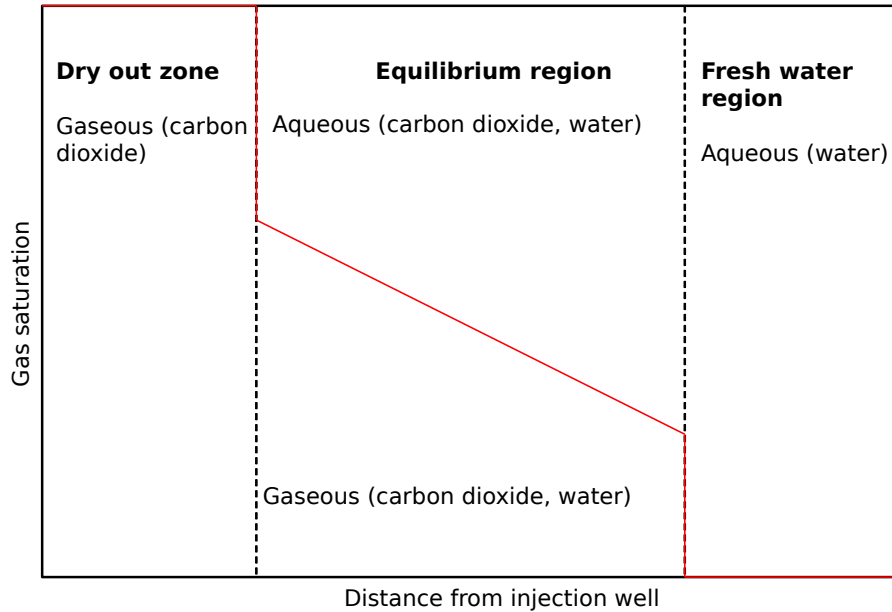


Figure 3.14: Schematic diagram illustrating the variation in gas saturation, including the discontinuities, from the point of injection for a two phase, two component system with constant fluid properties and partial miscibility.

The first region in Figure 3.14, on the left hand side, represents a dry out zone, where all the water has been evaporated by the CO₂. Moving to the right, the second region represents a two phase region where both phases are present and are in equilibrium. The third region, on the right hand side, represents the initial formation fluid, unperturbed by the injected CO₂. The discontinuity that separates regions 1 and 2 (the dry out zone and the equilibrium region) is referred to as a ‘trailing shock’, while the discontinuity separating regions 2 and 3 (the equilibrium region and the fresh water region) is referred to as a ‘leading shock’.

The constant fluid properties used for this system are the same as those given in Table 3.1, but the additional parameters of the dimensionless phase densities and the mass fractions at equilibrium are also needed. These are chosen to be $\rho_{gD} = 1$, $\rho_{aD} = 1.2704$, $x_{cg} = 0.9979$ and $x_{ca} = 0.0318$.

The solutions for G_{cD} as found by both the MOL and the MOC are shown in Figure 3.15. It should be noted that the ξ -axis is plotted on a logarithmic scale rather than linear, as was the case in Figure 3.13 to show the solutions for S_g in an immiscible system. A logarithmic scale has been chosen for this figure in order to ensure that both shocks and all three regions are easily visible. It can be seen from the figure that the trailing shock occurs at a value of less than $\xi = 10^{-2}$ for all values of τ , meaning that the trailing shock and dry out zone may not be easily seen if a linear scale is used, and so the difference between the immiscible and partially miscible systems may not be as obvious. As with Figure 3.13, it can be seen from Figure 3.15 that the MOL and MOC solutions match very well for the two phase region, the leading shock and the aqueous only region, with the only noticeable difference between the solutions being the less pronounced edges of the MOL solution at the leading shock, due to the increased numerical dispersion present in this method. However, it appears from first glance that the position of the trailing shock is noticeably different between the two solutions. This may be misleading in part due to the logarithmic scale; the positions of the trailing shocks are actually only a maximum of 6.52×10^{-4} apart in ξ , a very small difference that would be almost indistinguishable on a linear scale. The inequality of the shocks may also be partly related to the approximations necessary in the numerical MOL method.

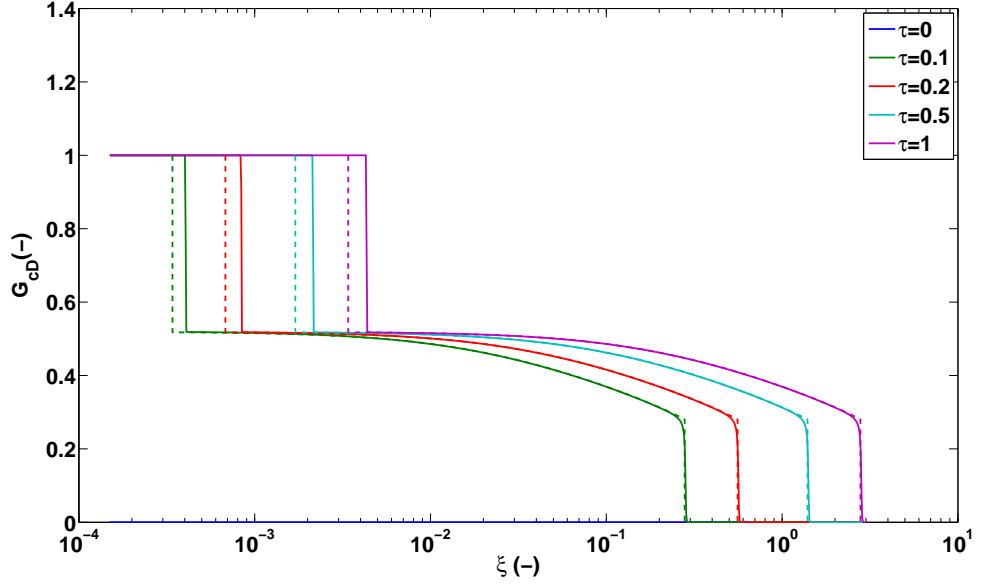


Figure 3.15: A graph to show G_{cD} plotted against ξ for several different values of τ , as found by both the MOC and the MOL, for the parameter values shown in Table 3.1 as well as those given above. The MOL solution is shown by the solid lines, and the MOC solution by the dashed lines. Note that the ξ -axis is plotted on a logarithmic scale.

3.5 Volume Change on Mixing

The earlier sections in this chapter have focused on examples with constant fluid properties. A consequence of this is that there is no volume change on mixing, i.e. the volume occupied by a given amount of a component is constant, regardless of which phase it is in. However, the MOC can also be used to solve the partial differential equations for a two component, two phase system with negligible capillary pressure, but in which volume change on mixing is accounted for, and so the volume occupied by a given amount of a component will change as it moves between phases.

As can be seen from equation (3.6), the local flow velocity, q_D , appears in the definition of H_{iD} . If volume change on mixing is accounted for, however, it will no longer be a constant value throughout the system, as q_D will change when components change volume as they transfer between phases or as the composition of a phase changes (Orr, 2007, p.84). However, in the two phase region of a binary system such as this, the assumption of equilibrium means that the values of x_{ij} remain constant even when the effects of volume change on mixing are considered, and as ρ_{jD} is calculated using a mixing rule based on the values of X_{ij} (see equation (4.29)), these values will also be constant in this region. This means that the local flow velocity, q_D , will remain constant for composition variations in

the two phase region (Orr, 2007, p.85).

Due to the constant values of x_{ij} and ρ_{jD} , and therefore q_D , it is still the case in the two phase region for a system including the effects of volume change on mixing that H_{iD} is a function of G_{iD} only. Therefore, the MOC can be used for the two phase region in the same way as it was for the system with constant fluid properties in Section 3.4.3, giving equation (3.58) as applied to both components, i :

$$\frac{d\xi}{d\tau} = \frac{dH_{iD}}{dG_{iD}} \quad (3.65)$$

However, q_D must be assumed to be a constant, currently unknown value, as opposed to being equal to one as was the case for the system with constant fluid properties. This means that, following the method used in equations (3.62) to (3.64) but without the assumption that $q_D = 1$, $\frac{dH_{cD}}{dG_{cD}}$ is found to be:

$$\frac{dH_{cD}}{dG_{cD}} = q_D \frac{df_g}{dS_g} \quad (3.66)$$

Therefore, by comparing equation (3.66) to equation (3.64), it can be seen that the wave velocity of a composition in the two phase region of a system accounting for volume change on mixing is simply the wave velocity of the composition in the system with no volume change on mixing scaled by the local flow velocity in the two phase region (Orr, 2007, p.86).

Although the value of q_D does not change when compositions vary in the equilibrium region, it does change at shocks entering or leaving the two phase region (Orr, 2007, p.86). It is therefore necessary to look at how flow velocity varies across the shocks.

Firstly, we will consider the trailing shock. Let the superscript d represent the point upstream of the shock, nearer the point of injection, and let the superscript c represent the point downstream of the shock. This means that the injection composition will be G_{cD}^d and the composition downstream of the shock will be G_{cD}^c . The Rankine-Hugoniot condition can be applied to give the shock wave velocity, Λ^{cd} (Orr, 2007, p.86):

$$\Lambda^{cd} = \frac{H_{iD}^d - H_{iD}^c}{G_{iD}^d - G_{iD}^c} \quad i = c, w \quad (3.67)$$

This equation can be solved to give both the downstream compositions, G_{iD}^c , and downstream shock velocity, q_D^c . In order to show this, it is easier to let:

$$\Omega_{iD} = \sum_{j=1}^{N_p} \rho_{jD} X_{ij} f_j \quad (3.68)$$

so that H_{iD} can be written in the form (Orr, 2007, p.87):

$$H_{iD} = q_D \sum_{j=1}^{N_p} \rho_{jD} X_{ij} f_j = q_D \Omega_{iD} \quad (3.69)$$

Considering equation (3.67) for both components and eliminating the shock wave velocity, Λ^{cd} , it can be seen that:

$$\frac{q_D^d \Omega_{cD}^d - q_D^c \Omega_{cD}^c}{G_{cD}^d - G_{cD}^c} = \frac{q_D^d \Omega_{wD}^d - q_D^c \Omega_{wD}^c}{G_{wD}^d - G_{wD}^c} \quad (3.70)$$

As q_D^d is the injection flow velocity, it must be equal to 1. In this case, pure, gaseous CO₂ is being injected, which means that $G_{cD}^d = 1$, $G_{wD}^d = 0$, $\Omega_{cD}^d = 1$ and $\Omega_{wD}^d = 0$. Equation (3.70) can therefore be simplified to:

$$\frac{1 - q_D^c \Omega_{cD}^c}{1 - G_{cD}^c} = \frac{q_D^c \Omega_{wD}^c}{G_{wD}^c} \quad (3.71)$$

which can be rearranged to give an expression for q_D^c in terms of the compositions downstream of the shock:

$$q_D^c = \frac{G_{wD}^c}{\Omega_{wD}^c (1 - G_{cD}^c) + G_{wD}^c \Omega_{cD}^c} \quad (3.72)$$

In order to satisfy the Rankine-Hugoniot condition, the velocity constraint and the entropy condition, it must be that the trailing shock is a semishock, such that the wave velocity on the downstream side of the shock is the same as the shock wave velocity (Orr, 2007, p.87). Therefore, it must be that:

$$q_D^c \frac{df_g}{dS_g} = \frac{H_{iD}^d - H_{iD}^c}{G_{iD}^d - G_{iD}^c} = \frac{\Omega_{iD}^d - q_D^c \Omega_{iD}^c}{G_{iD}^d - G_{iD}^c} \quad (3.73)$$

This can be applied to both components, and the resulting equations solved simultaneously with equation (3.72) to give the values of the compositions downstream of the trailing shock, G_{cD}^c and G_{wD}^c , and the flow velocity, q_D^c .

We can now consider the leading shock in a similar way. Let a represent the point downstream of the shock, where the composition is as it was initially, and let b represent the point upstream of the shock. Therefore, the initial composition will be G_{cD}^a and the composition upstream of the shock will be G_{cD}^b . The wave velocity of the leading shock, Λ^{ab} , can be found to be (Orr, 2007, p.87):

$$\Lambda^{ab} = \frac{H_{iD}^b - H_{iD}^a}{G_{iD}^b - G_{iD}^a} \quad (3.74)$$

Therefore:

$$\frac{q_D^b \Omega_{cD}^b - q_D^a \Omega_{cD}^a}{G_{cD}^b - G_{cD}^a} = \frac{q_D^b \Omega_{wD}^b - q_D^a \Omega_{wD}^a}{G_{wD}^b - G_{wD}^a} \quad (3.75)$$

Initially in the formation is pure, aqueous water. This means that $G_{cD}^a = 0$, $\Omega_{cD}^a = 0$, $G_{wD}^a = 1$ and $\Omega_{wD}^a = \rho_{aD}^a$, where ρ_{aD}^a is the constant, dimensionless ratio of the density of the pure, aqueous water in the fresh water region to the density of the injected fluid. As q_D is constant within the two phase region, it must also be the case that $q_D^b = q_D^c$, which will be known if it has already been calculated from the trailing shock. Equation (3.75) can therefore be simplified to:

$$\frac{q_D^c \Omega_{cD}^b}{G_{cD}^b} = \frac{q_D^c \Omega_{wD}^b - q_D^a \rho_{aD}^a}{G_{wD}^b - 1} \quad (3.76)$$

which can be rearranged to show that:

$$\frac{q_D^a}{q_D^c} = \frac{G_{cD}^b \Omega_{wD}^b - \Omega_{cD}^b (G_{wD}^b - 1)}{G_{cD}^b \rho_{aD}^a} \quad (3.77)$$

Again, applying the velocity constraint and entropy condition, it must be that the leading shock is a semishock, such that the wave velocity upstream of the shock is equal to the shock wave velocity (Orr, 2007, p.87). Therefore:

$$q_D^b \frac{df_g}{dS_g} = \frac{H_{iD}^b - H_{iD}^a}{G_{iD}^b - G_{iD}^a} = \frac{q_D^b \Omega_{iD}^b - q_D^a \Omega_{iD}^a}{G_{iD}^b - G_{iD}^a} \quad (3.78)$$

or equivalently:

$$q_D^c \frac{df_g}{dS_g} = \frac{q_D^c \Omega_{iD}^b - q_D^a \Omega_{iD}^a}{G_{iD}^b - G_{iD}^a} \quad (3.79)$$

which can be applied to both components, i .

G_{iD}^b and q_D^a can then be found by solving equations (3.77) and (3.79). It can be seen from the calculation of the flow velocities and compositions that, in a two phase and two component system such as this, there are only three different flow velocities, q_D . These are the flow velocity ahead of the leading shock, the flow velocity in the two phase region, and a value of $q_D = 1$ behind the trailing shock, as the total flow rate, q_t , in this region will be the same as the injection velocity, q_{inj} .

Figure 3.16 illustrates the differences that including volume change on mixing make to a solution. It compares the behaviour of a system in which gaseous CO₂ is injected into a formation containing aqueous decane, C₁₀, in one case when volume change on mixing is accounted for and another case in which it is not, by plotting the analytical, MOC solutions in both cases. It also plots the MOL solution for values of τ ranging from 0

to 30 for the scenario in which volume change on mixing is included. It was taken that both critical saturations were equal to zero. Figure 3.16a plots ξ/τ against z_{cD} , the non-dimensionalised mass fraction of CO₂, which is equal to (Orr, 2007, p.88):

$$z_{cD} = \frac{G_{cD}}{\rho_{gD}S_g + \rho_{aD}S_a} \quad (3.80)$$

Figure 3.16b shows how the gas saturation varies with ξ/τ , while Figure 3.16c plots ξ/τ against the flow velocity, q_D .

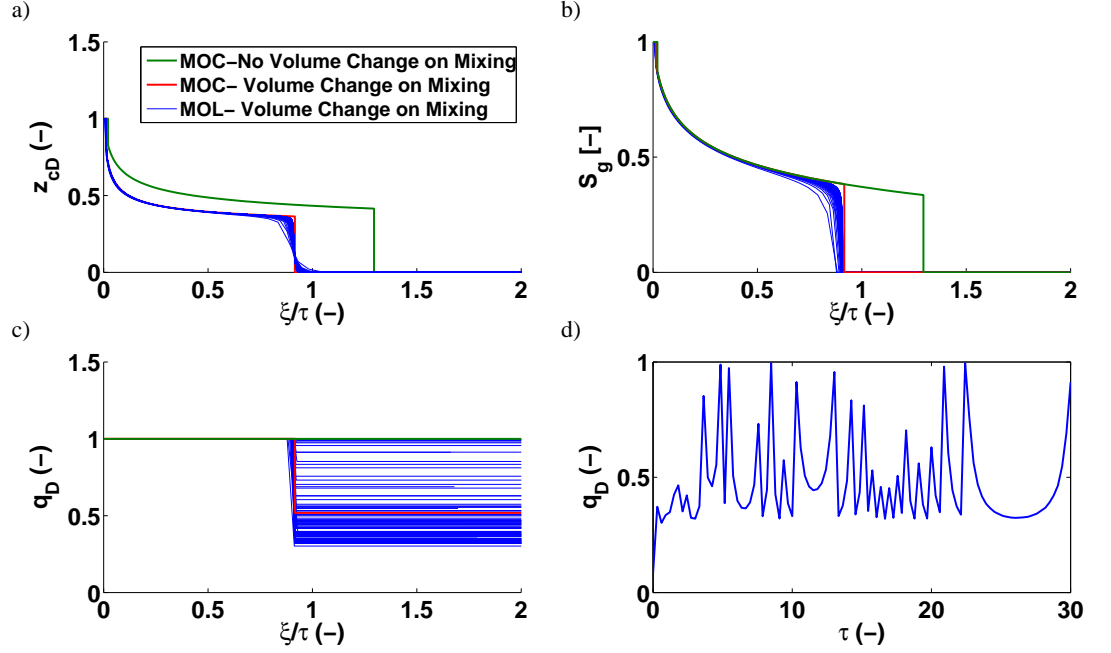


Figure 3.16: Plots showing the displacement of C₁₀ by CO₂ (Adapted from Orr (2007, p.91)). Solutions found using the MOC are shown with and without volume change as components transfer between phases, and a MOL solution is plotted for values of τ ranging from 0 to 30, in which the effects of volume change on mixing are included. (a) plots ξ/τ against the non-dimensionalised mass fraction of CO₂, z_{cD} (b) plots ξ/τ against the gas saturation, S_g (c) plots ξ/τ against the flow velocity, q_D (d) plots the values of τ against the value of q_D at the final point in space.

Focusing firstly on the two MOC solutions, it can be seen from subfigures (a)-(c) that the composition profiles are very similar in shape for the two different situations, but when volume change on mixing is taken into account, flow proceeds more slowly (Orr, 2007, p.89). This is particularly noticeable when looking at the wave velocity of the leading shock. The reason for this change in flow velocity is that when CO₂ is dissolved in the aqueous phase, it occupies a much lower volume than when it is in the gaseous phase. Therefore, when a proportion of CO₂ saturates the aqueous decane in the two phase region, the volume of CO₂ is lower than it would be if all of the CO₂ was in the gaseous phase, which causes flow to slow down (Orr, 2007, p.88). It can be seen from Figure 3.16c that the flow velocity, q_D , ahead of the leading shock is only about half of the flow velocity

at injection.

In this particular example, the trailing shock is very slow, due to the low solubility of C_{10} in CO_2 (Orr, 2007, p.88). It can be seen from the subfigures that the change in flow velocity at the trailing shock is small, and this is again because of the low solubility of C_{10} in CO_2 . The small amount of C_{10} in the gaseous phase has very little effect on the change in volume in the dry out zone, and therefore also has very little effect on the flow velocity (Orr, 2007, p.88). It should also be noted from Figure 3.16c that q_D remains constant for compositions within the two phase region, as was stated earlier in this section.

Figure 3.16 also plots the MOL solutions for varying values of τ and accounting for volume change on mixing. Figure 3.16a and Figure 3.16b show that the lines representing the differing values of τ are not so alike that they are indistinguishable from each other, but they do have very similar shapes and converge to almost the same points. They also compare well to the analytical solution representing the inclusion of volume change on mixing, such that the numerical solution could be considered to be a good approximation of both z_{cD} and S_g . However, this is not the case for Figure 3.16c. Although the numerical solutions follow the same pattern as the analytical solution, with the flow velocities, q_D , remaining at values very close to one in both the dry out and two phase regions, before dropping to a smaller value for the aqueous only region, this subfigure illustrates extreme instability for the value of q_D for different values of τ , with the flow velocity value beyond the leading shock varying wildly between 0.3 and 1. Figure 3.16d plots the flow velocity, q_D at the final point in space for each value of τ , and shows further the huge oscillations that occur within the flow velocity as τ varies. These indicate that, although the MOL is clearly a very useful method of approximating solutions to PDEs, and has compared very well to the outputs of the MOC in figures throughout this chapter, it can in some cases be severely affected by issues with numerical instability.

3.6 Chapter Summary and Conclusions

It can be seen from Figure 3.13 that the MOC and MOL produce very similar saturation outputs for two phase immiscible flow with constant fluid properties. The values of G_{cD} outputted for the two methods when partial miscibility was introduced also compared very well, in particular when an aqueous phase was still present, as shown by Figure 3.15. The inclusion of volume change on mixing meant that the MOL still gave reliable results for

z_{cD} and S_g as compared to the MOC solutions, but the MOL was not able to produce the true value of the flow velocity, q_D , with the value it gave varying wildly due to numerical instabilities, as illustrated by Figure 3.16. It can therefore be concluded that the numerical MOL, which, unlike the MOC, is not limited to solving hyperbolic PDEs, could be a very useful method for approximating the solutions to PDEs that incorporate compressibility, capillary pressure and other complexities, and hence could ultimately be used to simulate salt precipitation in saline aquifers using models with more realistic conditions. It is, however, important to be aware of the potential issue of numerical instabilities when using this method.

In order to test how accurate the numerical models we create are and to determine whether they can be relied upon, it is necessary to compare them to either real-life data or existing analytical solutions. For the situation of CO₂ being injected into a saline formation, the real-life data is limited, especially for the long time scales it is necessary to test for to determine whether CCS will be a feasible method for reducing greenhouse gas emissions. Therefore, it is very important to form analytical solutions to verify the output of our numerical models, and the MOC is highly useful for this.

Chapter 4

Method of Lines Solution for Compressible Two Component and Two Phase Flow with Capillary Pressure

Although the method of characteristics (MOC) is extremely useful, it is limited to relatively simple partial differential equations (PDEs) in which no dispersion or capillary pressure terms are included. If we wish to include these terms to make the PDEs more applicable to real-life situations, the MOC can no longer be used and it is necessary to move on to using approximate methods to solve our systems of PDEs. One possible method is the method of lines (MOL), which was shown in Chapter 3 to produce outputs that compare well to the MOC outputs for both immiscible and partially miscible two component and two phase flow with constant fluid properties and negligible capillary pressure. When volume change on mixing was introduced, the MOL gave very similar values as the MOC for how the non-dimensionalised mass fraction of CO₂, z_{cD} [-], and the gas saturation, S_g [-], varied throughout the system. However, the non-dimensionalised flow velocity, q_D [-], calculated by the MOL suffered from severe numerical instabilities.

Recall from Section 3.3 that the basis of the MOL is that PDEs are discretised in space to form a set of coupled ordinary differential equations (ODEs) that have derivatives purely with respect to time, which can then be solved by one of MATLAB's ODE solvers (Goudarzi et al., 2016). This chapter will describe how the MOL can be used to find

the global pressure and composition of a formation at any point in space and time whilst supercritical CO₂ is being injected into aqueous water, i.e. a two component, two phase system that does not yet take into account the effects of solid salt. The system is assumed to be isothermal, but does incorporate both volume change on mixing and capillary pressure. Chapter 5 will explain how this method can be extended to include the effects of salt and model a formation containing three components and three phases, as is needed to fully investigate the impact of counter-current imbibition and salt precipitation.

4.1 Conceptual Model

In Chapter 3, the systems that were looked at were considered to be linear. However, in order to gain a more realistic idea of the processes happening within the formations in the field and a more accurate picture of the composition and pressure at different points in space and time, this two component, two phase system will be modelled with radial coordinates. The formation is considered to be a homogeneous, radially-symmetric reservoir with radial extent r_E [L] and formation thickness H [L], which is initially filled with pure, aqueous water. At the centre of the formation is a fully penetrating injection well of radius r_w [L], into which supercritical CO₂ is injected at a constant rate of M_0 [MT⁻¹] for a period of time t [T]. This is illustrated in Figure 4.1. The permeability of the formation is considered to be horizontally isotropic, but a necessary simplifying assumption is that the vertical permeability is considerably smaller than the horizontal permeability, to the extent that the effects of gravity can be neglected. This means that, during the injection phase, it is possible to treat the flow of fluid as one-dimensional and radially symmetric (Kelly and Mathias, 2018).

4.2 Numerical Grid

In order to use finite difference within the MOL in order to solve the two component, two phase problem, it is necessary to discretise the r -axis into a block centred grid with N nodes, as illustrated in Figure 4.2. In the figure, a point denoted by r_k represents the node at the centre of a particular cell k , while r_{k-1} and r_{k+1} represent the nodes at the centres of the cells to the left and right of k , cells $k - 1$ and $k + 1$, respectively. $r_{k-\frac{1}{2}}$ and $r_{k+\frac{1}{2}}$ represent the boundaries between cells k and $k - 1$, and cells k and $k + 1$, respectively.

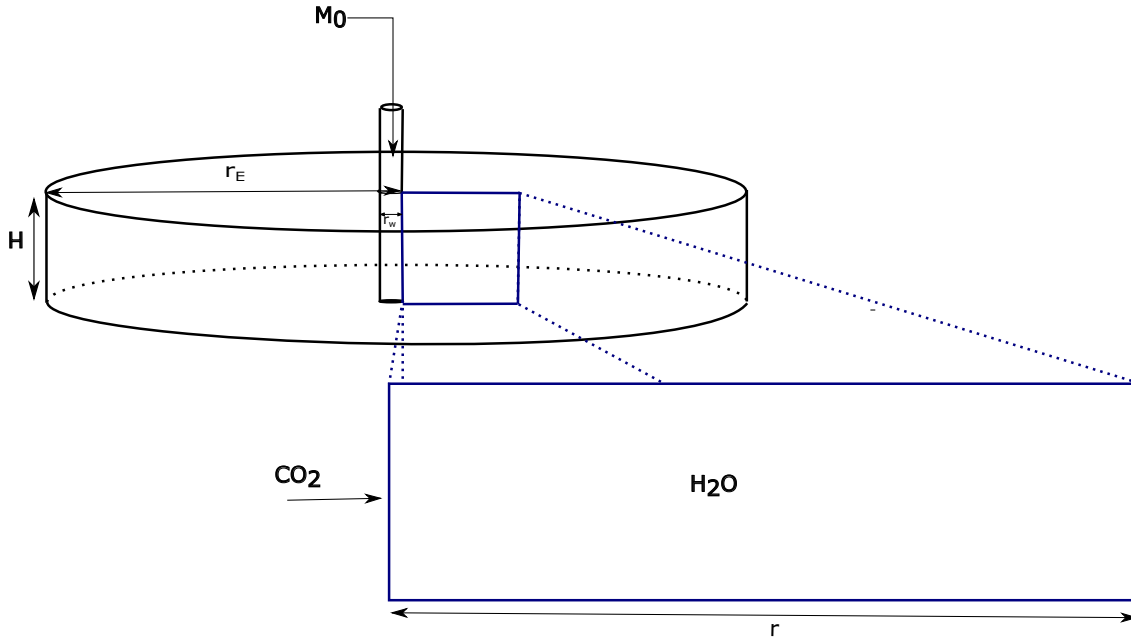


Figure 4.1: A schematic diagram showing the radial conceptual model of two component, two phase displacement. As is shown, pure CO_2 is injected into a formation initially filled with pure, aqueous H_2O at the constant rate M_0 . (Adapted from Zeidouni et al. (2009)).

For this particular problem, a logarithmically spaced grid has been used. This means that the nodes are more closely spaced near the point of injection, where there are higher flow gradients, and gradually become more coarse as the nodes move away from the injection well, and therefore gives an accurate solution for the pressure and composition within the formation for fewer nodes N than would be needed if a linear discretisation had been used, as well as increasing the stability of the formation (Goudarzi et al., 2016). The length of a particular cell, l_k , will hence vary for each cell; it will increase for each cell k that is further away from the point of injection. Within the MATLAB code used to solve this problem, $r_{k-\frac{1}{2}}$ is defined as being logarithmically spaced between the well radius r_w and the radial extent r_E . r_k can then be found using:

$$r_k = \frac{1}{2} \left(r_{k+\frac{1}{2}} + r_{k-\frac{1}{2}} \right) \quad (4.1)$$

The sizes of the time steps used will be determined by the ODE solver ode15s. As was explained in Section 3.3.2, this solver has been chosen due to the stiffness of the problem, which is caused by the fact that the pressure waves move through the formation at a significantly higher rate than the compositions, which propagate very slowly (Goudarzi et al., 2016).

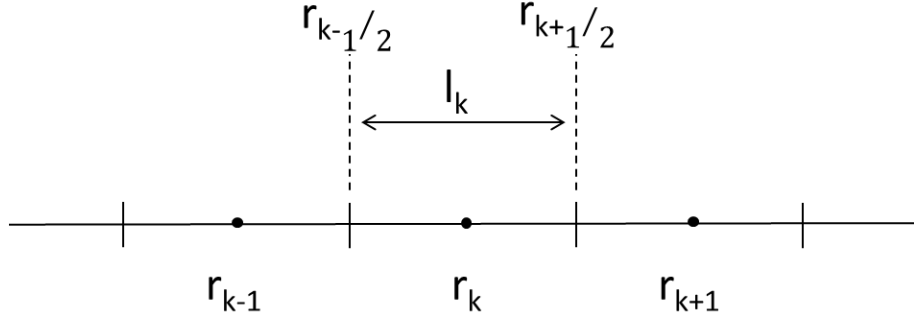


Figure 4.2: A diagram to show the discretisation of the r axis. Note that because the nodes are logarithmically spaced, l_k will vary for each cell. It will be smaller for cells nearer the point of injection and will increase logarithmically as the radial distance from the injection well increases.

4.3 Primary Dependent Variables

The primary dependent variables (PDVs) that have been chosen for this system, and hence the variables that it is necessary to produce partial derivatives with respect to time for to give to the ODE solver, are the global pressure, P [$\text{ML}^{-1}\text{T}^{-2}$], and the mass fraction of CO_2 , z_c [-]. z_i [-], where i represents the component CO_2 (denoted by c) or water (denoted by w) is defined as:

$$z_i = \frac{G_i}{F} \quad (4.2)$$

It can be recalled from equation (2.1) that:

$$G_i = \phi \sum_{j=1}^{N_p} \rho_j X_{ij} S_j \quad (4.3)$$

and F [ML^{-3}], the total mass of all components within a given volume of fluid mixture, can be found to be:

$$F = \sum_{i=1}^{N_c} G_i = \phi \sum_{j=1}^{N_p} \rho_j S_j \quad (4.4)$$

As was explained in Section 2.2.4, global pressure is often chosen as a PDV because it is defined at all points, regardless of which phases are present, in contrast to the phase pressures, P_j [$\text{ML}^{-1}\text{T}^{-2}$], whose definitions are more limited and can only be given when the relevant phase is present. z_c was chosen as a primary variable because it is independent of pressure, unlike G_i [ML^{-3}] and F , which may change with pressure depending on how the densities of the component i in the phase j , ρ_{ij} [ML^{-3}], vary with pressure (Goudarzi et al., 2016). Due to the assumption of equilibrium in the two phase region, all other values can be deduced from these PDVs.

Therefore, in order to solve this problem by the MOL, expressions for $\frac{\partial z_c}{\partial t}$ and $\frac{\partial P}{\partial t}$ must be found from the governing equations and the finite difference method. These can then be integrated with respect to time by the ODE solver ode15s, giving the values of the variables z_c and P , from which any other value can be found.

The basis of this problem is defined by the governing equations given in Section 2.2, as appropriate for a two component, two phase, one-dimensional, radial system that incorporates capillary pressure.

4.4 Defining Regions

As has been explained in previous chapters, discontinuities or ‘shocks’ develop in the gas saturation, S_g [-], when supercritical CO₂ is injected into aqueous water, which effectively separate the formation into three regions. The region nearest to the point of injection, referred to as Region 1, is made up of a gaseous phase only, as any water that was left behind residually by the advancing CO₂ plume has evaporated into the gaseous phase. Further out is Region 2, a region in which both a gaseous and an aqueous phase are present. Within this region, the phases are considered to be in equilibrium, meaning that the maximum solubility of each component in each phase has been reached, and so the mass fraction of each component in each phase can be considered to be at its equilibrium value, x_{ij} [-]. The values of x_{ij} are found using the method described in Section 2.3, which is based on work by [Spycher et al. \(2003\)](#) and [Spycher and Pruess \(2005\)](#). The region furthest away from the point of injection, Region 3, has not yet been reached by the injected CO₂, and so is comprised solely of an aqueous phase.

The assumption of equilibrium, and the mass fraction of the component i in the phase j , X_{ij} [-], are key to determining which region each point is in. If only a gaseous phase is present, then it must be the case that the mass fraction of CO₂ in the gaseous phase, X_{cg} , is greater than the equilibrium mass fraction of CO₂ in the gaseous phase, x_{cg} , and so, as $\sum_{j=1}^{N_p} X_{ij} = 1$ and $\sum_{j=1}^{N_p} x_{ij} = 1$, it must also be that the mass fraction of water in the gaseous phase, X_{wg} , is less than the equilibrium mass fraction of water in the gaseous phase, x_{wg} . x_{wg} represents the maximum solubility of water in the gaseous phase so, if this were not the case and $X_{wg} > x_{wg}$, a separate aqueous phase must form in order to accommodate this additional water. Similarly, if only an aqueous phase is present, it must be that both X_{ca} is less than x_{ca} and X_{wa} is greater than x_{wa} .

Which region a particular point is in can be determined simply by the values of z_c and the equilibrium mass fractions, x_{cg} and x_{ca} , at this point. Using equations (4.2) to (4.4) and the fact that the phase saturation, S_j , will be equal to one when only that phase is present, and zero when the phase is not present, z_c can be expressed for each region to be:

$$z_c = \frac{\rho_g X_{cg} S_g}{\rho_g S_g} = X_{cg} \quad S_g = 1 \quad S_a = 0 \quad \text{Region 1- Gas Only} \quad (4.5)$$

$$z_c = \frac{\rho_g x_{cg} S_g + \rho_a x_{ca} S_a}{\rho_g S_g + \rho_a S_a} \quad 0 < S_g < 1 \quad 0 < S_a < 1 \quad \text{Region 2- Two Phases} \quad (4.6)$$

$$z_c = \frac{\rho_a X_{ca} S_a}{\rho_a S_a} = X_{ca} \quad S_g = 0 \quad S_a = 1 \quad \text{Region 3- Aqueous Only} \quad (4.7)$$

As was explained above, in Region 1, $X_{cg} \geq x_{cg}$. It therefore follows from equation (4.5) that in this region, $z_c \geq x_{cg}$. Similarly, in Region 3 it must be that $X_{ca} \leq x_{ca}$, and so from equation (4.7), it must be that $z_c \leq x_{ca}$ within this region.

The solubility of CO₂ in the aqueous phase is small, meaning that $x_{ca} < x_{cg}$. This means that, looking at the expression for z_c in Region 2 in equation (4.6):

$$z_c = \frac{\rho_g x_{cg} S_g + \rho_a x_{ca} S_a}{\rho_g S_g + \rho_a S_a} < \frac{\rho_g x_{cg} S_g + \rho_a x_{cg} S_a}{\rho_g S_g + \rho_a S_a} = \frac{x_{cg}(\rho_g S_g + \rho_a S_a)}{\rho_g S_g + \rho_a S_a} = x_{cg} \quad (4.8)$$

Similarly:

$$z_c = \frac{\rho_g x_{cg} S_g + \rho_a x_{ca} S_a}{\rho_g S_g + \rho_a S_a} > \frac{\rho_g x_{ca} S_g + \rho_a x_{ca} S_a}{\rho_g S_g + \rho_a S_a} = \frac{x_{ca}(\rho_g S_g + \rho_a S_a)}{\rho_g S_g + \rho_a S_a} = x_{ca} \quad (4.9)$$

from which it follows that, within Region 2, $x_{ca} < z_c < x_{cg}$.

To summarise, the three regions within the two component, two phase formation can be defined by:

$$z_c \geq x_{cg} \quad \text{Region 1- Gas Only} \quad (4.10)$$

$$x_{ca} < z_c < x_{cg} \quad \text{Region 2- Two Phases} \quad (4.11)$$

$$z_c \leq x_{ca} \quad \text{Region 3- Aqueous Only} \quad (4.12)$$

Other variables can be derived much more easily when it is clear which region a particular point is in, and therefore which phases are present.

4.4.1 Finding Expressions for $\frac{\partial z_c}{\partial t}$ and $\frac{\partial F}{\partial t}$

Finding an Expression for $\frac{\partial z_c}{\partial t}$

Recall from equation (4.2) that:

$$z_c = \frac{G_c}{F} \quad (4.13)$$

This can be directly differentiated using the quotient rule, giving an overall derivative of z_c , dz_c of:

$$dz_c = \frac{FdG_c - G_c dF}{F^2} \quad (4.14)$$

which can be simplified to:

$$dz_c = \frac{1}{F} (dG_c - z_c dF) \quad (4.15)$$

From this, the partial derivative of z_c with respect to time can be found to be:

$$\boxed{\frac{\partial z_c}{\partial t} = \frac{1}{F} \left(\frac{\partial G_c}{\partial t} - z_c \frac{\partial F}{\partial t} \right)} \quad (4.16)$$

In order to define $\frac{\partial z_c}{\partial t}$ in such a way that it can be solved by the ODE solver, $\frac{\partial G_c}{\partial t}$ and $\frac{\partial F}{\partial t}$ must also be defined. It follows from equation (4.4) that:

$$\frac{\partial F}{\partial t} = \sum_{i=1}^{N_c} \frac{\partial G_i}{\partial t} \quad (4.17)$$

$\frac{\partial G_i}{\partial t}$ can be found by recalling equation (2.5), which states that:

$$\frac{\partial G_i}{\partial t} = -\frac{1}{r} \frac{\partial(rH_i)}{\partial r} \quad (4.18)$$

thus meaning that:

$$\frac{\partial F}{\partial t} = -\frac{1}{r} \sum_{i=1}^{N_c} \frac{\partial(rH_i)}{\partial r} \quad (4.19)$$

for all components i , which in this case are CO₂ and water. Given that the derivatives on the right hand side of equations (4.18) and (4.19) are all with respect to radial distance, the derivatives $\frac{\partial G_i}{\partial t}$ and $\frac{\partial F}{\partial t}$ can be approximated using finite differences. Further details about how best to do this accurately, ensuring that the derivatives are defined at the appropriate points, are given in Section 4.6, using upwinding as described in Section 3.3.4.

Finding an Expression for $\frac{\partial P}{\partial t}$

The variable F depends on both PDVs, z_c and P . Therefore, its overall derivative, dF , can be found using chain rule, such that:

$$dF = \frac{\partial F}{\partial z_c} dz_c + \frac{\partial F}{\partial P} dP \quad (4.20)$$

Accordingly, an equally valid expression for $\frac{\partial F}{\partial t}$ as equation (4.19) is:

$$\frac{\partial F}{\partial t} = \frac{\partial F}{\partial z_c} \frac{\partial z_c}{\partial t} + \frac{\partial F}{\partial P} \frac{\partial P}{\partial t} \quad (4.21)$$

This can be rearranged to express $\frac{\partial P}{\partial t}$ as:

$$\boxed{\frac{\partial P}{\partial t} = \left[\frac{\partial F}{\partial t} - \frac{\partial F}{\partial z_c} \frac{\partial z_c}{\partial t} \right] \left(\frac{\partial F}{\partial P} \right)^{-1}} \quad (4.22)$$

$\frac{\partial F}{\partial t}$ and $\frac{\partial z_c}{\partial t}$ can be found by equation (4.19) and equation (4.16), respectively. However, finding expressions for $\frac{\partial F}{\partial z_c}$ and $\frac{\partial F}{\partial P}$ is significantly more challenging.

4.5 Derivatives of F

4.5.1 Finding the Overall Derivative of F, dF

The first step to finding $\frac{\partial F}{\partial z_c}$ and $\frac{\partial F}{\partial P}$ is to express the overall derivative of F , dF . Recall from equation (4.4) that:

$$F = \phi \sum_{j=1}^{N_p} \rho_j S_j \quad (4.23)$$

Using chain rule on this equation leads to:

$$dF = \left(\sum_{j=1}^{N_p} \rho_j S_j \right) d\phi + \phi d \left(\sum_{j=1}^{N_p} \rho_j S_j \right) \quad (4.24)$$

The first term of equation (4.24) can be alternatively written as:

$$F \frac{d\phi}{\phi} \quad (4.25)$$

Product rule can be used on the second term of equation (4.24) to give:

$$\phi \sum_{j=1}^{N_p} (\rho_j dS_j + S_j d\rho_j) \quad (4.26)$$

or, equivalently:

$$\phi \sum_{j=1}^{N_p} \rho_j S_j \left(\frac{d\rho_j}{\rho_j} + \frac{dS_j}{S_j} \right) \quad (4.27)$$

leading to the overall derivative of F :

$$dF = F \frac{d\phi}{\phi} + \phi \sum_{j=1}^{N_p} \rho_j S_j \left(\frac{d\rho_j}{\rho_j} + \frac{dS_j}{S_j} \right) \quad (4.28)$$

Within this model, the phase densities ρ_j are given by the following mixing rule:

$$\rho_j = \left(\sum_{i=1}^{N_c} \frac{X_{ij}}{\rho_{ij}} \right)^{-1} \quad (4.29)$$

The overall derivative of ρ_j , $d\rho_j$, can therefore be found by letting $g_j = \sum_{i=1}^{N_c} \frac{X_{ij}}{\rho_{ij}}$, such that:

$$\rho_j = g_j^{-1} \quad (4.30)$$

and then using chain rule, to give:

$$d\rho_j = -g_j^{-2} dg_j \quad (4.31)$$

The derivative of g_j , dg_j can be found using quotient rule:

$$dg_j = \sum_{i=1}^{N_c} \frac{\rho_{ij} dX_{ij} - X_{ij} d\rho_{ij}}{\rho_{ij}^2} \quad (4.32)$$

or equivalently:

$$dg_j = \sum_{i=1}^{N_c} \frac{X_{ij}}{\rho_{ij}} \left(\frac{dX_{ij}}{X_{ij}} - \frac{d\rho_{ij}}{\rho_{ij}} \right) \quad (4.33)$$

Therefore, going back to equation (4.31):

$$d\rho_j = -g_j^{-2} \sum_{i=1}^{N_c} \frac{X_{ij}}{\rho_{ij}} \left(\frac{dX_{ij}}{X_{ij}} - \frac{d\rho_{ij}}{\rho_{ij}} \right) \quad (4.34)$$

and so:

$$d\rho_j = \rho_j^2 \sum_{i=1}^{N_c} \frac{X_{ij}}{\rho_{ij}} \left(\frac{d\rho_{ij}}{\rho_{ij}} - \frac{dX_{ij}}{X_{ij}} \right) \quad (4.35)$$

This means that the expression needed for equation (4.28) is:

$$\frac{d\rho_j}{\rho_j} = \rho_j \sum_{i=1}^{N_c} \frac{X_{ij}}{\rho_{ij}} \left(\frac{d\rho_{ij}}{\rho_{ij}} - \frac{dX_{ij}}{X_{ij}} \right) \quad (4.36)$$

In order to find dS_j , it is necessary to mathematically define the phase saturation, S_j . This can be done by considering the definition of z_i from equations (4.2) to (4.4), in a system in which only two phases, gaseous and aqueous, can exist:

$$z_i = \frac{\rho_g X_{ig} S_g + \rho_a X_{ia} S_a}{\rho_g S_g + \rho_a S_a} \quad (4.37)$$

As a maximum of two phases can be present at any point within the system, it must be the case that $S_a = 1 - S_g$, and so finding an expression for S_g will also enable S_a to be easily found. Therefore:

$$z_i = \frac{\rho_g X_{ig} S_g + \rho_a X_{ia} (1 - S_g)}{\rho_g S_g + \rho_a (1 - S_g)} \quad (4.38)$$

which can be rearranged to give:

$$S_g = \frac{h_{ia}}{h_{ia} - h_{ig}} \quad (4.39)$$

where:

$$h_{ig} = \rho_g (z_i - X_{ig}) \quad (4.40)$$

and

$$h_{ia} = \rho_a (z_i - X_{ia}) \quad (4.41)$$

It should also be noted that:

$$S_a = 1 - S_g = -\frac{h_{ig}}{h_{ia} - h_{ig}} \quad (4.42)$$

The derivative of S_g , dS_g , can then be found using quotient rule on equation (4.39), to give:

$$dS_g = \frac{(h_{ia} - h_{ig})dh_{ia} - h_{ia}(dh_{ia} - dh_{ig})}{(h_{ia} - h_{ig})^2} \quad (4.43)$$

Dividing equation (4.43) by equation (4.39) gives the term needed in equation (4.28), $\frac{dS_g}{S_g}$:

$$\frac{dS_g}{S_g} = \frac{(h_{ia} - h_{ig})dh_{ia} - h_{ia}(dh_{ia} - dh_{ig})}{h_{ia}(h_{ia} - h_{ig})} \quad (4.44)$$

which reduces to:

$$\frac{dS_g}{S_g} = \frac{h_{ia}dh_{ig} - h_{ig}dh_{ia}}{h_{ia}(h_{ia} - h_{ig})} \quad (4.45)$$

or equivalently, from rearranging and substituting in equation (4.42):

$$\frac{dS_g}{S_g} = -S_a \left(\frac{dh_{ig}}{h_{ig}} - \frac{dh_{ia}}{h_{ia}} \right) \quad (4.46)$$

The values of $\frac{dh_{ig}}{h_{ig}}$ and $\frac{dh_{ia}}{h_{ia}}$ can be found by using product rule on equations (4.40) and (4.41), respectively, to find that:

$$\frac{dh_{ig}}{h_{ig}} = \frac{d(z_i - X_{ig})}{(z_i - X_{ig})} + \frac{d\rho_g}{\rho_g} \quad (4.47)$$

and

$$\frac{dh_{ia}}{h_{ia}} = \frac{d(z_i - X_{ia})}{(z_i - X_{ia})} + \frac{d\rho_a}{\rho_a} \quad (4.48)$$

Equations (4.47) and (4.48) can be substituted into equation (4.46) to give:

$$\frac{dS_g}{S_g} = -S_a \left(\frac{d(z_i - X_{ig})}{(z_i - X_{ig})} + \frac{d\rho_g}{\rho_g} - \frac{d(z_i - X_{ia})}{(z_i - X_{ia})} - \frac{d\rho_a}{\rho_a} \right) \quad (4.49)$$

or, in the more succinct form used in Goudarzi et al. (2016):

$$\frac{dS_g}{S_g} = S_a \sum_{j=1}^2 (-1)^j \left[\left(\frac{dz_i - dX_{ij}}{z_i - X_{ij}} \right) + \frac{d\rho_j}{\rho_j} \right] \quad (4.50)$$

in which the gaseous phase can be denoted as phase 1, and the aqueous phase as phase 2.

It should be noted that these expressions can also easily be adapted to find $\frac{dS_a}{S_a}$. As $S_a = 1 - S_g$, it is also the case that:

$$dS_a = -dS_g \quad (4.51)$$

and

$$\frac{dS_a}{S_a} = -\frac{dS_g}{S_g} \frac{S_g}{S_a} \quad (4.52)$$

4.5.2 Finding an Expression for $\frac{\partial F}{\partial z_c}$

An expression for $\frac{\partial F}{\partial z_c}$ can now be found from equation (4.28), as appropriate for a system with two components and two phases. All derivatives in equation (4.28) need to be partial derivatives with respect to z_c , such that:

$$\frac{\partial F}{\partial z_c} = \frac{F}{\phi} \frac{\partial \phi}{\partial z_c} + \phi \left[\rho_g S_g \left(\frac{1}{\rho_g} \frac{\partial \rho_g}{\partial z_c} + \frac{1}{S_g} \frac{\partial S_g}{\partial z_c} \right) + \rho_a S_a \left(\frac{1}{\rho_a} \frac{\partial \rho_a}{\partial z_c} + \frac{1}{S_a} \frac{\partial S_a}{\partial z_c} \right) \right] \quad (4.53)$$

For this particular model, the porosity, ϕ , is not considered to vary with composition, and therefore will be constant with z_c . Thus:

$$\frac{\partial \phi}{\partial z_c} = 0 \quad (4.54)$$

It follows from this that the first term of equation (4.53) is also equal to zero, and $\frac{\partial F}{\partial z_c}$ can be written as:

$$\frac{\partial F}{\partial z_c} = \phi \left[\rho_g S_g \left(\frac{1}{\rho_g} \frac{\partial \rho_g}{\partial z_c} + \frac{1}{S_g} \frac{\partial S_g}{\partial z_c} \right) + \rho_a S_a \left(\frac{1}{\rho_a} \frac{\partial \rho_a}{\partial z_c} + \frac{1}{S_a} \frac{\partial S_a}{\partial z_c} \right) \right] \quad (4.55)$$

Using equation (4.50):

$$\frac{1}{S_g} \frac{\partial S_g}{\partial z_c} = S_a \left[-\frac{1}{(z_c - X_{cg})} \left(1 - \frac{\partial X_{cg}}{\partial z_c} \right) - \frac{1}{\rho_g} \frac{\partial \rho_g}{\partial z_c} + \frac{1}{(z_c - X_{ca})} \left(1 - \frac{\partial X_{ca}}{\partial z_c} \right) + \frac{1}{\rho_a} \frac{\partial \rho_a}{\partial z_c} \right] \quad (4.56)$$

and from equation (4.52):

$$\frac{1}{S_a} \frac{\partial S_a}{\partial z_c} = -\frac{S_g}{S_a} \left(\frac{1}{S_g} \frac{\partial S_g}{\partial z_c} \right) \quad (4.57)$$

$\frac{1}{\rho_g} \frac{\partial \rho_g}{\partial z_c}$ can be found from equation (4.36) to be:

$$\frac{1}{\rho_g} \frac{\partial \rho_g}{\partial z_c} = \rho_g \left[\frac{X_{cg}}{\rho_{cg}} \left(\frac{1}{\rho_{cg}} \frac{\partial \rho_{cg}}{\partial z_c} - \frac{1}{X_{cg}} \frac{\partial X_{cg}}{\partial z_c} \right) + \frac{X_{wg}}{\rho_{wg}} \left(\frac{1}{\rho_{wg}} \frac{\partial \rho_{wg}}{\partial z_c} - \frac{1}{X_{wg}} \frac{\partial X_{wg}}{\partial z_c} \right) \right] \quad (4.58)$$

The densities of a particular component, i , in a phase, j , ρ_{ij} , are determined by equations derived by [Spycher et al. \(2003\)](#), [Batzle and Wang \(1992\)](#) and [Garcia \(2001\)](#) that depend on pressure and temperature rather than composition. Therefore, ρ_{ij} does not depend on z_c , and hence it can be assumed that $\frac{\partial \rho_{ij}}{\partial z_c} = 0$. This means that equation (4.58) will reduce to:

$$\frac{1}{\rho_g} \frac{\partial \rho_g}{\partial z_c} = -\rho_g \left[\frac{1}{\rho_{cg}} \frac{\partial X_{cg}}{\partial z_c} + \frac{1}{\rho_{wg}} \frac{\partial X_{wg}}{\partial z_c} \right] \quad (4.59)$$

As there are only two components in this system, it must be that $X_{wg} = 1 - X_{cg}$. This means that $dX_{wg} = -dX_{cg}$ and $\frac{\partial X_{wg}}{\partial z_c} = -\frac{\partial X_{cg}}{\partial z_c}$, from which it follows that:

$$\frac{1}{\rho_g} \frac{\partial \rho_g}{\partial z_c} = \rho_g \left(\frac{1}{\rho_{wg}} - \frac{1}{\rho_{cg}} \right) \frac{\partial X_{cg}}{\partial z_c} \quad (4.60)$$

Similarly:

$$\frac{1}{\rho_a} \frac{\partial \rho_a}{\partial z_c} = \rho_a \left(\frac{1}{\rho_{wa}} - \frac{1}{\rho_{ca}} \right) \frac{\partial X_{ca}}{\partial z_c} \quad (4.61)$$

Many of the terms included in $\frac{\partial F}{\partial z_c}$ involve X_{ij} or $\frac{\partial X_{ij}}{\partial z_c}$. As was shown when determining regions in Section 4.4, X_{ij} is a piecewise function that will have differing values depending on which phases are present. Therefore, $\frac{\partial F}{\partial z_c}$ is also piecewise, and thus expressions for $\frac{\partial F}{\partial z_c}$ in each region must be determined separately.

$\frac{\partial F}{\partial z_c}$ in Region 1- Gas Only

When only a gaseous phase is present, $S_g = 1$ and $S_a = 0$. This means that equation (4.55) can be reduced to:

$$\frac{\partial F}{\partial z_c} = \phi \rho_g \left(\frac{1}{\rho_g} \frac{\partial \rho_g}{\partial z_c} \right) \quad (4.62)$$

where, from equation (4.60):

$$\frac{1}{\rho_g} \frac{\partial \rho_g}{\partial z_c} = \rho_g \left(\frac{1}{\rho_{wg}} - \frac{1}{\rho_{cg}} \right) \frac{\partial X_{cg}}{\partial z_c} \quad (4.63)$$

As was calculated in equation (4.5), in Region 1, $X_{cg} = z_c$. It therefore follows that, in this region:

$$\frac{\partial X_{cg}}{\partial z_c} = 1 \quad (4.64)$$

and so:

$$\frac{1}{\rho_g} \frac{\partial \rho_g}{\partial z_c} = \rho_g \left(\frac{1}{\rho_{wg}} - \frac{1}{\rho_{cg}} \right) \quad (4.65)$$

This means that the overall expression for $\frac{\partial F}{\partial z_c}$ in Region 1 is:

$$\frac{\partial F}{\partial z_c} = \phi \rho_g^2 \left(\frac{1}{\rho_{wg}} - \frac{1}{\rho_{cg}} \right) \quad (4.66)$$

$\frac{\partial F}{\partial z_c}$ in Region 2- Two Phases

If both phases are present, $0 < S_g < 1$, $0 < S_a < 1$ and the values of X_{ij} can be assumed to be at their equilibrium values, x_{ij} . As was shown in Section 2.3, the values of x_{ij} are calculated using methods described by [Spycher et al. \(2003\)](#) and [Spycher and Pruess \(2005\)](#), and depend upon the pressure and temperature within the system, and not the composition. It can therefore be assumed that $\frac{\partial x_{ij}}{\partial z_c}$ is equal to zero.

From this, it can be seen from equation (4.60) and equation (4.61) that, in Region 2:

$$\frac{1}{\rho_g} \frac{\partial \rho_g}{\partial z_c} = \rho_g \left(\frac{1}{\rho_{wg}} - \frac{1}{\rho_{cg}} \right) \frac{\partial x_{cg}}{\partial z_c} = 0 \quad (4.67)$$

and

$$\frac{1}{\rho_a} \frac{\partial \rho_a}{\partial z_c} = \rho_a \left(\frac{1}{\rho_{wa}} - \frac{1}{\rho_{ca}} \right) \frac{\partial x_{ca}}{\partial z_c} = 0 \quad (4.68)$$

Therefore, using equation (4.55):

$$\frac{\partial F}{\partial z_c} = \phi \left[\rho_g S_g \left(\frac{1}{S_g} \frac{\partial S_g}{\partial z_c} \right) + \rho_a S_a \left(\frac{1}{S_a} \frac{\partial S_a}{\partial z_c} \right) \right] \quad (4.69)$$

where:

$$\frac{1}{S_g} \frac{\partial S_g}{\partial z_c} = S_a \left(\frac{1}{(z_c - x_{ca})} - \frac{1}{(z_c - x_{cg})} \right) \quad (4.70)$$

and

$$\frac{1}{S_a} \frac{\partial S_a}{\partial z_c} = -\frac{S_g}{S_a} \left(\frac{1}{S_g} \frac{\partial S_g}{\partial z_c} \right) = S_g \left(\frac{1}{(z_c - x_{cg})} - \frac{1}{(z_c - x_{ca})} \right) \quad (4.71)$$

Equations (4.70) and (4.71) can be substituted into equation (4.69) to show that, when both phases are present:

$$\frac{\partial F}{\partial z_c} = \phi S_g S_a (\rho_a - \rho_g) \left(\frac{1}{(z_c - x_{cg})} - \frac{1}{(z_c - x_{ca})} \right) \quad (4.72)$$

$\frac{\partial F}{\partial z_c}$ in Region 3- Aqueous Only

In Region 3, only an aqueous phase is present, meaning that $S_g = 0$ and $S_a = 1$. Therefore, from equation (4.55):

$$\frac{\partial F}{\partial z_c} = \phi \rho_a \left(\frac{1}{\rho_a} \frac{\partial \rho_a}{\partial z_c} \right) \quad (4.73)$$

where, using equation (4.61):

$$\frac{1}{\rho_a} \frac{\partial \rho_a}{\partial z_c} = \rho_a \left(\frac{1}{\rho_{wa}} - \frac{1}{\rho_{ca}} \right) \frac{\partial X_{ca}}{\partial z_c} \quad (4.74)$$

Equation (4.7) illustrates that $X_{ca} = z_c$ in Region 3. This means that:

$$\frac{\partial X_{ca}}{\partial z_c} = 1 \quad (4.75)$$

from which it follows that:

$$\frac{1}{\rho_a} \frac{\partial \rho_a}{\partial z_c} = \rho_a \left(\frac{1}{\rho_{wa}} - \frac{1}{\rho_{ca}} \right) \quad (4.76)$$

Therefore, in Region 3, $\frac{\partial F}{\partial z_c}$ can be expressed as:

$$\frac{\partial F}{\partial z_c} = \phi \rho_a^2 \left(\frac{1}{\rho_{wa}} - \frac{1}{\rho_{ca}} \right) \quad (4.77)$$

4.5.3 Finding an Expression for $\frac{\partial F}{\partial P}$

An expression for $\frac{\partial F}{\partial P}$ for a two component and two phase system can also be found from equation (4.28). All derivatives should be partial derivatives with respect to P , giving the equation:

$$\frac{\partial F}{\partial P} = \frac{F}{\phi} \frac{\partial \phi}{\partial P} + \phi \left[\rho_g S_g \left(\frac{1}{\rho_g} \frac{\partial \rho_g}{\partial P} + \frac{1}{S_g} \frac{\partial S_g}{\partial P} \right) + \rho_a S_a \left(\frac{1}{\rho_a} \frac{\partial \rho_a}{\partial P} + \frac{1}{S_a} \frac{\partial S_a}{\partial P} \right) \right] \quad (4.78)$$

A more convenient way to write this equation is in terms of rock and fluid compressibility. As more fluid is injected into a formation, the fluid pressure increases. This leads to the rock grains within the formation being pushed closer together, which increases the available volume and therefore also increases the porosity of the formation. Rock compressibility, α_r [$M^{-1}LT^2$], illustrates how the porosity changes with increasing pressure, and is expressed as:

$$\alpha_r = \frac{1}{\phi} \frac{\partial \phi}{\partial P} \quad (4.79)$$

As well as increasing the formation porosity, an increase in fluid within the formation, and therefore an increase in fluid pressure, also leads to the particles of a particular phase being closer together. This means that the volume occupied by a phase is smaller, and consequently that the density of the phase will increase. Fluid compressibility for a phase j , α_j , [$M^{-1}LT^2$] can be written as:

$$\alpha_j = \frac{1}{\rho_j} \frac{\partial \rho_j}{\partial P_j} \quad (4.80)$$

Using the phase compressibilities and chain rule:

$$\frac{1}{\rho_j} \frac{\partial \rho_j}{\partial P} = \alpha_j \frac{\partial P_j}{\partial P} \quad (4.81)$$

and hence, by incorporating both the phase and the rock compressibilities, $\frac{\partial F}{\partial P}$ can be written as:

$$\frac{\partial F}{\partial P} = F\alpha_r + \phi \left[\rho_g S_g \left(\alpha_g \frac{\partial P_g}{\partial P} + \frac{1}{S_g} \frac{\partial S_g}{\partial P} \right) + \rho_a S_a \left(\alpha_a \frac{\partial P_a}{\partial P} + \frac{1}{S_a} \frac{\partial S_a}{\partial P} \right) \right] \quad (4.82)$$

For this particular model, the rock compressibility, α_r , is given a set value by the user. However, the phase compressibilities, α_j , can be found from equation (4.36) by giving the derivatives with respect to P_j , such that:

$$\alpha_j = \frac{1}{\rho_j} \frac{\partial \rho_j}{\partial P_j} = \rho_j \sum_{i=1}^{N_c} \frac{X_{ij}}{\rho_{ij}} \left(\alpha_{ij} - \frac{1}{X_{ij}} \frac{\partial X_{ij}}{\partial P_j} \right) \quad (4.83)$$

where the compressibility of component i in phase j , α_{ij} [$M^{-1}LT^2$], is given by:

$$\alpha_{ij} = \frac{1}{\rho_{ij}} \frac{\partial \rho_{ij}}{\partial P_j} \quad (4.84)$$

The values of α_{ij} are found by using differentiation on various equations of state, including equation (2.89) by Redlich and Kwong (1949), and the equations for water and brine density found by Batzle and Wang (1992).

Within equation (4.82), the expression $\frac{1}{S_g} \frac{\partial S_g}{\partial P}$ can be found from equation (4.46) to be:

$$\frac{1}{S_g} \frac{\partial S_g}{\partial P} = -S_a \left(\frac{1}{h_{cg}} \frac{\partial h_{cg}}{\partial P} - \frac{1}{h_{ca}} \frac{\partial h_{ca}}{\partial P} \right) \quad (4.85)$$

Using chain rule to incorporate the phase pressures, this becomes:

$$\frac{1}{S_g} \frac{\partial S_g}{\partial P} = -S_a \left(\frac{1}{h_{cg}} \frac{\partial h_{cg}}{\partial P_g} \frac{\partial P_g}{\partial P} - \frac{1}{h_{ca}} \frac{\partial h_{ca}}{\partial P_a} \frac{\partial P_a}{\partial P} \right) \quad (4.86)$$

where:

$$\frac{1}{h_{cg}} \frac{\partial h_{cg}}{\partial P_g} = \frac{1}{(z_c - X_{cg})} \left(\frac{\partial z_c}{\partial P_g} - \frac{\partial X_{cg}}{\partial P_g} \right) + \frac{1}{\rho_g} \frac{\partial \rho_g}{\partial P_g} \quad (4.87)$$

and

$$\frac{1}{h_{ca}} \frac{\partial h_{ca}}{\partial P_a} = \frac{1}{(z_c - X_{ca})} \left(\frac{\partial z_c}{\partial P_a} - \frac{\partial X_{ca}}{\partial P_a} \right) + \frac{1}{\rho_a} \frac{\partial \rho_a}{\partial P_a} \quad (4.88)$$

As was explained in Section 4.3, z_c does not depend upon pressure, meaning that $\frac{\partial z_c}{\partial P_j} = 0$.

Incorporating both this and equation (4.83) into equations (4.87) and (4.88) means that:

$$\frac{1}{h_{cg}} \frac{\partial h_{cg}}{\partial P_g} = \alpha_g - \frac{1}{(z_c - X_{cg})} \frac{\partial X_{cg}}{\partial P_g} \quad (4.89)$$

and

$$\frac{1}{h_{ca}} \frac{\partial h_{ca}}{\partial P_a} = \alpha_a - \frac{1}{(z_c - X_{ca})} \frac{\partial X_{ca}}{\partial P_a} \quad (4.90)$$

Within equations (4.83), (4.89) and (4.90), the derivatives $\frac{\partial X_{ij}}{\partial P_j}$ are needed. As X_{ij} is a piecewise function, and varies depending on which phases are present, this is also the case for $\frac{\partial X_{ij}}{\partial P_j}$. As was illustrated in Section 4.4, the value of X_{ij} will be:

$$X_{ij} = \begin{cases} 0, & S_j = 0 \\ x_{ij}, & 0 < S_j < 1 \\ z_i, & S_j = 1 \end{cases} \quad (4.91)$$

Taking into account that z_i does not depend on pressure, it follows that:

$$\frac{\partial X_{ij}}{\partial P_j} = \begin{cases} 0, & S_j = 0 \\ \frac{\partial x_{ij}}{\partial P_j}, & 0 < S_j < 1 \\ 0, & S_j = 1 \end{cases} \quad (4.92)$$

where $\frac{\partial x_{ij}}{\partial P_j}$ can be approximated by finite difference.

Recall from equations (2.13) and (2.14) that:

$$P_g = \frac{P(S_g + S_a) + P_c S_a}{S_g + S_a} \quad (4.93)$$

and

$$P_a = \frac{P(S_g + S_a) - P_c S_g}{S_g + S_a} \quad (4.94)$$

For a two phase system such as this, $S_g + S_a = 1$, from which it follows that:

$$P_g = P + P_c S_a \quad (4.95)$$

and

$$P_a = P - P_c S_g \quad (4.96)$$

Using product rule, equations (4.95) and (4.96) can be used to find that:

$$\frac{\partial P_g}{\partial P} = 1 + P_c \frac{\partial S_a}{\partial P} + S_a \frac{\partial P_c}{\partial P} \quad (4.97)$$

and

$$\frac{\partial P_a}{\partial P} = 1 - P_c \frac{\partial S_g}{\partial P} - S_g \frac{\partial P_c}{\partial P} \quad (4.98)$$

As was shown in equation (2.19), the capillary pressure, P_c , depends solely on the phase saturations. It is therefore possible to use chain rule to conclude that:

$$\frac{\partial P_c}{\partial P} = \frac{\partial P_c}{\partial S_g} \frac{\partial S_g}{\partial P} \quad (4.99)$$

which, along with the extrapolation from equation (4.51) that:

$$\frac{\partial S_a}{\partial P} = -\frac{\partial S_g}{\partial P} \quad (4.100)$$

can be substituted into equations (4.97) and (4.98) to give the expressions:

$$\frac{\partial P_g}{\partial P} = 1 + \left(S_a \frac{\partial P_c}{\partial S_g} - P_c \right) \frac{\partial S_g}{\partial P} \quad (4.101)$$

and

$$\frac{\partial P_a}{\partial P} = 1 - \left(S_g \frac{\partial P_c}{\partial S_g} + P_c \right) \frac{\partial S_g}{\partial P} \quad (4.102)$$

Within these equations, $\frac{\partial P_c}{\partial S_g} = -\frac{\partial P_c}{\partial S_a}$, using the expressions for $\frac{\partial P_c}{\partial S_a}$ given in equation (2.22).

Substituting in equations (4.101) and (4.102) to equation (4.86) gives:

$$\frac{1}{S_g} \frac{\partial S_g}{\partial P} = -S_a \left[\frac{1}{h_{cg}} \frac{\partial h_{cg}}{\partial P_g} \left(1 + \left(S_a \frac{\partial P_c}{\partial S_g} - P_c \right) \frac{\partial S_g}{\partial P} \right) - \frac{1}{h_{ca}} \frac{\partial h_{ca}}{\partial P_a} \left(1 - \left(S_g \frac{\partial P_c}{\partial S_g} + P_c \right) \frac{\partial S_g}{\partial P} \right) \right] \quad (4.103)$$

which can be rearranged to give a final expression for $\frac{\partial S_g}{\partial P}$ of:

$$\frac{\partial S_g}{\partial P} = \left(\frac{1}{h_{cg}} \frac{\partial h_{cg}}{\partial P_g} - \frac{1}{h_{ca}} \frac{\partial h_{ca}}{\partial P_a} \right) \left[-\frac{1}{S_g S_a} - \frac{1}{h_{cg}} \frac{\partial h_{cg}}{\partial P_g} \left(S_a \frac{\partial P_c}{\partial S_g} - P_c \right) - \frac{1}{h_{ca}} \frac{\partial h_{ca}}{\partial P_a} \left(S_g \frac{\partial P_c}{\partial S_g} + P_c \right) \right]^{-1} \quad (4.104)$$

From equation (4.100), $\frac{\partial S_a}{\partial P}$ can also be found from this, as:

$$\frac{\partial S_a}{\partial P} = -\frac{\partial S_g}{\partial P} \quad (4.105)$$

Using equation (4.82), $\frac{\partial F}{\partial P}$ can therefore be rewritten as:

$$\frac{\partial F}{\partial P} = F\alpha_r + \phi \left[\rho_g S_g \alpha_g \frac{\partial P_g}{\partial P} + \rho_g \frac{\partial S_g}{\partial P} + \rho_a S_a \alpha_a \frac{\partial P_a}{\partial P} + \rho_a \frac{\partial S_a}{\partial P} \right] \quad (4.106)$$

into which the outputs of equations (4.83), (4.101), (4.102), (4.104) and (4.105) can be substituted.

However, in many numerical codes, the values of α_{ij} are approximated using the value of the global pressure, P , rather than the phase pressures, P_j , such that α_{ij} can be assumed to be:

$$\alpha_{ij} = \frac{1}{\rho_{ij}} \frac{\partial \rho_{ij}}{\partial P} \quad (4.107)$$

This means that the overall phase compressibilities can also be assumed to vary with respect to P rather than P_j , meaning that they are taken to be:

$$\alpha_j = \frac{1}{\rho_j} \frac{\partial \rho_j}{\partial P} = \rho_j \sum_{i=1}^{N_c} \frac{X_{ij}}{\rho_{ij}} \left(\alpha_{ij} - \frac{1}{X_{ij}} \frac{\partial X_{ij}}{\partial P} \right) \quad (4.108)$$

in which:

$$\frac{\partial X_{ij}}{\partial P} = \begin{cases} 0, & S_j = 0 \\ \frac{\partial x_{ij}}{\partial P}, & 0 < S_j < 1 \\ 0, & S_j = 1 \end{cases} \quad (4.109)$$

This also means that the expressions for $\frac{1}{S_j} \frac{\partial S_j}{\partial P}$ are significantly simplified, such that they can be found from equation (4.50) and equation (4.52) to be:

$$\frac{1}{S_g} \frac{\partial S_g}{\partial P} = S_a \left[\frac{1}{(z_c - X_{cg})} \frac{\partial X_{cg}}{\partial P} - \alpha_g - \frac{1}{(z_c - X_{ca})} \frac{\partial X_{ca}}{\partial P} + \alpha_a \right] \quad (4.110)$$

and

$$\frac{1}{S_a} \frac{\partial S_a}{\partial P} = -\frac{S_g}{S_a} \left(\frac{1}{S_g} \frac{\partial S_g}{\partial P} \right) \quad (4.111)$$

Therefore, when the global pressure rather than phase pressure is used to approximate the compressibilities, $\frac{\partial F}{\partial P}$ can be found to be:

$$\frac{\partial F}{\partial P} = F\alpha_r + \phi \left[\rho_g S_g \left(\alpha_g + \frac{1}{S_g} \frac{\partial S_g}{\partial P} \right) + \rho_a S_a \left(\alpha_a + \frac{1}{S_a} \frac{\partial S_a}{\partial P} \right) \right] \quad (4.112)$$

into which equations (4.108), (4.110) and (4.111) can be substituted.

4.6 Use of Upwinding

Once the equations needed to find $\frac{\partial z_c}{\partial t}$ and $\frac{\partial P}{\partial t}$ have been derived, it is necessary to ensure that all equations are giving their solutions at the appropriate points in space within the numerical model. The final derivatives to be given to the ODE solver, $\frac{\partial z_c}{\partial t}$ and $\frac{\partial P}{\partial t}$, need to be defined at the nodes k , and therefore all terms within the equations defining these derivatives, whether the terms themselves are derivatives or individual parameters, must also be at k . The most difficult terms to ensure are defined at k are the derivatives for which no exact expression has been found, and hence require the use of finite difference, which, in the expressions for $\frac{\partial z_c}{\partial t}$ and $\frac{\partial P}{\partial t}$, are $\frac{\partial G_i}{\partial t}$ and $\frac{\partial F}{\partial t}$. Ensuring that the output of $\frac{\partial G_i}{\partial t}$, for all components i , is given at k will also mean that $\frac{\partial F}{\partial t}$ is at k , because, as can be recalled from equation (4.17):

$$\frac{\partial F}{\partial t} = \sum_{i=1}^{N_c} \frac{\partial G_i}{\partial t} \quad (4.113)$$

Discretising equation (4.18) to find the value of $\frac{\partial G_i}{\partial t}$ at node k using the central difference approximation gives:

$$\left. \frac{\partial G_i}{\partial t} \right|_k = -\frac{1}{r_k} \frac{r_{k+\frac{1}{2}} H_{i_{k+\frac{1}{2}}} - r_{k-\frac{1}{2}} H_{i_{k-\frac{1}{2}}}}{r_{k+\frac{1}{2}} - r_{k-\frac{1}{2}}} \quad (4.114)$$

Upwinding, as described in Section 3.3.4, is used here to ensure that H_i is defined at the cell boundaries, $k + \frac{1}{2}$ and $k - \frac{1}{2}$. In this system, the effects of capillary pressure are included, causing counter-current imbibition and meaning that it cannot be assumed that all flow is in an outwards direction from the point of injection. Therefore, it is not always the case that H_{i_k} should be the point chosen to represent $H_{i_{k+\frac{1}{2}}}$. Using equation (3.41), upwinding can define $H_{i_{k+\frac{1}{2}}}$ at each point as:

$$H_{i_{k+\frac{1}{2}}} = \begin{cases} H_{i_k}, & v > 0 \\ H_{i_{k+1}}, & v \leq 0 \end{cases} \quad (4.115)$$

where v represents the wave velocity at each point.

As can be seen from equation (2.2):

$$H_i = \sum_{j=1}^{N_p} \rho_j X_{ij} q_j \quad (4.116)$$

Recall from equation (2.8) that, for a one-dimensional radial system such as this:

$$q_j = -\frac{k k_{rj}}{\mu_j} \frac{\partial P_j}{\partial r} \quad (4.117)$$

It is therefore possible to say that for a system comprising of two components and two phases, equations (4.116) and (4.117) can be combined to give expressions of the form:

$$H_i = -\rho_g X_{ig} \frac{kk_{rg}}{\mu_g} \frac{\partial P_g}{\partial r} - \rho_a X_{ia} \frac{kk_{ra}}{\mu_a} \frac{\partial P_a}{\partial r} \quad (4.118)$$

which can also be written as:

$$H_i = H_{ig} + H_{ia} \quad (4.119)$$

where

$$H_{ig} = -\rho_g X_{ig} \frac{kk_{rg}}{\mu_g} \frac{\partial P_g}{\partial r} \quad (4.120)$$

and

$$H_{ia} = -\rho_a X_{ia} \frac{kk_{ra}}{\mu_a} \frac{\partial P_a}{\partial r} \quad (4.121)$$

The two separate terms that make up H_i , H_{ij} [$\text{ML}^{-2}\text{T}^{-1}$], are each comprised of a discontinuous term, a_i , which is equal to $-\rho_j X_{ij} \frac{kk_{rj}}{\mu_j}$, and the derivative with respect to r of a smooth function, b_i , which is equal to P_j . It should be noted that both a_i and b_i ultimately depend upon the value of G_i . Because b_i is a continuous function, its Taylor series expansion is valid at all points within the system, including the cell boundaries. This means that the derivative $\frac{\partial b_i}{\partial r}$ can be found regardless of the direction of flow, and can be given directly at the cell boundary, $k + \frac{1}{2}$, using:

$$\left. \frac{\partial b_i}{\partial r} \right|_{k+\frac{1}{2}} = \frac{b_{i_{k+1}} - b_{i_k}}{r_{k+1} - r_k} \quad (4.122)$$

However, a_i is discontinuous, and so its Taylor series is not valid at the point of the discontinuity, meaning that upwinding is necessary (Goudarzi, 2017).

Upwinding can be used to find the appropriate value of H_i at each cell boundary from:

$$H_{i_{k+\frac{1}{2}}} = \left[v^u a_{i_k} + v^d a_{i_{k+1}} \right] \left. \frac{\partial b_i}{\partial r} \right|_{k+\frac{1}{2}} \quad (4.123)$$

where

$$v^u = \frac{v + |v|}{2v} \quad (4.124)$$

and

$$v^d = \frac{v - |v|}{2v} \quad (4.125)$$

An example of upwinding being used to determine which value of a_i is used at the cell boundaries is shown in Figure 4.3. The figure illustrates that the wave velocity was negative at the cell boundary $k - \frac{3}{2}$, giving values of $v^u = 0$ and $v^d = 1$, and therefore meaning that the value of a_i at this boundary was approximated to be as it was at the

point to the right, a_{k-1} . At all other cell boundaries, however, the wave velocity was positive, leading to $v^u = 1$ and $v^d = 0$, and the values of a_i at the cell boundaries being approximated by the value at the node to the left of the boundary. It should be noted that upwinding can only be used to determine values of a variable at the internal cell boundaries. The values at the external boundaries, denoted by $k - \frac{5}{2}$ and $k + \frac{5}{2}$ in the system shown in Figure 4.3, must be set separately by the user.

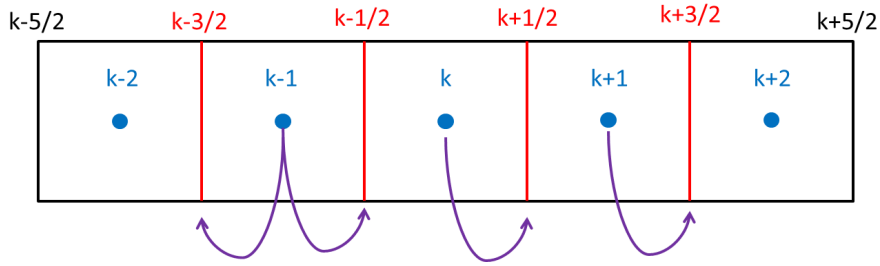


Figure 4.3: A diagram to illustrate how upwinding can be used to approximate the values of parameters at the cell boundaries. In this system, the wave velocity is negative at the cell boundary $k - \frac{3}{2}$, but positive elsewhere.

4.7 Model Output

Figure 4.4 shows the MOL solution that the numerical model outputted for the global pressure and the gas saturation plotted against the radial distance, r , at several different times, alongside the analytical solution found by Mathias et al. (2011b) that does not take into account the effects of capillary pressure. The initial parameters inputted into the model are given in Table 4.1. It should be noted that, although z_c was chosen as a PDV and so, along with the global pressure, P , was outputted from the ODE solver, S_g has been instead chosen to be plotted here to show the composition of the fluid mixture at different points in space and time. Once the PDVs are known, any parameter within the model can be easily outputted and plotted.

Parameter	Value	Parameter	Value	Parameter	Value
r_w (m)	0.25	k_{rg0} (-)	0.3	H (m)	30
r_E (m)	2.5×10^5	k_{ra0} (-)	1	P_{c0} (Pa)	19600
P_0 (Pa)	10^7	n_g (-)	3	m (-)	0.5
α_r (Pa ⁻¹)	3.54×10^{-10}	n_a (-)	3	M_0 (Mt/year)	0.3
k (m ²)	10^{-13}	S_{ar} (-)	0.3	T (°C)	40
ϕ (-)	0.2	S_{gc} (-)	0	P_{cd} (Pa)	10^6

Table 4.1: Constant parameters inputted into the two component and two phase model, to give the output in Figure 4.4.

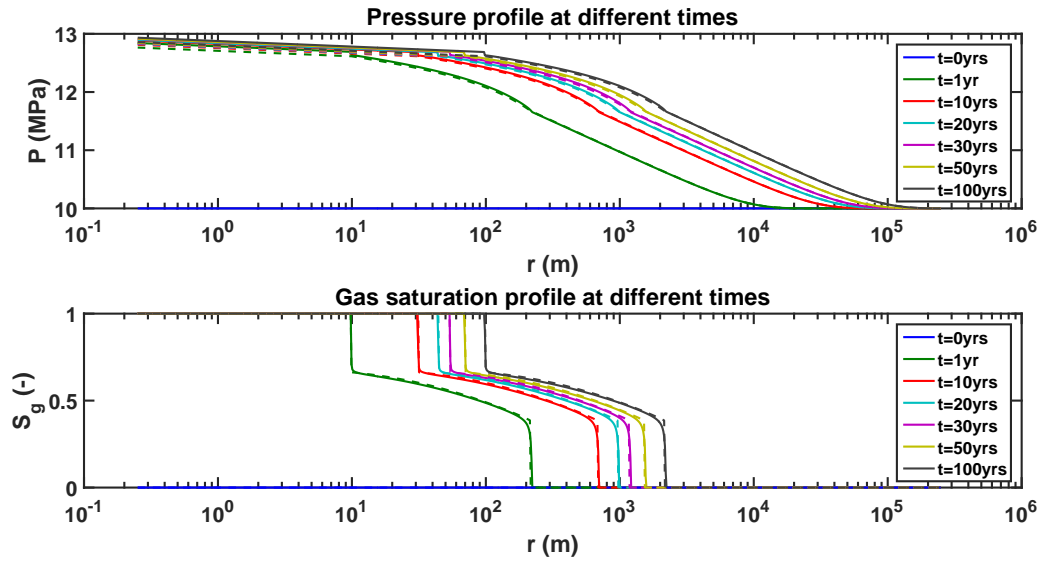


Figure 4.4: A graph to show the pressure and gas saturation output of the model for the initial parameters in Table 4.1, for the times shown in the legend. The solid lines represent the solution found by the MOL, while the dashed lines represent the analytical solution of Mathias et al. (2011b), which assumes negligible capillary pressure. The model was run for 1000 points in space.

From the bottom graph in Figure 4.4, which looks at how gas saturation varies with radial distance, it can be seen that, for all times, there are points at which all three possible phase combinations are present: gaseous phase only, both gaseous and aqueous, and aqueous phase only. The three possible ‘regions’ of different phase combinations within the formation are separated by the leading and trailing shocks. The CO₂ plume extends further into the formation as time progresses, as well as there being more time for water to evaporate into the gaseous phase, meaning that the curves representing the longer time scales have a larger dry out zone and smaller aqueous only region than the curves representing earlier times. The figure also indicates that the MOL solution compares very well with the analytical solution of Mathias et al. (2011b), with the only noticeable

differences between them being that the edges of the MOL solution at the shocks are less pronounced than the analytical solution, due to the increased dispersion in the numerical solution, and that the position of the trailing shock in the MOL solution is very slightly further out. This is caused by the inclusion of the effects of capillary pressure in the MOL solution.

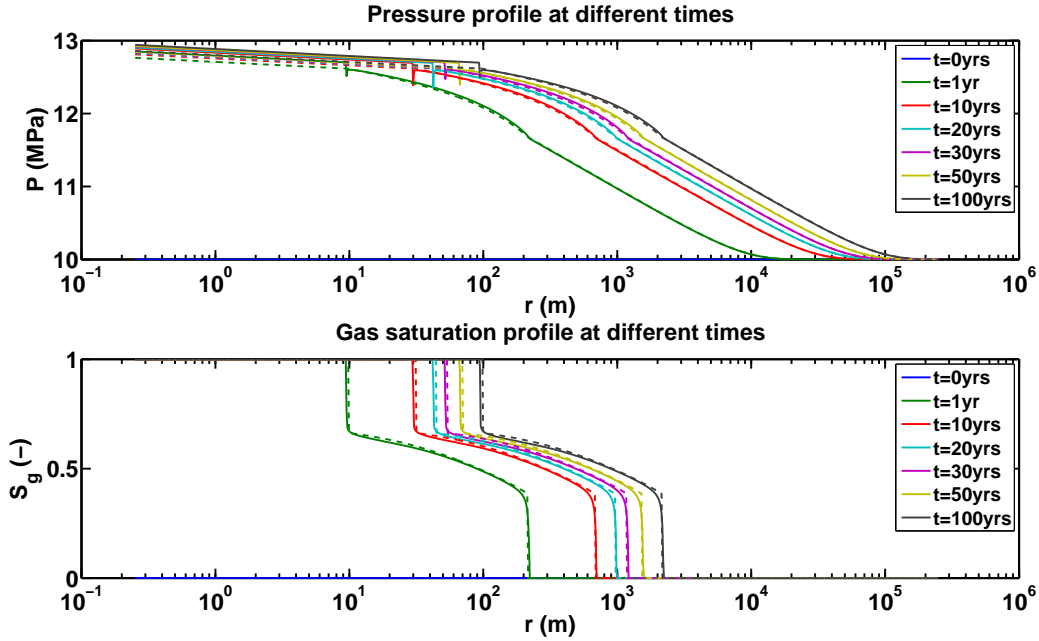


Figure 4.5: A graph to show the pressure and gas saturation output of the model for the initial parameters in Table 4.1, for the times shown in the legend, with the exception that P_{cd} is now equal to 10^7 Pa. The model was again run for 1000 points in space.

The graph at the top of Figure 4.4 shows the variation of global pressure with radial distance. It illustrates that the pressure is highest near the point of injection, and falls further along the formation, as well as showing that as time goes on and more CO_2 is injected into the formation, the pressure increases, as would be expected. As was the case with the graph that looked at gas saturation varying with distance, the numerical and analytical solutions compare very well. This is particularly true for the aqueous only region, in which the numerical and analytical solutions are almost indistinguishable. The solutions can be separated in the two phase region, in which the lines representing the pressure begin to curve slightly more, but are still very close. However, close to the boundary between the two phase and gaseous only regions, a small step can be seen in the MOL solution, while the analytical solution remains smooth. This is due to a significant difference in capillary pressure between the first and second points of the two phase region, and did not affect the analytical solution as it does not take capillary pressure into account. It should be noted that this difference in turn leads to a peak in the value of $\frac{\partial P_a}{\partial r}$. Using

equation (4.117), it can be seen that in this radial system, the flux of the aqueous phase can be found from Darcy's Law to be:

$$q_a = -\frac{kk_{ra}}{\mu_a} \frac{\partial P_a}{\partial r} \quad (4.126)$$

from which it follows that an increase in $\frac{\partial P_a}{\partial r}$ leads to a more negative value of q_a and hence increased backflow of the aqueous phase, i.e. counter-current imbibition.

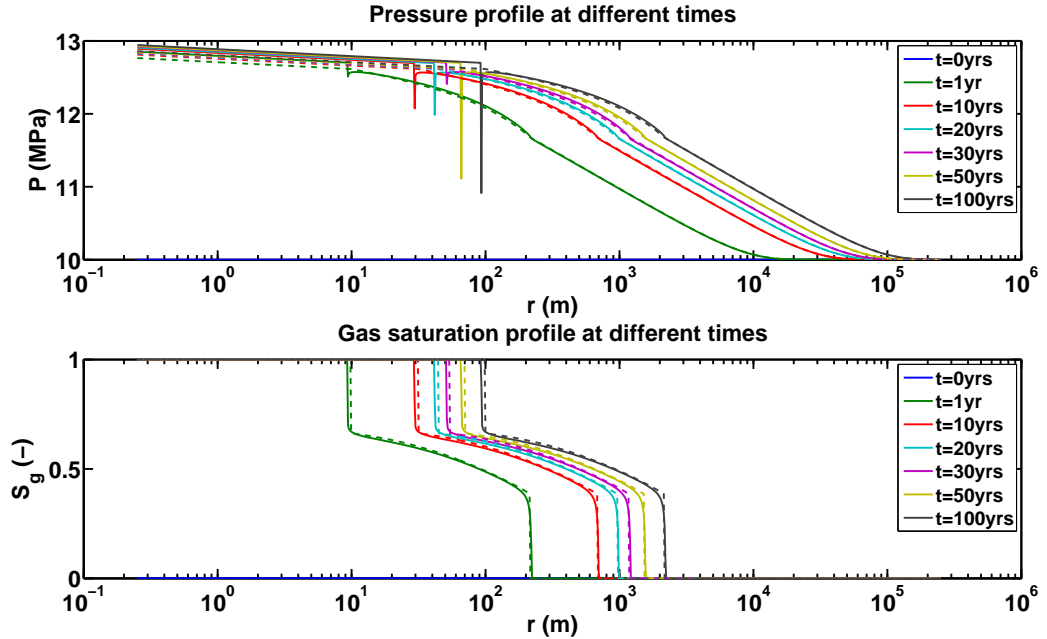


Figure 4.6: A graph to show the pressure and gas saturation output of the model for the initial parameters in Table 4.1, for the times shown in the legend, with the exception that P_{cd} is now equal to 10^8 Pa. The model was again run for 1000 points in space.

However, the change in pressure close to the boundary between the two phase and gaseous only regions becomes considerably more pronounced as the value of P_{cd} increases, as can be seen from Figures 4.5 and 4.6, which show the pressure and gas saturation outputs of the model for the same parameters as Figure 4.4, but taking the value of P_{cd} to be the higher values of 10^7 Pa and 10^8 Pa, respectively. For these higher values of P_{cd} , the change in pressure appears to be a dip that affects only one point in space. This suggests that the large difference in capillary pressure between the first and second points of the two phase region that seem to be the ultimate cause of the change in pressure may be at least in part due to a numerical instability within the code. The model will not run at all for a significant number of points when P_{cd} is set to 10^9 Pa, which is the value that Webb (2000) took to be the desired capillary pressure at zero aqueous saturation, because of this instability. Numerical instabilities similar to this are one of the main disadvantages of the use of a numerical model to simulate real-life processes.

The pressure and gas saturation outputs of the model when P_{cd} is set to 10^8 Pa, the value of P_{cd} for which the instability is at its most extreme, are also given in Figures 4.7 and 4.8 for 200 and 500 points in space, respectively. As would be expected, the numerical solutions are noticeably further away from the analytical solutions for the lower numbers of points in space. The dip in pressure between the gaseous only and two phase regions is still present for all times in both figures, and still seems to affect only one point in space, but by comparing Figure 4.6 to Figures 4.7 and 4.8 it can be seen that there does not appear to be a pattern between the size of the dip and the time that the model has been running for; the sizes of the dip vary for the different numbers of points. For example, in Figure 4.6 for 1000 points, it largely appears that the size of the dip in pressure grows for longer periods of time, whereas almost the opposite is true in Figure 4.7 when the model is run for 200 points. This only serves to emphasise that the dip is caused by an instability, and does not mean anything physically, as it seems almost impossible to predict how large the dip will be.

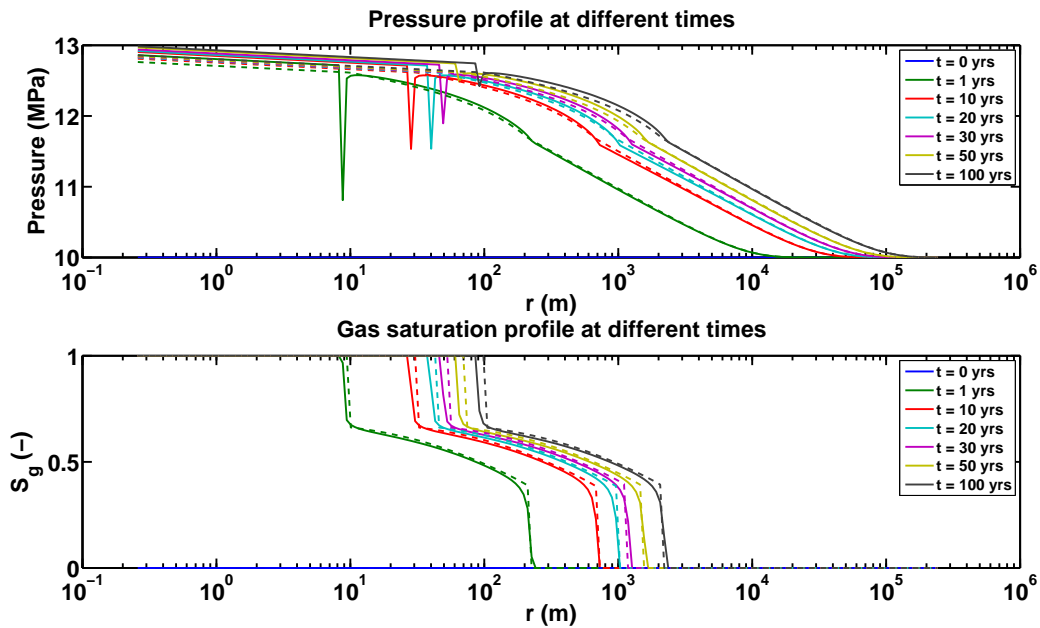


Figure 4.7: A graph to show the pressure and gas saturation output of the model for the initial parameters in Table 4.1, for the times shown in the legend, with P_{cd} equal to 10^8 Pa and for 200 points in space.

For comparison, the output of the model when no capillary pressure is included is given in Figure 4.9. It can be seen that the numerical instability is not present at all in this case, as there is no change in capillary pressure between the first two points of the two phase region due to the capillary pressure being set to zero at all points, and the solutions for both pressure and gas saturation are smooth curves that compare very well with the analytical solutions at all points.

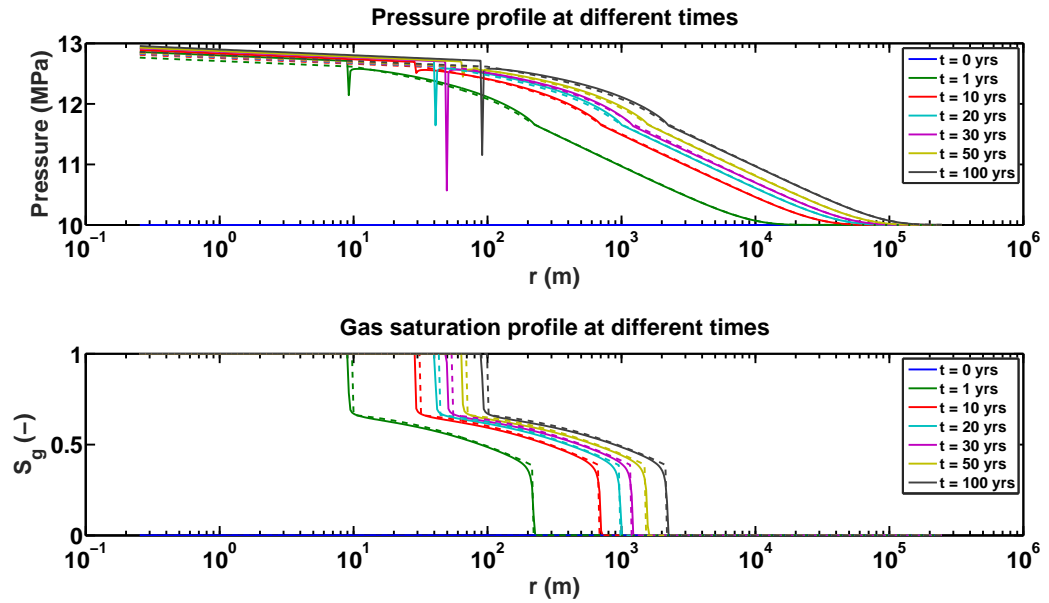


Figure 4.8: A graph to show the pressure and gas saturation output of the model for the initial parameters in Table 4.1, for the times shown in the legend, with P_{cd} equal to 10^8 Pa and for 500 points in space.

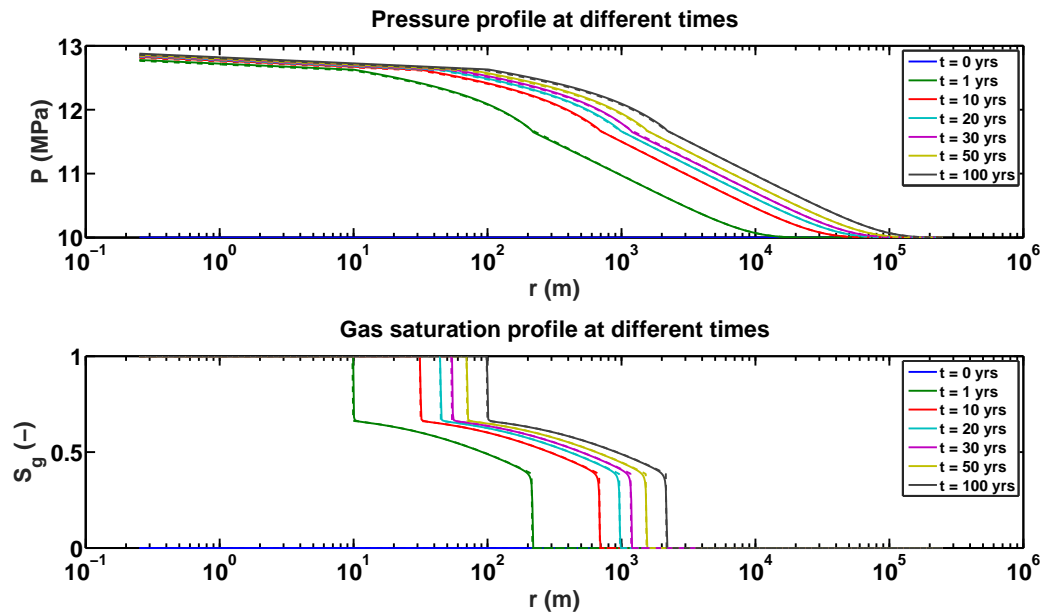


Figure 4.9: A graph to show the pressure and gas saturation output of the model for the initial parameters in Table 4.1, for the times shown in the legend, with the exception that the capillary pressure is now set to zero. The model was again run for 1000 points in space.

It should be noted that the output for gas saturation is not affected by the instability, and a smooth curve close to the analytical solution is produced regardless of the value of P_{cd} , or if the effects of capillary pressure are not included in the model.

Chapter 5

Method of Lines Solution for Compressible Three Component and Three Phase Flow with Capillary Pressure

This chapter extends the method of lines (MOL), as explained in the previous chapter for two phase and two components, to be applicable to a three component and three phase system, comprised of CO₂, water and salt and in which gaseous, aqueous and solid phases can be formed. The inclusion of the salt component and a solid phase means that this model has the capability to investigate the impact that capillary pressure has on counter-current imbibition and the amount of salt precipitation formed within the dry out zone, and how these are affected by varying the input parameters of the system. The principle of the MOL for a three component and three phase system is the same as previously described for two phases and two components: finite difference is used to discretise governing equations and form ordinary differential equations (ODEs) with respect to time, which are subsequently solved by the ODE solver `ode15s`. However, the involvement of three phases and three components means that it is necessary to have three primary dependent variables (PDVs) rather than two, and there are more possible combinations of phases that could be present at any one point in the system, meaning that it becomes considerably more complicated to find the required ODEs.

5.1 The Three Component, Three Phase System

The three component and three phase system consists of CO₂ (c), water (w) and salt (n), within gaseous (g), aqueous (a) and solid (s) phases, as was mentioned above. The assumptions of the model are similar to those for the two phase system, as illustrated in Figure 4.1: supercritical CO₂ is injected at a constant rate of M_0 [MT⁻¹] for time t [T] into an injection well with radius r_w [L], which is at the centre of a radially-symmetric reservoir with radial extent r_E [L]. In this case, however, the aqueous phase that initially fills the reservoir is not pure water, but also contains dissolved salt, meaning that the CO₂ is being injected into brine. Again, the permeability of the reservoir is assumed to be horizontally isotropic, and the vertical permeability to be so much smaller than the horizontal value that the effects of gravity can be considered to be negligible, such that fluid flow can be treated as one-dimensional and radially symmetric. The system is assumed to be isothermal, and the effects of both capillary pressure and volume change on mixing are included.

As was also the case when only two phases were involved, the radial axis is discretised into a block centred grid in which the points are spaced logarithmically, as shown by Figure 4.2. This means that the nodes are more closely spaced in the dry out zone, the region in which salt will precipitate, than in the regions further away from the point of injection, such that the model will give an accurate illustration of the amount of salt precipitation that has taken place within the system for fewer nodes than would be needed if a linear discretisation had been used (Goudarzi et al., 2016).

5.2 Primary Dependent Variables (PDVs)

Three PDVs are required for this system, and those used in this model are the global pressure, P [ML⁻¹T⁻²], the mass fraction of CO₂, z_c [-], and the mass fraction of water, z_w [-]. These parameters were chosen due to the global pressure being defined regardless of which phases are present, and the independence of z_i from pressure. The ODE solver therefore requires expressions for $\frac{\partial z_c}{\partial t}$, $\frac{\partial z_w}{\partial t}$ and $\frac{\partial P}{\partial t}$, in order to find values for the PDVs at all points in time and space.

5.3 Phases Present

The first step to finding the appropriate expressions for the derivatives of the PDVs with respect to time is to define the possible phase combinations that can occur, and subsequently determine which phases are present at different points in space and time. Within a three phase and three component system, either one, two or three different phases could be present at each point. In order to find which phase combination is at a particular point, it is necessary to use the governing equations to define conditions for when certain phases are either present or missing.

5.3.1 No Gaseous Phase

Recall from equations (4.2) to (4.4) that:

$$z_i = \frac{G_i}{F} \quad (5.1)$$

where

$$G_i = \phi \sum_{j=1}^{N_p} \rho_j X_{ij} S_j \quad (5.2)$$

and

$$F = \sum_{i=1}^{N_c} G_i = \phi \sum_{j=1}^{N_p} \rho_j S_j \quad (5.3)$$

Therefore, when no gas phase is present:

$$z_c = \frac{\rho_a X_{ca} S_a}{\rho_a S_a + \rho_s S_s} \quad (5.4)$$

and

$$z_n = \frac{\rho_a X_{na} S_a + \rho_s S_s}{\rho_a S_a + \rho_s S_s} \quad (5.5)$$

Note that it is not necessarily the case that both the aqueous and the solid phases are present: the condition that this subsection will derive is based only on the absence of the gaseous phase, and will hold regardless of whether both an aqueous and solid phase are present, or just one of them.

As there is no gaseous phase at this point, it must be that $S_s = 1 - S_a$. This can be substituted into equation (5.5) to give:

$$z_n = \frac{\rho_a X_{na} S_a + \rho_s (1 - S_a)}{\rho_a S_a + \rho_s (1 - S_a)} \quad (5.6)$$

which can subsequently be rearranged to show that:

$$S_a = \frac{\rho_s(1 - z_n)}{\rho_s(1 - z_n) + \rho_a(z_n - X_{na})} \quad (5.7)$$

It follows from this that:

$$S_s = 1 - S_a = \frac{\rho_a(z_n - X_{na})}{\rho_s(1 - z_n) + \rho_a(z_n - X_{na})} \quad (5.8)$$

The expressions for the phase saturations, equations (5.7) and (5.8), can then be substituted into the expression for z_c under these conditions, equation (5.4), which will reduce to:

$$z_c = \frac{X_{ca}(1 - z_n)}{1 - X_{na}} \quad (5.9)$$

As was explained in Section 2.3, the equilibrium mass fractions of a component i in a phase j , x_{ij} [-], represent the maximum solubility of component i in phase j . Therefore, it must be that, at points at which no gaseous phase exists, the mass fraction of CO₂ in the aqueous phase, X_{ca} [-], is less than the equilibrium mass fraction, x_{ca} [-]. If this were not the case, a separate gaseous phase would have formed to accommodate the additional CO₂, as no CO₂ is able to dissolve into the aqueous phase once it has reached its maximum solubility of x_{ca} . Substituting $X_{ca} \leq x_{ca}$ into equation (5.9):

$$z_c \leq \frac{x_{ca}(1 - z_n)}{1 - X_{na}} \quad (5.10)$$

As the equilibrium mass fractions represent the maximum solubility of a component in a phase, it must also be that the maximum value of X_{na} [-] is x_{na} [-]. This is the case regardless of whether or not a solid phase is present at this point in the system, as whether or not there is additional salt that could not dissolve into the aqueous phase and has thus formed a separate solid phase, the mass fraction of salt in the aqueous phase would still not go beyond the solubility limit, x_{na} . Hence:

$$\frac{x_{ca}(1 - z_n)}{1 - X_{na}} \leq \frac{x_{ca}(1 - z_n)}{1 - x_{na}} \quad (5.11)$$

and so the condition for there being no gaseous phase present at a particular point in the formation, relating the mass fractions of a component, z_i , and the equilibrium mass fractions of a component in a particular phase, x_{ij} , can be given as:

$$z_c \leq \frac{x_{ca}(1 - z_n)}{1 - x_{na}} \quad (5.12)$$

Note that z_c and z_w , as PDVs of the system, are found by the ODE solver, ode15s. Recall that:

$$\sum_{i=1}^{N_p} z_i = 1 \quad (5.13)$$

which means that z_n can then be easily defined as $z_n = 1 - z_c - z_w$. The equilibrium mass fractions for CO₂ and water are found using work by [Spycher et al. \(2003\)](#) and [Spycher and Pruess \(2005\)](#), while the value of x_{na} comes from an equation by [Potter et al. \(1977\)](#).

5.3.2 No Aqueous Phase

If there is no aqueous phase, then:

$$z_c = \frac{\rho_g X_{cg} S_g}{\rho_g S_g + \rho_s S_s} \quad (5.14)$$

and

$$z_n = \frac{\rho_s S_s}{\rho_g S_g + \rho_s S_s} \quad (5.15)$$

Due to the absence of an aqueous phase, it must be that: $S_s = 1 - S_g$, which can be substituted into equation (5.15) and rearranged to give:

$$S_g = \frac{\rho_s(1 - z_n)}{\rho_s(1 - z_n) + \rho_g z_n} \quad (5.16)$$

from which it follows that:

$$S_s = 1 - S_g = \frac{\rho_g z_n}{\rho_s(1 - z_n) + \rho_g z_n} \quad (5.17)$$

If these saturation expressions, equations (5.16) and (5.17), are substituted into equation (5.14), we obtain:

$$z_c = X_{cg}(1 - z_n) \quad (5.18)$$

At a point in the formation at which there is no aqueous phase, it must be that $X_{wg} \leq x_{wg}$, because there is no aqueous phase to hold any additional water that cannot evaporate into the gaseous phase. As $X_{wg} = 1 - X_{cg}$ and $x_{wg} = 1 - x_{cg}$, it follows that $X_{cg} \geq x_{cg}$, and hence the condition for there to be no aqueous phase at a particular point can be described as:

$$z_c \geq x_{cg}(1 - z_n) \quad (5.19)$$

5.3.3 Both Gaseous and Aqueous Phases Present

It follows from equation (5.12) and equation (5.19) that if both a gaseous and an aqueous phase are present at a point in the system, and hence neither of the two conditions previously stipulated apply, then:

$$\frac{x_{ca}(1 - z_n)}{1 - x_{na}} < z_c < x_{cg}(1 - z_n) \quad (5.20)$$

It should be noted that this condition in z_c holds regardless of whether or not a solid phase is present.

5.3.4 Presence or Absence of a Solid Phase

While the presence or absence of the gaseous and aqueous phases can be determined purely by the value of z_c , the question of whether or not there is a solid phase requires analysis of the values of both z_c and z_n . The value of z_c can be used to determine whether gaseous and aqueous phases are present, which can in turn simplify the condition in z_n that is required to look into the presence or absence of a solid phase.

Firstly, if no aqueous phase is present, then any salt must be in the solid phase. Therefore, if there is no aqueous phase, and hence $z_c \geq x_{cg}(1 - z_n)$, a solid phase must be present if $z_n > 0$, and absent if $z_n = 0$.

However, if an aqueous phase is present it becomes more complicated to determine the presence or absence of a solid phase. If there is no solid phase, then:

$$z_c = \frac{\rho_g X_{cg} S_g + \rho_a X_{ca} S_a}{\rho_g S_g + \rho_a S_a} \quad (5.21)$$

and

$$z_n = \frac{\rho_a X_{na} S_a}{\rho_g S_g + \rho_a S_a} \quad (5.22)$$

As the only phases that could be present are gaseous and aqueous, $S_g = 1 - S_a$. Substituting this into equation (5.21):

$$z_c = \frac{\rho_g X_{cg}(1 - S_a) + \rho_a X_{ca} S_a}{\rho_g(1 - S_a) + \rho_a S_a} \quad (5.23)$$

which can be rearranged to give:

$$S_a = \frac{\rho_g(X_{cg} - z_c)}{\rho_g(X_{cg} - z_c) + \rho_a(z_c - X_{ca})} \quad (5.24)$$

and hence:

$$S_g = 1 - S_a = \frac{\rho_a(z_c - X_{ca})}{\rho_g(X_{cg} - z_c) + \rho_a(z_c - X_{ca})} \quad (5.25)$$

These phase saturations can be substituted into equation (5.22) to show that, when there is no solid phase:

$$z_n = \frac{X_{na}(X_{cg} - z_c)}{X_{cg} - X_{ca}} \quad (5.26)$$

If an aqueous phase is present with no solid phase, then it must be the case that $X_{na} \leq x_{na}$, because no solid phase has formed to accommodate any additional salt, meaning that the amount of salt in the system cannot be above the maximum solubility of the aqueous phase. Therefore, substituting this into equation (5.26), as well as using the opposite of equation (5.19) to define when an aqueous phase is present rather than when it is absent, gives the conditions for an aqueous phase being present but a solid phase being absent as:

$$z_c < x_{cg}(1 - z_n) \quad \text{and} \quad z_n \leq \frac{x_{na}(X_{cg} - z_c)}{X_{cg} - X_{ca}} \quad (5.27)$$

and therefore both an aqueous and solid phase will be present if:

$$z_c < x_{cg}(1 - z_n) \quad \text{and} \quad z_n > \frac{x_{na}(X_{cg} - z_c)}{X_{cg} - X_{ca}} \quad (5.28)$$

It should be noted that these conditions hold whether or not a gaseous phase is present. However, one issue is that we have not yet defined the values of X_{cg} and X_{ca} .

5.4 X_{ij} Values

The mass fractions of the component i in the phase j , X_{ij} , are piecewise functions that will have different values depending on which phases are present.

X_{cg}

The expressions for X_{cg} are unaffected by the presence of a solid phase, and are based solely on whether gaseous and aqueous phases are present. Now that the boundary conditions for the appearance and disappearance of the gaseous and aqueous phases have been defined, it is also possible to find the values of X_{cg} .

If no gaseous phase is present, then there can be no CO_2 in a gaseous phase, so $X_{cg} = 0$. If both a gaseous and an aqueous phase are present, the two phases that CO_2 can appear

in, then X_{cg} will be at its equilibrium value, x_{cg} . When there is no aqueous phase, it was found from equation (5.18) that:

$$z_c = X_{cg}(1 - z_n) \quad (5.29)$$

This can be rearranged to show that, when no aqueous phase is present:

$$X_{cg} = \frac{z_c}{1 - z_n} \quad (5.30)$$

Therefore, using the phase boundaries in equations (5.12), (5.19) and (5.20), X_{cg} can be summarised as:

$$X_{cg} = \begin{cases} 0, & z_c \leq \frac{x_{ca}(1 - z_n)}{1 - x_{na}} \\ x_{cg}, & \frac{x_{ca}(1 - z_n)}{1 - x_{na}} < z_c < x_{cg}(1 - z_n) \\ \frac{z_c}{1 - z_n}, & z_c \geq x_{cg}(1 - z_n) \end{cases} \quad (5.31)$$

X_{ca}

The values of X_{ca} can be found in a similar way. Again, when no aqueous phase is present, $X_{ca} = 0$, and X_{ca} must be at its equilibrium value, x_{ca} , when there are both gaseous and aqueous phases. It was seen from equation (5.9) that, when no gaseous phase is present:

$$z_c = \frac{X_{ca}(1 - z_n)}{1 - X_{na}} \quad (5.32)$$

which can be rearranged to give:

$$X_{ca} = \frac{z_c(1 - X_{na})}{1 - z_n} \quad (5.33)$$

such that X_{ca} can be summarised as:

$$X_{ca} = \begin{cases} \frac{z_c(1 - X_{na})}{1 - z_n}, & z_c \leq \frac{x_{ca}(1 - z_n)}{1 - x_{na}} \\ x_{ca}, & \frac{x_{ca}(1 - z_n)}{1 - x_{na}} < z_c < x_{cg}(1 - z_n) \\ 0, & z_c \geq x_{cg}(1 - z_n) \end{cases} \quad (5.34)$$

However, an issue with this definition is that X_{na} has not yet been defined, and its values will vary depending on whether or not a solid phase is present, rather than just gaseous

and aqueous. The expression for X_{ca} that involves X_{na} is for when an aqueous phase is present, and no gaseous phase, so it is necessary to find and substitute into the expression the values of X_{na} for when both an aqueous and a solid phase are present, and when there is solely an aqueous phase.

If there are both an aqueous and a solid phase at a particular point, then it must be that X_{na} is at its equilibrium value, x_{na} , because both phases that the salt can appear in are present. It follows that, for this phase combination:

$$X_{ca} = \frac{z_c(1 - x_{na})}{1 - z_n} \quad (5.35)$$

If only an aqueous phase is present, then:

$$z_n = \frac{\rho_a X_{na} S_a}{\rho_a S_a} = X_{na} \quad (5.36)$$

and $X_{na} = z_n$ can be substituted into the expression for X_{ca} to give:

$$X_{ca} = \frac{z_c(1 - z_n)}{1 - z_n} = z_c \quad (5.37)$$

In order to differentiate between $X_{ca} = z_c$, which occurs when there is only an aqueous phase at a particular point, and $X_{ca} = \frac{z_c(1-x_{na})}{1-z_n}$, which is the case when both an aqueous and a solid phase are present, it is necessary to define conditions in z_c and z_n that differentiate between solely an aqueous phase, and an aqueous and solid phase. It was found in equation (5.27) that the necessary conditions for an aqueous phase but no solid are:

$$z_c < x_{cg}(1 - z_n) \quad \text{and} \quad z_n \leq \frac{x_{na}(X_{cg} - z_c)}{X_{cg} - X_{ca}} \quad (5.38)$$

However, these conditions can be reduced further. In this case, there is no gaseous phase, and only an aqueous phase, meaning that $X_{cg} = 0$ and $X_{ca} = z_c$. Substituting this in, as well as using equation (5.12) as the condition for z_c for no gaseous phase, the condition for solely an aqueous phase becomes:

$$z_c \leq \frac{x_{ca}(1 - z_n)}{1 - x_{na}} \quad \text{and} \quad z_n \leq x_{na} \quad (5.39)$$

The complete definition of X_{ca} can therefore be understood to be:

$$X_{ca} = \begin{cases} z_c, & z_c \leq \frac{x_{ca}(1-z_n)}{1-x_{na}}, & z_n \leq x_{na} \\ \frac{z_c(1-x_{na})}{1-z_n}, & z_c \leq \frac{x_{ca}(1-z_n)}{1-x_{na}}, & z_n > x_{na} \\ x_{ca}, & \frac{x_{ca}(1-z_n)}{1-x_{na}} < z_c < x_{cg}(1-z_n) \\ 0, & z_c \geq x_{cg}(1-z_n) \end{cases} \quad (5.40)$$

X_{na}

As has been previously explained, if the phase j is not present, then $X_{ij} = 0$. This means that if no aqueous phase is present, then it must be that $X_{na} = 0$. As has also been previously explained, if both aqueous and solid phases are present, regardless of whether or not there is a gaseous phase, then X_{na} must be at its equilibrium value, x_{na} . It was found from equation (5.26) that, when an aqueous phase is present but no solid phase:

$$z_n = \frac{X_{na}(X_{cg} - z_c)}{X_{cg} - X_{ca}} \quad (5.41)$$

This can be rearranged to give the value of X_{na} for this phase combination as:

$$X_{na} = \frac{z_n(X_{cg} - X_{ca})}{X_{cg} - z_c} \quad (5.42)$$

It should also be noted that, when only an aqueous phase is present with no gaseous phase, this expression reduces to $X_{na} = z_n$.

The conditions from equation (5.27) and equation (5.28) can be used to separate the values of X_{na} when a solid phase is present alongside the aqueous phase, and when there is no solid phase, such that the full range of values for X_{na} can be understood to be:

$$X_{na} = \begin{cases} \frac{z_n(X_{cg} - X_{ca})}{X_{cg} - z_c}, & z_c < x_{cg}(1-z_n), & z_n \leq \frac{x_{na}(X_{cg} - z_c)}{X_{cg} - X_{ca}} \\ x_{na}, & z_c < x_{cg}(1-z_n), & z_n > \frac{x_{na}(X_{cg} - z_c)}{X_{cg} - X_{ca}} \\ 0, & z_c \geq x_{cg}(1-z_n), & z_n \geq 0 \end{cases} \quad (5.43)$$

5.5 Phase Saturation Values

The values of phase saturations will again be piecewise functions that vary depending on which phases are present. In calculating the boundaries at which certain phases appear and disappear, some of the phase saturation values for certain combinations of phases have already been found. This section will give a full description of the phase saturation values for each phase combination, and how they are derived.

5.5.1 Solid Saturation (S_s)

No Solid Phase

If no solid phase is present, then it must be that $S_s = 0$. Using equation (5.26), it can be seen that this will be the case when $z_n \leq \frac{X_{na}(X_{cg} - z_c)}{X_{cg} - X_{ca}}$, regardless of the value of z_c .

No Gaseous Phase (Aqueous and Solid Only)

When calculating the phase boundary in z_c for no gaseous phase being present in Section 5.3.1, it was found in equation (5.8) that, when no gas is present:

$$S_s = \frac{\rho_a(z_n - X_{na})}{\rho_s(1 - z_n) + \rho_a(z_n - X_{na})} \quad (5.44)$$

If both an aqueous and a solid phase are present, then, using equation (5.43), it must be that $X_{na} = x_{na}$. Therefore:

$$S_s = \frac{\rho_a(z_n - x_{na})}{\rho_s(1 - z_n) + \rho_a(z_n - x_{na})} \quad (5.45)$$

or, written in an alternative way:

$$S_s = \left[1 + \frac{\rho_s(1 - z_n)}{\rho_a(z_n - x_{na})} \right]^{-1} \quad (5.46)$$

As no gaseous phase is present, it must be that the boundary in z_c for this condition is equation (5.12): $z_c \leq \frac{x_{ca}(1 - z_n)}{1 - x_{na}}$. As there is an aqueous phase, the same method as was used to derive the conditions in equation (5.39) can be used, leading to the conclusion that, in this case, there must be a solid phase if $z_n > x_{na}$.

No Aqueous Phase (Gaseous and Solid Only)

In a similar way to the expressions found when determining the phase boundary for no gaseous phase being present, when calculating the phase boundary in z_c for no aqueous phase being present in Section 5.3.2, an expression was defined to represent the solid saturation when there is no aqueous phase in equation (5.17). This was:

$$S_s = \frac{\rho_g z_n}{\rho_s(1 - z_n) + \rho_g z_n} \quad (5.47)$$

It can also be written as:

$$S_s = \left[1 + \frac{\rho_s(1 - z_n)}{\rho_g z_n} \right]^{-1} \quad (5.48)$$

This expression will represent the solid saturation when there is no aqueous phase, and so, from equation (5.19), when $z_c \geq x_{cg}(1 - z_n)$. As there is no aqueous phase, any salt that is present must be in a solid phase, so the only condition necessary to be on z_n is $z_n > 0$.

All Three Phases Present (Gaseous, Aqueous and Solid)

If all three phases are present, then all of the mass fractions of a component i in a phase j , X_{ij} , must be at their equilibrium values, x_{ij} . Therefore:

$$z_c = \frac{x_{cg}\rho_g S_g + x_{ca}\rho_a S_a}{\rho_g S_g + \rho_a S_a + \rho_s S_s} \quad (5.49)$$

and

$$z_n = \frac{x_{na}\rho_a S_a + \rho_s S_s}{\rho_g S_g + \rho_a S_a + \rho_s S_s} \quad (5.50)$$

Due to the presence of all three phases, it must be that $S_g = 1 - S_a - S_s$. Substituting this into equation (5.49):

$$z_c = \frac{x_{cg}\rho_g(1 - S_a - S_s) + x_{ca}\rho_a S_a}{\rho_g(1 - S_a - S_s) + \rho_a S_a + \rho_s S_s} \quad (5.51)$$

This can be rearranged to show that S_a can be written in terms of S_s and z_c , as well as the phase densities and equilibrium mass fractions, to be:

$$S_a = \frac{S_s(z_c\rho_g - x_{cg}\rho_g - z_c\rho_s) + x_{cg}\rho_g - z_c\rho_g}{\rho_a(z_c - x_{ca}) + \rho_g(x_{cg} - z_c)} \quad (5.52)$$

The fact that $S_g = 1 - S_a - S_s$ can also be substituted into equation (5.50). This gives:

$$z_n = \frac{x_{na}\rho_a S_a + \rho_s S_s}{\rho_g(1 - S_a - S_s) + \rho_a S_a + \rho_s S_s} \quad (5.53)$$

which can be rearranged to give an alternative expression for S_a , this time in terms of z_n , as well as the solid saturation, the phase densities and the equilibrium mass fractions:

$$S_a = \frac{S_s(\rho_s + z_n\rho_g - z_n\rho_s) - z_n\rho_g}{\rho_a(z_n - x_{na}) - z_n\rho_g} \quad (5.54)$$

The two expressions for S_a must be equal. This means that, using equations (5.52) and (5.54):

$$\frac{S_s(z_c\rho_g - x_{cg}\rho_g - z_c\rho_s) + x_{cg}\rho_g - z_c\rho_g}{\rho_a(z_c - x_{ca}) + \rho_g(x_{cg} - z_c)} = \frac{S_s(\rho_s + z_n\rho_g - z_n\rho_s) - z_n\rho_g}{\rho_a(z_n - x_{na}) - z_n\rho_g} \quad (5.55)$$

which, when rearranged, gives an expression for S_s when all three phases are present:

$$S_s = \frac{\rho_g\rho_a[z_n(x_{cg} - x_{ca}) - x_{na}(x_{cg} - z_c)]}{\rho_s\rho_a[z_c(1 - x_{na}) - x_{ca}(1 - z_n)] - \rho_g\rho_s[z_c - x_{cg}(1 - z_n)] + \rho_g\rho_a[z_n(x_{cg} - x_{ca}) - x_{na}(x_{cg} - z_c)]} \quad (5.56)$$

This can be alternatively written as:

$$S_s = \left[1 + \frac{\rho_s\rho_a[z_c(1 - x_{na}) - x_{ca}(1 - z_n)] - \rho_g\rho_s[z_c - x_{cg}(1 - z_n)]}{\rho_g\rho_a[z_n(x_{cg} - x_{ca}) - x_{na}(x_{cg} - z_c)]} \right]^{-1} \quad (5.57)$$

As was found in equation (5.20), for both the gaseous and aqueous phases to be present, it must be that $\frac{x_{ca}(1-z_n)}{1-x_{na}} < z_c < x_{cg}(1-z_n)$. Using equation (5.28), the condition in z_n for both an aqueous and a solid phase being present is $z_n > \frac{x_{na}(X_{cg}-z_c)}{X_{cg}-X_{ca}}$. However, as we know that in this case there is also a gaseous phase, and all the X_{ij} expressions can be assumed to be at their equilibrium values, this condition can be simplified to $z_n > \frac{x_{na}(x_{cg}-z_c)}{x_{cg}-x_{ca}}$.

Overall Expression for S_s

Putting together all of the above, the overall expression for S_s can be given as:

$$S_s = \begin{cases} 0, & z_c \geq 0, & z_n \leq \frac{X_{na}(X_{cg}-z_c)}{X_{cg}-X_{ca}} \\ \left[1 + \frac{\rho_s(1-z_n)}{\rho_a(z_n - x_{na})} \right]^{-1}, & z_c \leq \frac{x_{ca}(1-z_n)}{1-x_{na}}, & z_n > x_{na} \\ \left[1 + \frac{\rho_s\rho_a[z_c(1-x_{na}) - x_{ca}(1-z_n)] - \rho_g\rho_s[z_c - x_{cg}(1-z_n)]}{\rho_g\rho_a[z_n(x_{cg}-x_{ca}) - x_{na}(x_{cg}-z_c)]} \right]^{-1}, & \frac{x_{ca}(1-z_n)}{1-x_{na}} < z_c < x_{cg}(1-z_n), & z_n > \frac{x_{na}(x_{cg}-z_c)}{x_{cg}-x_{ca}} \\ \left[1 + \frac{\rho_s(1-z_n)}{\rho_g z_n} \right]^{-1}, & z_c \geq x_{cg}(1-z_n), & z_n > 0 \end{cases} \quad (5.58)$$

5.5.2 Aqueous Saturation (S_a)

No Aqueous Phase

If no aqueous phase is present at a particular point, then $S_a = 0$. This will be the case if, as found in equation (5.19), $z_c \geq x_{cg}(1 - z_n)$, regardless of the value of z_n .

Aqueous Phase Only (No Gaseous or Solid Phases)

If only an aqueous phase is present, then it must be that $S_a = 1$. The conditions for this to be the case can be given by $z_c \leq \frac{x_{ca}(1-z_n)}{1-x_{na}}$, which is the inequality from equation (5.12) that eliminates the gaseous phase, and $z_n \leq x_{na}$, which, as can be seen from equation (5.39), is the condition for the absence of a solid phase while an aqueous phase is present.

No Gaseous Phase (Aqueous and Solid Phases Only)

In the case of no gaseous phase, it must be that $S_a = 1 - S_s$, using the expression for S_s as calculated in equation (5.46), when there were also only aqueous and solid phases present. The conditions for this to be the case are also as they were described for equation (5.46): $z_c \leq \frac{x_{ca}(1-z_n)}{1-x_{na}}$ and $z_n > x_{na}$.

No Solid Phase (Gaseous and Aqueous Phases Present)

When calculating the boundary for a solid phase being absent in Section 5.3.4, it was found by equation (5.24) that, when only aqueous and gaseous phases are present, the aqueous saturation can be expressed as:

$$S_a = \frac{\rho_g(X_{cg} - z_c)}{\rho_g(X_{cg} - z_c) + \rho_a(z_c - X_{ca})} \quad (5.59)$$

As CO_2 can only be found in either the gaseous or the aqueous phases, both of which are present, X_{cg} and X_{ca} must be at their equilibrium values of x_{cg} and x_{ca} , respectively. Therefore:

$$S_a = \frac{\rho_g(x_{cg} - z_c)}{\rho_g(x_{cg} - z_c) + \rho_a(z_c - x_{ca})} \quad (5.60)$$

or, alternatively:

$$S_a = \left[1 + \frac{\rho_a(z_c - x_{ca})}{\rho_g(x_{cg} - z_c)} \right]^{-1} \quad (5.61)$$

The conditions for both gaseous and aqueous phases being present are given by equation (5.20), such that $\frac{x_{ca}(1-z_n)}{1-x_{na}} < z_c < x_{cg}(1-z_n)$. Using equation (5.27) and the fact that X_{cg} and X_{ca} can be understood to be at their equilibrium values, the condition to ensure that no solid phase is also present is $z_n \leq \frac{x_{na}(x_{cg}-z_c)}{x_{cg}-x_{ca}}$.

All Three Phases Present (Gaseous, Aqueous and Solid)

When finding the solid saturation for the case in which all three phases are present, two expressions were found for S_a for this phase combination that depend on S_s . As S_s has already been defined for this region, either equation (5.52) or equation (5.54) are adequate definitions for S_a when all three phases are present, with S_s being taken as is given in equation (5.57). The conditions needed for three phases to be present were also found when calculating S_s : $\frac{x_{ca}(1-z_n)}{1-x_{na}} < z_c < x_{cg}(1-z_n)$ and $z_n > \frac{x_{na}(x_{cg}-z_c)}{x_{cg}-x_{ca}}$.

Overall Expression for S_a

Putting together S_a as defined for the various different phase combinations, an overall expression for S_a can be given as:

$$S_a = \begin{cases} 0, & z_c \geq x_{cg}(1-z_n), & z_n \geq 0, \\ 1, & z_c \leq \frac{x_{ca}(1-z_n)}{1-x_{na}}, & z_n \leq x_{na}, \\ \left[1 + \frac{\rho_a(z_c - x_{ca})}{\rho_g(x_{cg} - z_c)} \right]^{-1}, & \frac{x_{ca}(1-z_n)}{1-x_{na}} < z_c < x_{cg}(1-z_n), & z_n \leq \frac{x_{na}(x_{cg}-z_c)}{x_{cg}-x_{ca}} \\ 1 - S_s, & z_c \leq \frac{x_{ca}(1-z_n)}{1-x_{na}}, & z_n > x_{na} \\ \frac{S_s(\rho_s + z_n\rho_g - z_n\rho_s) - z_n\rho_g}{\rho_a(z_n - x_{na}) - z_n\rho_g}, & \frac{x_{ca}(1-z_n)}{1-x_{na}} < z_c < x_{cg}(1-z_n), & z_n > \frac{x_{na}(x_{cg}-z_c)}{x_{cg}-x_{ca}} \end{cases} \quad (5.62)$$

5.5.3 Gaseous Saturation (S_g)

As the solid and aqueous saturations have already been defined for all possible phase combinations, the gaseous saturation, S_g , can be found by using $S_g = 1 - S_a - S_s$ at all points. However, this can be simplified slightly depending on which phases are present. When there is no gaseous phase, $S_g = 0$, regardless of which other phases are present, and when gas is the only phase present, $S_g = 1$. If gas is present alongside only one of the other phases (i.e. either an aqueous or a solid phase is absent), then $S_g = 1 - S_h$, where the subscript h represents the other phase that is present (either the aqueous or the solid phase). Therefore, the gaseous saturation can be defined as:

$$S_g = \begin{cases} 0, & z_c \leq \frac{x_{ca}(1 - z_n)}{1 - x_{na}}, & z_n \geq 0, \\ 1, & z_c \geq x_{cg}(1 - z_n), & z_n = 0, \\ 1 - S_a, & \frac{x_{ca}(1 - z_n)}{1 - x_{na}} < z_c < x_{cg}(1 - z_n), & z_n \leq \frac{x_{na}(x_{cg} - z_c)}{x_{cg} - x_{ca}} \\ 1 - S_s, & z_c \geq x_{cg}(1 - z_n), & z_n > 0 \\ 1 - S_a - S_s, & \frac{x_{ca}(1 - z_n)}{1 - x_{na}} < z_c < x_{cg}(1 - z_n), & z_n > \frac{x_{na}(x_{cg} - z_c)}{x_{cg} - x_{ca}} \end{cases} \quad (5.63)$$

5.6 Finding Expressions for $\frac{\partial z_c}{\partial t}$, $\frac{\partial z_w}{\partial t}$ and $\frac{\partial P}{\partial t}$

As was explained in Section 5.2, it is necessary to give the ODE solver expressions for the derivatives of all of the PDVs (z_c , z_w and P) with respect to time in order to find their values at all points in space and time.

5.6.1 Expressions for $\frac{\partial z_c}{\partial t}$ and $\frac{\partial z_w}{\partial t}$

Again, recall from equations (4.2) to (4.4) that the mass fraction of component i , z_i [-], is given by:

$$z_i = \frac{G_i}{F} \quad (5.64)$$

where:

$$G_i = \phi \sum_{j=1}^{N_p} \rho_j X_{ij} S_j \quad (5.65)$$

and F [ML^{-3}], the total mass of all components within a given volume of fluid mixture, can be given by:

$$F = \sum_{i=1}^{N_c} G_i = \phi \sum_{j=1}^{N_p} \rho_j S_j \quad (5.66)$$

As was illustrated in equations (4.13) to (4.15), expressions for dz_i can be found by using quotient rule on equation (5.64), such that:

$$dz_i = \frac{F dG_i - G_i dF}{F^2} \quad (5.67)$$

or equivalently:

$$dz_i = \frac{1}{F} (dG_i - z_i dF) \quad (5.68)$$

From this, the partial derivative of z_i with respect to time is:

$$\frac{\partial z_i}{\partial t} = \frac{1}{F} \left(\frac{\partial G_i}{\partial t} - z_i \frac{\partial F}{\partial t} \right) \quad (5.69)$$

meaning that $\frac{\partial z_c}{\partial t}$ and $\frac{\partial z_w}{\partial t}$ can be found from:

$$\boxed{\frac{\partial z_c}{\partial t} = \frac{1}{F} \left(\frac{\partial G_c}{\partial t} - z_c \frac{\partial F}{\partial t} \right)} \quad (5.70)$$

and

$$\boxed{\frac{\partial z_w}{\partial t} = \frac{1}{F} \left(\frac{\partial G_w}{\partial t} - z_w \frac{\partial F}{\partial t} \right)} \quad (5.71)$$

respectively.

Within these equations, $\frac{\partial G_i}{\partial t}$ can be defined, as it was in equation (4.18) as:

$$\frac{\partial G_i}{\partial t} = -\frac{1}{r} \frac{\partial(rH_i)}{\partial r} \quad (5.72)$$

where:

$$H_i = \sum_{j=1}^{N_p} \rho_j X_{ij} q_j \quad (5.73)$$

where q_j [LT^{-1}] is the volumetric flux of phase j and N_p is the number of phases.

Subsequently, it can be seen that:

$$\frac{\partial F}{\partial t} = \sum_{i=1}^{N_c} \frac{\partial G_i}{\partial t} = -\frac{1}{r} \sum_{i=1}^{N_c} \frac{\partial(rH_i)}{\partial r} \quad (5.74)$$

where N_c is the number of components.

The derivatives on the right hand side of equation (5.72) and equation (5.74) are all with respect to radial distance. They can therefore be approximated by finite difference, which

was fully explained in Section 3.3.1. More details on using upwinding to ensure that the approximations are given at the correct points in space were given in Section 3.3.4 and Section 4.6.

5.6.2 An Expression for $\frac{\partial P}{\partial t}$

In a three component and three phase system, the variable F depends on all three PDVs: z_c , z_w and P . This means that dF could be found using chain rule as:

$$dF = \frac{\partial F}{\partial z_c} dz_c + \frac{\partial F}{\partial z_w} dz_w + \frac{\partial F}{\partial P} dP \quad (5.75)$$

Therefore, an equally valid expression for $\frac{\partial F}{\partial t}$ as equation (5.74) is:

$$\frac{\partial F}{\partial t} = \frac{\partial F}{\partial z_c} \frac{\partial z_c}{\partial t} + \frac{\partial F}{\partial z_w} \frac{\partial z_w}{\partial t} + \frac{\partial F}{\partial P} \frac{\partial P}{\partial t} \quad (5.76)$$

This can be rearranged to be in terms of $\frac{\partial P}{\partial t}$, giving the following expression:

$$\boxed{\frac{\partial P}{\partial t} = \left[\frac{\partial F}{\partial t} - \frac{\partial F}{\partial z_c} \frac{\partial z_c}{\partial t} - \frac{\partial F}{\partial z_w} \frac{\partial z_w}{\partial t} \right] \left(\frac{\partial F}{\partial P} \right)^{-1}} \quad (5.77)$$

However, in order to use this expression for $\frac{\partial P}{\partial t}$ it is also necessary to define $\frac{\partial F}{\partial z_c}$, $\frac{\partial F}{\partial z_w}$ and $\frac{\partial F}{\partial P}$, which is significantly more complicated than finding $\frac{\partial G_i}{\partial t}$ and $\frac{\partial F}{\partial t}$.

5.7 Derivatives of F

5.7.1 Finding the Overall Derivative of F, dF

The first step to finding the derivatives $\frac{\partial F}{\partial z_c}$, $\frac{\partial F}{\partial z_w}$ and $\frac{\partial F}{\partial P}$ is to find an overall expression for the derivative, dF . This was found in Section 4.5.1 by using chain rule and product rule on equation (5.66), giving the expression in equation (4.28):

$$dF = F \frac{d\phi}{\phi} + \phi \sum_{j=1}^{N_p} \rho_j S_j \left(\frac{d\rho_j}{\rho_j} + \frac{dS_j}{S_j} \right) \quad (5.78)$$

Within this equation, $\frac{d\rho_j}{\rho_j}$ was also found in Section 4.5.1 by using chain rule and quotient rule on equation (4.29), to give equation (4.36):

$$\frac{d\rho_j}{\rho_j} = \rho_j \sum_{i=1}^{N_c} \frac{X_{ij}}{\rho_{ij}} \left(\frac{d\rho_{ij}}{\rho_{ij}} - \frac{dX_{ij}}{X_{ij}} \right) \quad (5.79)$$

In Chapter 4, when only two phases were involved in the system, it was also possible to produce an exact expression for $\frac{dS_j}{S_j}$. However, this becomes significantly more complicated in the three phase and three component system, and it becomes easier to consider the combination of phases present before evaluating the derivative of the saturations. It is possible to find the piecewise function $\frac{dS_j}{S_j}$ by expressing each of the terms given in the piecewise function S_j in the form:

$$S_j = \frac{v_{11}}{v_{11} + v_{12}} \quad (5.80)$$

where v_{11} and v_{12} are terms involving z_i , X_{ij} and ρ_j .

Quotient rule can be used on this expression to show that:

$$dS_j = \frac{dv_{11}(v_{11} + v_{12}) - v_{11}(dv_{11} + dv_{12})}{(v_{11} + v_{12})^2} \quad (5.81)$$

and so:

$$\frac{dS_j}{S_j} = \frac{dv_{11}(v_{11} + v_{12}) - v_{11}(dv_{11} + dv_{12})}{(v_{11} + v_{12})^2} \cdot \frac{v_{11} + v_{12}}{v_{11}} \quad (5.82)$$

which simplifies to:

$$\frac{dS_j}{S_j} = \frac{v_{12}dv_{11} - v_{11}dv_{12}}{v_{11}(v_{11} + v_{12})} \quad (5.83)$$

It should also be recalled that in parts of the system in which only one phase is present, $dS_j = 0$, and when only two phases are present:

$$S_j + S_h = 1 \quad (5.84)$$

where j and h represent the subscripts of two different phases.

This means that:

$$dS_h = -dS_j \quad (5.85)$$

and so:

$$\frac{dS_h}{S_h} = -\frac{dS_j}{1 - S_j} \quad (5.86)$$

5.7.2 Finding an Expression for $\frac{\partial F}{\partial z_c}$

Using equation (5.78), $\frac{\partial F}{\partial z_c}$ can be seen to be:

$$\frac{\partial F}{\partial z_c} = \frac{F}{\phi} \frac{\partial \phi}{\partial z_c} + \phi \left[\rho_g S_g \left(\frac{1}{\rho_g} \frac{\partial \rho_g}{\partial z_c} + \frac{1}{S_g} \frac{\partial S_g}{\partial z_c} \right) + \rho_a S_a \left(\frac{1}{\rho_a} \frac{\partial \rho_a}{\partial z_c} + \frac{1}{S_a} \frac{\partial S_a}{\partial z_c} \right) + \rho_s S_s \left(\frac{1}{\rho_s} \frac{\partial \rho_s}{\partial z_c} + \frac{1}{S_s} \frac{\partial S_s}{\partial z_c} \right) \right] \quad (5.87)$$

For this model, porosity is not considered to vary with composition. Therefore, it can be said that:

$$\frac{\partial \phi}{\partial z_c} = 0 \quad (5.88)$$

and hence equation (5.87) reduces to:

$$\frac{\partial F}{\partial z_c} = \phi \left[\rho_g S_g \left(\frac{1}{\rho_g} \frac{\partial \rho_g}{\partial z_c} + \frac{1}{S_g} \frac{\partial S_g}{\partial z_c} \right) + \rho_a S_a \left(\frac{1}{\rho_a} \frac{\partial \rho_a}{\partial z_c} + \frac{1}{S_a} \frac{\partial S_a}{\partial z_c} \right) + \rho_s S_s \left(\frac{1}{\rho_s} \frac{\partial \rho_s}{\partial z_c} + \frac{1}{S_s} \frac{\partial S_s}{\partial z_c} \right) \right] \quad (5.89)$$

Finding the Derivatives $\frac{1}{\rho_j} \frac{\partial \rho_j}{\partial z_c}$

Within this expression, $\frac{1}{\rho_g} \frac{\partial \rho_g}{\partial z_c}$ can be found from equation (5.79), and by considering which components can exist in each phase, can be written as:

$$\frac{1}{\rho_g} \frac{\partial \rho_g}{\partial z_c} = \rho_g \left[\frac{X_{cg}}{\rho_{cg}} \left(\frac{1}{\rho_{cg}} \frac{\partial \rho_{cg}}{\partial z_c} - \frac{1}{X_{cg}} \frac{\partial X_{cg}}{\partial z_c} \right) + \frac{X_{wg}}{\rho_{wg}} \left(\frac{1}{\rho_{wg}} \frac{\partial \rho_{wg}}{\partial z_c} - \frac{1}{X_{wg}} \frac{\partial X_{wg}}{\partial z_c} \right) \right] \quad (5.90)$$

Similarly:

$$\frac{1}{\rho_a} \frac{\partial \rho_a}{\partial z_c} = \rho_a \left[\frac{X_{ca}}{\rho_{ca}} \left(\frac{1}{\rho_{ca}} \frac{\partial \rho_{ca}}{\partial z_c} - \frac{1}{X_{ca}} \frac{\partial X_{ca}}{\partial z_c} \right) + \frac{X_{wa}}{\rho_{wa}} \left(\frac{1}{\rho_{wa}} \frac{\partial \rho_{wa}}{\partial z_c} - \frac{1}{X_{wa}} \frac{\partial X_{wa}}{\partial z_c} \right) + \frac{X_{na}}{\rho_{na}} \left(\frac{1}{\rho_{na}} \frac{\partial \rho_{na}}{\partial z_c} - \frac{1}{X_{na}} \frac{\partial X_{na}}{\partial z_c} \right) \right] \quad (5.91)$$

and

$$\frac{1}{\rho_s} \frac{\partial \rho_s}{\partial z_c} = \rho_s \left[\frac{X_{ns}}{\rho_{ns}} \left(\frac{1}{\rho_{ns}} \frac{\partial \rho_{ns}}{\partial z_c} - \frac{1}{X_{ns}} \frac{\partial X_{ns}}{\partial z_c} \right) \right] \quad (5.92)$$

As has been previously explained, the values of ρ_{ij} depend on pressure and temperature, but do not vary with composition. This means that $\frac{\partial \rho_{ij}}{\partial z_c} = 0$, and therefore equations (5.90) to (5.92) can be simplified to:

$$\frac{1}{\rho_g} \frac{\partial \rho_g}{\partial z_c} = -\rho_g \left[\frac{1}{\rho_{cg}} \frac{\partial X_{cg}}{\partial z_c} + \frac{1}{\rho_{wg}} \frac{\partial X_{wg}}{\partial z_c} \right] \quad (5.93)$$

$$\frac{1}{\rho_a} \frac{\partial \rho_a}{\partial z_c} = -\rho_a \left[\frac{1}{\rho_{ca}} \frac{\partial X_{ca}}{\partial z_c} + \frac{1}{\rho_{wa}} \frac{\partial X_{wa}}{\partial z_c} + \frac{1}{\rho_{na}} \frac{\partial X_{na}}{\partial z_c} \right] \quad (5.94)$$

and

$$\frac{1}{\rho_s} \frac{\partial \rho_s}{\partial z_c} = -\rho_s \left[\frac{1}{\rho_{ns}} \frac{\partial X_{ns}}{\partial z_c} \right] \quad (5.95)$$

respectively.

Equation (5.95) can be simplified as salt is the only component that can be present in the solid phase, meaning that $X_{ns} = 1$, and this will not change with z_c . Therefore, $\frac{\partial X_{ns}}{\partial z_c} = 0$,

and:

$$\frac{1}{\rho_s} \frac{\partial \rho_s}{\partial z_c} = 0 \quad (5.96)$$

Equation (5.93) can be simplified further using the fact that only two components can exist in the gaseous phase, and hence $X_{wg} = 1 - X_{cg}$. This means that:

$$\frac{\partial X_{wg}}{\partial z_c} = -\frac{\partial X_{cg}}{\partial z_c} \quad (5.97)$$

and hence equation (5.93) can be written as:

$$\frac{1}{\rho_g} \frac{\partial \rho_g}{\partial z_c} = \rho_g \left(\frac{1}{\rho_{wg}} - \frac{1}{\rho_{cg}} \right) \frac{\partial X_{cg}}{\partial z_c} \quad (5.98)$$

It should be recalled from equation (5.31) that:

$$X_{cg} = \begin{cases} 0, & z_c \leq \frac{x_{ca}(1 - z_n)}{1 - x_{na}} \\ x_{cg}, & \frac{x_{ca}(1 - z_n)}{1 - x_{na}} < z_c < x_{cg}(1 - z_n) \\ \frac{z_c}{1 - z_n}, & z_c \geq x_{cg}(1 - z_n) \end{cases} \quad (5.99)$$

As was shown in Section 2.3, the values of the equilibrium mass fractions x_{ij} are calculated using the methods of Spycher et al. (2003) and Spycher and Pruess (2005), and depend on pressure and temperature rather than composition. It can therefore be assumed that $\frac{\partial x_{ij}}{\partial z_i} = 0$ for all components i and phases j . Using this assumption and noting that $\frac{\partial z_i}{\partial z_k} = 0$ when $i \neq k$ and z_i and z_k are PDVs, it can be found from equation (5.99) that:

$$\frac{\partial X_{cg}}{\partial z_c} = \begin{cases} 0, & z_c < x_{cg}(1 - z_n) \\ \frac{z_w}{(1 - z_n)^2}, & z_c \geq x_{cg}(1 - z_n) \end{cases} \quad (5.100)$$

This expression can be substituted into equation (5.98) to illustrate that $\frac{1}{\rho_g} \frac{\partial \rho_g}{\partial z_c}$ is also a piecewise function. Its value will vary with the value of z_c .

It can be seen from equation (5.94) that $\frac{\partial X_{ca}}{\partial z_c}$, $\frac{\partial X_{wa}}{\partial z_c}$ and $\frac{\partial X_{na}}{\partial z_c}$ need to be evaluated in order to find an expression for $\frac{1}{\rho_a} \frac{\partial \rho_a}{\partial z_c}$. Recall from equation (5.40) that:

$$X_{ca} = \begin{cases} z_c, & z_c \leq \frac{x_{ca}(1-z_n)}{1-x_{na}}, & z_n \leq x_{na} \\ \frac{z_c(1-x_{na})}{1-z_n}, & z_c \leq \frac{x_{ca}(1-z_n)}{1-x_{na}}, & z_n > x_{na} \\ x_{ca}, & \frac{x_{ca}(1-z_n)}{1-x_{na}} < z_c < x_{cg}(1-z_n) \\ 0, & z_c \geq x_{cg}(1-z_n) \end{cases} \quad (5.101)$$

Again using the assumptions that $\frac{\partial x_{ij}}{\partial z_i} = 0$ and $\frac{\partial z_i}{\partial z_k} = 0$ when $i \neq k$ and z_i and z_k are PDVs, it follows that:

$$\frac{\partial X_{ca}}{\partial z_c} = \begin{cases} 1, & z_c \leq \frac{x_{ca}(1-z_n)}{1-x_{na}}, & z_n \leq x_{na} \\ \frac{z_w(1-x_{na})}{(1-z_n)^2}, & z_c \leq \frac{x_{ca}(1-z_n)}{1-x_{na}}, & z_n > x_{na} \\ 0, & z_c > \frac{x_{ca}(1-z_n)}{1-x_{na}} \end{cases} \quad (5.102)$$

Similarly, it can be recalled from equation (5.43) that:

$$X_{na} = \begin{cases} \frac{z_n(X_{cg} - X_{ca})}{X_{cg} - z_c}, & z_c < x_{cg}(1-z_n), & z_n \leq \frac{x_{na}(X_{cg} - z_c)}{X_{cg} - X_{ca}} \\ x_{na}, & z_c < x_{cg}(1-z_n), & z_n > \frac{x_{na}(X_{cg} - z_c)}{X_{cg} - X_{ca}} \\ 0, & z_c \geq x_{cg}(1-z_n), & z_n \geq 0 \end{cases} \quad (5.103)$$

Use of the same assumptions as when finding the previous derivatives $\frac{\partial X_{ij}}{\partial z_c}$, as well as quotient rule, gives that:

$$\frac{\partial X_{na}}{\partial z_c} = \begin{cases} \frac{z_n \left[\frac{\partial X_{cg}}{\partial z_c} (X_{ca} - z_c) + \frac{\partial X_{ca}}{\partial z_c} (z_c - X_{cg}) \right] + (X_{cg} - X_{ca})(z_n + z_c - X_{cg})}{(X_{cg} - z_c)^2}, & z_c < x_{cg}(1-z_n), & z_n \leq \frac{x_{na}(X_{cg} - z_c)}{X_{cg} - X_{ca}} \\ 0, & z_c < x_{cg}(1-z_n), & z_n > \frac{x_{na}(X_{cg} - z_c)}{X_{cg} - X_{ca}} \\ 0, & z_c \geq x_{cg}(1-z_n), & z_n \geq 0 \end{cases} \quad (5.104)$$

Finally, as $X_{ca} + X_{wa} + X_{na} = 1$, it must be that:

$$\frac{\partial X_{wa}}{\partial z_c} = -\frac{\partial X_{ca}}{\partial z_c} - \frac{\partial X_{na}}{\partial z_c} \quad (5.105)$$

Therefore, all of the terms in equation (5.94) have been evaluated for every possible combination of phases present, and thus $\frac{1}{\rho_a} \frac{\partial \rho_a}{\partial z_c}$ can be expressed.

Finding the Derivatives $\frac{1}{S_j} \frac{\partial S_j}{\partial z_c}$

As was explained in Section 5.7.1, it is much more difficult to find exact expressions for $\frac{dS_j}{S_j}$ when three phases are involved than only two phases, as was the case in Chapter 4. This means that it is fairly complicated to find expressions for $\frac{1}{S_j} \frac{\partial S_j}{\partial z_c}$, as is needed to evaluate $\frac{\partial F}{\partial z_c}$ in equation (5.87). However, the necessary expressions can be found by writing the saturations in the format given in equation (5.80).

Recall from equation (5.58) that:

$$S_s = \begin{cases} 0, & z_c \geq 0, & z_n \leq \frac{X_{na}(X_{cg} - z_c)}{X_{cg} - X_{ca}} \\ \left[1 + \frac{\rho_s(1-z_n)}{\rho_a(z_n - x_{na})}\right]^{-1}, & z_c \leq \frac{x_{ca}(1-z_n)}{1-x_{na}}, & z_n > x_{na} \\ \left[1 + \frac{\rho_s \rho_a [z_c(1-x_{na}) - x_{ca}(1-z_n)] - \rho_g \rho_s [z_c - x_{cg}(1-z_n)]}{\rho_g \rho_a [z_n(x_{cg} - x_{ca}) - x_{na}(x_{cg} - z_c)]}\right]^{-1}, & \frac{x_{ca}(1-z_n)}{1-x_{na}} < z_c < x_{cg}(1-z_n), & z_n > \frac{x_{na}(x_{cg} - z_c)}{x_{cg} - x_{ca}} \\ \left[1 + \frac{\rho_s(1-z_n)}{\rho_g z_n}\right]^{-1}, & z_c \geq x_{cg}(1-z_n), & z_n > 0 \end{cases} \quad (5.106)$$

It can immediately be seen from this that when no solid phase is present, i.e. when $z_n \leq \frac{X_{na}(X_{cg} - z_c)}{X_{cg} - X_{ca}}$, that $S_s = 0$, and hence $\frac{\partial S_s}{\partial z_c} = 0$. Additionally, it should be recalled that in Section 5.5.1, in which the values in equation (5.106) were calculated, the saturations were initially expressed in the format described in equation (5.80). Focusing firstly on the case in which there is no gaseous phase, and only aqueous and solid phases are present (i.e. when $z_c \leq \frac{x_{ca}(1-z_n)}{1-x_{na}}$ and $z_n > x_{na}$), it can be seen from equation (5.45) that the expression for solid saturation can also be written as:

$$S_s = \frac{\rho_a(z_n - x_{na})}{\rho_s(1 - z_n) + \rho_a(z_n - x_{na})} \quad (5.107)$$

This can be expressed as:

$$S_s = \frac{v_{11}}{v_{11} + v_{12}} \quad (5.108)$$

where:

$$v_{11} = \rho_a(z_n - x_{na}) \quad (5.109)$$

and

$$v_{12} = \rho_s(1 - z_n) \quad (5.110)$$

From equation (5.83):

$$\frac{dS_s}{S_s} = \frac{v_{12}dv_{11} - v_{11}dv_{12}}{v_{11}(v_{11} + v_{12})} \quad (5.111)$$

and hence:

$$\frac{1}{S_s} \frac{\partial S_s}{\partial z_c} = \frac{v_{12} \frac{\partial v_{11}}{\partial z_c} - v_{11} \frac{\partial v_{12}}{\partial z_c}}{v_{11}(v_{11} + v_{12})} \quad (5.112)$$

where:

$$\frac{\partial v_{11}}{\partial z_c} = (z_n - x_{na}) \frac{\partial \rho_a}{\partial z_c} - \rho_a \quad (5.113)$$

and

$$\frac{\partial v_{12}}{\partial z_c} = \rho_s + (1 - z_n) \frac{\partial \rho_s}{\partial z_c} \quad (5.114)$$

Within these derivatives, $\frac{\partial \rho_j}{\partial z_c}$ can be found by from the density derivatives evaluated earlier in this section.

The same can be done to evaluate the derivative of the solid saturation when there is no aqueous phase, and only gaseous and solid phases are present. When this is the case, it must be that $z_c \geq x_{cg}(1 - z_n)$ and $z_n > 0$. Equation (5.47) shows that the solid saturation in this situation can be written as:

$$S_s = \frac{\rho_g z_n}{\rho_s(1 - z_n) + \rho_g z_n} \quad (5.115)$$

Therefore:

$$v_{11} = \rho_g z_n \quad (5.116)$$

and

$$v_{12} = \rho_s(1 - z_n) \quad (5.117)$$

As with the previous case in which there was no gaseous phase present, $\frac{1}{S_s} \frac{\partial S_s}{\partial z_c}$ can be found by use of equation (5.112):

$$\frac{1}{S_s} \frac{\partial S_s}{\partial z_c} = \frac{v_{12} \frac{\partial v_{11}}{\partial z_c} - v_{11} \frac{\partial v_{12}}{\partial z_c}}{v_{11}(v_{11} + v_{12})} \quad (5.118)$$

In this case:

$$\frac{\partial v_{11}}{\partial z_c} = z_n \frac{\partial \rho_g}{\partial z_c} - \rho_g \quad (5.119)$$

and

$$\frac{\partial v_{12}}{\partial z_c} = \rho_s + (1 - z_n) \frac{\partial \rho_s}{\partial z_c} \quad (5.120)$$

When all three phases are present, and hence $\frac{x_{ca}(1-z_n)}{1-x_{na}} < z_c < x_{cg}(1-z_n)$ and $z_n > \frac{x_{na}(x_{cg}-z_c)}{x_{cg}-x_{ca}}$, it can be seen from equation (5.56) that:

$$S_s = \frac{\rho_g \rho_a [z_n(x_{cg} - x_{ca}) - x_{na}(x_{cg} - z_c)]}{\rho_s \rho_a [z_c(1 - x_{na}) - x_{ca}(1 - z_n)] - \rho_g \rho_s [z_c - x_{cg}(1 - z_n)] + \rho_g \rho_a [z_n(x_{cg} - x_{ca}) - x_{na}(x_{cg} - z_c)]} \quad (5.121)$$

from which it follows that, when all three phases are present, the solid saturation can be expressed as:

$$S_s = \frac{v_{11}}{v_{11} + v_{12}} \quad (5.122)$$

with

$$v_{11} = \rho_g \rho_a [z_n(x_{cg} - x_{ca}) - x_{na}(x_{cg} - z_c)] \quad (5.123)$$

and

$$v_{12} = \rho_s \rho_a [z_c(1 - x_{na}) - x_{ca}(1 - z_n)] - \rho_g \rho_s [z_c - x_{cg}(1 - z_n)] \quad (5.124)$$

and hence the derivatives that must be substituted into equation (5.112) to find $\frac{1}{S_s} \frac{\partial S_s}{\partial z_c}$ are:

$$\frac{\partial v_{11}}{\partial z_c} = \left[\rho_a \frac{\partial \rho_g}{\partial z_c} + \rho_g \frac{\partial \rho_a}{\partial z_c} \right] [z_n(x_{cg} - x_{ca}) - x_{na}(x_{cg} - z_c)] + \rho_g \rho_a (x_{ca} + x_{na} - x_{cg}) \quad (5.125)$$

and

$$\begin{aligned} \frac{\partial v_{12}}{\partial z_c} = & \left[\rho_s \frac{\partial \rho_a}{\partial z_c} + \rho_a \frac{\partial \rho_s}{\partial z_c} \right] [z_c(1 - x_{na}) - x_{ca}(1 - z_n)] + \rho_s \rho_a x_{wa} \\ & - \left[\rho_g \frac{\partial \rho_s}{\partial z_c} + \rho_s \frac{\partial \rho_g}{\partial z_c} \right] [z_c - x_{cg}(1 - z_n)] - \rho_g \rho_s x_{wg} \end{aligned} \quad (5.126)$$

By expressing each piecewise component of S_s in terms of v_{11} and v_{12} , the full piecewise expression for $\frac{1}{S_s} \frac{\partial S_s}{\partial z_c}$ has therefore been found.

Recall from equation (5.62) that the aqueous saturation is given by:

$$S_a = \begin{cases} 0, & z_c \geq x_{cg}(1 - z_n), & z_n \geq 0, \\ 1, & z_c \leq \frac{x_{ca}(1 - z_n)}{1 - x_{na}}, & z_n \leq x_{na}, \\ \left[1 + \frac{\rho_a(z_c - x_{ca})}{\rho_g(x_{cg} - z_c)} \right]^{-1}, & \frac{x_{ca}(1 - z_n)}{1 - x_{na}} < z_c < x_{cg}(1 - z_n), & z_n \leq \frac{x_{na}(x_{cg} - z_c)}{x_{cg} - x_{ca}} \\ 1 - S_s, & z_c \leq \frac{x_{ca}(1 - z_n)}{1 - x_{na}}, & z_n > x_{na} \\ \frac{S_s(\rho_s + z_n\rho_g - z_n\rho_s) - z_n\rho_g}{\rho_a(z_n - x_{na}) - z_n\rho_g}, & \frac{x_{ca}(1 - z_n)}{1 - x_{na}} < z_c < x_{cg}(1 - z_n), & z_n > \frac{x_{na}(x_{cg} - z_c)}{x_{cg} - x_{ca}} \end{cases} \quad (5.127)$$

It can be instantly seen from this expression that when the aqueous saturation is constant, either by there being no aqueous phase present, and so $S_a = 0$, or the aqueous phase being the only phase present, and so $S_a = 1$, it must be that $\frac{\partial S_a}{\partial z_c} = 0$. It can also be seen that when there is no gaseous phase, and only the aqueous and solid phases are present (and so $z_c \leq \frac{x_{ca}(1-z_n)}{1-x_{na}}$ and $z_n > x_{na}$), $\frac{\partial S_a}{\partial z_c}$ can be found from the derivative of the solid saturation in this region that has already been calculated, such that:

$$\frac{\partial S_a}{\partial z_c} = -\frac{\partial S_s}{\partial z_c} \quad (5.128)$$

or

$$\frac{1}{S_a} \frac{\partial S_a}{\partial z_c} = -\frac{1}{1 - S_s} \frac{\partial S_s}{\partial z_c} \quad (5.129)$$

However, when only aqueous and gaseous phases are present in the system, it is necessary to return to equation (5.80) in order to calculate $\frac{1}{S_a} \frac{\partial S_a}{\partial z_c}$. It can be recalled from equation (5.60) that when only aqueous and gaseous phases are present, and hence $\frac{x_{ca}(1-z_n)}{1-x_{na}} < z_c < x_{cg}(1-z_n)$ and $z_n \leq \frac{x_{na}(x_{cg}-z_c)}{x_{cg}-x_{ca}}$, the aqueous saturation can also be expressed as:

$$S_a = \frac{\rho_g(x_{cg} - z_c)}{\rho_g(x_{cg} - z_c) + \rho_a(z_c - x_{ca})} \quad (5.130)$$

or, equivalently:

$$S_a = \frac{v_{11}}{v_{11} + v_{12}} \quad (5.131)$$

where:

$$v_{11} = \rho_g(x_{cg} - z_c) \quad (5.132)$$

and

$$v_{12} = \rho_a(z_c - x_{ca}) \quad (5.133)$$

From equation (5.80), it must be that:

$$\frac{1}{S_a} \frac{\partial S_a}{\partial z_c} = \frac{v_{12} \frac{\partial v_{11}}{\partial z_c} - v_{11} \frac{\partial v_{12}}{\partial z_c}}{v_{11}(v_{11} + v_{12})} \quad (5.134)$$

where:

$$\frac{\partial v_{11}}{\partial z_c} = (x_{cg} - z_c) \frac{\partial \rho_g}{\partial z_c} - \rho_g \quad (5.135)$$

and

$$\frac{\partial v_{12}}{\partial z_c} = (z_c - x_{ca}) \frac{\partial \rho_a}{\partial z_c} + \rho_a \quad (5.136)$$

The aqueous saturation when all three phases are present, and hence $\frac{x_{ca}(1-z_n)}{1-x_{na}} < z_c < x_{cg}(1-z_n)$ and $z_n > \frac{x_{na}(x_{cg}-z_c)}{x_{cg}-x_{ca}}$, has been calculated in terms of S_s , the derivative of which has already been found. It is best to express S_a in this case as it is written in equation (5.54):

$$S_a = \frac{S_s(\rho_s + z_n \rho_g - z_n \rho_s) - z_n \rho_g}{\rho_a(z_n - x_{na}) - z_n \rho_g} \quad (5.137)$$

Quotient rule can then be used to calculate $\frac{\partial S_a}{\partial z_c}$, such that:

$$\frac{\partial S_a}{\partial z_c} = \frac{v \frac{\partial u}{\partial z_c} - u \frac{\partial v}{\partial z_c}}{v^2} \quad (5.138)$$

where:

$$u = S_s(\rho_s + z_n \rho_g - z_n \rho_s) - z_n \rho_g \quad (5.139)$$

and

$$v = \rho_a(z_n - x_{na}) - z_n \rho_g \quad (5.140)$$

and so:

$$\frac{\partial u}{\partial z_c} = (\rho_s + z_n \rho_g - z_n \rho_s) \frac{\partial S_s}{\partial z_c} + S_s \left[(1 - z_n) \frac{\partial \rho_s}{\partial z_c} + z_n \frac{\partial \rho_g}{\partial z_c} + \rho_s - \rho_g \right] + \rho_g - z_n \frac{\partial \rho_g}{\partial z_c} \quad (5.141)$$

and

$$\frac{\partial v}{\partial z_c} = (z_n - x_{na}) \frac{\partial \rho_a}{\partial z_c} + \rho_g - z_n \frac{\partial \rho_g}{\partial z_c} - \rho_a \quad (5.142)$$

The derivative of the gas saturation with respect to z_c , $\frac{\partial S_g}{\partial z_c}$, can now be found from:

$$\frac{\partial S_g}{\partial z_c} = -\frac{\partial S_a}{\partial z_c} - \frac{\partial S_s}{\partial z_c} \quad (5.143)$$

as $\frac{\partial S_a}{\partial z_c}$ and $\frac{\partial S_s}{\partial z_c}$ have been defined for all possible phase combinations.

In all cases, the value of $\frac{1}{S_j} \frac{\partial S_j}{\partial z_c}$ can be found from $\frac{\partial S_j}{\partial z_c}$ by simply dividing by the relevant saturation value, S_j .

It is now possible to give an expression for $\frac{\partial F}{\partial z_c}$, as all terms within equation (5.89) have been defined.

5.7.3 Finding an Expression for $\frac{\partial F}{\partial z_w}$

An expression for $\frac{\partial F}{\partial z_w}$ can be found using a very similar method to that used to find $\frac{\partial F}{\partial z_c}$. Using equation (5.78) and again taking into account that porosity does not vary with composition, and hence $\frac{\partial \phi}{\partial z_w} = 0$, $\frac{\partial F}{\partial z_w}$ can be calculated to be:

$$\frac{\partial F}{\partial z_w} = \phi \left[\rho_g S_g \left(\frac{1}{\rho_g} \frac{\partial \rho_g}{\partial z_w} + \frac{1}{S_g} \frac{\partial S_g}{\partial z_w} \right) + \rho_a S_a \left(\frac{1}{\rho_a} \frac{\partial \rho_a}{\partial z_w} + \frac{1}{S_a} \frac{\partial S_a}{\partial z_w} \right) + \rho_s S_s \left(\frac{1}{\rho_s} \frac{\partial \rho_s}{\partial z_w} + \frac{1}{S_s} \frac{\partial S_s}{\partial z_w} \right) \right] \quad (5.144)$$

Finding the Derivatives $\frac{1}{\rho_j} \frac{\partial \rho_j}{\partial z_w}$

In the previous subsection, expressions for $\frac{1}{\rho_j} \frac{\partial \rho_j}{\partial z_c}$ were found by use of equation (5.79), which gives the general derivative $\frac{d\rho_j}{\rho_j}$. The assumption was then made that ρ_{ij} does not vary with composition and so $\frac{\partial \rho_{ij}}{\partial z_i} = 0$, and consideration was made of which components can exist in which phases in order to simplify the equations as much as possible. By following the same steps to find $\frac{1}{\rho_j} \frac{\partial \rho_j}{\partial z_w}$, the following equations can be found:

$$\frac{1}{\rho_g} \frac{\partial \rho_g}{\partial z_w} = \rho_g \left(\frac{1}{\rho_{wg}} - \frac{1}{\rho_{cg}} \right) \frac{\partial X_{cg}}{\partial z_w} \quad (5.145)$$

$$\frac{1}{\rho_a} \frac{\partial \rho_a}{\partial z_w} = -\rho_a \left[\frac{1}{\rho_{ca}} \frac{\partial X_{ca}}{\partial z_w} + \frac{1}{\rho_{wa}} \frac{\partial X_{wa}}{\partial z_w} + \frac{1}{\rho_{na}} \frac{\partial X_{na}}{\partial z_w} \right] \quad (5.146)$$

and

$$\frac{1}{\rho_s} \frac{\partial \rho_s}{\partial z_w} = 0 \quad (5.147)$$

In order to fully evaluate these expressions, the derivatives $\frac{\partial X_{ij}}{\partial z_w}$ must be calculated. Recall from equation (5.31) that:

$$X_{cg} = \begin{cases} 0, & z_c \leq \frac{x_{ca}(1-z_n)}{1-x_{na}} \\ x_{cg}, & \frac{x_{ca}(1-z_n)}{1-x_{na}} < z_c < x_{cg}(1-z_n) \\ \frac{z_c}{1-z_n}, & z_c \geq x_{cg}(1-z_n) \end{cases} \quad (5.148)$$

Again using the assumptions that $\frac{\partial x_{ij}}{\partial z_i} = 0$ and $\frac{\partial z_i}{\partial z_k} = 0$ when $i \neq k$ and z_i and z_k are

PDVs, it follows that:

$$\frac{\partial X_{cg}}{\partial z_w} = \begin{cases} 0, & z_c < x_{cg}(1 - z_n) \\ -\frac{z_c}{(1 - z_n)^2}, & z_c \geq x_{cg}(1 - z_n) \end{cases} \quad (5.149)$$

This derivative can be substituted into equation (5.145) to give the complete equation for $\frac{1}{\rho_g} \frac{\partial \rho_g}{\partial z_w}$.

The derivatives $\frac{\partial X_{ca}}{\partial z_w}$, $\frac{\partial X_{wa}}{\partial z_w}$ and $\frac{\partial X_{na}}{\partial z_w}$ must be calculated in order to find $\frac{1}{\rho_a} \frac{\partial \rho_a}{\partial z_w}$. It can be seen from equation (5.40) that:

$$X_{ca} = \begin{cases} z_c, & z_c \leq \frac{x_{ca}(1 - z_n)}{1 - x_{na}}, & z_n \leq x_{na} \\ \frac{z_c(1 - x_{na})}{1 - z_n}, & z_c \leq \frac{x_{ca}(1 - z_n)}{1 - x_{na}}, & z_n > x_{na} \\ x_{ca}, & \frac{x_{ca}(1 - z_n)}{1 - x_{na}} < z_c < x_{cg}(1 - z_n) \\ 0, & z_c \geq x_{cg}(1 - z_n) \end{cases} \quad (5.150)$$

which means that:

$$\frac{\partial X_{ca}}{\partial z_w} = \begin{cases} 0, & z_c \leq \frac{x_{ca}(1 - z_n)}{1 - x_{na}}, & z_n \leq x_{na} \\ -\frac{z_c(1 - x_{na})}{(1 - z_n)^2}, & z_c \leq \frac{x_{ca}(1 - z_n)}{1 - x_{na}}, & z_n > x_{na} \\ 0, & z_c > \frac{x_{ca}(1 - z_n)}{1 - x_{na}} \end{cases} \quad (5.151)$$

X_{na} was found by equation (5.43) to be:

$$X_{na} = \begin{cases} \frac{z_n(X_{cg} - X_{ca})}{X_{cg} - z_c}, & z_c < x_{cg}(1 - z_n), & z_n \leq \frac{x_{na}(X_{cg} - z_c)}{X_{cg} - X_{ca}} \\ x_{na}, & z_c < x_{cg}(1 - z_n), & z_n > \frac{x_{na}(X_{cg} - z_c)}{X_{cg} - X_{ca}} \\ 0, & z_c \geq x_{cg}(1 - z_n), & z_n \geq 0 \end{cases} \quad (5.152)$$

from which it follows that:

$$\frac{\partial X_{na}}{\partial z_w} = \begin{cases} \frac{z_n \left[\frac{\partial X_{cg}}{\partial z_w} (X_{ca} - z_c) + \frac{\partial X_{ca}}{\partial z_w} (z_c - X_{cg}) \right] + (X_{cg} - z_c)(X_{ca} - X_{cg})}{(X_{cg} - z_c)^2}, & z_c < x_{cg}(1 - z_n), \quad z_n \leq \frac{x_{na}(X_{cg} - z_c)}{X_{cg} - X_{ca}} \\ 0, & z_c < x_{cg}(1 - z_n), \quad z_n > \frac{x_{na}(X_{cg} - z_c)}{X_{cg} - X_{ca}} \\ 0, & z_c \geq x_{cg}(1 - z_n), \quad z_n \geq 0 \end{cases} \quad (5.153)$$

Finally, as $X_{ca} + X_{wa} + X_{na} = 1$, $\frac{\partial X_{wa}}{\partial z_w}$ can be found from:

$$\frac{\partial X_{wa}}{\partial z_w} = -\frac{\partial X_{ca}}{\partial z_w} - \frac{\partial X_{na}}{\partial z_w} \quad (5.154)$$

All terms in equations (5.145) to (5.147) have now been evaluated, and therefore $\frac{1}{\rho_j} \frac{\partial \rho_j}{\partial z_w}$ can be fully expressed for each phase j .

Finding the Derivatives $\frac{1}{S_j} \frac{\partial S_j}{\partial z_w}$

It was shown in Section 5.7.1 that by writing saturations in the form given in equation (5.80), the derivative $\frac{dS_j}{S_j}$ can be found from equation (5.83). The previous subsection, in which the derivative $\frac{\partial F}{\partial z_c}$ was found, has already expressed the saturations in the required format.

Looking first at solid saturation, it can be seen from equation (5.58) that when no solid phase is present and hence $S_s = 0$, it must also be the case that $\frac{\partial S_s}{\partial z_w} = 0$. When no gaseous phase is present, and the only phases present in the system are aqueous and solid (i.e. when $z_c \leq \frac{x_{ca}(1-z_n)}{1-x_{na}}$ and $z_n > x_{na}$), it was illustrated in equations (5.107) to (5.110) that the solid saturation can be written as:

$$S_s = \frac{\rho_a(z_n - x_{na})}{\rho_s(1 - z_n) + \rho_a(z_n - x_{na})} \quad (5.155)$$

which can also be expressed as:

$$S_s = \frac{v_{11}}{v_{11} + v_{12}} \quad (5.156)$$

where:

$$v_{11} = \rho_a(z_n - x_{na}) \quad (5.157)$$

and

$$v_{12} = \rho_s(1 - z_n) \quad (5.158)$$

From equation (5.83):

$$\frac{dS_s}{S_s} = \frac{v_{12}dv_{11} - v_{11}dv_{12}}{v_{11}(v_{11} + v_{12})} \quad (5.159)$$

and hence:

$$\frac{1}{S_s} \frac{\partial S_s}{\partial z_w} = \frac{v_{12} \frac{\partial v_{11}}{\partial z_w} - v_{11} \frac{\partial v_{12}}{\partial z_w}}{v_{11}(v_{11} + v_{12})} \quad (5.160)$$

where:

$$\frac{\partial v_{11}}{\partial z_w} = (z_n - x_{na}) \frac{\partial \rho_a}{\partial z_w} - \rho_a \quad (5.161)$$

and

$$\frac{\partial v_{12}}{\partial z_w} = \rho_s + (1 - z_n) \frac{\partial \rho_s}{\partial z_w} \quad (5.162)$$

Similarly, when there is no aqueous phase and only the gaseous and solid phases are present, and therefore the conditions in the system are that $z_c \geq x_{cg}(1 - z_n)$ and $z_n > 0$, equations (5.116) and (5.117) illustrated that to write S_s in the form of equation (5.80) the necessary terms will be:

$$v_{11} = \rho_g z_n \quad (5.163)$$

and

$$v_{12} = \rho_s(1 - z_n) \quad (5.164)$$

This means that the derivatives that need to be substituted into equation (5.160) in order to find $\frac{1}{S_s} \frac{\partial S_s}{\partial z_w}$ for this phase combination are:

$$\frac{\partial v_{11}}{\partial z_w} = z_n \frac{\partial \rho_g}{\partial z_w} - \rho_g \quad (5.165)$$

and

$$\frac{\partial v_{12}}{\partial z_w} = \rho_s + (1 - z_n) \frac{\partial \rho_s}{\partial z_w} \quad (5.166)$$

When all three phases are present, and so $\frac{x_{ca}(1-z_n)}{1-x_{na}} < z_c < x_{cg}(1-z_n)$ and $z_n > \frac{x_{na}(x_{cg}-z_c)}{x_{cg}-x_{ca}}$, equations (5.123) and (5.124) showed that S_s can be written in the form of equation (5.80) with:

$$v_{11} = \rho_g \rho_a [z_n(x_{cg} - x_{ca}) - x_{na}(x_{cg} - z_c)] \quad (5.167)$$

and

$$v_{12} = \rho_s \rho_a [z_c(1 - x_{na}) - x_{ca}(1 - z_n)] - \rho_g \rho_s [z_c - x_{cg}(1 - z_n)] \quad (5.168)$$

Therefore, in order to find $\frac{1}{S_s} \frac{\partial S_s}{\partial z_w}$ for the condition in which all three phases are present, the derivatives that need to be substituted into equation (5.160) are:

$$\frac{\partial v_{11}}{\partial z_w} = \left[\rho_a \frac{\partial \rho_g}{\partial z_w} + \rho_g \frac{\partial \rho_a}{\partial z_w} \right] [z_n(x_{cg} - x_{ca}) - x_{na}(x_{cg} - z_c)] + \rho_g \rho_a (x_{ca} - x_{cg}) \quad (5.169)$$

and

$$\begin{aligned} \frac{\partial v_{12}}{\partial z_w} = & \left[\rho_s \frac{\partial \rho_a}{\partial z_w} + \rho_a \frac{\partial \rho_s}{\partial z_w} \right] [z_c(1 - x_{na}) - x_{ca}(1 - z_n)] - \rho_s \rho_a x_{ca} \\ & - \left[\rho_g \frac{\partial \rho_s}{\partial z_w} + \rho_s \frac{\partial \rho_g}{\partial z_w} \right] [z_c - x_{cg}(1 - z_n)] + \rho_g \rho_s x_{cg} \end{aligned} \quad (5.170)$$

The full piecewise expression for $\frac{1}{S_s} \frac{\partial S_s}{\partial z_w}$ has now been found, as it has been calculated for every possible combination of phases present.

Referring back to equation (5.62), it can be seen that, as was the case when taking derivatives with respect to z_c , $\frac{\partial S_a}{\partial z_w} = 0$ when S_a is constant. This occurs in the aqueous only zone, in which $S_a = 1$, and when there is no aqueous phase present, and so $S_a = 0$. Equation (5.62) shows that when no gaseous phase is present, and hence $z_c \leq \frac{x_{ca}(1-z_n)}{1-x_{na}}$ and $z_n > x_{na}$, $S_a = 1 - S_s$. This means that $\frac{\partial S_a}{\partial z_w}$ can be calculated from the value of $\frac{\partial S_s}{\partial z_w}$ for this zone that has already been found, such that:

$$\frac{\partial S_a}{\partial z_w} = - \frac{\partial S_s}{\partial z_w} \quad (5.171)$$

When $\frac{x_{ca}(1-z_n)}{1-x_{na}} < z_c < x_{cg}(1-z_n)$ and $z_n > \frac{x_{na}(x_{cg}-z_c)}{x_{cg}-x_{ca}}$, which corresponds to only gaseous and aqueous phases present in the system, equations (5.130) to (5.133) showed that the aqueous saturation can be written as:

$$S_a = \frac{\rho_g(x_{cg} - z_c)}{\rho_g(x_{cg} - z_c) + \rho_a(z_c - x_{ca})} \quad (5.172)$$

or:

$$S_a = \frac{v_{11}}{v_{11} + v_{12}} \quad (5.173)$$

where:

$$v_{11} = \rho_g(x_{cg} - z_c) \quad (5.174)$$

and

$$v_{12} = \rho_a(z_c - x_{ca}) \quad (5.175)$$

Therefore, using equation (5.80), it must be that:

$$\frac{1}{S_a} \frac{\partial S_a}{\partial z_w} = \frac{v_{12} \frac{\partial v_{11}}{\partial z_w} - v_{11} \frac{\partial v_{12}}{\partial z_w}}{v_{11}(v_{11} + v_{12})} \quad (5.176)$$

in which:

$$\frac{\partial v_{11}}{\partial z_w} = (x_{cg} - z_c) \frac{\partial \rho_g}{\partial z_w} \quad (5.177)$$

and

$$\frac{\partial v_{12}}{\partial z_w} = (z_c - x_{ca}) \frac{\partial \rho_a}{\partial z_w} \quad (5.178)$$

As was shown when calculating the saturation derivatives with respect to z_c , when all three phases are present (i.e. when $\frac{x_{ca}(1-z_n)}{1-x_{na}} < z_c < x_{cg}(1-z_n)$ and $z_n > \frac{x_{na}(x_{cg}-z_c)}{x_{cg}-x_{ca}}$), the aqueous saturation has been expressed in terms of S_s . In order to calculate the derivative of S_a in this scenario, it is best to express it as it is written in equation (5.54), such that:

$$S_a = \frac{S_s(\rho_s + z_n\rho_g - z_n\rho_s) - z_n\rho_g}{\rho_a(z_n - x_{na}) - z_n\rho_g} \quad (5.179)$$

$\frac{\partial S_a}{\partial z_w}$ can then be calculated using quotient rule, where:

$$\frac{\partial S_a}{\partial z_w} = \frac{v \frac{\partial u}{\partial z_w} - u \frac{\partial v}{\partial z_w}}{v^2} \quad (5.180)$$

in which:

$$u = S_s(\rho_s + z_n\rho_g - z_n\rho_s) - z_n\rho_g \quad (5.181)$$

and

$$v = \rho_a(z_n - x_{na}) - z_n\rho_g \quad (5.182)$$

and hence:

$$\frac{\partial u}{\partial z_w} = (\rho_s + z_n\rho_g - z_n\rho_s) \frac{\partial S_s}{\partial z_w} + S_s \left[(1-z_n) \frac{\partial \rho_s}{\partial z_w} + z_n \frac{\partial \rho_g}{\partial z_w} + \rho_s - \rho_g \right] + \rho_g - z_n \frac{\partial \rho_g}{\partial z_w} \quad (5.183)$$

and

$$\frac{\partial v}{\partial z_w} = (z_n - x_{na}) \frac{\partial \rho_a}{\partial z_w} + \rho_g - z_n \frac{\partial \rho_g}{\partial z_w} - \rho_a \quad (5.184)$$

The derivative of the gas saturation with respect to z_w , $\frac{\partial S_g}{\partial z_w}$ can now be found at all points using:

$$\frac{\partial S_g}{\partial z_w} = -\frac{\partial S_a}{\partial z_w} - \frac{\partial S_s}{\partial z_w} \quad (5.185)$$

A full expression for $\frac{\partial F}{\partial z_w}$ can now be calculated, as all terms within equation (5.144) have been defined.

5.7.4 Finding an Expression for $\frac{\partial F}{\partial P}$

The expression for dF given in equation (5.78) is also needed to find the derivative $\frac{\partial F}{\partial P}$. Taking the derivatives in this equation to be with respect to P gives:

$$\frac{\partial F}{\partial P} = \frac{F}{\phi} \frac{\partial \phi}{\partial P} + \phi \left[\rho_g S_g \left(\frac{1}{\rho_g} \frac{\partial \rho_g}{\partial P} + \frac{1}{S_g} \frac{\partial S_g}{\partial P} \right) + \rho_a S_a \left(\frac{1}{\rho_a} \frac{\partial \rho_a}{\partial P} + \frac{1}{S_a} \frac{\partial S_a}{\partial P} \right) + \rho_s S_s \left(\frac{1}{\rho_s} \frac{\partial \rho_s}{\partial P} + \frac{1}{S_s} \frac{\partial S_s}{\partial P} \right) \right] \quad (5.186)$$

As was explained in Section 4.5.1 when looking at the two component and two phase system, it is often more convenient to write the equation for $\frac{\partial F}{\partial P}$ in terms of rock and fluid compressibility. It should be recalled that the rock compressibility, α_r [$M^{-1}LT^2$], shows how porosity changes with varying pressure, and is equal to:

$$\alpha_r = \frac{1}{\phi} \frac{\partial \phi}{\partial P} \quad (5.187)$$

Fluid compressibility for a phase j , α_j [$M^{-1}LT^2$], illustrates how phase density changes with pressure, and is expressed as:

$$\alpha_j = \frac{1}{\rho_j} \frac{\partial \rho_j}{\partial P_j} \quad (5.188)$$

The compressibility of a component i in a phase j , α_{ij} [$M^{-1}LT^2$], is similarly given by:

$$\alpha_{ij} = \frac{1}{\rho_{ij}} \frac{\partial \rho_{ij}}{\partial P_j} \quad (5.189)$$

However, as was described in Section 4.5.1, many numerical codes approximate the value of α_{ij} by taking derivatives to be with respect to the global pressure, P , rather than the phase pressure, P_j , which in turn means that the overall phase compressibility, α_j , also uses derivatives with respect to P as opposed to P_j . This approximation is adopted here, as it makes the code significantly easier to implement and makes very little difference to the final output. Therefore, within this model, α_{ij} is approximated as:

$$\alpha_{ij} = \frac{1}{\rho_{ij}} \frac{\partial \rho_{ij}}{\partial P} \quad (5.190)$$

and α_j can be assumed to be:

$$\alpha_j = \frac{1}{\rho_j} \frac{\partial \rho_j}{\partial P} \quad (5.191)$$

By incorporating both the rock and phase compressibilities, equation (5.186) can be written as:

$$\frac{\partial F}{\partial P} = F\alpha_r + \phi \left[\rho_g S_g \left(\alpha_g + \frac{1}{S_g} \frac{\partial S_g}{\partial P} \right) + \rho_a S_a \left(\alpha_a + \frac{1}{S_a} \frac{\partial S_a}{\partial P} \right) + \rho_s S_s \left(\alpha_s + \frac{1}{S_s} \frac{\partial S_s}{\partial P} \right) \right] \quad (5.192)$$

Finding the Compressibilities α_j

Within this model, α_r and α_s are both given a set value by the user. The value used for α_s is $4.17 \times 10^{13} \text{ Pa}^{-1}$. This was found by assuming the system to be at the constant temperature of 40°C and interpolating from the compressibilities of NaCl at varying temperatures given by Robertson et al. (1958).

The compressibilities of the gaseous and aqueous phases, α_g and α_a respectively, can be calculated using equation (5.79), such that:

$$\alpha_j = \frac{1}{\rho_j} \frac{\partial \rho_j}{\partial P} = \rho_j \sum_{i=1}^{N_c} \frac{X_{ij}}{\rho_{ij}} \left(\frac{1}{\rho_{ij}} \frac{\partial \rho_{ij}}{\partial P} - \frac{1}{X_{ij}} \frac{\partial X_{ij}}{\partial P} \right) \quad (5.193)$$

or, equivalently:

$$\alpha_j = \rho_j \sum_{i=1}^{N_c} \frac{X_{ij}}{\rho_{ij}} \left(\alpha_{ij} - \frac{1}{X_{ij}} \frac{\partial X_{ij}}{\partial P} \right) \quad (5.194)$$

As was stated in Section 4.5.1, the values of α_{ij} are found by differentiation of several different equations of state.

Taking into account the components that can exist in the gaseous and aqueous phases, equation (5.194) can be used to conclude that:

$$\alpha_g = \rho_g \left[\frac{X_{cg}}{\rho_{cg}} \left(\alpha_{cg} - \frac{1}{X_{cg}} \frac{\partial X_{cg}}{\partial P} \right) + \frac{X_{wg}}{\rho_{wg}} \left(\alpha_{wg} - \frac{1}{X_{wg}} \frac{\partial X_{wg}}{\partial P} \right) \right] \quad (5.195)$$

and

$$\alpha_a = \rho_a \left[\frac{X_{ca}}{\rho_{ca}} \left(\alpha_{ca} - \frac{1}{X_{ca}} \frac{\partial X_{ca}}{\partial P} \right) + \frac{X_{wa}}{\rho_{wa}} \left(\alpha_{wa} - \frac{1}{X_{wa}} \frac{\partial X_{wa}}{\partial P} \right) + \frac{X_{na}}{\rho_{na}} \left(\alpha_{na} - \frac{1}{X_{na}} \frac{\partial X_{na}}{\partial P} \right) \right] \quad (5.196)$$

It is clear from equations (5.195) and (5.196) that in order to evaluate expressions for the compressibilities α_j it is necessary to calculate $\frac{\partial X_{ij}}{\partial P}$ for all required combinations of i and j .

Recalling the piecewise expression for X_{cg} , equation (5.31), and that composition does not depend on pressure, from which it follows that $\frac{\partial z_i}{\partial P} = 0$, it can be calculated that:

$$\frac{\partial X_{cg}}{\partial P} = \begin{cases} 0, & z_c \leq \frac{x_{ca}(1-z_n)}{1-x_{na}} \\ \frac{\partial x_{cg}}{\partial P}, & \frac{x_{ca}(1-z_n)}{1-x_{na}} < z_c < x_{cg}(1-z_n) \\ 0, & z_c \geq x_{cg}(1-z_n) \end{cases} \quad (5.197)$$

The values of $\frac{\partial x_{ij}}{\partial P}$ can be found using finite difference, with the exception of $\frac{\partial x_{na}}{\partial P}$ which is assumed to be equal to zero, as its value is calculated using an equation by [Potter et al. \(1977\)](#) that does not take pressure into account.

The derivative $\frac{\partial X_{wg}}{\partial P}$ can also be found from equation (5.197) as:

$$\frac{\partial X_{wg}}{\partial P} = -\frac{\partial X_{cg}}{\partial P} \quad (5.198)$$

Similarly, recalling the full piecewise expression for X_{ca} from equation (5.40) and using the same assumptions for taking derivatives with respect to pressure gives that:

$$\frac{\partial X_{ca}}{\partial P} = \begin{cases} 0, & z_c \leq \frac{x_{ca}(1-z_n)}{1-x_{na}}, \\ \frac{\partial x_{ca}}{\partial P}, & \frac{x_{ca}(1-z_n)}{1-x_{na}} < z_c < x_{cg}(1-z_n) \\ 0, & z_c \geq x_{cg}(1-z_n) \end{cases} \quad (5.199)$$

Additionally, taking pressure derivatives of the expressions in equation (5.43) leads to:

$$\frac{\partial X_{na}}{\partial P} = \begin{cases} \frac{z_n \left[(X_{ca} - z_c) \frac{\partial X_{cg}}{\partial P} + (z_c - X_{cg}) \frac{\partial X_{ca}}{\partial P} \right]}{(X_{cg} - z_c)^2}, & z_c < x_{cg}(1-z_n), \quad z_n \leq \frac{x_{na}(X_{cg} - z_c)}{X_{cg} - X_{ca}} \\ \frac{\partial x_{na}}{\partial P}, & z_c < x_{cg}(1-z_n), \quad z_n > \frac{x_{na}(X_{cg} - z_c)}{X_{cg} - X_{ca}} \\ 0, & z_c \geq x_{cg}(1-z_n), \quad z_n \geq 0 \end{cases} \quad (5.200)$$

$\frac{\partial X_{wa}}{\partial P}$ can subsequently be found from:

$$\frac{\partial X_{wa}}{\partial P} = -\frac{\partial X_{ca}}{\partial P} - \frac{\partial X_{na}}{\partial P} \quad (5.201)$$

meaning that all necessary values of $\frac{\partial X_{ij}}{\partial P}$ have been defined, and hence expressions can be given for all compressibilities α_j .

Finding the Derivatives $\frac{1}{S_j} \frac{\partial S_j}{\partial P}$

The only remaining terms left to express in order to fully define $\frac{\partial F}{\partial P}$ from equation (5.192) are the saturation derivatives with respect to pressure, $\frac{1}{S_j} \frac{\partial S_j}{\partial P}$. These derivatives can again be calculated by writing the saturation expressions in the form given in equation (5.80), from which it follows that the derivatives can be found using equation (5.83).

By looking at equation (5.58), it can be seen that when no solid phase is present, $S_s = 0$ and so $\frac{\partial S_s}{\partial P}$ will also be zero. When it is the case that $z_c \leq \frac{x_{ca}(1-z_n)}{1-x_{na}}$ and $z_n > x_{na}$, and

so no gaseous phase is present but both aqueous and solid phases are, equations (5.107) to (5.110) illustrated that the solid saturation can be written as:

$$S_s = \frac{\rho_a(z_n - x_{na})}{\rho_s(1 - z_n) + \rho_a(z_n - x_{na})} \quad (5.202)$$

which can also be expressed as:

$$S_s = \frac{v_{11}}{v_{11} + v_{12}} \quad (5.203)$$

where:

$$v_{11} = \rho_a(z_n - x_{na}) \quad (5.204)$$

and

$$v_{12} = \rho_s(1 - z_n) \quad (5.205)$$

Using equation (5.83):

$$\frac{dS_s}{S_s} = \frac{v_{12}dv_{11} - v_{11}dv_{12}}{v_{11}(v_{11} + v_{12})} \quad (5.206)$$

and so:

$$\frac{1}{S_s} \frac{\partial S_s}{\partial P} = \frac{v_{12} \frac{\partial v_{11}}{\partial P} - v_{11} \frac{\partial v_{12}}{\partial P}}{v_{11}(v_{11} + v_{12})} \quad (5.207)$$

Taking the derivatives with respect to pressure of v_{11} and v_{12} , using the assumptions that $\frac{\partial x_{na}}{\partial P} = 0$ and $\frac{\partial z_i}{\partial P} = 0$, gives:

$$\frac{\partial v_{11}}{\partial P} = (z_n - x_{na}) \frac{\partial \rho_a}{\partial P} \quad (5.208)$$

and

$$\frac{\partial v_{12}}{\partial P} = (1 - z_n) \frac{\partial \rho_s}{\partial P} \quad (5.209)$$

Recall from equation (5.191) that:

$$\alpha_j = \frac{1}{\rho_j} \frac{\partial \rho_j}{\partial P} \quad (5.210)$$

which can be rearranged to show that:

$$\frac{\partial \rho_j}{\partial P} = \alpha_j \rho_j \quad (5.211)$$

Given that the compressibilities α_j have already been calculated, it is more convenient to write the derivatives $\frac{\partial \rho_j}{\partial P}$ in this form. Therefore, $\frac{\partial v_{11}}{\partial P}$ and $\frac{\partial v_{12}}{\partial P}$ can be written as:

$$\frac{\partial v_{11}}{\partial P} = (z_n - x_{na}) \alpha_a \rho_a \quad (5.212)$$

and

$$\frac{\partial v_{12}}{\partial P} = (1 - z_n) \alpha_s \rho_s \quad (5.213)$$

In the situation when both gaseous and solid phases are present without an aqueous phase, which means that $z_c \geq x_{cg}(1 - z_n)$ and $z_n > 0$, equations (5.116) and (5.117) showed that the solid saturation can be expressed in the form of equation (5.80) with:

$$v_{11} = \rho_g z_n \quad (5.214)$$

and

$$v_{12} = \rho_s(1 - z_n) \quad (5.215)$$

and hence $\frac{1}{S_s} \frac{\partial S_s}{\partial P}$ can be found using equation (5.207) with:

$$\frac{\partial v_{11}}{\partial P} = z_n \alpha_g \rho_g \quad (5.216)$$

and

$$\frac{\partial v_{12}}{\partial P} = (1 - z_n) \alpha_s \rho_s \quad (5.217)$$

Finally, if all three phases are present and so $\frac{x_{ca}(1-z_n)}{1-x_{na}} < z_c < x_{cg}(1 - z_n)$ and $z_n > \frac{x_{na}(x_{cg}-z_c)}{x_{cg}-x_{ca}}$, the solid saturation can be written in the format given by equation (5.80) with:

$$v_{11} = \rho_g \rho_a [z_n(x_{cg} - x_{ca}) - x_{na}(x_{cg} - z_c)] \quad (5.218)$$

and

$$v_{12} = \rho_s \rho_a [z_c(1 - x_{na}) - x_{ca}(1 - z_n)] - \rho_g \rho_s [z_c - x_{cg}(1 - z_n)] \quad (5.219)$$

as illustrated by equations (5.123) and (5.124).

Using these terms, $\frac{1}{S_s} \frac{\partial S_s}{\partial P}$ for this zone can be calculated by using equation (5.207) with:

$$\frac{\partial v_{11}}{\partial P} = \rho_g \rho_a \left[(\alpha_g + \alpha_a) [z_n(x_{cg} - x_{ca}) - x_{na}(x_{cg} - z_c)] + (z_n - x_{na}) \frac{\partial x_{cg}}{\partial P} - z_n \frac{\partial x_{ca}}{\partial P} \right] \quad (5.220)$$

and

$$\begin{aligned} \frac{\partial v_{12}}{\partial P} = \rho_a \rho_s \left[(\alpha_a + \alpha_s) [z_c(1 - x_{na}) - x_{ca}(1 - z_n)] - (1 - z_n) \frac{\partial x_{ca}}{\partial P} \right] \\ - \rho_g \rho_s \left[(\alpha_g + \alpha_s) [z_c - x_{cg}(1 - z_n)] - (1 - z_n) \frac{\partial x_{cg}}{\partial P} \right] \end{aligned} \quad (5.221)$$

A piecewise function for $\frac{1}{S_s} \frac{\partial S_s}{\partial P}$ can now be expressed, as terms have been calculated for every possible combination of phases.

It is now necessary to calculate derivatives with respect to pressure for the aqueous saturation. The values of S_a for different phase combinations were expressed in equation (5.62). Again, in situations where the aqueous saturation is constant, i.e. $S_a = 0$ due to no

aqueous phase being present or $S_a = 1$ as both the gaseous and solid phases are absent, $\frac{\partial S_a}{\partial P} = 0$. Additionally, if only aqueous and solid phases are present, and so $z_c \leq \frac{x_{ca}(1-z_n)}{1-x_{na}}$ and $z_n > x_{na}$, it must be that $\frac{\partial S_a}{\partial P} = -\frac{\partial S_s}{\partial P}$. Within this equation, the expression for $\frac{\partial S_s}{\partial P}$ that was previously calculated for these conditions can be used.

When $\frac{x_{ca}(1-z_n)}{1-x_{na}} < z_c < x_{cg}(1-z_n)$ and $z_n \leq \frac{x_{na}(x_{cg}-z_c)}{x_{cg}-x_{ca}}$, and hence only aqueous and gaseous phases are present, it is necessary to return to the use of equation (5.80) and equation (5.83) to find an expression for $\frac{1}{S_a} \frac{\partial S_a}{\partial P}$. Equations (5.130) to (5.133) illustrated that in this case, the aqueous saturation can be given as:

$$S_a = \frac{\rho_g(x_{cg} - z_c)}{\rho_g(x_{cg} - z_c) + \rho_a(z_c - x_{ca})} \quad (5.222)$$

or, equivalently:

$$S_a = \frac{v_{11}}{v_{11} + v_{12}} \quad (5.223)$$

where:

$$v_{11} = \rho_g(x_{cg} - z_c) \quad (5.224)$$

and

$$v_{12} = \rho_a(z_c - x_{ca}) \quad (5.225)$$

Using equation (5.83), it must be that:

$$\frac{1}{S_a} \frac{\partial S_a}{\partial P} = \frac{v_{12} \frac{\partial v_{11}}{\partial P} - v_{11} \frac{\partial v_{12}}{\partial P}}{v_{11}(v_{11} + v_{12})} \quad (5.226)$$

in which:

$$\frac{\partial v_{11}}{\partial P} = \rho_g \left[\alpha_g(x_{cg} - z_c) + \frac{\partial x_{cg}}{\partial P} \right] \quad (5.227)$$

and

$$\frac{\partial v_{12}}{\partial P} = \rho_a \left[\alpha_a(z_c - x_{ca}) - \frac{\partial x_{ca}}{\partial P} \right] \quad (5.228)$$

As was shown in equation (5.54), the aqueous saturation when all three phases are present is expressed in terms of the solid saturation, such that:

$$S_a = \frac{S_s(\rho_s + z_n \rho_g - z_n \rho_s) - z_n \rho_g}{\rho_a(z_n - x_{na}) - z_n \rho_g} \quad (5.229)$$

The quotient rule can now be used to find $\frac{\partial S_a}{\partial P}$, such that:

$$\frac{\partial S_a}{\partial P} = \frac{v \frac{\partial u}{\partial P} - u \frac{\partial v}{\partial P}}{v^2} \quad (5.230)$$

where:

$$u = S_s(\rho_s + z_n \rho_g - z_n \rho_s) - z_n \rho_g \quad (5.231)$$

and

$$v = \rho_a(z_n - x_{na}) - z_n\rho_g \quad (5.232)$$

and hence:

$$\frac{\partial u}{\partial P} = (\rho_s + z_n\rho_g - z_n\rho_s)\frac{\partial S_s}{\partial P} + S_s[\rho_s\alpha_s(1 - z_n) + z_n\rho_g\alpha_g] - z_n\rho_g\alpha_g \quad (5.233)$$

and

$$\frac{\partial v}{\partial P} = (z_n - x_{na})\rho_a\alpha_a - z_n\rho_g\alpha_g \quad (5.234)$$

Finally, the derivative of the gaseous saturation with respect to pressure, $\frac{\partial S_g}{\partial P}$ can be found by:

$$\frac{\partial S_g}{\partial P} = -\frac{\partial S_a}{\partial P} - \frac{\partial S_s}{\partial P} \quad (5.235)$$

All terms in equation (5.192) have now been defined, and so a full, piecewise expression for $\frac{\partial F}{\partial P}$ can now be found by substituting all of the necessary terms into equation (5.192).

It follows that the derivatives $\frac{\partial F}{\partial z_c}$, $\frac{\partial F}{\partial z_w}$ and $\frac{\partial F}{\partial P}$ have now all been fully defined. This means that all terms within $\frac{\partial P}{\partial t}$ have now been found, and hence an expression for $\frac{\partial P}{\partial t}$ can be given to the ODE solver, alongside those for $\frac{\partial z_c}{\partial t}$ and $\frac{\partial z_w}{\partial t}$. The values of the PDVs, z_c , z_w and P , can therefore be found at all times and all points in space.

5.8 Model Output

The first output of the three phase model is the global pressure and gas saturation plotted against the radial distance, r , at several different times up to 100 years, as shown in Figure 5.1. As was the case with the output of the two phase model in Chapter 4, both the pressure and gas saturation are compared to the analytical solution found by Mathias et al. (2011b), which does not take into account the effects of capillary pressure. The parameters inputted into the model to produce Figure 5.1 and the figure illustrating the variation in solid saturation with radial distance for up to 100 years, Figure 5.2, are:

Parameter	Value	Parameter	Value	Parameter	Value
r_w (m)	0.25	k_{rg0} (-)	0.3	H (m)	30
r_E (m)	2.5×10^5	k_{ra0} (-)	1	P_{c0} (Pa)	19600
P_0 (Pa)	10^7	n_g (-)	3	m (-)	0.5
α_r (Pa ⁻¹)	3.54×10^{-10}	n_a (-)	3	M_0 (Mt/year)	0.3
k (m ²)	10^{-13}	S_{ar} (-)	0.5	T (°C)	40
ϕ (-)	0.2	S_{gc} (-)	0	P_{cd} (Pa)	10^8
α_s (Pa ⁻¹)	4.17×10^{-13}	X_{nb} (-)	0.15		

Table 5.1: Constant parameters inputted into the three component and three phase model, to give the output in Figures 5.1 and 5.2.

Note that X_{nb} [-] represents the initial mass fraction of salt dissolved within the brine.

The model again appears to be unstable, because, like the two phase model, it will not run for a significant number of points when P_{cd} is set to the desired value of capillary pressure at zero aqueous saturation of Webb (2000), which was 10^9 Pa. It should be noted from Table 5.1 that P_{cd} is therefore set to 10^8 Pa, in order to use a value as close as possible to Webb's desired value that the model will run for. However, the addition of an extra component and phase seems to have also added to the instability of the model, as it failed to run for up to 100 years when the number of spatial points went over 150. Figure 5.1 and Figure 5.2 have therefore been created using a model that was run for 150 points in space, which is the maximum spatial accuracy possible over the desired time period.

Despite the model now incorporating three components and phases, Figure 5.1 illustrates that the wave structure for the gas saturation has been preserved, with the leading and trailing shock dividing the aqueous only and equilibrium regions, and the equilibrium region and dry out zone, respectively. In this particular model, it can be seen by looking at both the gas saturation in Figure 5.1 and the solid saturation in Figure 5.2 that no points in space are in the three phase or aqueous and solid phase regions. It should be noted, however, that the gas saturation in the dry out zone does not reach one. This is due to the presence of the solid salt in this region, as illustrated in Figure 5.2. Taking into account the lower resolution of Figure 5.1 relative to the figures of the two phase model in Chapter 4 that were created using 1000 points in space, the gas saturation output of the model compares well to the analytical solution. Again, the main difference between the numerical and analytical solutions is the sharper edges of the analytical solution, which is

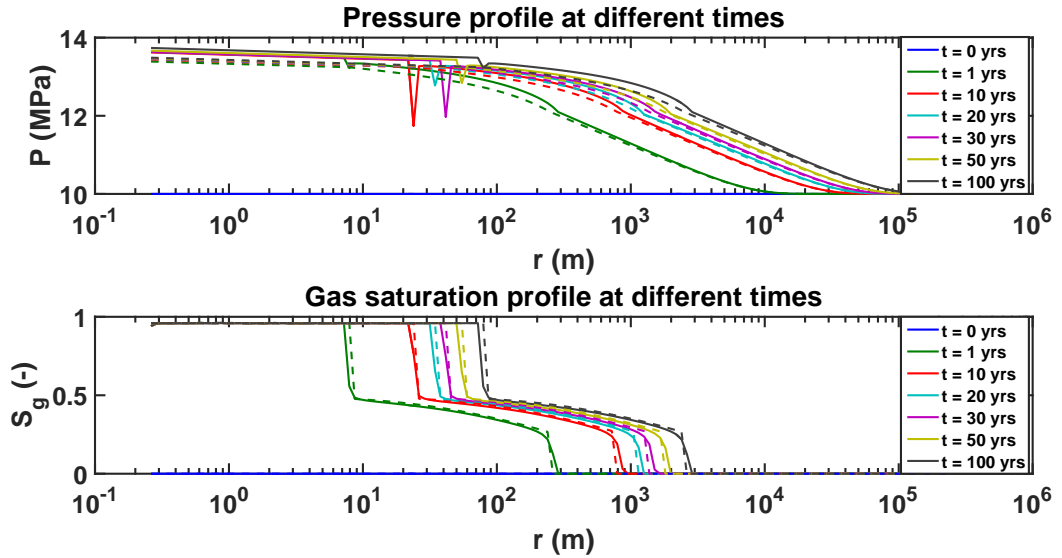


Figure 5.1: A graph to show the pressure and gas saturation output of the model for the initial parameters in Table 5.1 and for the times shown in the legend. The model was run for 150 points in space.

not replicated in the MOL solution due to increased dispersion. The edge of the leading shock is also slightly further forward in the numerical solution due to the inclusion of the effects of capillary pressure.

Figure 5.1 also shows that global pressure is at its highest near the point of injection, and that pressure increases as time goes on. The numerical and analytical solutions compare well in the aqueous only region and the majority of the equilibrium region, but the dip in pressure near the boundary of the dry out zone and the equilibrium region is noticeable in the numerical solution. As was explained in Section 4.7, this dip is a numerical instability caused by a large drop in capillary pressure between the first two points at which an aqueous phase is present, and becomes larger as the value of P_{cd} increases. The inclusion of capillary pressure effects in the numerical solution also means that the global pressure in the dry out zone is underestimated by the analytical solution.

Figure 5.2 has clear instabilities, as illustrated by the very small variations in solid saturation across the dry out zone and the sharp rise near to the injection point. It is, however, still a very useful figure for its illustration that salt only forms behind the trailing shock where the liquid water has evaporated, and for making it clear that the dry out zone grows as time passes. The variations in solid saturation are so small, especially when the scale that the graph is plotted on is considered, that they seem to be caused purely by numerical instability, which would suggest that the solid saturation can be assumed to be

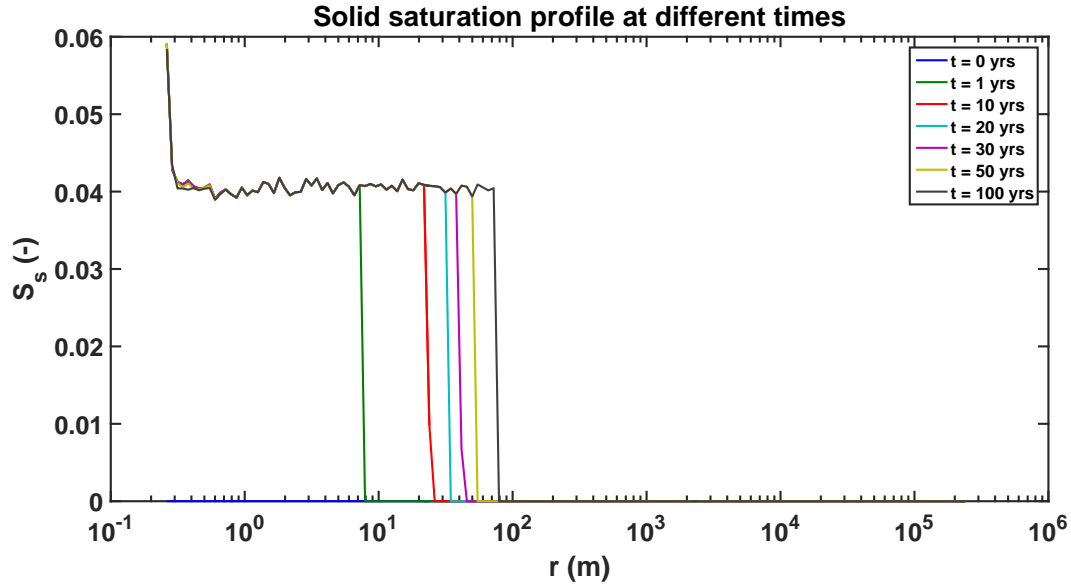


Figure 5.2: A graph to show the solid saturation output of the model for the initial parameters in Table 5.1 and for the times shown in the legend. The model was run for 150 points in space.

constant throughout the dry out zone. This assumption cannot be relied upon from this model alone, however.

In order to assist in gaining a good idea of the processes and parameters that can increase salt precipitation in a saline aquifer, a phase saturation can be plotted against the varying capillary number, Ca [-]. This is a dimensionless constant, found from:

$$Ca = \frac{Q_0 \mu_g}{4\pi H k P_{c0}} \quad (5.236)$$

where Q_0 [$L^3 T^{-1}$] is the rate of injection of CO_2 into the saline formation, μ_g [$ML^{-1} T^{-1}$] is the dynamic viscosity of the gaseous phase, H [L] is the formation thickness, k [L^2] is the permeability of the formation and P_{c0} [$ML^{-1} T^{-2}$] is a reference “air-entry” pressure of the formation.

It can therefore be seen that the capillary number represents the ratio of the CO_2 injection rate to the product of the CO_2 mobility and the air-entry pressure of the porous medium, and hence it compares the relative effect of the frictional resistance associated with fluid movement with the surface tension that acts across the interface between the gaseous and aqueous phases. Small values of Ca imply that capillary processes are important (Kelly and Mathias, 2018).

Figures 5.3 and 5.4 show how varying the value of Ca in the three phase numerical model affects the gas saturation pattern in the formation. Any of the parameters in equation (5.236) could be changed in order to obtain the different values of Ca , but in this

case it was the rate of injection, Q_0 , that was altered. The remaining parameters were kept at their values in Table 5.1, and the corresponding rates of injection calculated for each of the values of Ca modelled in Figures 5.3 and 5.4. The time taken to inject 4.73Mt of CO₂ was then calculated for each injection rate, and the model run for this amount of time for the associated injection rates and values of Ca. This measure ensures that the same amount of CO₂ has been injected in each simulation, and hence the effects of the different values of Ca can be legitimately compared.

Figure 5.3 plots gas saturation against radial distance for various values of Ca for 50 points in space, while Figure 5.4 does the same for 80 points in space. It should be noted that P_{cd} has been lowered to 10^7 Pa for increased stability for these simulations, and that the output of the numerical reservoir simulator, TOUGH2 (Pruess and Spycher, 2007) is also plotted for verification. Both figures clearly illustrate that decreasing the value of Ca, which is analogous to decreasing the injection rate into the formation, result in a lower value of gas saturation in the dry out zone, which corresponds to increased salt precipitation. This is due to high capillary pressure gradients causing increased backflow of brine towards the site of injection in counter-current imbibition, therefore providing additional salt that is then also able to precipitate in the dry out zone of the aquifer. The lower the injection rate, the higher the relative effect of counter-current imbibition on flow within the formation. However, comparison of Figures 5.3 and 5.4 reveals that, although they both show the same pattern in that the gas saturation values decrease as Ca decreases, the actual values of gas saturation do not correlate for the same values of Ca across the figures. It appears that the drop in gas saturation as Ca decreases is noticeably less for 80 points in comparison to for 50 points, in particular for values of Ca below 0.13. This indicates that the instabilities within the model are also having an effect here, and the actual gas saturation values given cannot be relied upon as the drop in gas saturation appears to reduce considerably as the number of points in space increases.

In addition, both Figure 5.3 and Figure 5.4 show that the output for Ca = 1.7 and the TOUGH2 output, which is equivalent to Ca $\rightarrow \infty$, match very well. This illustrates that the value of Ca has very little effect on solid saturation as it falls through the higher numbers, but, as can be seen from the figures, it has an increasingly larger impact as Ca falls below 1.7. Finally, it can be seen that the leading shock reaches further out in the formation as Ca decreases. This is again due to the increasing importance in capillary processes as the value of Ca falls.

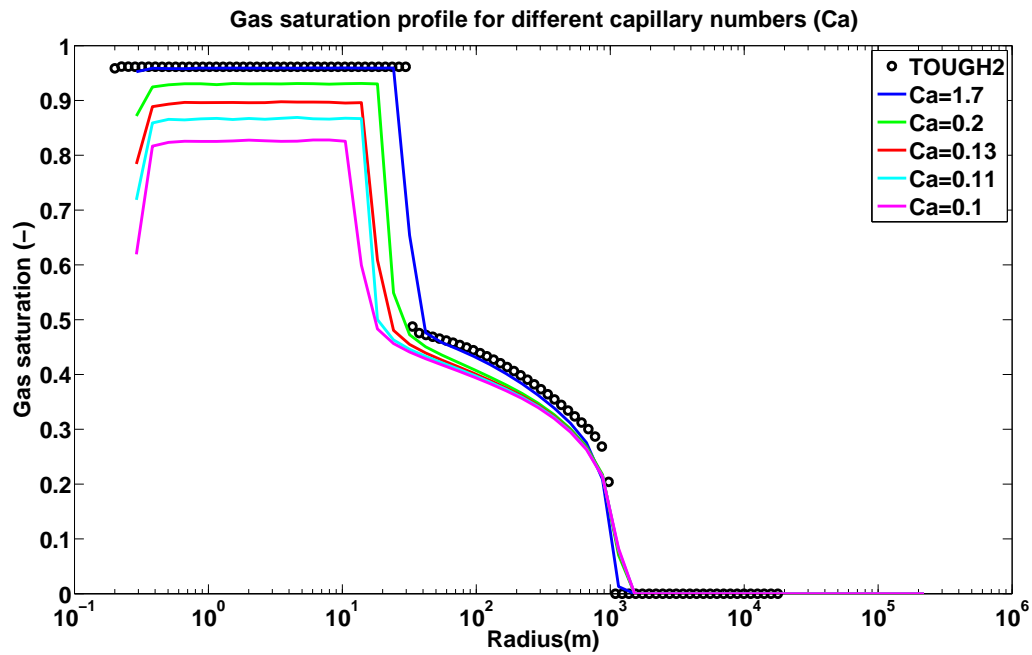


Figure 5.3: A graph to show gas saturation varying with formation radius for several different values of Ca , alongside the output from the numerical reservoir simulator, TOUGH2. To create this, the model was run for 50 points in space and it was assumed that $P_{cd} = 10^7$ Pa

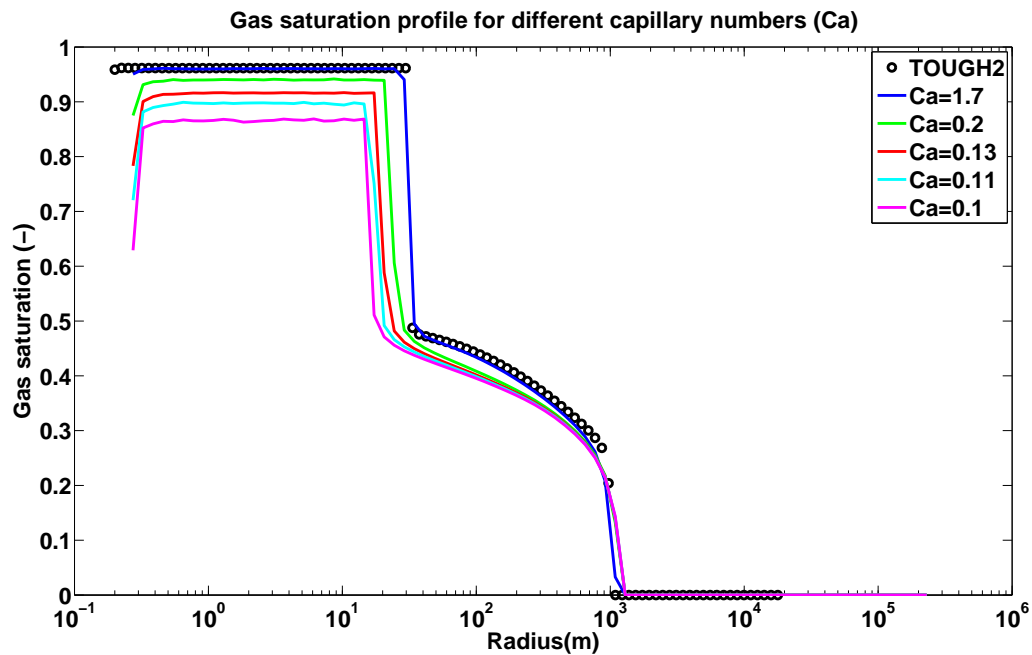


Figure 5.4: A graph to show gas saturation varying with formation radius for several different values of Ca , alongside the output from the numerical reservoir simulator, TOUGH2. To create this, the model was run for 80 points in space and it was assumed that $P_{cd} = 10^7$ Pa

Although all of the figures produced from models formed using the MOL and ODE solver ode15s in Chapters 4 and 5 are useful in that they compare well to the analytical solutions

and allow us to vary different parameters in order to investigate their effects on counter-current imbibition and salt precipitation, they clearly suffer from numerical instability. It is therefore necessary to consider other methods of finding solutions to the three phase flow problem that lessen this instability. Most simulations in fluid dynamics attempt to reduce numerical diffusion to the lowest level possible in order to achieve a high level of accuracy in the solution produced, and the lack of numerical diffusion added to the solution is one of the reasons that the ODE solvers were chosen to solve this problem over other possible methods, as discussed in Section 3.3.2. However, numerical diffusion can also be an advantage in that it can smooth out instabilities, and hence using a method that has a higher level of numerical diffusion may reduce the instability in the current figures. The possibility of solving the problem using the semi-implicit method is discussed as a part of the future work that could be done on this project in Section 7.2, but Chapter 6 will look into another alternative: the use of pseudospectral methods.

Chapter 6

Self-Similar Pseudospectral Solution for Incompressible Three Component and Three Phase Flow

As was explained at the end of Chapter 5, the method of lines (MOL) solutions described in Chapters 4 and 5 have been very useful, but they still appear to have some numerical issues. Therefore, it is necessary to consider other methods that can be used to accurately study partially miscible three component and three phase flow and the build-up of salt precipitation in the dry out zone of a saline aquifer.

One useful mathematical solution for two phase flow in porous media is the McWhorter and Sunada solution (McWhorter and Sunada, 1990). This, like the Buckley-Leverett solution (Buckley and Leverett, 1942), looks at the immiscible flow of two phases but, in contrast to the Buckley-Leverett solution, does incorporate the effects of capillary pressure, meaning that it cannot be solved by the method of characteristics (MOC) as the Buckley-Leverett solution was in Chapter 3. The McWhorter and Sunada solution was commonly solved by iterative integrals, which often led to convergence problems, until Bjørnarå and Mathias formed a different, more robust solution using a pseudospectral Chebyshev differentiation matrix (Bjørnarå and Mathias, 2013). This chapter introduces the McWhorter and Sunada solution and pseudospectral methods, and uses the method of Bjørnarå and Mathias (2013) to extend the similarity solution of McWhorter and Sunada (1990) to incorporate the partial miscibility of phases and account for three component and three phase flow. This gives a solution that can accurately study the control that capillary pressure and other

parameters have on salt precipitation when CO₂ is injected into a saline aquifer.

A version of this chapter is published in the following article:

Kelly, H.L. and Mathias, S.A. (2018). Capillary processes increase salt precipitation during CO₂ injection in saline formations. *Journal of Fluid Mechanics*, 852, 398-421.

6.1 Introduction

A number of numerical modelling studies have been undertaken to investigate important controls on salt precipitation in the dry out zone, some of which have been introduced in previous chapters of this thesis. [Zeidouni et al. \(2009\)](#) derived an analytical solution using the MOC to estimate the volume fraction of precipitated salt in the dry out zone (hereafter referred to as C_{30}) due to CO₂ injection in saline formations. They concluded that the distribution of precipitated salt was uniform within the dry out zone. However, an important limiting assumption in their study is that the capillary pressure, i.e. the difference between the pressures of the non-wetting phase and the wetting phase (the CO₂-rich and aqueous phases, respectively, in this context), is assumed to be negligible. [Pruess and Müller \(2009\)](#) explored the same problem using the numerical reservoir simulator, TOUGH2, with the CO₂ storage module, ECO2N ([Pruess and Spycher, 2007](#)). When capillary pressure is set to zero, C_{30} is found to be insensitive to injection rate. However, when capillary pressure is accounted for, C_{30} is found to increase with reducing CO₂ injection rate.

As was described in Section 1.4, the physical explanation for this is that the capillary pressure is significantly increased as the wetting saturation is reduced ([Pruess and Müller, 2009](#)). This can lead to a reversal of the direction of the wetting pressure gradient, which in turn results in counter-current flow, whereby brine flows in the opposite direction to the injected CO₂. The counter-current flow provides additional brine to the dry out zone leading to an increased availability of salt for precipitation. The counter-current flow rate is driven by phase saturation gradients. As the injection rate increases, the counter-current flow becomes less significant in comparison ([Pruess and Müller, 2009](#)).

[Kim et al. \(2012\)](#) extended the work of [Pruess and Müller \(2009\)](#) by performing a wider sensitivity analysis. They found that the value of C_{30} was significantly increased for

scenarios involving high permeability and low injection rates. Furthermore, contrary to [Zeidouni et al. \(2009\)](#), they found that C_{30} was non-uniform, with the highest values present at the edge of the dry out zone. This localised increase in salt precipitation is attributed to the combined effects of gravity and capillary pressure driven counter-current flow.

[Li et al. \(2013\)](#) found that smoother capillary pressure curves lead to faster dissolution of CO_2 into the aqueous phase. This is presumably because smoother capillary pressure curves lead to more capillary diffusion of the CO_2 -rich phase and hence greater interfacial area between the CO_2 -rich phase and the aqueous phase.

The suite of numerical simulations described by [Pruess and Müller \(2009\)](#) and [Kim et al. \(2012\)](#) have provided significant insight into the processes that control salt precipitation during CO_2 injection in saline formations. However, probably due to the perceived computational expense of numerically simulating this problem to an adequate accuracy, a more widespread sensitivity analysis has not been undertaken to further understand this process.

Analytical solutions have been developed to better understand many other aspects of the CO_2 storage process. [Nordbotten and Celia \(2006\)](#) developed a similarity solution to study the propagation rate of a CO_2 plume and its associated dry out zone during injection of CO_2 into a cylindrical saline formation. [Hesse et al. \(2007, 2008\)](#) and [MacMinn et al. \(2010, 2011\)](#) developed MOC solutions to study the migration of CO_2 plumes following the cessation of injection. [Mathias et al. \(2011a\)](#) extended the analytical solution of [Nordbotten and Celia \(2006\)](#) to estimate the resulting pressure buildup within an injection well. [Mathias et al. \(2011b\)](#) combined the work of [Mathias et al. \(2011a\)](#) and [Zeidouni et al. \(2009\)](#) to study the role of partial miscibility between the CO_2 and brine on pressure buildup. More recently, [Mathias et al. \(2014\)](#) derived a MOC solution to estimate the temperature distribution around a CO_2 injection well in a depleted gas reservoir. There are many other such examples in the literature. However, all the analytical solutions presented to date revolve around the CO_2 transport problem reducing to a hyperbolic partial differential equation (PDE), such that MOC or some variant can be used for the solution procedure. The difficulty of accounting for capillary pressure is that this leads to a diffusive component within the equations, rendering the MOC inadequate in this regard.

However, as was explained at the beginning of the chapter, [McWhorter and Sunada \(1990\)](#) derived a similarity solution to look at two-phase immiscible flow around an injection

well, which explicitly captures the counter-current flow associated with capillary pressure effects. In the past, their solution has not been commonly used due to difficulties with evaluating the necessary nonlinear multiple integrals associated with their equations (Fučík et al., 2007). More recently, however, Bjørnarå and Mathias (2013) have provided a more efficient evaluation procedure by applying the equations as a boundary value problem, which they then solve using a Chebyshev polynomial differentiation matrix (Weideman and Reddy, 2000).

This chapter will begin by describing the work of McWhorter and Sunada (1990) and the process that they went through to form their similarity solution in more detail. Then, the pseudospectral methods used by Bjørnarå and Mathias (2013) to solve the boundary value problem of McWhorter and Sunada (1990) and the advantages of these methods are explained. The process of McWhorter and Sunada (1990) is then applied to find a similarity solution for partially miscible, three component and three phase flow. This begins with the formation of a PDE to describe multiphase flow under these conditions. This is then reduced to an ordinary differential equation (ODE) by application of a similarity transform, and the resulting boundary value problem is solved using a Chebyshev polynomial differentiation matrix. The necessary equations are then presented to determine the volume fraction of precipitated salt in the dry out zone. A set of verification examples are presented based on a gas-displacing-oil scenario, previously presented by Orr (2007). A CO₂-injection-in-a-saline-formation scenario is then presented, which is compared with simulation results from TOUGH2 for verification. Finally, a wider sensitivity analysis is conducted to better understand the main controls in this context.

6.2 The McWhorter and Sunada Solution

As was explained above, McWhorter and Sunada (1990) formed a solution for the one-dimensional immiscible flow of two incompressible fluids, in which one is a ‘wetting’ phase and one is a ‘non-wetting’ phase. This solution was not originally intended to be solely for the injection of CO₂ into water, but can easily be applied to this situation by assuming the supercritical CO₂ to be the non-wetting phase and the water to be the wetting phase. It can be considered to be analogous to the Buckley-Leverett solution, with the difference between the two solutions being that the McWhorter and Sunada solution incorporates the effects of capillary pressure, while the Buckley-Leverett solution does not. Therefore, comparisons between the two solutions can be used to evaluate the impact of capillary

pressure (Bjørnarå and Mathias, 2013).

McWhorter and Sunada (1990) found solutions to the linear displacement of both wetting and non-wetting phases by injection of the other phase, looking at both unidirectional and counter-current flow. They also found a solution to the radial, unidirectional displacement of a non-wetting phase by injection of a wetting phase. These solutions were found by considering the mass conservation equation (equation (2.3)) as applicable to the one-dimensional flow of two immiscible, incompressible fluids in a rigid, homogeneous, porous medium. This means that, by considering equations (2.1) to (2.3), the mass conservation equation will reduce to:

$$\phi \frac{\partial S_j}{\partial t} = -\nabla \cdot q_j \quad j = 1, 2 \quad (6.1)$$

where, as can be recalled from Chapter 2, ϕ [-] represents the porosity of the medium, S_j [-] is the volume fraction or saturation of the phase j , q_j [LT⁻¹] is the volumetric flux of the phase j , t [T] represents time and phases 1 and 2 represent the gaseous and aqueous phases, respectively.

It is also necessary to consider equation (2.6), which uses Darcy's Law for multiphase flow to give an expression for q_j , as adapted for one-dimensional flow:

$$q_j = -\frac{k k_{rj}}{\mu_j} (\nabla P_j) \quad (6.2)$$

Here, k [L²] is the permeability of the system, k_{rj} [-] is the relative permeability of phase j , μ_j [ML⁻¹T⁻¹] is the dynamic viscosity of phase j and P_j [ML⁻¹T⁻²] is the phase pressure for phase j .

Also needed is equation (2.12), which expresses the capillary pressure, P_c [ML⁻¹T⁻²], in terms of the two phase pressures, P_1 and P_2 :

$$P_c = P_1 - P_2 \quad (6.3)$$

By rearranging equation (6.3) to be in terms of the phase pressure of the phase being injected, P_j , and substituting this expression into equation (6.2), and in turn substituting the resulting equation for q_j into equation (6.1), McWhorter and Sunada (1990) formed a partial differential equation (PDE), as appropriate to the linear or radial system and the phase that was being injected into the porous medium in each particular solution. For the linear system when a wetting phase is injected into a non-wetting phase, this PDE was:

$$\phi \frac{\partial S_2}{\partial t} = \frac{\partial}{\partial x} \left(J \frac{\partial S_2}{\partial x} \right) - q_t \frac{df_2}{dS_2} \frac{\partial S_2}{\partial x} \quad (6.4)$$

where f_2 [-] is the fractional flow of the aqueous phase, represented by:

$$f_2 = \left(1 + \frac{k_{r1}\mu_2}{k_{r2}\mu_1}\right)^{-1} \quad (6.5)$$

and J [L^2T^{-1}] is a term that represents the capillary-hydraulic properties of the system, given by:

$$J = -\frac{kk_{r1}f_2}{\mu_1} \frac{dP_c}{dS_2} \quad (6.6)$$

In addition, x [L] is the linear distance and q_t [LT^{-1}] represents the total volumetric flux. For the linear system in which a non-wetting phase is being injected into a wetting phase, the PDE formed was:

$$\phi \frac{\partial S_2}{\partial t} = \frac{\partial}{\partial x} \left(J \frac{\partial S_2}{\partial x} \right) + q_t \frac{d(1-f_2)}{dS_2} \frac{\partial S_2}{\partial x} \quad (6.7)$$

Finally, for the radial system, in which only the injection of a wetting phase into a non-wetting phase was looked into, the PDE was:

$$\phi \frac{\partial S_2}{\partial t} = \frac{1}{r} \frac{\partial}{\partial r} \left(rJ \frac{\partial S_2}{\partial r} - \frac{f_2 Q_t}{2\pi H} \right) \quad (6.8)$$

where r [L] is the radial distance, H [L] is the thickness of the formation, and Q_t [L^3T^{-1}] is the total volumetric flow rate. Note that [McWhorter and Sunada \(1990\)](#) give all PDEs in terms of the saturation of the wetting phase, S_2 , but as they are considering a two phase system in which $S_1 = 1 - S_2$, the PDEs can be easily adapted to be written in terms of S_1 if required.

Unfortunately, it is not possible to solve the PDEs formed by [McWhorter and Sunada \(1990\)](#) by the MOC, as was done for the Buckley-Leverett equation in Chapter 3, as the PDEs are no longer hyperbolic due to the highly nonlinear term resulting from the inclusion of capillary pressure ([McWhorter and Sunada, 1990](#)). It would be possible to use the MOL, as was shown in Chapters 4 and 5, to discretise the equations in space and hence reduce the PDEs to ordinary differential equations (ODEs), which could subsequently be solved using an ODE solver in MATLAB, but this is a numerical rather than an exact method and its accuracy can vary. Instead, [McWhorter and Sunada \(1990\)](#) used the property of self-similarity to reduce the PDEs to ODEs.

The property of symmetry within a system is the property of remaining unchanged or invariant when certain transformations are performed ([Gratton, 1991](#)). Self-similarity is when the symmetry of a physical problem means that it is possible to reduce the number of independent variables within the problem, thus leading to a considerable simplification ([Gratton, 1991](#)). [McWhorter and Sunada \(1990\)](#), using the work of [Chen \(1988\)](#), noticed

that their PDEs became self-similar when the injection rate was inversely proportional to the square root of time for the linear systems, and when the injection rate was constant for the radial systems. When this is the case, it is possible to group the space and time variables into one new variable, λ [$\text{LT}^{-\frac{1}{2}}$], which is equal to $xt^{-\frac{1}{2}}$ for the linear systems and $rt^{-\frac{1}{2}}$ for the radial systems. This means that λ is the only independent variable within the problem, and thus all other terms depend on λ rather than space and time. Consequently, all derivatives within the PDEs must be written with respect to λ rather than space and time, and hence the PDEs have been reduced to ODEs. The initial and boundary conditions of the problem, which give the initial values of the phase saturations as well as their values at the boundaries of the porous medium, are also converted to be written in terms of λ rather than space and time. This method is also known as applying a similarity transform.

McWhorter and Sunada (1990) then solved the resulting ODEs using iterative integrals. However, this solution involves the difficult evaluation of nonlinear multiple integrals, and also has issues with convergence as the injection saturation approaches unity (Bjørnarå and Mathias, 2013). Bjørnarå and Mathias (2013) focused on the linear version of the problem in which a wetting phase is injected into a porous medium to displace a non-wetting phase. They initially formed a PDE, which they then reduced to an ODE in a similar way to the work of McWhorter and Sunada (1990), albeit that the equation was written in a normalised form and used a slightly different notation. However, they subsequently solved the ODE using a pseudospectral Chebyshev differentiation matrix, forming a more robust and accurate solution to the equation of McWhorter and Sunada. The use of pseudospectral methods will be fully explained in Section 6.3, and will also form the basis of the solution formed in this chapter that looks at three phase, partially miscible flow in a radial system.

6.3 Pseudospectral Methods

Matrix notation is extremely useful in mathematics due to its conciseness and flexibility. Using matrices, it is possible to reduce complicated formulae to just a few symbols, therefore gaining a better insight into the essential properties of mathematical models and facilitating algebraic manipulations (Piché and Kanninen, 2009). One area in which it can be helpful is in the discretisation of differential equations using differentiation matrices, \mathbf{D} (Piché and Kanninen, 2009). The idea behind the use of these matrices is that the

d th derivative of a univariate scalar function y can be calculated at certain, distinct nodes \mathbf{x} using:

$$y^{(d)}(\mathbf{x}) = \mathbf{D}^{(d)}y(\mathbf{x}) \quad (6.9)$$

and this forms the basis of the pseudospectral method that Bjørnarå and Mathias (2013) used to solve the boundary value problem (the ODE with boundary conditions) found by McWhorter and Sunada (1990), rather than using direct integration.

The pseudospectral method is also known as the spectral collocation method or the ‘interpolating’ spectral method (Boyd, 2001, p.12). It is a form of the spectral method, in which the solution of the differential equation is written in the form of a sum of certain basis functions and then the coefficients of the sum are chosen to be the best fit to satisfy the differential equation as well as possible. The best basis functions to use will vary depending on the problem, and the technique used to find the appropriate coefficients will also differ depending on the type of spectral method (Boyd, 2001, p.1). Within the pseudospectral method, the coefficients are chosen such that the differential equation is exactly satisfied at the set of points \mathbf{x} , known as the collocation or interpolation points. As the solution given by the pseudospectral method is exact at these points, it will converge to the exact solution at all points within the domain as the number of interpolation points, N , increases (Boyd, 2001, p.12).

The boundary conditions of the ODE being considered here are non-periodic, which suggests that Chebyshev polynomials are the most appropriate basis functions to use in this case (Boyd, 2001, p.10). The Chebyshev polynomial of the second kind, p , interpolates a function, y , at the interpolation points (which in this case are the Chebyshev points) (Weideman and Reddy, 2000):

$$\mathbf{x}_k = \cos\left(\frac{(k-1)\pi}{N-1}\right) \quad k = 1, 2, \dots, N \quad (6.10)$$

such that $p(\mathbf{x}) = y(\mathbf{x})$ (Bjørnarå and Mathias, 2013). It should be noted that $\mathbf{x}_1 = 1$ and $\mathbf{x}_N = -1$. The spacing of the Chebyshev points is shown in Figure 6.1.

The differentiation matrix, \mathbf{D} , will have dimensions $N \times N$, while the differentiated Chebyshev polynomial, $p'(\mathbf{x})$, will have N terms. The terms of the N th column of \mathbf{D} can be found by substituting the values of x_k into the coefficient of the N th term of $p'(\mathbf{x})$. In other words, the number in position (i, j) in the matrix \mathbf{D} (which from now on will be referred to as $\mathbf{D}_{(i,j)}$) is equal to the coefficient of the j th term in $p'(\mathbf{x})$ when $\mathbf{x}_k = \mathbf{x}_i$ (Trefethen, 2000, p.52).

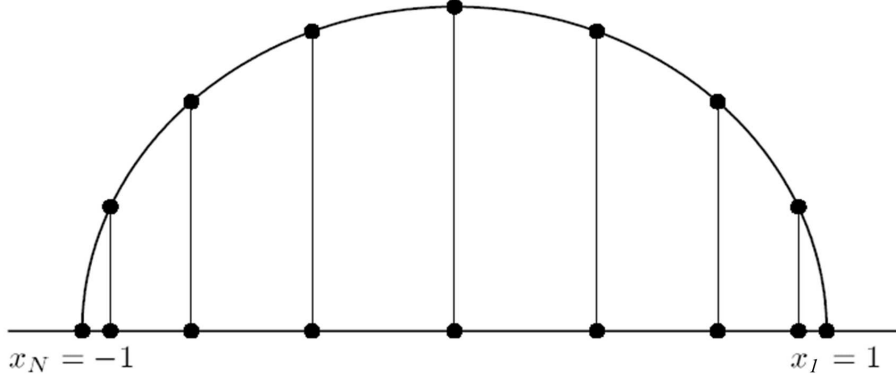


Figure 6.1: A figure to illustrate the spacing of the Chebyshev points. They are the projections onto the x-axis of equally spaced points on the unit circle (Adapted from [Trefethen \(2000, p.43\)](#)).

The value of the Chebyshev polynomial's d th derivative at the Chebyshev points is given by ([Weideman and Reddy, 2000](#)):

$$p^{(d)}(\mathbf{x}) = \mathbf{D}^{(d)}y(\mathbf{x}) \quad (6.11)$$

Here, $\mathbf{D}^{(d)}$ represents the d th order Chebyshev differentiation matrix, which can be found from $(\mathbf{D}^{(1)})^d$ ([Weideman and Reddy, 2000](#)).

The interpolating polynomial is only required to satisfy the differential equation at the interior nodes ([Bjørnarå and Mathias, 2013](#)). At these interior nodes, the values of the interpolating polynomial and the derivatives are, respectively ([Bjørnarå and Mathias, 2013](#)):

$$p(\mathbf{x}_{2:N-1}) = y(\mathbf{x}_{2:N-1}) = \mathbf{I}_{2:N-1,:}\mathbf{y} \quad (6.12)$$

and

$$p^{(d)}(\mathbf{x}_{2:N-1}) = \mathbf{D}_{2:N-1,:}^{(d)}\mathbf{y} \quad (6.13)$$

where $\mathbf{I}_{2:N-1,:}$ and $\mathbf{D}_{2:N-1,:}^{(d)}$ represent the interior rows of a $N \times N$ identity matrix and a $N \times N$ d th order Chebyshev differentiation matrix, respectively.

Boundary conditions are given for the end nodes, which correspond to the first and last rows of the differentiation matrix. The form that the boundary conditions are written in will depend on whether they are Dirichlet or Neumann boundary conditions. Dirichlet conditions will be given as a constraint while Neumann conditions will be written as a derivative, such that ([Bjørnarå and Mathias, 2013](#)):

Dirichlet:

$$p(x = 1) = \mathbf{y}_1 = \mathbf{I}_{1,:}\mathbf{y} \quad (6.14)$$

$$p(x = -1) = \mathbf{y}_N = \mathbf{I}_{N,:}\mathbf{y} \quad (6.15)$$

where $\mathbf{I}_{1,:}$ and $\mathbf{I}_{N,:}$ correspond to the first and last rows of the $N \times N$ identity matrix, respectively.

Neumann:

$$p^{(d)}(x = 1) = \mathbf{D}_{1,:}^{(d)}\mathbf{y} \quad (6.16)$$

$$p^{(d)}(x = -1) = \mathbf{D}_{N,:}^{(d)}\mathbf{y} \quad (6.17)$$

where $\mathbf{D}_{1,:}^{(d)}$ and $\mathbf{D}_{N,:}^{(d)}$ correspond to the first and last rows of the $N \times N$ d th order Chebyshev differentiation matrix, respectively.

One of the key advantages of the use of the pseudospectral method is its high level of accuracy. If the finite difference method was written in matrix form, the matrices would be extremely sparse, as only the immediately surrounding nodes are involved in calculating the derivative at a certain point, as was shown in Section 3.3.1. In contrast, the matrices used in the pseudospectral method are very dense, and the method will achieve as much as ten digits of accuracy in a situation in which using a finite difference method would give only two or three (Trefethen, 2000, p.x). It can be considered that the pseudospectral error is of order $(\frac{1}{N})^N$, meaning that it decreases exponentially as N increases, and the method therefore has exponential convergence (Boyd, 2001, p.8).

The ease of use of pseudospectral methods has improved significantly since merging of matrix-based modelling and matrix-based coding of problems involving differential equations was established by Weideman and Reddy (2000) and Trefethen (2000). They found numerical solutions for boundary value and eigenvalue problems in only 4-10 lines of MATLAB code (Piché and Kannianen, 2009). Particularly useful to this problem is the ‘chebdif.m’ code of Weideman and Reddy (2000), which is used within this chapter to find the Chebyshev points, \mathbf{x} , and the differentiation matrix, \mathbf{D} .

Pseudospectral methods are therefore considered to be a more robust and accurate, and hence preferable, method to finding a solution for boundary value problems with smooth solutions, such as the ODE found by McWhorter and Sunada (1990). The remainder of this chapter is dedicated to using the methods of McWhorter and Sunada (1990) to find an ODE with boundary conditions to represent three component, three phase partially miscible flow when CO_2 is injected into a radial saline aquifer, and using pseudospectral methods, in a similar way to Bjørnarå and Mathias (2013), to subsequently find a solution. This is then analysed in order to investigate the control that capillary pressure and other

parameters have on salt precipitation when CO₂ is injected into a saline aquifer.

6.4 Mathematical Model

A homogenous, cylindrical and porous saline formation is invoked with a thickness of H [L] and an infinite radial extent. The pore space is initially fully saturated with a brine of uniform NaCl concentration. Pure CO₂ is injected at a constant rate of Q_0 [L³T⁻¹] into the centre of the saline formation via a fully penetrating injection well of infinitesimally small radius. The permeability of the saline formation is horizontally isotropic. However, a necessary simplifying assumption is that the vertical permeability is significantly smaller than the horizontal permeability such that gravity effects can be neglected. In this way, during the injection phase, fluid flow can be treated as a one-dimensional radially symmetric process.

Now we will describe the material mixture that resides within the pore space. Consider a mixture of three components: $i = 1, 2$ and 3 . Components 1 and 2 are mutually soluble and can reside within both a non-wetting fluid phase and a wetting fluid phase, denoted hereafter as $j = 1$ and 2 , respectively. Component 3 can dissolve into phase 2 and precipitate to form a solid phase, denoted hereafter as $j = 3$. However, component 3 is assumed not to be able to reside in phase 1 and components 1 and 2 are assumed not to be able to reside in phase 3 . In the context of a CO₂-H₂O-NaCl system, $i = 1, 2$ and 3 for CO₂, H₂O and NaCl, respectively, and $j = 1, 2$ and 3 for the gaseous, aqueous and solid phases, respectively. Note that letter notation has generally been used in previous chapters to denote the components i and phases j (i.e. $i = c, w$ and n and $j = g, a$ and s). Within this chapter, however, numerical notation will be used for easier application to systems that do not necessarily use the components CO₂, H₂O and NaCl, such as the gas-displacing-oil problem from Orr (2007), which the pseudospectral solution is applied to in Section 6.5.1.

All components are assumed to be incompressible and not to experience volume change on mixing, such that component densities can be treated as constant throughout.

The volume fraction of component i for the combined mixture, C_i [-], is defined by:

$$C_i = \sum_{j=1}^3 \sigma_{ij} S_j \quad (6.18)$$

where σ_{ij} [-] is the volume fraction of component i in phase j and, as was mentioned in Section 6.2, S_j [-] is the volume fraction of phase j for the combined mixture, often referred to as the saturation of phase j .

With no additional assumptions, it can be said that:

$$\sum_{i=1}^3 C_i = \sum_{i=1}^3 \sigma_{ij} = \sum_{j=1}^3 S_j = 1 \quad (6.19)$$

By considering the information above about which components can exist in which phases, and applying the concept of equilibrium from Chapter 2 in a similar way to how it was used in Chapters 4 and 5 to find of the mass fraction of component i in phase j , X_{ij} [-], to the volume fractions, the piecewise function, σ_{ij} , can be found to be:

$$\sigma_{ij} = \begin{cases} C_i/(1 - S_3), & C_1 \notin (c_{12}(1 - S_3), c_{11}(1 - S_3)), & i \in \{1, 2\}, & j \in \{1, 2\} \\ c_{ij}, & C_1 \in (c_{12}(1 - S_3), c_{11}(1 - S_3)), & i \in \{1, 2\}, & j \in \{1, 2\} \\ 0, & C_1 \in [0, 1], & i \in \{1, 2\}, & j = 3 \\ 0, & C_3 \in [0, 1], & i = 3, & j = 1 \\ C_3/S_2, & C_3 \in [0, c_{32}S_2), & i = 3, & j = 2 \\ c_{32}, & C_3 \in [c_{32}S_2, 1], & i = 3, & j = 2 \\ 1, & C_3 \in [0, 1], & i = 3, & j = 3 \end{cases} \quad (6.20)$$

where c_{ij} [-] is the constant equilibrium volume fraction of component i in phase j .

It further follows that:

$$S_1 = \begin{cases} 0, & C_1 \leq c_{12}(1 - S_3) \\ \frac{C_1 - c_{12}(1 - S_3)}{c_{11} - c_{12}}, & c_{12}(1 - S_3) < C_1 < c_{11}(1 - S_3) \\ 1 - S_3, & C_1 \geq c_{11}(1 - S_3) \end{cases} \quad (6.21)$$

and

$$S_3 = \begin{cases} 0, & 0 \leq C_1 \leq 1, & C_3 < c_{32}S_2 \\ \frac{C_3 - c_{32}}{1 - c_{32}}, & C_1 \leq c_{12}(1 - S_3), & C_3 \geq c_{32}S_2 \\ \frac{(c_{11} - c_{12})C_3 - (c_{11} - C_1)c_{32}}{(1 - c_{32})c_{11} - c_{12}}, & c_{12}(1 - S_3) < C_1 < c_{11}(1 - S_3), & C_3 \geq c_{32}S_2 \\ C_3, & C_1 \geq c_{11}(1 - S_3), & C_3 \geq c_{32}S_2 \end{cases} \quad (6.22)$$

It should be noted that within equations (6.20) to (6.22), the value of C_1 is used to determine the presence of the gaseous and aqueous phases, and the value of C_3 determines whether or not there is a solid phase. $C_1 \leq c_{12}(1 - S_3)$ denotes the absence of a gaseous

phase and $C_1 \geq c_{11}(1 - S_3)$ denotes the absence of an aqueous phase, while $c_{12}(1 - S_3) < C_1 < c_{11}(1 - S_3)$ means that both gaseous and aqueous phases are present. If $C_3 < c_{32}S_2$, this means that no solid phase has yet formed and all salt in the system is in the aqueous phase, whereas if $C_3 \geq c_{32}S_2$, the salt has reached its equilibrium and maximum volume fraction within the aqueous phase, which has led to the formation of a separate solid phase.

Under the above set of assumptions, fluid flow is controlled by the following set of one-dimensional radially symmetric mass conservation equations, adapted from equation (2.3) to be in terms of volume fractions:

$$\phi \frac{\partial C_i}{\partial t} = -\frac{1}{r} \frac{\partial}{\partial r} \left(r \sum_{j=1}^2 q_j \sigma_{ij} \right), \quad i \in \{1, 2, 3\} \quad (6.23)$$

As was explained in Section 6.2, the volumetric flux, or flow per unit area, of phase j , q_j , can be found from Darcy's Law. When applied to one-dimensional, radial flow, this is in the form it was given in equation (2.8):

$$q_j = -\frac{kk_{rj}}{\mu_j} \frac{\partial P_j}{\partial r}, \quad j \in \{1, 2\} \quad (6.24)$$

A detailed discussion with regards to justification for the above set of assumptions is provided in Section 6.6 below.

The capillary pressure, P_c , is the difference between the pressures of the wetting and non-wetting phases, as given by equation (6.3) as:

$$P_c = P_1 - P_2 \quad (6.25)$$

Because the component densities are assumed to be constant, the system of equations is divergence free and:

$$\sum_{j=1}^2 q_j = \frac{Q_0}{2\pi Hr} \quad (6.26)$$

Substituting equation (6.24) and equation (6.25) into equation (6.26), solving for the partial derivatives of P_j and then substituting these back into equation (6.24) leads to:

$$q_j = \frac{Q_0 f_j}{2\pi Hr} + \frac{(-1)^j k k_{r1} f_2}{\mu_1} \frac{\partial P_c}{\partial r} \quad (6.27)$$

where, with further consideration of equation (6.21):

$$f_j = \begin{cases} [1 + (-1)^j] / 2, & C_1 \leq c_{12}(1 - S_3) \\ \frac{k_{rj}}{\mu_j} \left(\sum_{j=1}^2 \frac{k_{rj}}{\mu_j} \right)^{-1}, & c_{12}(1 - S_3) < C_1 < c_{11}(1 - S_3) \\ [1 + (-1)^{j-1}] / 2, & C_1 \geq c_{11}(1 - S_3) \end{cases} \quad (6.28)$$

Also note that there is no capillary pressure gradient when only one fluid phase is present, i.e.,

$$\frac{\partial P_c}{\partial r} = 0, \quad C_1 \notin (c_{12}(1 - S_3), c_{11}(1 - S_3)) \quad (6.29)$$

Substituting equation (6.27) into equation (6.23) therefore leads to:

$$\frac{\partial C_i}{\partial \eta} = - \frac{\partial F_i}{\partial \omega} \quad (6.30)$$

where:

$$F_i = \begin{cases} \sigma_{i2}, & C_1 \leq c_{12}(1 - S_3) \\ \sum_{j=1}^2 f_j \sigma_{ij} + \left(\frac{k_{r1} f_2}{\text{Ca}} \sum_{j=1}^2 (-1)^j \sigma_{ij} \right) \omega \frac{\partial \psi}{\partial \omega}, & c_{12}(1 - S_3) < C_1 < c_{11}(1 - S_3) \\ \sigma_{i1}, & C_1 \geq c_{11}(1 - S_3) \end{cases} \quad (6.31)$$

and

$$\eta = \frac{Q_0 t}{\pi \phi H r_e^2} \quad (6.32)$$

$$\omega = \frac{r^2}{r_e^2} \quad (6.33)$$

$$\psi = \frac{P_c}{P_{c0}} \quad (6.34)$$

where r_e [L] is an arbitrary reference length and P_{c0} [ML⁻¹T⁻²] is a reference “air-entry” pressure for the porous medium of concern. Recall from equation (5.236) that Ca [-] is a dimensionless constant often referred to as the capillary number, found from:

$$\text{Ca} = \frac{Q_0 \mu_1}{4\pi H k P_{c0}} \quad (6.35)$$

The capillary number represents the ratio of the CO₂ injection rate to the product of the CO₂ mobility and air-entry pressure of the porous medium. It compares the relative effect of the frictional resistance associated with fluid movement with the surface tension, which

acts across the interface between the CO₂-rich phase and the aqueous phase. Small values of Ca imply that capillary processes are important.

With regards to the initial condition and boundary conditions, let C_{iI} [-] represent a uniform initial value of C_i in the saline formation and C_{i0} [-] represent a constant boundary value of C_i at the injection well for $i \in \{1, 2, 3\}$.

6.4.1 Writing Capillary Pressure in Terms of C_1

As CO₂ is injected into the saline formation, H₂O evaporates from the brine leaving NaCl behind as a precipitate in a dry out zone that develops around the injection well. Following the commencement of CO₂ injection, there are therefore three distinct zones within the saline formation that should be considered (see Figure 6.2):

1. The dry out zone, which surrounds the injection well and contains only precipitated salt and CO₂ in the non-wetting fluid phase.
2. The full mixture, or equilibrium, zone, which surrounds the dry out zone and contains CO₂, H₂O and NaCl, distributed between the wetting and non-wetting fluid phases.
3. The initial saline formation fluid zone, which surrounds the full mixture zone and contains only H₂O and NaCl in a wetting fluid phase.

More details as to why these particular zones develop were given in Section 1.3.

Inspection of equation (6.30) and equation (6.31) reveals that the problem is hyperbolic for $C_1 \notin (c_{12}(1-S_3), c_{11}(1-S_3))$ and not hyperbolic for $C_1 \in (c_{12}(1-S_3), c_{11}(1-S_3))$, because of the $\partial\psi/\partial\omega$ term. For the CO₂ injection scenario described above, both Zones 1 and 3 are hyperbolic. In contrast, Zone 2 is not hyperbolic. The discontinuities that separate the three zones are shock waves, which must satisfy the Rankine-Hugoniot condition (e.g. Orr, 2007, p.71). This was further explained in Section 3.4.2.

Within Zone 2, the displacement of a wetting phase by a non-wetting phase represents a continuous drainage cycle such that ψ can be treated as a unique function of S_2 . Furthermore, because $S_3 = 0$ and $S_2 = 1 - S_1$ within this zone, it follows, from equation (6.21),

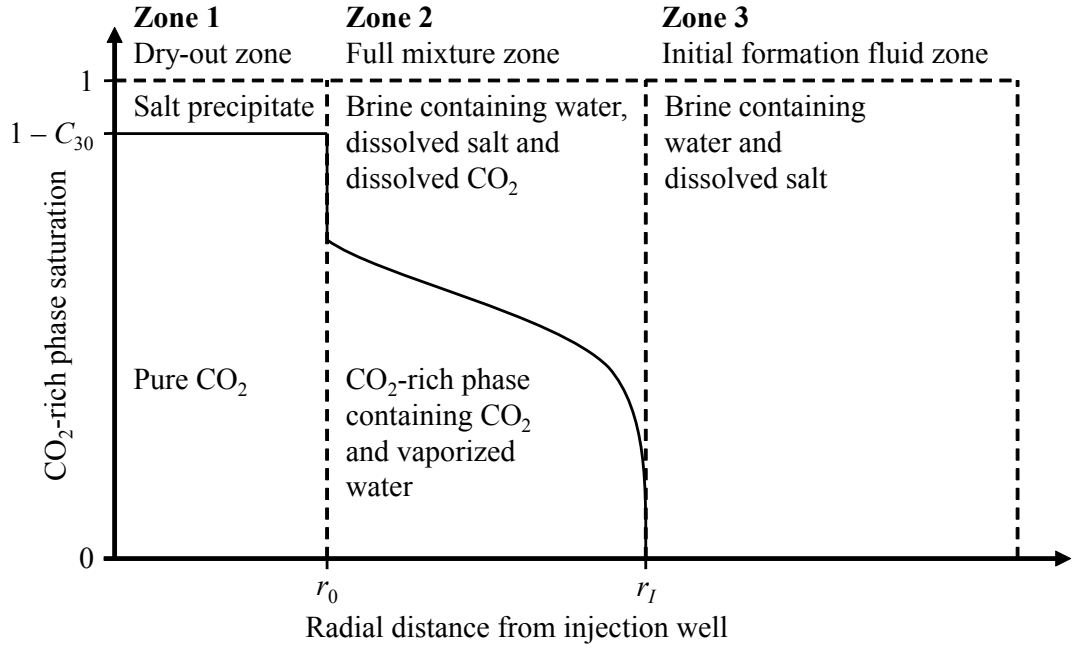


Figure 6.2: A schematic diagram illustrating the distribution of CO₂, water and salt around a CO₂ injection well in a saline formation.

that:

$$S_2 = \begin{cases} 1, & C_1 \leq c_{12} \\ \frac{c_{11} - C_1}{c_{11} - c_{12}}, & c_{12} < C_1 < c_{11} \\ 0, & C_1 \geq c_{11} \end{cases} \quad (6.36)$$

and

$$\frac{\partial S_2}{\partial C_1} = \frac{1}{(c_{12} - c_{11})}, \quad C_1 \in (c_{12}, c_{11}) \quad (6.37)$$

such that it can be said that, using chain rule:

$$\frac{\partial \psi}{\partial \omega} = \frac{1}{(c_{12} - c_{11})} \frac{\partial \psi}{\partial S_2} \frac{\partial C_1}{\partial \omega} \quad (6.38)$$

In this way, equation (6.31) can be substantially simplified to obtain:

$$F_i = \alpha_i - \beta_i \omega \frac{\partial C_1}{\partial \omega} \quad (6.39)$$

where

$$\alpha_i = \begin{cases} C_i, & C_1 \notin (c_{12}, c_{11}), \quad i \in \{1, 2\} \\ \sum_{j=1}^2 f_j c_{ij}, & C_1 \in (c_{12}, c_{11}), \quad i \in \{1, 2\} \\ f_2 \sigma_{32}, & C_1 \in [0, 1], \quad i = 3 \end{cases} \quad (6.40)$$

$$\beta_i = \begin{cases} 0, & C_1 \notin (c_{12}, c_{11}), \quad i \in \{1, 2, 3\} \\ G \sum_{j=1}^2 (-1)^j c_{ij}, & C_1 \in (c_{12}, c_{11}), \quad i \in \{1, 2\} \\ G \sigma_{32}, & C_1 \in (c_{12}, c_{11}), \quad i = 3 \end{cases} \quad (6.41)$$

and

$$G = \frac{f_2 k_{r1}}{\text{Ca}(c_{11} - c_{12})} \frac{\partial \psi}{\partial S_2} \quad (6.42)$$

Within these equations, α_i [-] looks at the fractional flow of the component i without considering capillary pressure, while β_i [-] is a term that represents the capillary-hydraulic properties of the system. When $\text{Ca} \rightarrow \infty$ and $\sigma_{32} = 0$, the above problem reduces to the hyperbolic problem solved by [Orr \(2007\)](#) using the MOC. When $c_{11} = 1$, $c_{12} = 0$ and $\sigma_{32} = 0$, the above problem reduces to the immiscible two-phase flow problem with capillary pressure, previously solved by [McWhorter and Sunada \(1990\)](#) and [Bjørnarå and Mathias \(2013\)](#). The G term in equation (6.42) is analogous to the G term in equation (16) of [Bjørnarå and Mathias \(2013\)](#), and the J term from equation (6.6) that was from the PDEs found by [McWhorter and Sunada \(1990\)](#).

6.4.2 Relative Permeability and Capillary Pressure Functions

Relative permeability is calculated from Corey curves but with relative permeability assumed to linearly increase with saturation to one beyond residual saturations, as was explained in Section 2.2.3 and by equation (2.10).

Dimensionless capillary pressure, ψ , is calculated using the empirical equation of [van Genuchten \(1980\)](#) in conjunction with the dry-region extension of [Webb \(2000\)](#), in the same way as P_c was found in Section 2.2.4. It therefore follows from equation (2.19) that:

$$\psi = \begin{cases} (S_e^{-1/m} - 1)^{1/n}, & S_2 > S_{2m} \\ \psi_d \exp \left[\ln \left(\frac{\psi_m}{\psi_d} \right) \frac{S_2}{S_{2m}} \right], & S_2 \leq S_{2m} \end{cases} \quad (6.43)$$

where S_e [-] is an effective saturation found from:

$$S_e = \frac{S_2 - S_{2c}}{1 - S_{2c}} \quad (6.44)$$

and S_{2c} [-], m [-] and n [-] are residual aqueous saturation and empirical exponents associated with van Genuchten's function, respectively. ψ_d [-] can be taken to be:

$$\psi_d = P_{cd}/P_{c0} \quad (6.45)$$

where P_{cd} [$\text{ML}^{-1}\text{T}^{-2}$] is the capillary pressure at which “oven-dry” conditions are said to have occurred, which is assumed by [Webb \(2000\)](#) to be 10^9 Pa.

S_{2m} [-] is the aqueous saturation matching point, which is the aqueous saturation at which ψ can be assumed to change from being calculated by van Genuchten's function to being found by Webb's linear extension. It is found by:

$$S_{2m} = (1 - S_{2c})S_{em} + S_{2c} \quad (6.46)$$

Finally:

$$\psi_m = (S_{em}^{-1/m} - 1)^{1/n} \quad (6.47)$$

where S_{em} [-] is a critical effective saturation at which the switch over between van Genuchten's function and Webb's extension take place.

Differentiation of equation (6.43) with respect to S_2 leads to:

$$\frac{\partial \psi}{\partial S_2} = \begin{cases} \frac{\psi}{(1 - S_{2c})mnS_e(S_e^{1/m} - 1)}, & S_2 > S_{2m} \\ \frac{\psi}{S_{2m}} \ln \left(\frac{\psi_m}{\psi_d} \right), & S_2 \leq S_{2m} \end{cases} \quad (6.48)$$

6.4.3 Determination of S_{em}

As was described in Section 2.2.4, by considering equation (6.43), S_{em} can be defined as the effective saturation at which:

$$\frac{\psi_m}{(1 - S_{2c})mnS_{em}(S_{em}^{1/m} - 1)} = \frac{\psi_m}{S_{2m}} \ln \left(\frac{\psi_m}{\psi_d} \right) \quad (6.49)$$

Substituting equation (6.47) and equation (6.46) into equation (6.49) and rearranging leads to

$$S_{em} = \frac{S_{em} + S_{2c}(1 - S_{2c})^{-1}}{mn(S_{em}^{1/m} - 1) \ln \left[(S_{em}^{-1/m} - 1)^{1/n} \psi_d^{-1} \right]} \quad (6.50)$$

which must be solved iteratively. Webb (2000) suggests that four to five iterations are sufficient. However, this will be strongly dependent on the initial estimate of S_{em0} applied.

For $S_{2c} > 0$, a good initial estimate of S_{em} , S_{em0} , can be obtained by assuming $S_{em0} \ll 1$ such that equation (6.50) reduces to:

$$S_{em0} = \frac{S_{2c}(1 - S_{2c})^{-1}}{\ln \left[S_{em0} \psi_d^{nm} \right]} \quad (6.51)$$

which can be rearranged to get:

$$W \exp(W) = z \quad (6.52)$$

where

$$z = \frac{S_{2c}\psi_d^{nm}}{(1 - S_{2c})} \quad (6.53)$$

and

$$W = \frac{S_{2c}}{(1 - S_{2c})S_{em0}} \quad (6.54)$$

Note that the functional inverse of $z(W)$ in equation (6.52), $W(z)$, is given by the Lambert W function, which was explained in more detail in Section 2.2.4. Furthermore, because z is always positive and real, $W(z) = W_0(z)$, otherwise referred to as the zero branch, which has the following asymptotic expansion (Corless et al., 1996):

$$W_0(z) = L_1 - L_2 + \frac{L_2}{L_1} + O\left(\left[\frac{L_2}{L_1}\right]^2\right) \quad (6.55)$$

where $L_2 = \ln L_1$ and $L_1 = \ln z$.

In this way, it can be said that:

$$S_{em0} = \frac{S_{2c}}{(1 - S_{2c})W_0(z)} \quad (6.56)$$

where z is found from equation (6.53).

Examples of the iterative calculation of S_{em} from initial guesses obtained from equation (6.56) are presented in Table 6.1. When $S_{2c} \leq 0.3$, it can be seen that convergence is achieved after just two iterations. When $S_{2c} = 0.5$, three iterations are required, whereas when $S_{2c} = 0.7$, six iterations are required. The increase in the number of iterations required with increasing S_{2c} is due to reducing validity of the $S_{em} \ll 1$ assumption.

6.4.4 Application of a Similarity Transform

The PDE in equation (6.30) can be reduced to an ODE by application of a similarity transform. For this problem, the new variable, λ , is equal to:

$$\lambda = \frac{\omega}{\eta} \quad (6.57)$$

Substituting equation (6.57) into equation (6.30) and equation (6.39) leads to:

$$\frac{dF_i}{dC_i} = \lambda \quad (6.58)$$

Iteration / S_{2c}	0.1	0.3	0.5	0.7
0	0.016496	0.054104	0.11525	0.2472
1	0.018951	0.061087	0.13012	0.29011
2	0.018927	0.061082	0.1305	0.29695
3	0.018927	0.061082	0.13051	0.29825
4	0.018927	0.061082	0.13051	0.29850
5	0.018927	0.061082	0.13051	0.29855
6	0.018927	0.061082	0.13051	0.29856
7	0.018927	0.061082	0.13051	0.29856

Table 6.1: Examples of the iterative calculation of S_{em} for different values of S_{2c} (as indicated in the top row) using equation (6.50) with $m = 0.5$, $P_{c0} = 19.6$ kPa and $P_{cd} = 10^9$ Pa. The initial guess, S_{em0} , is calculated using equation (6.56).

and

$$F_i = \alpha_i - \beta_i \lambda \frac{dC_1}{d\lambda} \quad (6.59)$$

Differentiating both sides of equation (6.58) with respect to C_i yields:

$$\frac{d^2 F_i}{dC_i^2} = \frac{d\lambda}{dC_i} \quad (6.60)$$

which on substitution into equation (6.59), along with equation (6.58), and rearranging leads to:

$$\frac{d^2 F_1}{dC_1^2} + \frac{\beta_1}{(F_1 - \alpha_1)} \frac{dF_1}{dC_1} = 0 \quad (6.61)$$

In the event that the boundary and initial values of C_1 , C_{10} and C_{1I} , respectively, are $\notin (c_{12}, c_{11})$, the boundary conditions for equation (6.61) must satisfy the Rankine-Hugoniot conditions (similar to [Orr, 2007](#), p.75):

$$\frac{dF_1}{dC_1} = \frac{\alpha_{10} - F_1}{C_{10} - C_1}, \quad C_1 \geq c_{11} \quad (6.62)$$

$$\frac{dF_1}{dC_1} = \frac{\alpha_{1I} - F_1}{C_{1I} - C_1}, \quad C_1 \leq c_{12} \quad (6.63)$$

where α_{10} and α_{1I} represent the boundary and initial values of α_1 associated with C_{10} and C_{1I} , respectively. Alternatively, when C_{10} and C_{1I} are $\in (c_{12}, c_{11})$:

$$\begin{aligned} F_1 &= \alpha_{10}, & C_1 &= C_{10} \\ F_1 &= \alpha_{1I}, & C_1 &= C_{1I} \end{aligned} \quad (6.64)$$

An efficient way of expressing both equation (6.63) and equation (6.64) simultaneously is to state instead:

$$\begin{aligned} (C_{10} - C_1) \frac{dF_1}{dC_1} + F_1 &= \alpha_{10}, & C_1 &= \tilde{C}_{10} \\ (C_{1I} - C_1) \frac{dF_1}{dC_1} + F_1 &= \alpha_{1I}, & C_1 &= \tilde{C}_{1I} \end{aligned} \quad (6.65)$$

where

$$\tilde{C}_{10} = H(C_{10} - c_{11})c_{11} + H(c_{11} - C_{10})C_{10} \quad (6.66)$$

$$\tilde{C}_{1I} = H(c_{12} - C_{1I})c_{12} + H(C_{1I} - c_{12})C_{1I} \quad (6.67)$$

and $H(x)$ is a Heaviside function. This is a function that gives a value of one for a positive x and a value of zero for a negative x .

6.4.5 Pseudospectral Solution

Following Bjørnarå and Mathias (2013), the boundary value problem described in the previous section is solved using a Chebyshev polynomial differentiation matrix, \mathbf{D} (Weideman and Reddy, 2000).

The coordinate space for the Chebyshev nodes is $x \in [-1, 1]$. However, the solution space for F_1 is $C_1 \in [\tilde{C}_{1I}, \tilde{C}_{10}]$. Therefore the Chebyshev nodes, \mathbf{x}_k , need to be mapped to the C_1 space by the following transform:

$$C_1 = \frac{\tilde{C}_{10} + \tilde{C}_{1I}}{2} + \left(\frac{\tilde{C}_{10} - \tilde{C}_{1I}}{2} \right) x \quad (6.68)$$

Consequently, it is necessary to introduce an appropriately transformed differentiation matrix, \mathbf{E} , where:

$$\mathbf{E} = \frac{dx}{dC_1} \mathbf{D} \quad (6.69)$$

and from equation (6.68):

$$\frac{dx}{dC_1} = \frac{2}{\tilde{C}_{10} - \tilde{C}_{1I}} \quad (6.70)$$

By applying the Chebyshev polynomial on the internal nodes and the Robin boundary conditions in equation (6.65) on the end nodes, equation (6.61) can be written in matrix form (similar to Piché and Kannianen (2009) and Bjørnarå and Mathias (2013)) as:

$$\mathbf{R}(\mathbf{F}) = \begin{bmatrix} \mathbf{E}_{2:N-1,:}^{(2)} \mathbf{F} + \mathbf{I}_{2:N-1,:} \text{diag} \left[\frac{\beta_1}{F_1 - \alpha_1} \right] \mathbf{E}^{(1)} \mathbf{F} \\ (\mathbf{C}_N - C_{1I}) \mathbf{E}_{N,:}^{(1)} \mathbf{F} - \mathbf{I}_{N,:} \mathbf{F} + \alpha_{1I} \\ (\mathbf{C}_1 - C_{10}) \mathbf{E}_{1,:}^{(1)} \mathbf{F} - \mathbf{I}_{1,:} \mathbf{F} + \alpha_{10} \end{bmatrix} \quad (6.71)$$

where \mathbf{F} is the solution vector for the dependent variable F_1 , \mathbf{C} is the vector containing the corresponding values of C_1 , N denotes the number of Chebyshev nodes to be solved for and \mathbf{R} is the residual vector, which represents the error in the matrix approximation from the exact solution, and should be minimised. It will be equal to zero if the solution is exact. The two last rows on the right-hand side of equation (6.71) impose the Robin boundary conditions. Also note that $\mathbf{E}^{(n)}$ can be obtained from \mathbf{E}^n .

Newton's method can now be used to find \mathbf{F} . This is a method for successively finding closer approximations for a root, and in the case of finding closer approximations, y_{n+1} , for a root y , would use the equation (Hoffman and Frankel, 2001, p.158):

$$y_{n+1} = y_n - \frac{g(y_n)}{g'(y_n)} \quad (6.72)$$

where $g(y)$ is a function of y . In this case of finding the solution vector \mathbf{F} , new iterations, $\mathbf{F}_{(n+1)}$, are hence obtained from:

$$\mathbf{F}_{(n+1)} = \mathbf{F}_{(n)} - (\partial\mathbf{R}/\partial\mathbf{F}_{(n)})^{-1} \mathbf{R}(\mathbf{F}_{(n)}) \quad (6.73)$$

for each iteration n , where $\partial\mathbf{R}/\partial\mathbf{F}$ is the Jacobian matrix defined as:

$$\frac{\partial\mathbf{R}}{\partial\mathbf{F}} = \begin{bmatrix} \mathbf{E}_{2:N-1,:}^{(2)} + \mathbf{I}_{2:N-1,:} \text{diag} \left[\frac{\beta_1}{F_1 - \alpha_1} \right] \mathbf{E}^{(1)} - \mathbf{I}_{2:N-1,:} \text{diag} \left[\text{diag} \left[\frac{\beta_1}{(F_1 - \alpha_1)^2} \right] \mathbf{E}^{(1)} \mathbf{F} \right] \\ (\mathbf{C}_N - C_{1I}) \mathbf{E}_{N,:}^{(1)} - \mathbf{I}_{N,:} \\ (\mathbf{C}_1 - C_{10}) \mathbf{E}_{1,:}^{(1)} - \mathbf{I}_{1,:} \end{bmatrix} \quad (6.74)$$

Note that F_1 is bounded by α_1 and α_{10} . Therefore, a good initial guess is to set $F_1 = \alpha_{10}$. Following Bjørnarå and Mathias (2013), an additional correction step should be applied in the Newton iteration to force the solution, F_1 , to be less than α_1 . The Newton iteration loop is assumed to have converged when the mean absolute value of $\mathbf{R} \leq 10^{-9}$. With 100 Chebyshev nodes (i.e., $N = 100$), convergence is typically achieved with less than 200 iterations.

6.4.6 Dealing with Salt Precipitation in the Dry Out Zone

Now consider the case where pure CO_2 is injected into a porous medium (i.e., $\alpha_{10} = 1$) initially fully saturated with brine (i.e., $\alpha_{1I} = 0$). Let σ_{32} be the volume fraction of NaCl in the aqueous phase throughout the system. In this way, the volume fraction of H_2O in the aqueous phase prior to CO_2 injection is $(1 - \sigma_{32})$.

Let r_0 [L] and r_I [L] be the radial extents of the dry out zone and injected CO₂ plume respectively. At any given time, the volume of H₂O evaporated by the CO₂, V_e [L³], can be found from:

$$V_e = 2\pi\phi H(1 - c_{11}) \int_{r_0}^{r_I} r S_1 dr \quad (6.75)$$

V_e can be alternatively expressed as:

$$V_e = (1 - \sigma_{32})V_b \quad (6.76)$$

where V_b [L³] is the volume of brine. The volume of salt precipitated in the dry out zone, V_s [L³], is given by:

$$V_s = \sigma_{32}V_b \quad (6.77)$$

Rearranging equation (6.76) to be in terms of V_b and substituting this into equation (6.77) gives an expression for V_s in terms of V_e and σ_{32} :

$$V_s = \frac{\sigma_{32}V_e}{1 - \sigma_{32}} \quad (6.78)$$

The volume of the dry out zone where the salt is precipitated, V_d [L³], is found from

$$V_d = \pi\phi H r_0^2 \quad (6.79)$$

Another quantity of interest is the volume of CO₂ dissolved in the brine, V_c [L³], which can be calculated using:

$$V_c = 2\pi\phi H c_{12} \int_{r_0}^{r_I} r(1 - S_1) dr \quad (6.80)$$

Considering the definition of λ in equation (6.57) in conjunction with equation (6.32) and equation (6.33):

$$r_0^2 = \frac{Q_0 t \lambda_0}{\pi\phi H} \quad \text{and} \quad r_I^2 = \frac{Q_0 t \lambda_I}{\pi\phi H} \quad (6.81)$$

where, recalling equation (6.58) and equation (6.65), λ_0 and λ_I can be found from:

$$\lambda_0 = \left. \frac{dF_1}{dC_1} \right|_{C_1=c_{11}} \quad \text{and} \quad \lambda_I = \left. \frac{dF_1}{dC_1} \right|_{C_1=c_{12}} \quad (6.82)$$

In this way it can be understood that:

$$V_e = (1 - c_{11})Q_0 t \int_{\lambda_0}^{\lambda_I} S_1 d\lambda \quad (6.83)$$

$$V_d = Q_0 t \lambda_0 \quad (6.84)$$

$$V_c = c_{12}Q_0t \int_{\lambda_0}^{\lambda_I} (1 - S_1)d\lambda \quad (6.85)$$

Noting that the rates at which V_s and V_d grow with time are constant, it can also be understood that the volume fraction of precipitated salt, C_3 , will be both uniform within the dry out zone and constant with time. The value of C_3 within the dry out zone, hereafter denoted as C_{30} , can be found from:

$$C_{30} = \frac{V_s}{V_d} = \frac{(1 - c_{11})\sigma_{32}}{(1 - \sigma_{32})\lambda_0} \int_{\lambda_0}^{\lambda_I} S_1 d\lambda \quad (6.86)$$

Given that $C_{10} = 1 - C_{30}$, $C_{1I} = 0$, $\alpha_{10} = 1$ and $\alpha_{1I} = 0$, the boundary conditions in equation (6.65) reduce to:

$$\begin{aligned} \frac{dF_1}{dC_1} &= \frac{1 - F_1}{1 - C_{30} - c_{11}}, & C_1 &= c_{11} \\ \frac{dF_1}{dC_1} &= \frac{F_1}{c_{12}}, & C_1 &= c_{12} \end{aligned} \quad (6.87)$$

Values of C_{30} can be obtained iteratively by repeating the procedures outlined in Section 6.4.5 with successive estimates of C_{30} obtained from equation (6.86). Using an initial guess of $C_{30} = 0$, this process is found to typically converge after less than 60 iterations. The integrals in equation (6.85) and equation (6.83) can be found by trapezoidal integration.

6.5 Sensitivity Analysis

6.5.1 Gas Displacing Oil

As a first example, the gas-displacing-oil scenario previously presented in Figures 4.13 and 4.15 of Orr (2007) is adopted. The parameters describing the scenario include $c_{11} = 0.95$, $c_{12} = 0.20$, $\sigma_{32} = 0$, $\mu_2/\mu_1 = 2$, $S_{1c} = 0.05$, $S_{2c} = 0.1$, $k_{r10} = k_{r20} = 1$ and $n_1 = n_2 = 2$, where S_{jc} [-] represents the critical or residual saturation for the phase j , k_{rj0} [-] represents the relative permeability endpoint for phase j and n_j [-] is the power law exponent for phase j . For the pseudospectral solution, a value for the van Genuchten (1980) parameter, m , is set to 0.5.

Plots of C_1 against dF_1/dC_1 (which, recall, is equal to ω/η) for this scenario are shown in Figure 6.3. The different subplots show the effect of varying the boundary volume fraction, C_{10} , and the initial volume fraction, C_{1I} . The different colours relate to different assumed

values of Ca. Increasing Ca can be thought of as analogous to an increased injection rate. The $Ca \rightarrow \infty$ curves were obtained from the MOC solutions previously presented in Figures 4.13 and 4.15 of Orr (2007). The finite Ca value solutions were obtained using the pseudospectral solution described above, with 100 Chebyshev nodes.

When $Ca = 100$, the pseudospectral solution is virtually identical to the infinite-Ca-MOC solutions. As Ca is decreased, the solution becomes more diffused. In Figure 6.3a, d, e and f, the infinity Ca results exhibit a trailing shock, which represents a dry out zone where all the liquid oil has been evaporated by the gas. Of particular interest is that decreasing Ca leads to a reduction in the thickness of the dry out zone, ultimately leading to its complete elimination.

6.5.2 CO₂ Injection in a Saline Formation

Here the CO₂-injection-in-a-saline-formation scenario, previously presented by Mathias et al. (2013), is revisited. The example involves injecting pure CO₂ at a constant rate via a fully penetrating injection well at the centre of a cylindrical, homogenous and confined saline formation, initially fully saturated with brine. Relevant model parameters are presented in Table 6.2. In this case, components 1, 2 and 3 are CO₂, H₂O and NaCl, respectively, and phases 1, 2 and 3 represent a CO₂-rich phase, an H₂O rich phase and precipitated salt, respectively.

Mathias et al. (2011a) found that when using analytical solutions in this context, to account for the relatively high compressibility of CO₂, it is important to use an estimate of the final pressure rather than the initial pressure for calculating the fluid properties relating to CO₂. Mathias et al. (2013) found that, for the scenario described in Table 6.2, the well pressure increased by just over 5 MPa after ten years. Therefore, for the current study, fluid properties are calculated using 15 MPa as opposed to 10 MPa.

As was shown in Chapter 2, the equations of state (EOS) of Spycher et al. (2003) and Spycher and Pruess (2005) provide equilibrium mole fractions as opposed to volume fractions. Pruess and Spycher (2007) show how mole fractions can be converted to mass fractions, X_{ij} [-], which can be converted to volume fractions, σ_{ij} [-], using (similar to Orr, 2007, p.19):

$$\sigma_{ij} = \frac{\rho_j X_{ij}}{\rho_{ij}} \quad (6.88)$$

where ρ_{ij} [ML⁻³] is the density of component i in phase j and ρ_j [ML⁻³] is the composite

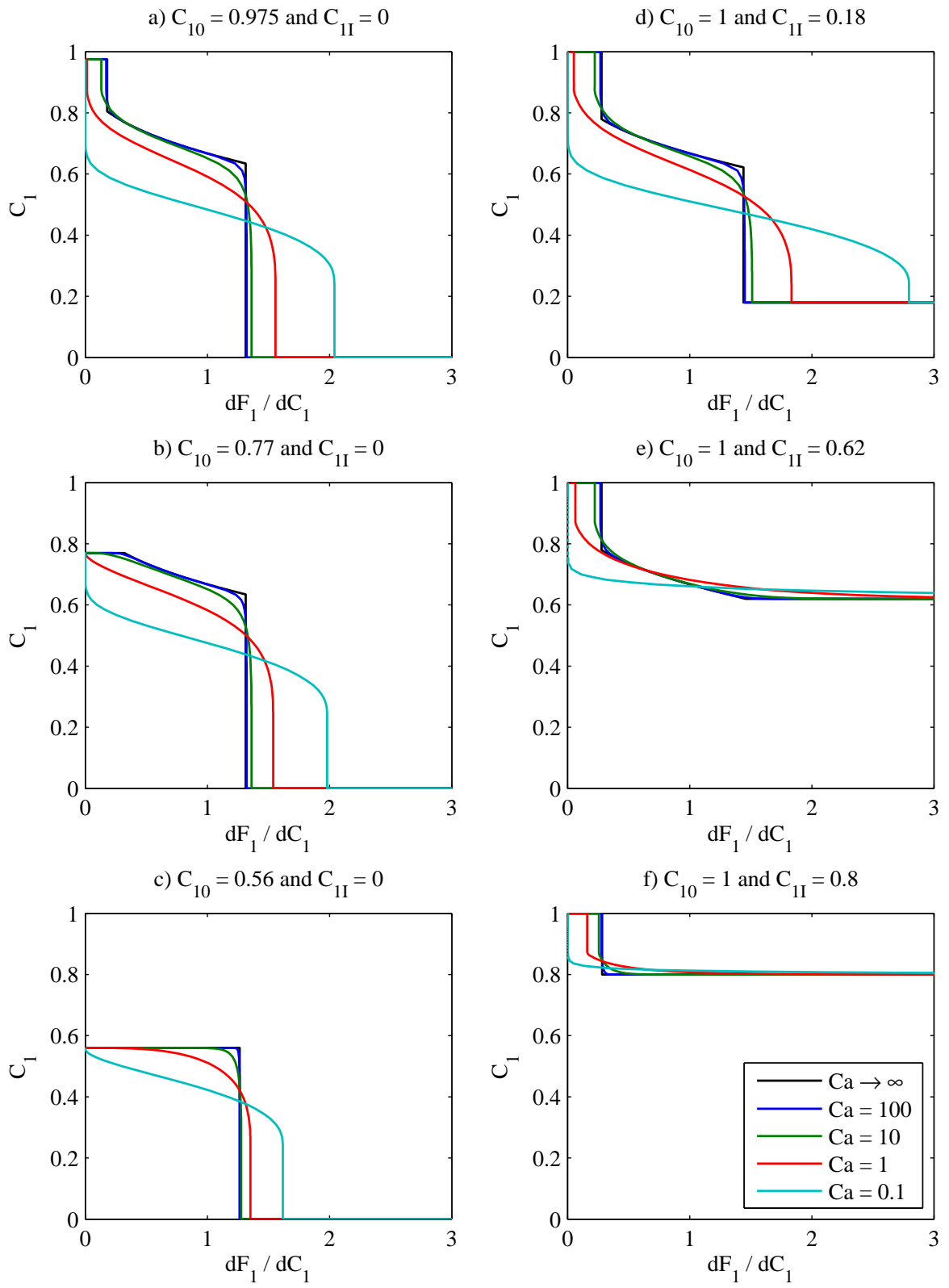


Figure 6.3: Sensitivity analysis based on gas-displacing-oil examples. The infinite Ca value curves were obtained from the method of characteristics solutions presented in Figures 4.13 and 4.15 of Orr (2007). The finite Ca value curves were obtained using the pseudospectral solution documented in this chapter.

CO ₂ injection rate,	15 kg s ⁻¹
Porosity, ϕ	0.2
Initial pressure	10 MPa
Temperature	40 °C
Mass fraction of salt in brine, X_{32}	0.15
Critical gas saturation, S_{1c}	0.0
Residual water saturation, S_{2c}	0.5
Endpoint relative permeability for CO ₂ , k_{r10}	0.3
Endpoint relative permeability for brine, k_{r20}	1.0
Relative permeability exponents, n_1, n_2	3
Formation thickness, H	30 m
Permeability, k	10 ⁻¹³ m ²

Table 6.2: Relevant model parameters used for the CO₂ injection in saline formation scenario, previously presented by [Mathias et al. \(2013\)](#).

phase density, which can be found from the mixing rule given in equation (4.29):

$$\rho_j = \left(\sum_{i=1}^{N_c} \frac{X_{ij}}{\rho_{ij}} \right)^{-1} \quad (6.89)$$

where N_c [-] is the number of components present. Because the pseudospectral solution above assumes component densities remain constant throughout, a decision is made that $\rho_{12} = \rho_{11}$, $\rho_{21} = \rho_{22}$ and $\rho_{32} = \rho_{33}$.

Table 6.3 shows how the various fluid properties vary with depth below sea level in this context. Depth is related to pressure by assuming hydrostatic conditions and then adding 5 MPa to allow for pressure induced by CO₂ injection. Depth is related to temperature by assuming a geothermal gradient of 40°C per km. It can be seen that the volume fractions are largely unaffected by depth. However, the variation in brine viscosity and CO₂ density are more noticeable.

A comparison of results from the pseudospectral solution with those from the TOUGH2 simulation reported by [Mathias et al. \(2013\)](#) is shown in Figure 6.4, alongside results for when $\text{Ca} \rightarrow \infty$, obtained using a MOC solution similar to that previously presented by [Zeidouni et al. \(2009\)](#) and [Mathias et al. \(2011b\)](#). [Mathias et al. \(2013\)](#) assumed $P_{c0} = 19.6$ kPa. Considering the other parameters in Table 6.2 and Table 6.3, this leads to a Ca value of 1.7. There is excellent correspondence between the MOC solution, the TOUGH2 results

Depth (m)	1000	1500	2000
Pressure (MPa)	15	20	25
Temperature ($^{\circ}\text{C}$)	40	60	80
Density of CO_2 , ρ_{11} (kg m^{-3})	754	704	673
Density of H_2O , ρ_{22} (kg m^{-3})	998	992	984
Density of NaCl , ρ_{33} (kg m^{-3})	2160	2160	2160
Volume fraction of CO_2 in phase 1, c_{11} (-)	0.999	0.998	0.996
Volume fraction of CO_2 in phase 2, c_{12} (-)	0.041	0.043	0.045
Volume fraction of NaCl in phase 2, σ_{32} (-)	0.075	0.074	0.073
Dynamic viscosity of CO_2 , μ_1 (cP)	0.064	0.057	0.054
Dynamic viscosity of brine, μ_2 (cP)	0.963	0.730	0.573

Table 6.3: Relevant model parameters used for the CO_2 injection in a saline formation scenario with a brine salinity of 150 ppt.

and the pseudospectral solution when $\text{Ca} = 1.7$.

A value of $P_{c0} = 19.6$ kPa is often used to describe saline formations in a CO_2 storage context, e.g. (Mathias et al., 2013; Rutqvist et al., 2007; Zhou et al., 2008; Zhu et al., 2015). Experimental analysis looking at four different sandstone reservoirs revealed a range of P_{c0} values from 1.3 to 7.1 kPa (Oostrom et al., 2016). Smaller values of P_{c0} imply larger pore diameters.

A hallmark of hyperbolic theory is that the problem can be reduced to a fundamental wave structure which constitutes the solution. In Figure 6.4, it can be seen that such a wave structure is largely preserved, despite the inclusion of capillary diffusion. Furthermore, the wave velocity of the leading shock is virtually independent of Ca for the range of Ca values studied. However, decreasing Ca leads to a more diffused spreading wave caused by the increase in capillary diffusion, which in turn leads to a reduction in the wave velocity of the trailing shock, as also seen in Figure 6.3a. The decrease in steady-state CO_2 saturation in the dry out zone is caused by an increase in the volume fraction of precipitated salt (recall that $C_{10} = 1 - C_{30}$).

For the scenarios depicted in Figure 6.4, C_{30} is found to be insensitive to Ca for Ca values greater than or equal to 1.7. However for Ca values less than 1.7, the volume of the dry out zone is significantly reduced and the volume fraction of precipitated salt is significantly increased. The value of C_{30} for $\text{Ca} = 0.2$ is almost double the value for $\text{Ca} = 1.7$. The

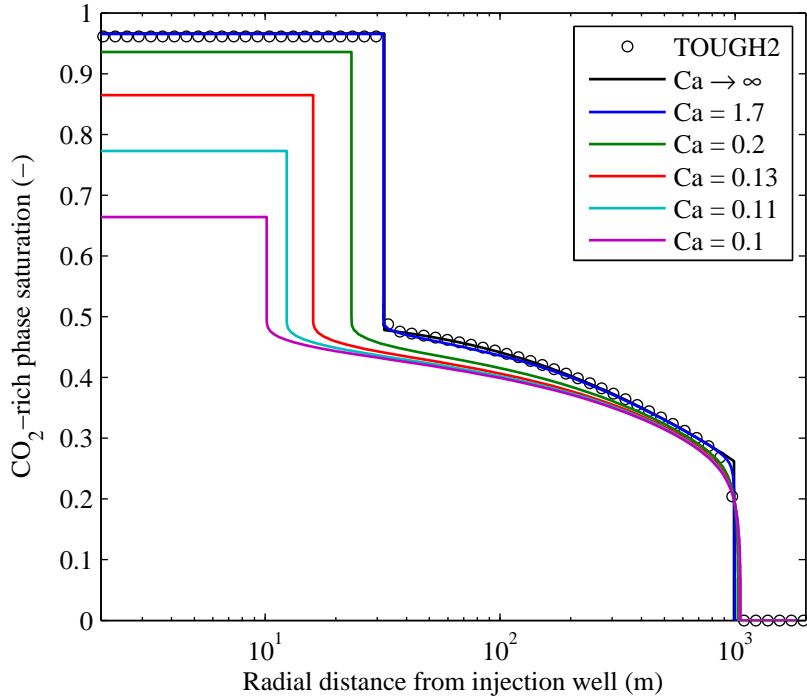


Figure 6.4: Plots of CO_2 saturation against radial distance after injecting 4.73 Mt of CO_2 whilst assuming a range of different capillary numbers, Ca . The TOUGH2 results are from the simulations previously presented by Mathias et al. (2013). Other associated model parameters are presented in Table 6.2. The results for $\text{Ca} \rightarrow \infty$ were obtained using a method of characteristics solution, also presented by Mathias et al. (2013). The results for finite Ca values were obtained using the pseudospectral solution.

value of C_{30} for $\text{Ca} = 0.1$ is around ten times that of when $\text{Ca} = 1.7$. The $\text{Ca} = 1.7$ scenario described in Table 6.2 assumes an injection rate of 15 kg s^{-1} . The results shown in Figure 6.4 therefore suggest that reducing the injection rate down to 1.8 kg s^{-1} would lead to a doubling of the volume fraction of precipitated salt around the injection well. Furthermore, reducing the injection rate from 15 kg s^{-1} down to 0.9 kg s^{-1} would lead to an almost ten times larger volume fraction of precipitated salt around the injection well.

Recall that the effect of Ca on the three phase numerical model in Chapter 5 was examined in Figures 5.3 and 5.4. The output from the three phase numerical model for the parameters in Table 5.1, with the exception that $P_{cd} = 10^7$, is given in Figure 6.5, alongside the output from the similarity solution found in this chapter for the same parameters. It can be seen that the two solutions are comparable in that the wave structures for the CO_2 -rich phase saturation are the same, and the outputs for $\text{Ca} = 1.7$ are very close. However, although they follow a similar pattern in that the value of C_{10} drops for both solutions as Ca decreases, the actual values for C_{10} given by the two solutions for the same

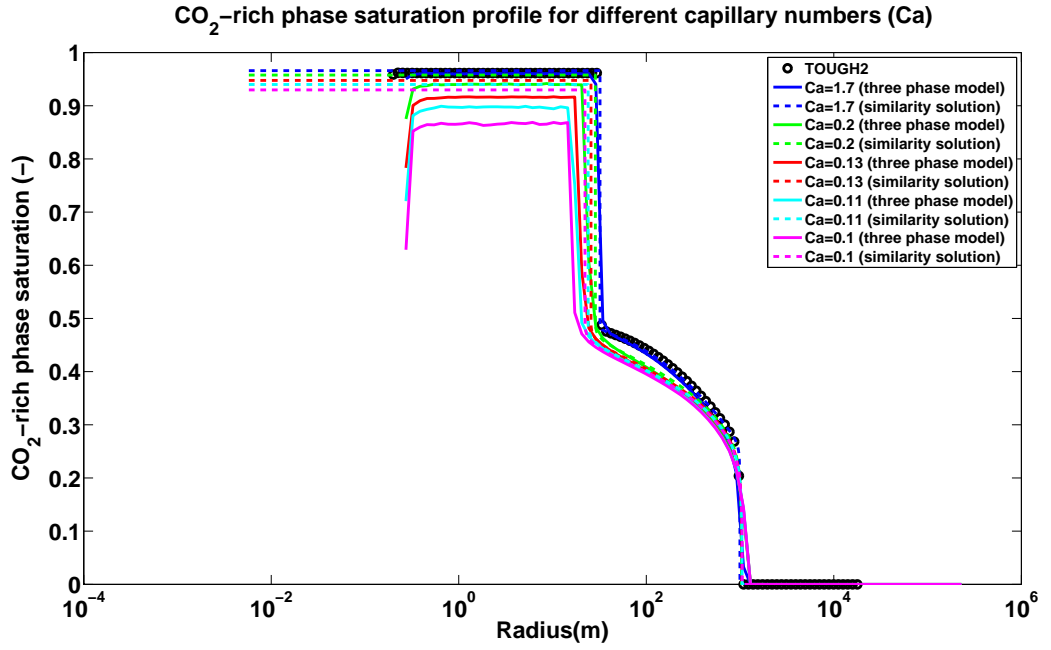


Figure 6.5: Plots of CO₂-rich phase saturation against formation radius for different values of Ca, for both the similarity solution (indicated by the dashed lines) and the three phase numerical model from Chapter 5 (indicated by the solid lines). Both solutions use the parameters in Table 5.1, with the exception that P_{cd} is set to 10^7 , and the three phase numerical model was run for 80 points in space.

value of Ca become further and further apart as Ca falls. As was shown in Figures 5.3 and 5.4, the CO₂-rich phase saturation values found for each value of Ca seem to increase as the number of points in space increases in the three phase numerical model, so the output shown in Figure 6.5, which is only for 80 points as this is the highest number of points for which it is stable enough to run for for the full range of Ca values, cannot be completely relied upon. It also shows evidence of numerical instability, due to the sharp drop in CO₂-rich phase saturation close to the point of injection.

For the hyperbolic case when $Ca \rightarrow \infty$, it is common to study plots of F_1 and C_1 (Orr, 2007). Figure 6.6a shows plots of F_1 against C_1 for all the values of Ca presented in Figure 6.4 along with a plot of α_1 . The MOC solution (i.e., with $Ca \rightarrow \infty$), which sits almost exactly underneath the $Ca = 1.7$ line, intersects the α_1 line at tangents, which is symptomatic of satisfying the shock waves satisfying the Rankine-Hugoniot condition. To better visualize the results for finite Ca values, $(1 - F_1)$ is shown on a log scale in Figure 6.6b. Here it can be seen that the models approach a value of $F_1 = 1$ at different C_1 values depending on the volume fraction of precipitated salt. The volume fraction of precipitated salt increases with decreasing Ca. Figure 6.6c shows a close-up view of the trailing shocks on linear axes for further reference. For finite Ca values, the F_1 lines

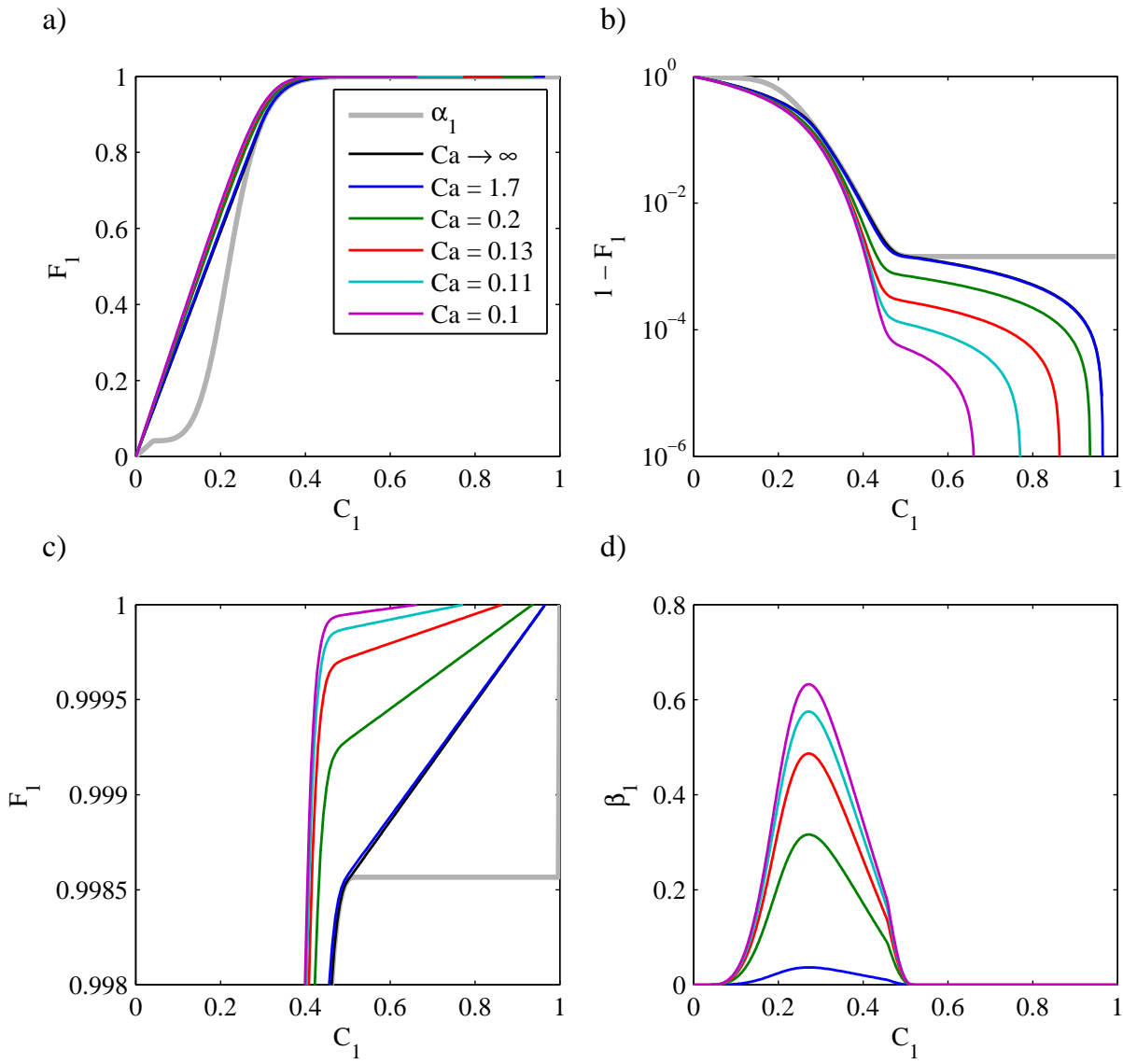


Figure 6.6: Plots of F_1 , α_1 and β_1 against C_1 for the simulation results presented in Figure 6.4.

never actually intersect the α_1 line except at where $C_1 = 0$. The reason for this is due to β_1 , which is plotted in Figure 6.6d. The highest values of β_1 are at the centre of the two-phase region, $C_1 \in (c_{12}, c_{11})$, and it can be seen that the lower the capillary number, the higher the value of β_1 reached, and hence the further away the F_1 line from the α_1 line in Figure 6.6c. β_1 smoothly grades down to zero as it reaches the single-phase regions, $C_1 \notin (c_{12}, c_{11})$.

A further sensitivity analysis is presented in Figure 6.7. The three depth scenarios presented in Table 6.3 are applied with three different brine salinities. Figure 6.7a shows how the volume of the dry out zone decreases with decreasing Ca . The size of the dry out zone increases with increasing depth. In contrast, brine salinity has very little impact on dry out zone volume.

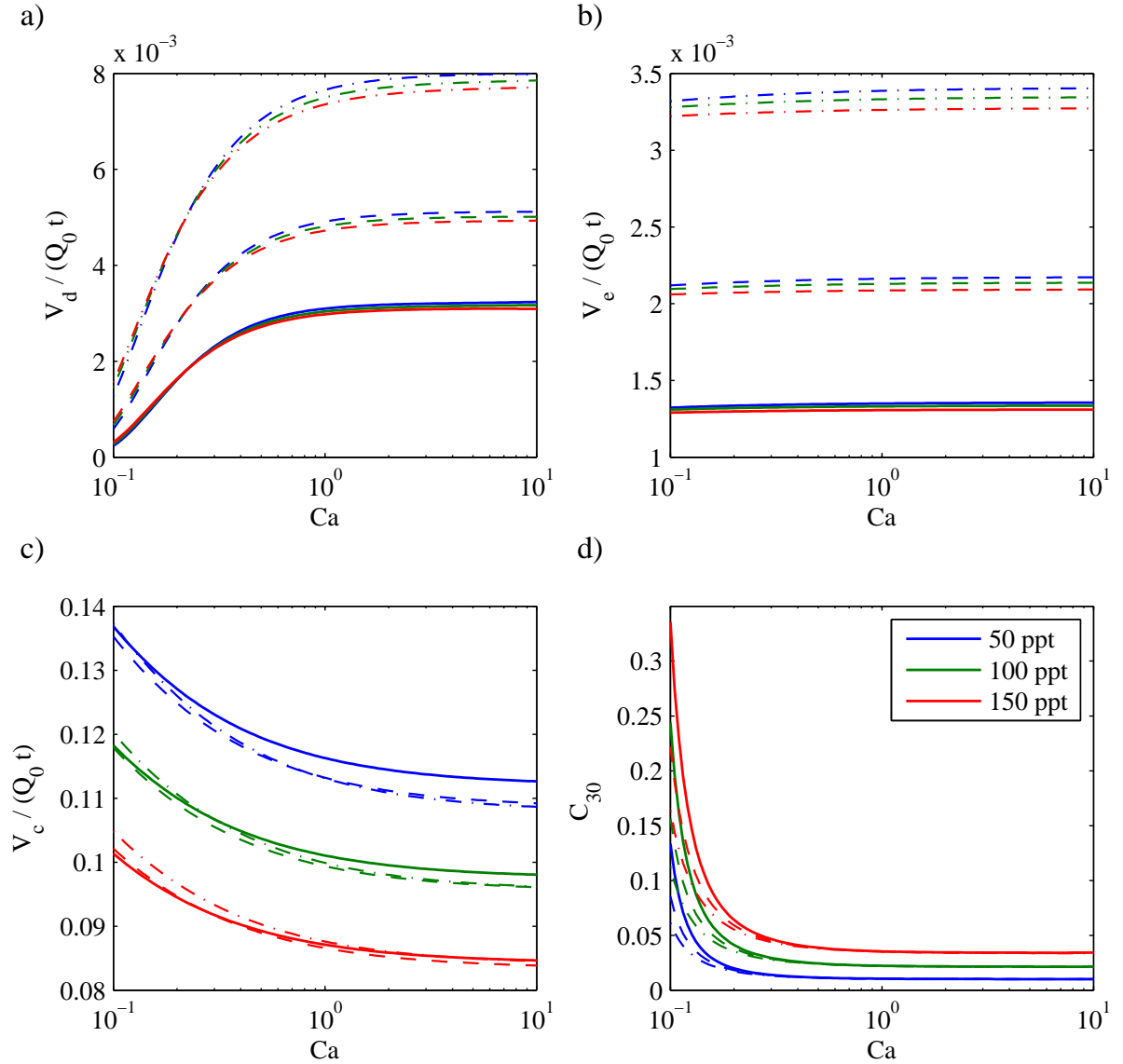


Figure 6.7: Sensitivity analysis based around the scenario presented in Figure 6.4. The different colours relate to different brine salinities, as indicated in the legend. The solid lines, dashed lines and dash-dotted lines represent results obtained using fluid properties calculated assuming the saline formation exists at a depth of 1000 m, 1500 m and 2000 m, respectively (based on hydrostatic pressure conditions and a geothermal gradient of 40°C per km as in Table 6.3). a) shows plots of the ratio of dry out zone volume (V_d) to injected CO₂ volume ($Q_0 t$) against capillary number (Ca). b) shows plots of the ratio of volume of evaporated water (V_e) to $Q_0 t$ against Ca. c) shows plots of the ratio of volume of dissolved CO₂ (V_c) to $Q_0 t$ against Ca. d) shows plots of precipitated salt volume fraction in the dry out zone (C_{30}) against Ca.

Figure 6.7b shows that the volume of the evaporated water also reduces with decreasing Ca . At first this seems surprising given that capillary pressure effects should bring more water into the dry out zone. However, the effect of the capillary pressure is also to spread the CO_2 out further (see leading edge of CO_2 plumes in Figure 6.4). As a consequence, more CO_2 is dissolved (see Figure 6.7c). Consequently, less of the CO_2 -rich phase is available for water from the brine to evaporate into. The volume of evaporated water increases with depth because the equilibrium volume fraction of water in the CO_2 -rich phase increases with depth (see Table 6.3). The volume of dissolved CO_2 is insensitive to depth but decreases with increasing brine salinity. The latter is because the solubility limit of CO_2 in brine decreases substantially with increasing salinity (Spycher and Pruess, 2005).

Figure 6.7d shows how volume fraction of precipitated salt in the dry out zone, C_{30} , superlinearly increases with decreasing Ca . For $Ca > 0.25$, the quantity of precipitated salt is mostly controlled by brine salinity. However, for $Ca < 0.25$, depth plays an increasingly important role, with higher levels of salt precipitation in shallower formations. This is because the dry out zone increases with depth, despite increasing water evaporation with depth. Figure 6.8 shows the same results as Figure 6.7d but with C_{30} normalized by dividing by the salinity of the brine, X_{32} . Here it can be seen that C_{30} almost linearly scales with X_{32} .

The volume fraction of precipitated salt is also strongly controlled by the relative permeability parameters, k_{rj0} , S_{jc} and n_j (Zhang et al., 2016). The analysis performed to provide Figure 6.8 was repeated for the 1000 m depth scenario for each of the six groups of relative permeability parameters presented in Table 6.4. These six parameter sets were selected from a database of 25 core experiments previously compiled by Mathias et al. (2013). The six cores were selected to provide a representative range of possible outcomes given the wide variability generally observed in such data sets.

From Figure 6.9 it can be seen that the high Ca values of C_{30} range from 0.019 to 0.044. Furthermore, the critical Ca value below which C_{30} superlinearly increases ranges from 0.025 to 10. Comparing these results with the parameter sets in Table 6.4 it can be seen that when the relative permeability for brine is more linear, the value of C_{30} at high values of Ca tends to be lower. However, this linearity also leads to the superlinearly increasing of C_{30} with decreasing Ca to occur at a relatively low value of C_{30} (see for example Cardium #1 and Basal Cambrian). Exactly the opposite happens when the relative permeability

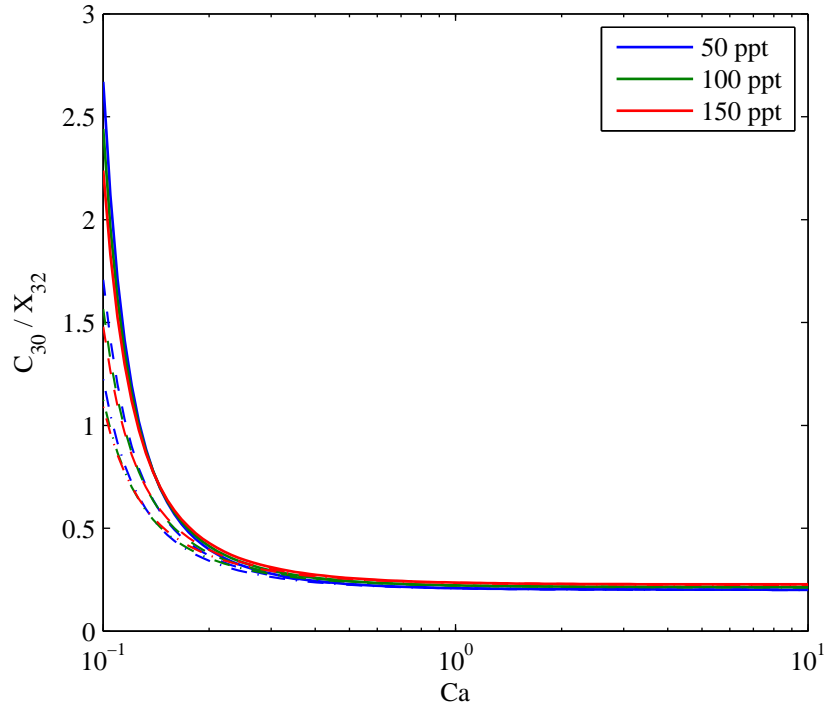


Figure 6.8: The same as Figure 6.7d except that salt volume fraction, C_{30} , is divided by the salinity of the brine, X_{32} .

for brine is highly nonlinear (see for example Paaratte and Tuscaloosa). This is probably due to counter-current flow of water being less efficient when relative permeability is highly nonlinear.

6.6 Discussion of Key Modelling Assumptions

6.6.1 Incompressible Fluids

Fluid densities are assumed to be independent of pressure. The compressibilities of H_2O and $NaCl$ are commonly ignored. Depleted gas reservoirs are often abandoned at pressures below 1MPa, and for these pressures and the usual temperatures of the reservoirs, the compressibility of CO_2 is very high and has a significant impact on fluid movement (Mathias et al., 2014). However, for CO_2 injection in saline formations, fluid pressures are expected to be hydrostatic or above. Under these conditions, providing a sensible reference pressure is used to determine the fluid properties of CO_2 (i.e., an estimate of pressure towards the end of the injection cycle), the compressibility of CO_2 has been found to have a negligible effect in this context (Mathias et al., 2011a,b).

Unit	k_{r10}	S_{2c}	n_1	n_2
Cardium #1	0.526	0.197	1.7	1.3
Basal Cambrian	0.545	0.294	5.0	1.8
Otway	0.332	0.558	3.2	2.9
Viking #1	0.659	0.437	6.5	2.5
Paaratte	0.328	0.389	3.0	4.6
Tuscaloosa	0.077	0.703	3.2	4.7

Table 6.4: Relative permeability parameters for six different sandstone cores (after [Mathias et al., 2013](#)). Note that for each core $k_{r20} = 1$ and $S_{1c} = 0$. Data for Cardium #1, Basal Cambrian and Viking #1 was originally obtained by [Bennion and Bachu \(2008\)](#). Data for Otway was originally obtained by [Perrin and Benson \(2010\)](#). Data for Paaratte and Tuscaloosa was originally obtained by [Krevor et al. \(2012\)](#).

6.6.2 No Volume Change on Mixing

Component densities are assumed to be uniform across phases. In fact, the densities of CO_2 and H_2O are both higher in the aqueous phase as compared to in the CO_2 -rich phase. For a wide range of different CO_2 injection scenarios, this volume change on mixing is found to lead to an increase in volumetric flow rate of around 0.05% in Zone 2 and a decrease in volumetric flow rate of around 5% in Zone 3 (see Table 2 of [Mathias et al., 2011b](#)). See Section 6.4.1 above for an explanation of the zone numbers.

With regards to NaCl, the density of precipitated NaCl, ρ_{33} , is 2160 kg m^{-3} . Using Equation (6.89) in conjunction with the EOS for brine given by [Batzle and Wang \(1992\)](#), it can be shown that the density of NaCl dissolved in brine, ρ_{32} , is around 2800 kg m^{-3} . In the above analysis we have set $\rho_{32} = \rho_{33}$ such that the model precipitates the correct volume of salt in the dry out zone. The consequence is that the volume fractions of water and CO_2 in the brine are underestimated by around 2%.

Figure 6.4 compares model results from TOUGH2 with those from the similarity solution. TOUGH2 properly incorporates fluid compressibility and volume change on mixing and there is negligible difference between the two models.

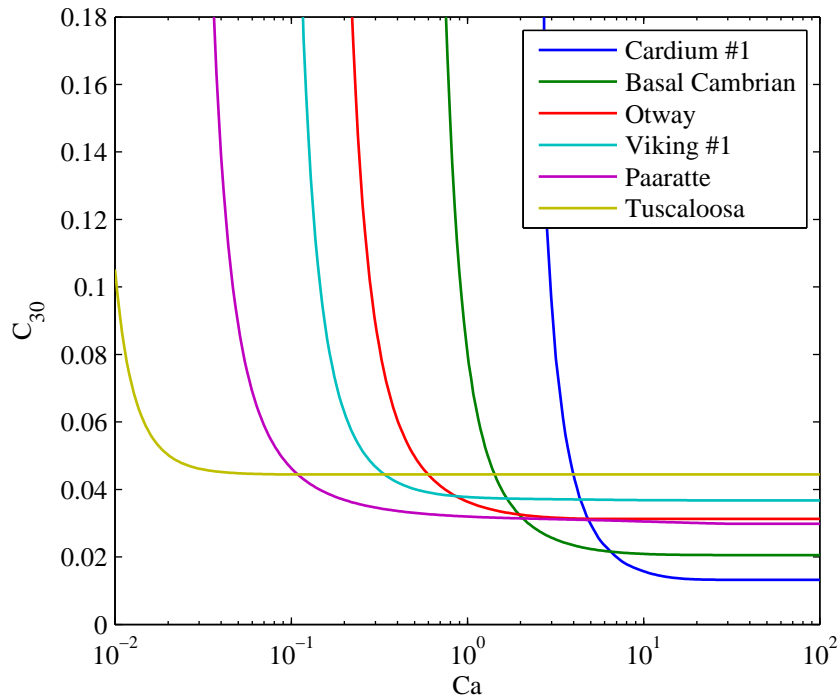


Figure 6.9: Plot of precipitated salt volume fraction, C_{30} , against capillary number, Ca , using the 1000 m depth model scenario described in Tables 6.2 and 6.3 in conjunction with the different relative permeability parameters given in Table 6.4.

6.6.3 Ignoring Gravity Effects

As stated earlier, another important assumption is that the vertical permeability of the formation is sufficiently low that gravity effects can be ignored. Extreme changes in density and/or viscosity can lead to instabilities and fingering phenomena, which cannot be represented using one-dimensional models. Indeed, [Kim et al. \(2012\)](#) found that buoyancy driven flow, associated with the different densities of brine and CO_2 , played an important part in controlling the spatial distribution of precipitated salt around an injection well. However, this was mostly after the cessation of injection. During the injection phase, gravity segregation within the dry out zone was much less significant and no viscous fingering was observed.

[Mathias et al. \(2011b\)](#) presented a comparison of simulation results where gravity was accounted for and ignored using TOUGH2 and the MOC solution of [Zeidouni et al. \(2009\)](#), respectively. For a 100 m thick isotropic saline formation, gravity was found to have a strong effect on the leading edge of the CO_2 plume. However, gravity effects were found to be negligible on the dry out zone development and the associated volume fraction of the precipitated salt. For a 50 m thick isotropic saline formation, gravity effects were found

to be negligible throughout.

The dry out zone is generally unaffected by gravity segregation due to the larger velocities situated close around the injection well, which are mostly horizontal due to the horizontal driving force provided by the injection well boundary (Mathias et al., 2011b). From the discussion above it is expected that gravity effects are unlikely to significantly affect the dry out zone in the 30 m thick saline formations studied in this chapter, at least for the higher capillary numbers studied. However, as the capillary numbers are decreased, the horizontal injection velocities will become less significant and gravity will play a more important role. However, the analysis within this chapter has shown that excessive salt precipitation can also develop in the absence of gravity effects due to the counter-current imbibition associated with capillary pressure.

6.7 Chapter Summary and Conclusions

A new similarity solution has been presented to study the role of capillary pressure on salt precipitation during CO₂ injection in a saline formation. Dimensional analysis has revealed that the problem is largely controlled by a capillary number, $Ca = Q_0\mu_1/(4\pi HkP_{c0})$, where H [L] is the formation thickness, k [L²] is permeability, P_{c0} [ML⁻¹T⁻²] is an air-entry pressure associated with the porous medium, Q_0 [L³T⁻¹] is the injection rate and μ_1 [ML⁻¹T⁻¹] is the dynamic viscosity of CO₂. The volume fraction of precipitated salt around the injection well, C_{30} [-], is found to superlinearly increase with decreasing Ca . Subsequent sensitivity analysis also reveals that C_{30} linearly scales with the salinity of brine. C_{30} is found to reduce with increasing storage depth. This latter point is largely attributed to the equilibrium volume fraction of water in the CO₂-rich phase increasing with depth. Relative permeability parameters are found to have a significant effect on the value of Ca below which C_{30} superlinearly increases. For highly nonlinear relative permeabilities, C_{30} remains stable for much lower capillary numbers.

The new similarity solution represents a significant extension of the work of Zeidouni et al. (2009) by accounting for capillary pressure and an extension of the work of Bjørnara and Mathias (2013) by accounting for radially symmetric flow, partial miscibility and salt precipitation.

In one scenario studied, reducing the CO₂ injection rate from 15 kg s⁻¹ to 0.9 kg s⁻¹ led to

almost a ten times larger volume fraction of precipitated salt. In the past, pressure buildup in injection wells has been widely perceived to increase monotonically with CO₂ injection rate. However, these results clearly demonstrate that as injection rate is decreased the volume fraction of precipitated salt around the injection well will significantly increase leading to potentially significant loss of injectivity. It follows that below a critical threshold, pressure buildup can be expected to increase with reducing injection rates as well. The similarity solution presented in this chapter can serve as a useful tool to determine the critical capillary number at which these effects are likely to take place.

Chapter 7

Summary, Conclusions and Future Work

This chapter will provide a summary of the earlier chapters in the thesis, before bringing the points that they make together to give a conclusion. It will then explore options for future work within this area.

7.1 Summary and Conclusions

This work aims to simulate the salt precipitation that occurs when CO₂ is injected into a saline aquifer. As was highlighted in Chapter 1, the geological storage of CO₂ in saline aquifers involves many different processes that all have an effect on each other and occur on different scales. Forming either a numerical model or analytical solution that accurately encompasses them all would be close to impossible. Therefore, simplifications and assumptions have had to be made in order to create the models and solutions found within this thesis. However, two aspects that are considered to be key to the volume of salt precipitation formed, and hence are focused on within this work, are the partial miscibility of the phases and the inclusion of the effects of capillary pressure. It is as a result of partial miscibility that water is able to evaporate into the CO₂-rich gaseous phase and cause formation dry out, hence leading to there being no aqueous water for the salt to dissolve in and it precipitating as a solid, and high capillary pressure gradients can provide a driving force for the backflow of brine towards the site of injection, which supplies additional salt to precipitate in the dry out zone.

Chapter 2 introduces the governing equations that describe the physical processes within the formation when CO₂ is injected. These equations are the basis of all models and solutions found, and are used in every chapter in the thesis, as appropriate to the coordinates used and the phases and components present. The chapter also describes the concepts of equilibrium and the maximum solubility of components in certain phases, which are essential for fully understanding the mixing of components between phases in a multicomponent and multiphase system.

Chapter 3 introduces two techniques for solving partial differential equations (PDEs), the method of characteristics (MOC) and the method of lines (MOL), and illustrates how they can be used to solve the mass conservation equation when fluid properties are assumed to be constant with pressure and temperature and the capillary pressure is negligible, and hence model two phase incompressible flow. It is shown that the outputs of the two methods compare very well for both the immiscible and partially miscible two phase systems when there is assumed to be no volume change on mixing, as well as for the gas saturation and dimensionless mass fraction of CO₂ when volume change on mixing is introduced. However, extreme instability is seen in the MOL solution for the value of the dimensionless flow velocity, q_D , after the leading shock for the system incorporating volume change on mixing. This instability highlights a potential issue to be aware of in the use of a numerical method such as the MOL.

The MOC is limited to solving hyperbolic PDEs whereas the MOL uses approximations and can be used for more complex systems, so this is the method that is chosen to model the more realistic systems in Chapters 4 and 5 when compressibility and capillary pressure are introduced. The MOC is, however, a very useful method for forming analytical solutions for simplified conditions of injecting CO₂ into a saline aquifer. These analytical solutions are vital to have as they provide a benchmark to compare to the outputs of the numerical models that are built in later chapters of the thesis, and therefore help to verify their accuracy. This is particularly important to have when modelling a situation such as this, when the real-life data, especially for the time scales needed, is limited.

Chapter 4 uses the MOL to create a numerical model for two component (CO₂ and water) and two phase (gaseous and aqueous) flow in a radial system, incorporating both capillary pressure and compressibility. The first step to doing this is to choose appropriate primary dependent variables (PDVs) to solve for (in this case, the global pressure, P , and the mass fraction of CO₂, z_c). Expressions are then found using the governing equations for $\frac{\partial z_c}{\partial t}$ and

$\frac{\partial P}{\partial t}$, and the finite difference method is used to discretise in space, hence reducing these expressions to ODEs in which the only derivatives are with respect to time. These ODEs are solved by MATLAB's ODE solver, ode15s, to give the values of the PDVs at all points in time and space. Plots are then given of the global pressure and gas saturation at all points in space for various times up to 100 years. These outputs are largely as expected, as the graph for gas saturation shows the three different phase 'regions' that have been shown on schematic diagrams in previous chapters (gaseous only, two phases, and aqueous only) as well as a larger dry out zone as time passes, as water has had more time to evaporate into the gas only region. The graph for pressure illustrates that pressure increases as more CO₂ is injected into the formation, and that the pressure is at its highest near the point of injection. Both figures also compare very well with the analytical solution of [Mathias et al. \(2011b\)](#), which shows the variation in pressure and gas saturation for the partially miscible two phase system in which capillary pressure is neglected. However, as the value of the capillary pressure at oven dry conditions is increased, a dip in the graph for pressure close to the boundary between the gaseous only and two phase regions becomes clearer. As this only seems to affect one point in space, it is thought that this may again be due to a numerical instability. With the exception of this one point, the model appears to simulate two phase flow very well.

Chapter 5 also uses the MOL, and very similar methods to Chapter 4, to form a numerical model for three component (CO₂, water and salt) and three phase (gaseous, aqueous and solid) flow, which can therefore more accurately simulate the conditions in a real-life saline aquifer. However, the additional component and phase make the model significantly more complicated to form mathematically, as more possible combinations of phases need to be considered and three PDVs (P , z_c and z_w) are required, as opposed to two for the two phase model, meaning that it is necessary to form an additional ODE. Conditions are derived in z_c and z_n to denote the presence and absence of certain phases, and piecewise functions are given for the values of parameters depending on the phases present. The output of the model again shows that the pressure and gas saturation compare well to the analytical solution of [Mathias et al. \(2011b\)](#) for times up to 100 years, although the instability causing the dip in pressure as an aqueous phase begins to appear is still present. The solid saturation (the volume fraction of precipitated salt) for times up to 100 years is also plotted, and, despite some instability, appears to be as expected. It is zero for all points in space outside of the dry out zone, and is almost constant throughout this region. The chapter also introduces the capillary number, Ca, which takes into account the thickness, permeability and air entry pressure of the porous medium and the injection

rate and viscosity of CO_2 . It illustrates that the gas saturation value in the dry out zone decreases as Ca decreases, corresponding to an increase in solid saturation as Ca decreases. A decrease in Ca corresponds to a decrease in the injection rate, and so this indicates that reducing the rate that CO_2 is injected into an aquifer can considerably increase the volume of salt precipitation formed.

The MOL has been useful in allowing us to create a three component and three phase numerical model which is able to show how the phase saturations and pressure would vary with space and time in a saline aquifer, as well as give an idea of the parameters that control the volume of solid saturation in the dry out zone. However, the resulting model has numerical problems. Numerical instabilities have given rise to an unrealistic dip in pressure at the end of the dry out zone. In addition to this, the MOL models predict an unrealistic spike in solid saturation within the dry out zone. Furthermore, it is found that the MOL scheme is unable to complete simulations of interest when appropriate grid resolutions are applied, due to numerical convergence problems within the ode15s solver.

Therefore, Chapter 6 moves on to finding an alternative method of solution by extending the McWhorter and Sunada equation (McWhorter and Sunada, 1990), which looks at two phase immiscible flow with capillary pressure. In particular, the similarity solution of McWhorter and Sunada (1990) is extended by providing an additional component and phase and allowing for the effects of partial miscibility, therefore producing a solution that can simulate the three phase conditions with partial miscibility and capillary pressure when CO_2 is injected into a saline aquifer, and look into the effects that varying certain parameters has on the volume of salt precipitation formed.

One of the key findings from this chapter is related to the capillary number, Ca , that was introduced in Chapter 5. As was the case with the output of the three phase numerical model, it was found that the volume fraction of precipitated salt in the dry out zone (C_{30}) is largely controlled by Ca , and that decreasing the value of Ca , which can be seen as analogous to reducing the rate of injection of CO_2 into the formation, leads to a superlinear increase in the volume fraction of precipitated salt. The solution shows that reducing the injection rate from 15 kg s^{-1} to 1.8 kg s^{-1} leads to a doubling of the volume fraction of precipitated salt around the injection well, while reducing the rate of injection from 15 kg s^{-1} to 0.9 kg s^{-1} means that the volume fraction of salt precipitated almost multiplies by ten. It should also be noted that a decreasing Ca means that the thickness of the dry out zone reduces, to the extent that it would eventually be completely eliminated.

Both of these observations can be attributed to the increased effect of counter-current imbibition bringing additional water and salt to the site of injection at a lower rate of injection.

This chapter also looks at the effect of fluid property changes associated with changes in aquifer formation depth. When the value of Ca is greater than 0.25, the main control on C_{30} is the salinity of the brine, and the depth of the formation has very little effect. However, as Ca decreases below 0.25, depth has an increasingly larger role. The shallower the formation, the smaller the volume of the dry out zone, and so the higher the volume fraction of precipitated salt around the site of injection.

Another area that the chapter investigates is the effect of the value of the relative permeability parameters, k_{rj0} , S_{jc} and n_j , on salt precipitation. It is found that both the maximum value of C_{30} and the critical Ca value below which the volume fraction of salt precipitation begins to superlinearly increase vary considerably depending on these parameters, and in particular with n_2 , which controls the linearity of the relative permeability of brine. When n_2 is lower, and so the relative permeability of brine is more linear, the value of C_{30} is lower at high values of Ca , but begins to superlinearly increase at a relatively high value of Ca . For higher values of n_2 , and so a highly nonlinear relative permeability of brine, the opposite happens, and the value of C_{30} remains stable for lower capillary numbers. This is due to counter-current imbibition not being as efficient for highly nonlinear relative permeability.

The main conclusions of this thesis can be summarised as follows. Several parameters have a significant effect on the volume fraction of salt formed, including the depth of the aquifer, the salinity of the brine and the linearity of the relative permeabilities, but the main control is the dimensionless capillary number, Ca . Decreasing the value of Ca is analogous to reducing the injection rate of CO_2 into the formation, and leads to a superlinear increase in the volume fraction of salt precipitation in the aquifer. This is mainly explained by capillary pressure processes. High capillary pressure gradients in the dry out zone of a saline aquifer provide a driving force for the backflow of brine towards the point of CO_2 injection, resulting in additional salt in the dry out zone that can also precipitate. The lower the rate of injection and hence the lower the value of Ca , the higher the relative effect that this counter-current imbibition has, resulting in a higher volume fraction of salt precipitation. The method of characteristics is not a suitable method for studying this problem because capillary pressure effects give rise to a non-hyperbolic equation. The

method of lines should be an appropriate framework for studying this problem. However, the presence of salt gives rise to significant numerical stability that has prevented useful MOL solutions to be developed during this project. Instead, improved understanding in this area has been achieved by extending the similarity solution for immiscible two phase flow of McWhorter and Sunada to account for three phases and partial miscibility.

7.2 Future Work

Future work on the simulation of salt precipitation as CO₂ is injected into brine aquifers could aim to improve the numerical models formed in Chapters 4 and 5, in particular the three phase model in Chapter 5, as their outputs are strongly affected by numerical instabilities. Due to the instabilities produced in the models with the finite difference scheme currently used and the use of the MOL, it may be best to look into alternative numerical schemes and methods to solve the partial differential equations (PDEs) in order improve their accuracy. One possible way to do this would be to change the numerical scheme to a higher order finite difference method, but a disadvantage would be that this would mean more surrounding grid points would be used when approximating a solution at a particular point, meaning that the model would be more computationally intensive to run. It appears that the time stepping used in the models needs to be at a better resolution, so it may be that the use of MATLAB's ODE solvers was not the best option, and alternative time stepping methods should be considered.

One potential method is the use of a semi-implicit ImPEM (Implicit Pressure Explicit Mass) implementation, in which the pressure and transport equations are decoupled and the pressure equation is firstly solved implicitly, followed by the transport equation being solved explicitly (Doster et al., 2014). The pressure equation is typically of an elliptic or parabolic nature and so must be discretised implicitly to avoid severe time step restrictions, while the transport equations are often dominated by hyperbolic advection and so time step restrictions are less severe. As the scheme is not fully implicit, it is not unconditionally stable and time steps need to be chosen carefully, but it provides a reasonably accurate, easy to implement and computationally efficient numerical scheme. Doster et al. (2014) looked into implementing an ImPEM scheme on a system with two component and two phase flow, including the effects of compressibility, capillary pressure and gravity, and so extending this to a three component and three phase system so that it could be used to simulate salt precipitation in a saline formation would be a promising possibility.

It would also be interesting to extend the models in Chapters 4 and 5, as well as the similarity solution found in Chapter 6, to two dimensions. Although Chapter 6 concluded that the inclusion of the effects of gravity were unlikely to significantly influence the dry out zone in the saline formations studied, especially for the lower capillary numbers, it would still be beneficial to conduct a full investigation of saline formations in two dimensions in order to more realistically model real-life saline aquifers and look further into the phenomenons that can occur within them that will be strongly affected by gravity, such as buoyancy driven flow and viscous fingering.

Another area to look into, and perhaps incorporate into models and solutions for the build-up of salt precipitation in a saline aquifer, is potential ways to mitigate the salt precipitation formed. The work that has been done on this was summarised by [Miri and Hellevang \(2016\)](#). [Hurter et al. \(2008\)](#) and [Pruess and Müller \(2009\)](#) both simulated the injection of CO₂ into saline formations and found that the injection of fresh water, even for a short time, before beginning CO₂ injection delayed the onset of salt precipitation and reduced its severity, as well as reducing the pressure build-up. Other potential mitigation strategies involve the regular injection of a 90:10 mixture of methyl ethyl glycol and water, which has been shown to be effective in improving injectivity at Snøhvit ([Hansen et al., 2013](#)), and filling the perforation interval between the borehole and the aquifer with highly permeable materials ([Miri and Hellevang, 2016](#)). Simulating potential methods for the mitigation of salt precipitation would provide a more detailed insight into the level that salt precipitation in a saline aquifer impacts on the viability of saline aquifers as a storage option for CO₂ as part of CCS.

Bibliography

- Anderson, G.M. (2005) *Thermodynamics of natural systems*. Second Edition. New York: Cambridge University Press.
- Ashino, R., Nagase, M. and Vaillancourt, R. (2000) 'Behind and beyond the MATLAB ODE suite' *Computers and Mathematics with Applications*, 40(4-5), pp.491-512.
- Bacci, G., Korre, A. and Durucan, S. (2011) 'Experimental investigation into salt precipitation during CO₂ injection in saline aquifers', *Energy Procedia*, 4, pp.4450-4456.
- Batzle, M. and Wang, Z. (1992) 'Seismic properties of pore fluids' *Geophysics*, 57(11), pp.1396-1408.
- Bear, J. (1988) *Dynamics of Fluids in Porous Media*. Rev. edition. New York: American Elsevier Publishing Company, Inc.
- Bennion, B. and Bachu, S. (2008) 'Drainage and imbibition relative permeability relationships for supercritical CO₂/brine and H₂S/brine systems in intergranular sandstone, carbonate, shale, and anhydrite rocks', *SPE Reservoir Evaluation and Engineering*, 11(03), pp.487-496.
- Bickle, M.J. (2009) 'Geological carbon storage', *Nature Geoscience*, 2(12), pp.815-818.
- Bjørnarå, T.I. and Mathias, S.A. (2013) 'A pseudospectral approach to the McWhorter and Sunada equation for two-phase flow in porous media with capillary pressure' *Computational Geosciences*, 17, pp.889-897.
- Blunt, M.J. (2017) *Multiphase flow in permeable media: a pore-scale perspective*. Cambridge: Cambridge University Press.
- Boyd, J.P. (2001) *Chebyshev and Fourier spectral methods*. Second Edition. New York: Dover Publications, Inc.
- Brooks, R. and Corey, T. (1964) *Hydraulic Properties of Porous Media*. Hydrology Papers, Colorado State University, 24.

- Buckley, S.E. and Leverett, M. (1942) 'Mechanism of fluid displacement in sands' *Transactions of the AIME*, 146(01), pp.107-116.
- Campbell, G.S. and Shiozawa, S. (1992), 'Prediction of hydraulic properties of soils using particle-size distribution and bulk density data', *International Workshop on Indirect Methods for Estimating the Hydraulic Properties of Unsaturated Soils*. University of California, Riverside, October 1992. pp.317-328.
- Carpita, M., Giorgis, T. and Battistelli, A. (2006) 'Modeling CO₂ injection with halite precipitation using an extended Verma and Pruess porosity-permeability model', *Proceedings of the TOUGH Symposium*, Berkeley, California, 15-17 May. Available at: https://www.researchgate.net/profile/Alfredo_Battistelli/publication/260283819_Modeling_CO2_injection_with_halite_precipitation_using_an_extended_Verma_Pruess_porosity-permeability_model/links/0deec5309c013862d0000000.pdf (Accessed: 28th March 2018).
- Cavanagh, A.J. and Hazeldine, R.S. (2014) 'The Sleipner storage site: Capillary flow modeling of a layered CO₂ plume requires fractured shale barriers within the Utsira Formation', *International Journal of Greenhouse Gas Control*, 21, pp.101-112.
- Celia, M.A., Bachu, S., Nordbotten, J.M. and Bandilla, K.W. (2015) 'Status of CO₂ storage in deep saline aquifers with emphasis on modeling approaches and practical simulations', *Water Resources Research*, 51, pp.6846-6892, doi:10.1002/2015WR017609.
- Cengel, Y.A. and Boles, M.A. (2002) *Thermodynamics: an Engineering Approach*. Fifth Edition. New York: McGraw-Hill Higher Education.
- Chadwick, R.A., Noy, D.J. and Holloway, S. (2009), 'Flow processes and pressure evolution in aquifers during the injection of supercritical CO₂ as a greenhouse gas mitigation measure', *Petroleum Geoscience*, 15(1), pp.59-73.
- Chen, Z.X. (1988) 'Some invariant solutions to two-phase fluid displacement problems including capillary effect (includes associated papers 18744 and 19037)' *SPE reservoir engineering*, 3(02), pp.691-700.
- Class, H., Ebigbo, A., Helmig, R., Dahle, H.K., Nordbotten, J.M., Celia, M.A.,... and Wei, L. (2009) 'A benchmark study on problems related to CO₂ storage in geologic formations. Summary and discussion of the results', *Computational Geosciences*, 13, pp.409-434, doi:10.1007/s10596-009-9146-x

- Coan, C.R. and King Jr, A.D. (1971) ‘Solubility of water in compressed carbon dioxide, nitrous oxide, and ethane. Evidence for hydration of carbon dioxide and nitrous oxide in the gas phase’, *Journal of the American Chemical Society*, 93(8), pp.1857-1862.
- Corey, A.T. (1954) ‘The interrelation between gas and oil relative permeabilities’, *Producers Monthly*, 19(1), pp.38-41.
- Corless, R.M., Gonnet, G.H., Hare, D.E., Jeffrey, D.J., and Knuth, D.E. (1996) ‘On the Lambert W function’, *Advances in Computational Mathematics*, 5(1), pp.329-359.
- Denbigh, K. (1966) *The Principles of Chemical Equilibrium: With Applications in Chemistry and Chemical Engineering*. Second Edition. Cambridge University Press.
- Doster, F., Keilegavlen, E., and Nordbotten, J. M. (2014) ‘Multi-phase multi-component flow including capillary pressure and buoyancy: a robust implicit pressure explicit mass finite volume method’, *Computational Models for CO₂*.
- Duan, Z. and Sun, R. (2003) ‘An improved model calculating CO₂ solubility in pure water and aqueous NaCl solutions from 273 to 533 K and from 0 to 2000 bar’, *Chemical Geology*, 193(3-4), pp.257-271.
- Eiken, O., Ringrose, P., Hermanrud, C., Nazarian, B., Torp, T.A. and Høier, L. (2011) ‘Lessons Learned from 14 years of CCS Operations: Sleipner, In Salah and Snøhvit’, *Energy Procedia*, 4, pp.5541-5548.
- Fučík, R., Mikyška, J., Beneš, M. and Illangasekare, T.H. (2007) ‘An improved semi-analytical solution for verification of numerical models of two-phase flow in porous media’ *Vadose Zone Journal*, 6(1), pp.93-104.
- Fuller, R.C., Prevost, J.H. and Piri, M. (2006) ‘Three-phase equilibrium and partitioning calculations for CO₂ sequestration in saline aquifers’ *Journal of Geophysical Research: Solid Earth*, 111(B6), doi: 10.1029/2005JB003618.
- Garcia, J.E. (2001) ‘Density of aqueous solutions of CO₂’ *Lawrence Berkeley National Laboratory*.
- Gershenson, N.I., Ritzi Jr, R.W., Dominic, D.F., Mehnert, E. and Okwen, R.T. (2016) ‘Comparison of CO₂ trapping in highly heterogeneous reservoirs with Brooks-Corey and van Genuchten type capillary pressure curves’, *Advances in Water Resources*, 96, pp.225-236.
- Gillepsie, P.C. and Wilson, G.M. (1982) ‘Vapor-Liquid and Liquid-Liquid Equilibria: Water-Methane, Water-Carbon Dioxide, Water-Hydrogen Sulfide, Water-nPentane,

- Water-Methane-nPentane', *Research Report RR-48, Gas Processors Association, Tulsa, OK*.
- Goudarzi, S., Mathias, S.A. and Gluyas, J.G. (2016). 'Simulation of three-component two-phase flow in porous media using method of lines' *Transport in Porous Media*, 112(1), pp.1-19.
- Goudarzi, S. (2017) *Modelling Enhanced Gas Recovery by CO₂ Injection in Partially-Depleted Reservoirs*. PhD Thesis. Durham University. Available at: <http://etheses.dur.ac.uk/11645/> (Accessed: 23rd July 2018).
- Gratton, J. (1991) 'Similarity and self similarity in fluid dynamics' *Fundamentals of Cosmic Physics*, 15, pp.1-106.
- Hansen, O., Gilding, D., Nazarian, B., Osdal, B., Ringrose, P., Kristoffersen, J. B.,... and Hansen, H. (2013) 'Snøhvit: The history of injecting and storing 1 Mt CO₂ in the fluvial Tubåen Fm', *Energy Procedia*, 37, pp.3565-3573.
- Helfferich, F.G. (1981) 'Theory of Multicomponent, Multiphase Displacement in Porous Media' *Society of Petroleum Engineers Journal*, 21, pp.52-62
- Hesse, M.A., Tchelepi, H.A., Cantwel, B.J. and Orr, F.M. (2007) 'Gravity currents in horizontal porous layers: transition from early to late self-similarity' *Journal of Fluid Mechanics*, 577, pp.363-383.
- Hesse, M.A., Orr, F.M. and Tchelepi, H.A. (2008) 'Gravity currents with residual trapping' *Journal of Fluid Mechanics*, 611, pp.35-60.
- Hoffman, J. and Frankel, S. (2001) *Numerical Methods for Engineers and Scientists*. Second Edition. New York: CRC Press.
- Hosa, A., Esentia, M., Stewart, J., Hazeldine, S. (2011) 'Injection of CO₂ into saline formations: Benchmarking worldwide projects', *Chemical Engineering Research and Design*, 89, pp.1855-1864.
- Hosseini, S.A., Mathias, S.A. and Javadpour, F. (2012) 'Analytical Model for CO₂ Injection into Brine Aquifers- Containing Residual CH₄', *Transport in Porous Media*, 94, pp.795-815.
- Hurter, S., Labregere, D., Berge, J. and Desitter, A. (2008). 'Impact of mutual solubility of H₂O and CO₂ on injection operations for geological storage of CO₂' *In International Conference of the Properties of Water and Steam ICPWS*, Berlin, September (pp. 8-11).

- Kelly, H.L. and Mathias, S.A. (2018) ‘Capillary processes increase salt precipitation during CO₂ injection in saline formations’ *Journal of Fluid Mechanics*, 852, pp.398-421.
- Kessel, D.G. (2000) ‘Global warming- facts, assessment, countermeasures’, *Journal of Petroleum Science and Engineering*, 26, pp.157-168.
- Kim, K.Y., Han, W.S., Oh, J., Kim, T., and Kim, J.C. (2012) ‘Characteristics of salt-precipitation and the associated pressure build-up during CO₂ storage in saline aquifers’ *Transport in Porous Media*, 92(2), pp.397-418.
- King, M.B., Mubarak, A., Kim, J.D. and Bott, T.R. (1992) ‘The mutual solubilities of water with supercritical and liquid carbon dioxide’, *The Journal of Supercritical Fluids*, 5(4), pp.296-302.
- Knobel, R. (2000) *An Introduction to the Mathematical Theory of Waves*. United States of America: American Mathematical Society.
- Krevor, S., Pini, R., Zuo, L. and Benson, S.M. (2012) ‘Relative permeability and trapping of CO₂ and water in sandstone rocks at reservoir conditions’, *Water Resources Research*, 48(2).
- Le Quéré, C., Moriarty, R., Andrew, R.M., Canadell, J.G., Sitch, S., Korsbakken, J.I.,... and Zeng, N. (2015) ‘Global Carbon Budget 2015’, *Earth System Science Data*, 7, pp.349-396.
- LeVeque, R.J. (1992) *Numerical Methods for Conservation Laws*. Second Edition. Basel, Switzerland: Birkhauser Verlag.
- LeVeque, R.J. (2004) *Finite-Volume Methods for Hyperbolic Problems*. Cambridge: Cambridge University Press.
- LeVeque, R.J. (2007) *Finite Difference Methods for Ordinary and Partial Differential Equations: Steady-State and Time-Dependent Problems*. Philadelphia: Society for Industrial and Applied Mathematics.
- Li, B., Tchelepi, H.A. and Benson, S.M. (2013) ‘Influence of capillary-pressure models on CO₂ solubility trapping’, *Advances in Water Resources*, 62, pp.488-498.
- MacMinn, C.W., Szulczewski, M.L. and Juanes, R. (2010) ‘CO₂ migration in saline aquifers. Part 1. Capillary trapping under slope and groundwater flow’ *Journal of Fluid Mechanics*, 662, pp.329-351.

- MacMinn, C.W., Szulczewski, M.L. and Juanes, R. (2011) 'CO₂ migration in saline aquifers. Part 2. Capillary and solubility trapping' *Journal of Fluid Mechanics*, 688, pp.321-351.
- Marle, C.M. (1981) *Multiphase Flow in Porous Media*. Paris: Technip.
- Mathias, S.A., González Martínez de Miguel, G.J., Thatcher, K.E. and Zimmerman, R.W. (2011) 'Pressure buildup during CO₂ injection into a closed brine aquifer' *Transport in Porous Media*, 89(3), pp.383-397.
- Mathias, S.A., Gluyas, J.G., González Martínez de Miguel, G.J. and Hosseini, S.A. (2011). 'Role of partial miscibility on pressure buildup due to constant rate injection of CO₂ into closed and open brine aquifers' *Water Resources Research*, 47(12), doi:10.1029/2011WR011051.
- Mathias, S.A., Gluyas, J.G., González Martínez de Miguel, G.J., Bryant, S.L. and Wilson, D. (2013) 'On relative permeability data uncertainty and CO₂ injectivity estimation for brine aquifers', *International Journal of Greenhouse Gas Control*, 12, pp.200-212.
- Mathias, S.A., McElwaine, J.N. and Gluyas, J.G. (2014) 'Heat transport and pressure buildup during carbon dioxide injection into depleted gas reservoirs' *Journal of Fluid Mechanics*, 756, pp.89-109.
- McWhorter, D.B. and Sunada, D.K. (1990) 'Exact Integral Solutions for Two-Phase Flow' *Water Resources Research*, 26(3), pp.399-413.
- Miri, R. and Hellevang, H. (2016) 'Salt precipitation during CO₂ storage- A review', *International Journal of Greenhouse Gas Control*, 51, pp.136-147.
- National Oceanic and Atmospheric Administration: National Centers for Environmental Information (2010) *Global Climate Change Indicators* Available at: <https://www.ncdc.noaa.gov/monitoring-references/faq/indicators.php> (Accessed: 13th March 2018).
- Nordbotten, J.M. and Celia, M.A. (2006) 'Similarity solutions for fluid injection into confined aquifers' *Journal of Fluid Mechanics*, 561, pp.307-327.
- Oostrom, M., White, M.D., Porse, S.L., Krevor, S.C.M. and Mathias, S.A. (2016) 'Comparison of relative permeability-saturation-capillary pressure models for simulation of reservoir CO₂ injection', *International Journal of Greenhouse Gas Control*, 45, pp.70-85.
- Orr, F.M. (2007) *Theory of Gas Injection Processes*. Holte, Denmark: Tie-Line Publications.

- Perrin, J.C. and Benson, S. (2010) ‘An experimental study on the influence of sub-core scale heterogeneities on CO₂ distribution in reservoir rocks’, *Transport in Porous Media*, 82(1), pp.93-109.
- Peysson, Y., André, L. and Azaroual, M. (2014) ‘Well injectivity during CO₂ storage operations in deep saline aquifers- Part 1: Experimental investigation of drying effects, salt precipitation and capillary forces’, *International Journal of Greenhouse Gas Control*, 22, pp.291-300.
- Piché, R., and Kanninen, J. (2009) ‘Matrix-based numerical modelling of financial differential equations’ *International Journal of Mathematical Modelling and Numerical Optimisation*, 1(1-2), pp.88-100.
- Potter, R.W., Babcock, R.S. and Brown, D.L. (1977) ‘A new method for determining the solubility of salts in aqueous solutions at elevated temperatures’, *Journal of Research of the U.S. Geological Survey*, 5(3), pp.389-395.
- Prausnitz, J.M., Lichtenthaler, R.N. and de Azevedo, E.G. (1998) *Molecular thermodynamics of fluid-phase equilibria*. Third Edition. New Jersey: Prentice Hall PTR.
- Pruess, K. and Müller, N. (2009) ‘Formation dry-out from CO₂ injection into saline aquifers: 1. Effects of solids precipitation and their mitigation’, *Water Resources Research*, 45, W03402, doi:10.1029/2008WR007101.
- Pruess, K. and Spycher, N. (2007) ‘ECO2N- A fluid property module for the TOUGH2 code for studies of CO₂ storage in saline aquifers’ *Energy Conversion and Management*, 48(6), pp.1761-1767.
- Redlich, O. and Kwong, J.N. (1949) ‘On the thermodynamics of solutions. V. An equation of state. Fugacities of gaseous solutions’, *Chemical Reviews*, 44(1), pp.233-244.
- Riebeek, H. (2010) *Global warming* Available at: <http://earthobservatory.nasa.gov/Features/GlobalWarming/page6.php> (Accessed: 13th March 2018).
- Robertson, E.C., Robie, R.A. and Books, K.G. (1958) ‘Physical properties of salt, anhydrite and gypsum: preliminary report’, No. 1048.
- Rumpf, B., Nicolaisen, H., Öcal, C. and Maurer, G. (1994) ‘Solubility of carbon dioxide in aqueous solutions of sodium chloride: experimental results and correlation’, *Journal of Solution Chemistry*, 23(3), pp.431-448.
- Rutqvist, J., Birkholzer, J., Cappa, F. and Tsang, C.F. (2007) ‘Estimating maximum sustainable injection pressure during geological sequestration of CO₂ using coupled fluid

- flow and geomechanical fault-slip analysis', *Energy Conversion and Management*, 48(6), pp.1798-1807.
- Smith, E.B. (2004) *Basic chemical thermodynamics*. Fifth Edition. London: Imperial College Press.
- Spycher, N., Pruess, K. and Ennis-King, J. (2003) 'CO₂-H₂O mixtures in the geological sequestration of CO₂. I. Assessment and calculation of mutual solubilities from 12 to 100°C and up to 600 bar', *Geochimica et Cosmochimica Acta*, 67(16), pp.3015-3031.
- Spycher, N. and Pruess, K. (2005) 'CO₂-H₂O mixtures in the geological sequestration of CO₂. II. Partitioning in chloride brines at 12-100°C and up to 600 bar' *Geochimica et Cosmochimica Acta*, 69(13), pp.3309-3320.
- Trefethen, L.N. (2000) *Spectral methods in MATLAB*. Vol. 10. Philadelphia: Siam.
- van Genuchten, M.T. (1980) 'A closed-form equation for predicting the hydraulic conductivity of unsaturated soils', *Soil Science Society of America Journal*, 44(5), pp.892-898.
- Verma, A. and Pruess, K. (1988) 'Thermohydrological conditions and silica redistribution near high-level nuclear wastes emplaced in saturated geological formations', *Journal of Geophysical Research: Solid Earth*, 93(B2), pp.1159-1173.
- Webb, S.W. (2000) 'A simple extension of two-phase characteristic curves to include the dry region', *Water Resources Research*, 36(6), pp.1425-1430.
- Weideman, J.A. and Reddy, S.C. (2000) 'A MATLAB differentiation matrix suite', *ACM Transactions on Mathematical Software (TOMS)*, 26(4), pp.465-519.
- Welge, H.J. (1952) 'A simplified method for computing oil recovery by gas or water drive' *Journal of Petroleum Technology*, 4(04), pp.91-98.
- Wiebe, R. and Gaddy, V.L. (1940) 'The solubility of carbon dioxide in water at various temperatures from 12 to 40° and at pressures to 500 atmospheres', *Journal of the American Chemical Society*, 62(4), pp.815-17.
- Wiebe, R. and Gaddy, V.L. (1941) 'Vapor phase composition of carbon dioxide-water mixtures at various temperatures and at pressures to 700 atmospheres', *Journal of the American Chemical Society*, 63(2), pp.475-477.
- Younis, M.I. (2011) *MEMS Linear and Nonlinear Statics and Dynamics*. New York: Springer Science and Business Media.

- Zeidouni, M., Pooladi-Darvish, M. and Keith, D. (2009) 'Analytical solution to evaluate salt precipitation during CO₂ injection in saline aquifers', *International Journal of Greenhouse Gas Control*, 3, pp.600-611.
- Zhang, Z.F., Oostrom, M. and White, M.D. (2016) 'Relative permeability for multiphase flow for oven-dry to full saturation conditions', *International Journal of Greenhouse Gas Control*, 49, pp.259-266.
- Zhou, Q., Birkholzer, J.T., Tsang, C.F. and Rutqvist, J. (2008) 'A method for quick assessment of CO₂ storage capacity in closed and semi-closed saline formations', *International Journal of Greenhouse Gas Control*, 2(4), pp.626-639.
- Zhao, J. and Wen, D. (2017) 'Pore-scale simulation of wettability and interfacial tension effects on flooding process for enhanced oil recovery', *RSC advances*, 7(66), pp.41391-41398.
- Zhu, Q., Zuo, D., Zhang, S., Zhang, Y., Wang, Y. and Wang, L. (2015) 'Simulation of geomechanical responses of reservoirs induced by CO₂ multilayer injection in the Shenhua CCS project, China', *International Journal of Greenhouse Gas Control*, 42, pp.405-414.